UC Merced

UC Merced Electronic Theses and Dissertations

Title

Superconducting quantum circuits theory and application

Permalink

https://escholarship.org/uc/item/4z51f5nd

Author

Deng, Xiuhao

Publication Date

2015

Copyright Information

This work is made available under the terms of a Creative Commons Attribution License, availalbe at https://creativecommons.org/licenses/by/4.0/

Peer reviewed|Thesis/dissertation

eScholarship.org Powered by the California Digital Library
University of California

UNIVERSITY OF CALIFORNIA, MERCED

Superconducting quantum circuits theory and application

by

Xiuhao Deng

A dissertation submitted in partial satisfaction of the
requirements for the degree of
Doctor of Philosophy

in

Physics

Committee in charge:
Professor Kevin Mitchell, Chair
Professor Raymond Chiao
Professor Jay Sharping
Professor Chih-Chun Chien
Professor Boaz Ilan

Spring 2015

© 2015 Xiuhao Deng
All rights are reserved.

The dissertation of Xiuhao Deng is approved:

Kevin Mitchell, Chair	Date
Raymond Chiao	Date
Jay Sharping	Date
Chih-Chun Chien	Date
Boaz Ilan	Date

University of California, Merced

©Spring 2015

To my parents

Acknowledgments

First of all, I would like to sincerely thank my advisor Professor Raymond Chiao. Two years ago, when I was very frustrated, he gave me a lot of helpful advice and inspiration. He encouraged me to do what I am interested in. His enthusiasm in scientific research is like a lighthouse guiding me. Finally I am finishing this Ph.D. program, I have so many thanks to give for all of his help. Wish Ray sincerely for the best and a good health.

Thank professor Chih-Chun Chien for advising me. He is always nice and patient for discussion and answering my questions. He also gave me a lot of thoughtful suggestions for my career and study. I enjoy a lot working with him for recent projects. Thank all the committee. Especially, professor Kevin Mitchell has been my committee member since 2010. I am so glad to have him as my committee chair for knowing my stories and what I have been working on since the beginning. Thank professor Jay Sharping for being so patient and considerable. Whenever there is a chance we have group meeting together, he can give detailed advice for me. I learned a lot from him about organizing details with notes, tables and spreadsheet. Thank professor Boaz Ilan for encouraging me on the thesis. This dissertation for me personally is some kind of legacy that can be saved for the future and as a summary of my work during these years.

Thank my group members. It was so enjoyable to have discussion with them. Wish the best for our future career! Thank all my friends and the people that have been helping!

Most specially, thank my parents. My doctoral degree would be a gift for them two, particularly, my father who didn't get a chance to pursue a Ph.D. when he was quite capable for research.

Curriculum Vitae

Education:

Ph.D. in Physics, School of Natural Science. University of California, Merced (UCM). Merced, CA, USA. Sep. 2009-Aug. 2015

Ph.D. candidate in Physics, University of Science and Technology of China (USTC). Hefei, Anhui, China. Sep. 2006-Jun. 2009

B.S. in Theoretical Physics, University of Science and Technology of China (USTC) Sep. 2001-Jul. 2005

Publications:

[1] Xiu-Hao Deng, Chunjing Jia, Chih-Chun Chien, Sitewise manipulations and Mott insulator-superfluid transition of interacting photons using superconducting circuit simulators, Physical Review B 91, 054515 (2015)

[2] RY Chiao, XH Deng, KM Sundqvist, NA Inan, GA Munoz, DA Singleton, BS Kang, LA Martinez, Observability of the scalar Aharonov-Bohm effect inside a 3D Faraday cage with time-varying exterior charges and masses, arXiv:1411.3627

[3] XH Deng, Y Hu, L Tian, Protecting superconducting qubits with a universal quantum degeneracy point, Superconductor Science and Technology 26, 114002 (2013)

[4] AV Sharypov, X Deng, L Tian, Parametric four-wave mixing toolbox for superconducting resonators, Physical Review B 86 (1), 014516 (2012)

[5] Y Dong, X Deng, M Jiang, Q Chen, S Yu, Entanglement-enhanced quantum error-correcting codes, Physical Review A 79, 042342 (2009)

Honors and Awards:

Jan. 2014	UC Merced Graduate Student Fellowship
Jun. 2009	China Scholarship Council (CSC) scholarship for studying abroad.
Oct. 2001	USTC Freshmen Scholarship.

Contents

List of Figures

Abstract

Superconducting quantum circuits theory and application
by
Xiuhao Deng
Doctor of Philosophy
in
School of Natural Science
University of California, Merced
Advisor: Professor Raymond Chiao

Superconducting quantum circuit models are widely used to understand superconducting devices. This thesis consists of four studies wherein the superconducting quantum circuit is used to illustrate challenges related to quantum information encoding and processing, quantum simulation, quantum signal detection and amplification.

The existence of scalar Aharanov-Bohm phase has been a controversial topic for decades. Scalar AB phase, defined as time integral of electric potential, gives rises to an extra phase factor in wavefunction. We proposed a superconducting quantum Faraday cage to detect temporal interference effect as a consequence of scalar AB phase. Using the superconducting quantum circuit model, the physical system is solved and resulting AB effect is predicted. Further discussion in this chapter shows that treating the experimental apparatus quantum mechanically, spatial scalar AB effect, proposed by Aharanov-Bohm, can't be observed. Either a decoherent interference apparatus is used to observe spatial scalar AB effect, or a quantum Faraday cage is used to observe temporal scalar AB effect.

The second study involves protecting a quantum system from losing coherence, which is crucial to any practical quantum computation scheme. We present a theory to encode any qubit, especially superconducting qubits, into a universal quantum degeneracy point (UQDP) where low frequency noise is suppressed significantly. Numerical simulations for superconducting charge qubit using experimental parameters show that its coherence time is prolong by two orders of magnitude using our universal degeneracy point approach. With this improvement, a set of universal quantum gates can be performed at high fidelity without losing too much quantum coherence.

Starting in 2004, the use of circuit QED has enabled the manipulation of superconducting qubits with photons. We applied quantum optical approach to model coupled resonators and obtained a four-wave mixing toolbox to operate photons states. The model and toolbox are engineered with a superconducting quantum circuit where two superconducting resonators are coupled via the UQDP circuit. Using fourth order perturbation theory one can realize a complete set of quantum operations between these two photon modes. This helps open a new field to treat photon modes as qubits. Additional, a three-wave mixing scheme using phase qubits permits one to engineer the coupling Hamiltonian using a phase qubit as a tunable coupler.

Along with Feynman's idea using quantum to simulate quantum, superconducting quantum simulators have been studied intensively recently. Taking the advantage of mesoscopic size

of superconducting circuit and local tunability, we came out the idea to simulate quantum phase transition due to disorder. Our first paper was to propose a superconducting quantum simulator of Bose-Hubbard model to do site-wise manipulation and observe Mott-insulator to superfluid phase transition. The side-band cooling of an array of superconducting resonators is solved after the paper was published.

In light of the developed technology in manipulating quantum information with superconducting circuit, one can couple other quantum oscillator system to superconducting resonators in order manipulation of its quantum states or parametric amplification of weak quantum signal. A theory that works for different coupling schemes has been studied in chapter 5. This will be a platform for further research.

Chapter 1

Introduction

1.1 Background

Extrordinary progress has been made in building and improving superconducting quantum devices for various applications throughout these two decades. In biological and medical area, superconducting quantum devices are widely used to detect and manipulate weak signals at quantum level, such as SQUID and other Josephson junction devices. Along the line of operating information at quantum level, quantum computer is expected to be built with superconducting quantum circuits. In 2011, D-wave machine has become the first commercialized quantum computation platform. Using Quantum Annealing approach, one can implement some demonstrative computation on D-wave syistem [1]. Although the algorithm in a quantum annealor is different from traditional quantum algorithm, such as Shor's algorithm, [2] where quantum coherence needs to be preserved consistantly, D-wave machine can solve some optimization problems [3] and is aimed to eventually solve problems such as traveling salesman problem. After all, D-wave machine is just a specialized computation machine for some particular problems. In order to build a generic quantum computer on superconducting circuits, Google, IBM, Microsoft and some other high-tech companies have been investing in research on quantum computing machine using quantum algorithm based on superconducting quantum circuits. Nevertheless, to realize a complete quantum computer that can solve NP-complete problem, [2] there are still a lot of fundamental research to pursue and problems to solve, such as improving coherence time up to shreshold of fault tolerent quantum computing, improving the robustness of superconducting qubits, integrating massive qubits on to a chip, improving quantum operation implemented on chips, improving measurement especially quantum nondemolition measurement (QND), etc. Feymann's idea "using quantum to simulate quantum" inspires physicists to study quantum systems using a quantum simulator. Along the journey towards building quantum computers, intensive research is also focus on using a quantum system based on superonconducting circuits to simulate and study quantum many body physics. [4–6]

Note that, besides the low loss from superconductivity, a key feature of superconducting quantum circuits is its nonlinearity. One of the most important ingredients is Josephson junction, named after B.D.Josephson who discovered and predicted nonlinear Cooper pairs tunneling current through a barrier sandwiched by two superconductors. In 1962, B.D. Josephson

published a suggestion that it should be possible for electron pairs to tunnel between closely spaced superconductors even with no potential difference [7]. Based on this effect, a type of active devices has been popular in superconductor electronics is a junction between two superconductors which is weak enough to allow only a slight overlap of the electron pair wave functions of the two superconductors. Under this condition, electron pairs can pass from one superconductor to the other even with no applied voltage. Such weak links can be formed with fdinsulating tunnel barriers, metal or semiconductors, and even superconductor with grain boundaries, very narrow constrictions or damaged regions.

1.2 Cooper pairs Tunneling: The Josephson Relations

Barriers embeded in-between two superconductors will scatter supercurrent running through each superconductor. Current pass across the barrier in tunneling way. Let's formulate the tunneling current in this section following B.D. Josephson's theory [7, 8]. First consider qualitatively the effect on the pair wave functions in two superconductors that are brought close together. Remember that if the separation between the superconductors is large, the pairs in each can be described by a macroscopic wave function

$$\Psi(\overrightarrow{r}, t) = \left|\Psi(\overrightarrow{r})\right| \exp\{i[\theta(\overrightarrow{r}) - (2E_F/\hbar)t]\}.$$

θ is the gauge invariant phase in a superconductor bulk. The phases of the two wave functions are unrelated and, in fact, are only definable to within arbitrary additive constants. As the separation of the superconductors is reduced, the wave functions penetrate the barrier sufficiently to couple and the system energy is reduced by the coupling. When the energy associated with the coupling exceeds the thermal fluctuation energy, the phases become locked and pairs can pass from one superconductor to the other without energy loss. We shall see that phases of the wave functions are not locked together but rather slip relative to each other at a rate that is precisely related to the voltage.

We now give a simple derivation of the Josephson relations for an arbitrary location in the plane of the junction. [9] The time evolution of the wave functions of the superconductors on each side of a coupled Josephson junction can be described by

$$\begin{aligned} i\hbar\frac{\partial\Psi_1}{\partial t} &= U_1\Psi_1 + K\Psi_2 \\ i\hbar\frac{\partial\Psi_2}{\partial t} &= U_2\Psi_2 + K\Psi_1 \end{aligned} \tag{1.1}$$

where the Us are the energies of the wave functions for the two superconductors and K is a coupling constant that measures the interaction of the two wave functions. It is asumed that a voltage source is applied between the two sides; a difference of energy $e^*(V_2 - V_1) = e^*V$ is imposed between the two sides so that $U_2 - U_1 = e^*V$, e^* is the charge of a pair. For convenience, the zero of energy can be taken midway between the energies U_1 and U_2. Then equations (1.1) become

$$\begin{aligned} i\hbar\frac{\partial\Psi_1}{\partial t} &= \frac{-e^*V}{2}\Psi_1 + K\Psi_2 \\ i\hbar\frac{\partial\Psi_2}{\partial t} &= \frac{e^*V}{2}\Psi_2 + K\Psi_1 \end{aligned} \tag{1.2}$$

It is convenient to express the wave functions in terms of the pair density

$$\Psi_k = \sqrt{n_{s1}^*} e^{i\theta_k} \tag{1.3}$$

where k is 1 or 2. Substituting (1.3) into (1.2), separating real and imaginary parts, and introducing the phase difference across the junction as $\phi = \theta_2 - \theta_1$, we find the following:

$$\frac{\partial n_{s1}^*}{\partial t} = \frac{2}{\hbar} K \sqrt{n_{s1}^* n_{s2}^*} \sin\phi \tag{1.4}$$

$$\frac{\partial n_{s2}^*}{\partial t} = -\frac{2}{\hbar} K \sqrt{n_{s1}^* n_{s2}^*} \sin\phi \tag{1.5}$$

$$\frac{\partial \theta_1}{\partial t} = -\frac{K}{\hbar} \sqrt{\frac{n_{s2}^*}{n_{s1}^*}} \cos\phi + \frac{e^* V}{2\hbar} \tag{1.6}$$

$$\frac{\partial \theta_2}{\partial t} = -\frac{K}{\hbar} \sqrt{\frac{n_{s1}^*}{n_{s2}^*}} \cos\phi - \frac{e^* V}{2\hbar} \tag{1.7}$$

From (1.4) and (1.5) we see that the rate of decrease of pair density in one superconductor is the negative of that in the other. This rate of change represents only a tendency to change. There cannot be an actual change of pair density since that would create a charge imbalance between the electrons and the background of ions; the imbalance is avoided by the currents that flow in the circuit connected to the junction. Thus, the tendency toward rate of change of pair charge density $e^* n_s^*$ times the thickness of the junction electrodes is the density of current flowing from one electrode to the other.

The sign of the current density can be deduced from a comparison with the phenomena in a bulk superconductor. There the current density $\overrightarrow{J}$ is in the opposite direction from that of the gradient of phase $\nabla\theta$, as seen from the following equation

$$p = \hbar \nabla\theta = \frac{m^*}{n^* e^*} \overrightarrow{J}_s + e^* \overrightarrow{A}. \tag{1.8}$$

In the Josephson junction, $\phi > 0$ corresponds to a positive gradient of phase from 1 to 2. Therefore, current density from 2 to 1 is positive when $\phi > 0$. Since there must be a transfer of electrons from 1 to 2 for this current polarity, then $\partial n_{s2}^* / \partial t > 0$. Therefore, K is a negative quantity. Equation (1.4) gives, for the current density from 2 to 1:

$$J = J_c \sin\phi \tag{1.9}$$

where the constant J_c is the critical current density whose value must be found by more sophisticated means [8]. Subtracting (1.6) from (1.7) and equating n_{s1}^* and n_{s2}^* gives the time evolution of the difference of phase across the junction at any point.

$$\frac{\partial \phi}{\partial t} = \frac{2e}{\hbar} V \tag{1.10}$$

where we have used $e^* = -2e$. Equations (1.9) and (1.10) are the Josephson relations that express the behavior of the electron pairs. At nonzero temperature and with nonzero voltage across the junction, there is also a current of quasiparticles. [8] I am not going to details about the theory to treat the simultaneous presence of *pair* and *quasiparticle currents* instead I will just refer to Tinkham's book [[8]] and Duzer's book [[10]].

It can be inferred from (1.9) and (1.10) that coupling of the wave functions reduces the energy below the uncoupled system (for small junctions) by an amount

$$E_c = \frac{\hbar I_c}{2e} \cos\phi \tag{1.11}$$

Here I_c is the critical current in the junction. When $\phi = 0$, the current density is zero and the coupling energy has its maximum value. As the current density is raised to its maximum, $\phi \to \pi/2$ and the coupling energy is reduced to zero. For higher currents, the wave functions become uncoupled and begin to slip relative to each other at a rate determined by (1.10).

The general expression for the maximum zero-voltage current density, the critical current density, in a tunnel junction has been derived from microscopic theory: [9]

$$J_{ctu} = \frac{G_n}{A}\left(\frac{\pi\Delta(T)}{2e}\right) \tanh\frac{\Delta(T)}{2k_BT} \tag{1.12}$$

where G_n is the tunneling conductance for $V \gg 2\Delta/e$ and A is the junction area. Fig.1.1(a) shows the I-V characteristic of a tunnel junction at $T = 0$. The critical current I_c is J_c times the area, assuming the coupling energy is constant over the junction surface, which is the case for a small junction with no applied magnetic field. Notice that I_c equals the tunneling current that would have existed in the absence of pairing at a voltage of about three-quarters ($\pi/4$) of the gap voltage $V_g = 2\Delta/e$. Fig.1.1(b) shows the effect of temperature on lead-insulator-thin and tin-insulator-tin Josephson junctions, as calculated using (1.12) and from experiment.

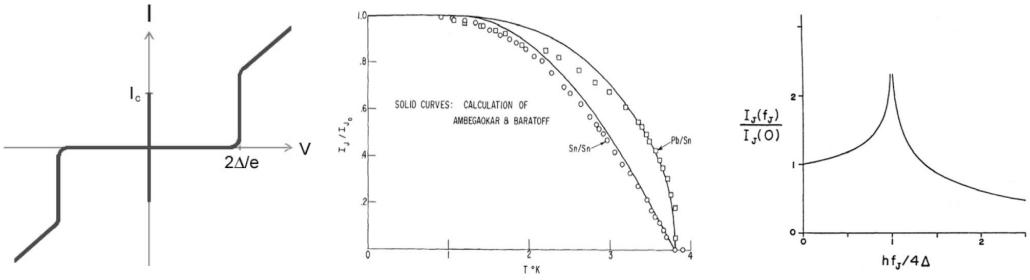

Figure 1.1: (a) I-V characteristic of a tunnel junction at $T = 0$. (b) Temperature dependence of the maximum zero-voltage current from experiment. [11] (c) Dependence of the critical current I_c on the Josephson frequency. The peak occurs where the applied dc voltage is $2\Delta/e$. [12]

1.2.0.1 *DC Effects:*

The DC Josephson effect is a direct current crossing the insulator in the absence of any external electromagnetic field, owing to tunneling. This DC Josephson current is proportional to the sine of the phase difference across the insulator, and may take values between $-I_c$ and I_c, as discribed by Eq.(1.9).

1.2.0.2 *AC Effects:*

If a dc voltage V is applied to a junction, integration of (1.10) shows that

$$\phi = \phi_0 + (2e/\hbar)Vt \tag{1.13}$$

Substitut this into (1.9) one obtains the result

$$I = I_c \sin(\omega_J t + \phi_0) \tag{1.14}$$

so there is an ac current at the frequency

$$f_J = \frac{\omega_J}{2\pi} = (\frac{1}{2\pi})\frac{2e}{\hbar}V. \tag{1.15}$$

The coefficient in the last term in (1.15) is $483.6 \times 10^{12} Hz/V$.(Ref. [10]) It has been shown that I_c is frequency dependent; thus the amplitude of the current oscillations varies with frequency. Riedel [9] predicted the form shown in Fig.1.1(c) and this has been verified experimentally [9]. One important aspect of this result is that substantial ac pair currents flow even when the junction voltage exceeds the gap by several times.

It is of interest to make an observation here about the $I - V$ characteristic in Fig.1.1(a). There it appears that it is possible to increase the current along the ordinate from zero to I_c without developing any voltage. That is not true, since by (1.10), it takes voltage to change the phase, and through (1.9), the current. At I_c the phase difference is $\pi/2$; to reach this value from $\phi = 0$ in say, $20ps$, it would be necessary to apply a voltage of about $25\mu V$.

It should be pointed out that the derivation of the Josephson relations (1.9) and (1.10) was based on the use of a simple coupling constant K in (1.1) and was not at all specific to the physics of tunneling. Ref.[[8]] and [[10]] discussed a number of different structures in which there is a weak coupling between two superconductors; they all obey the Josephson relations as long as the coupling is weak enough, and not too weak. When the coupling strength is increased, the sinusoidal dependence in (1.9) changes to another function, but the periodicity of oscillations in (1.15) remains the same.

We should comment about the idealization in Fig.1.1(a). In real tunnel junctions there is some current in the sub-gap range of voltages for various reasons; it usually rises with voltage and is considered a defect. The sub-gap current can be characterized by

$$V_m = I_c \times R(2mV) \tag{1.16}$$

where $R(2mV)$ is the inverse of the slope of a line from the origin to the characteristic at $2mV$.

For some applications, it is essential to have the highest possible V_m and for others it is less critical.

I_c depends on a lot of physical quantities. In this article, I am not studying its properties so I skipped the discussion about the physics of critical current of JJ.

1.2.0.3 *Inverse AC Effects:*

When a Josephson junction is irradiated with radiation of angular frequency ω_1, the response of the supercuddrent gives rise to constant-voltage Shapiro steps [13, 14] in the dc I-V curve at voltages $V_n = n\hbar\omega_1/2e$,

For simplicity, we start by treating a junction with an ideal voltage bias of

$$V = V_0 + V_1 \cos \omega_1 t \tag{1.17}$$

we obtain

$$\phi = \phi_0 + \omega_{0t} + (2eV_1/\hbar\omega_1) \sin \omega_1 t \tag{1.18}$$

where ϕ_0 is a constant of integration and $\omega_0 \equiv 2eV_0/\hbar$. Inserting this into Eq.(1.9) to calculate the current through junction, and using the standard mathematical expansion of the sine of a sine in terms of Bessel functions, we have

$$I_s = I_c \sum (-1)^n J_n(2eV_1/\hbar\omega_1) \sin(\phi_0 + \omega_0 t - n\omega_1 t) \tag{1.19}$$

This contributes a dc component only when $\omega_0 = n\omega_1$, i.e. when the dc voltage V_0 has one of the Shapiro step values

$$V_n = n\hbar\omega_1/2e. \tag{1.20}$$

If we include the normal current V_n/R as well, the total dc current on the nth Shapiro step can take on any value in the range

$$V_n/R - I_c J_n(2eV_1/\hbar\omega_1) \leq I \leq V_n/R + I_c J_n(2eV_1/\hbar\omega_1) \tag{1.21}$$

In other words, the half-width of the nth step is $I_n = I_c J_n(2eV_1/\hbar\omega_1)$.

Note that the dc average supercurrent giving the steps exists only for V exactly equal to one of the V_n for this simple voltage-biased case. At all voltages between the V_n there would be no dc effect of the supercurrent. Of course, the same would be true of the dc I-V curve of unirradiated junction, if it could be coltage-biased. The I-V curves that we have been discussing were all based on the more realistic assumption of dc-current bias, on the basis that the current of a zero resistance device is fixed by the external resistance in the circuit. SImilarly, in the rf case, the drive is never an ideal voltage source, and in most cases, it is closer to a current drive for rf as well as for dc. Numerical calculations are then required to obtain the step widths [8].

1.3 Gauge Invariant phase: Effect of a Magnetic Field

We saw in Eq.(1.9) that the current density is directly related to the phase difference. In this section we shall see how to re-define the phase difference in such a way that the choice of mathematical formulation for any magnetic field that may be present will not affect the value of current density. That is, we shall ensure that the current density is gauge invariant.

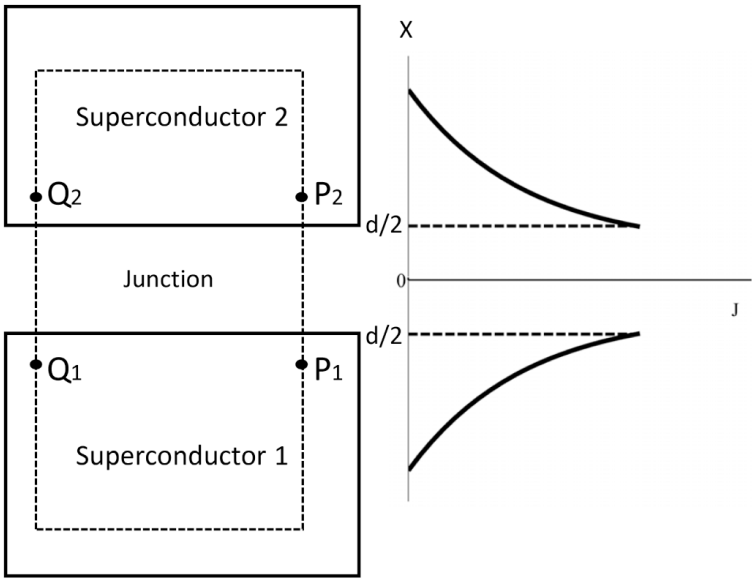

Figure 1.2: Integration path to relate flux in a junction and the phase difference along the junction. Current density in the bounding superconductors. [10]

Consider two points on opposite sides of the barrier in a JJ as shown in Fig.1.2. If a gauge change is made so that

$$\overrightarrow{A}' = \overrightarrow{A} + \nabla\chi \tag{1.22}$$

where χ is an arbitrary scalar function, the phases at the two points become

$$\begin{aligned} \theta_1' &= \theta_1 - (2e/\hbar)\chi_1 \\ \theta_2' &= \theta_2 - (2e/\hbar)\chi_2 \end{aligned} \tag{1.23}$$

Let us define the gauge invariant phase difference between points 1 and 2 to be

$$\phi = \theta_2 - \theta_1 + \frac{2e}{\hbar}\int_1^2 \overrightarrow{A}(x,t)\cdot\overrightarrow{dl} \tag{1.24}$$

We can easily see by substitution of (1.22) and (1.23) that ϕ is independent of the choice of gauge, i.e., the choice of χ. This modified definition of ϕ does not affect its being canonically conjugate to the number of pairs transferred, so the Josephson relations still apply.

Now let us use (1.24) to develop a relation between the phase difference and the magnetic field passing through a junction in the plane of the barrier. Consider two pairs of points Q_1, Q_2 and P_1, P_2 at two different positions along the junction as in Fig.1.2. The choice of gauge is arbitrary, so let us choose the London gauge in which $\nabla\theta = 0$ inside each of the two electrodes. Then θ_2 is the same at P_2 and Q_2, so it is for θ_1. Using (1.24), we can form

$$\phi(P) - \phi(Q) = \frac{2e}{\hbar}[\int_{P_1}^{P_2} \overrightarrow{A}'(P,t) \cdot \overrightarrow{dl} - \int_{Q_1}^{Q_2} \overrightarrow{A}'(Q,t) \cdot \overrightarrow{dl}] \tag{1.25}$$

The outward-directed magnetic flux through the rectangular contour in Fig.1.2 is

$$\begin{aligned} \Phi_y &= \int_S \overrightarrow{B} \cdot \overrightarrow{dS} = \oint \overrightarrow{A}' \cdot \overrightarrow{dl} \\ &= \int_{Q_1}^{Q_2} \overrightarrow{A}' \cdot \overrightarrow{dl} + \int_{Q_1}^{P_1} \overrightarrow{A}' \cdot \overrightarrow{dl} + \int_{P_1}^{P_2} \overrightarrow{A}' \cdot \overrightarrow{dl} + \int_{P_1}^{Q_2} \overrightarrow{A}' \cdot \overrightarrow{dl} \end{aligned} \tag{1.26}$$

It can readily be argued as follows that the second and fourth integrals on the right side of (1.26) are negligible if the superconductors are much deeper than the penetration depth. The canonical momentum in the transformed gauge is $\overrightarrow{p}' = m^*/n^*e^* - (2e/\hbar)\chi_1$ and $\overrightarrow{p}' = \hbar\nabla\theta'$. Since the gauge was chosen so $\nabla\theta' = 0$ in the superconductors, then $\frac{m^*}{n^*e^{*2}} \overrightarrow{J}_s = -\overrightarrow{A}'$. The integrals in (1.26) are equivalent to integrals of current density. The current is predominantly parallel to the junction surface, so those portions of the contour that are perpendicular to the surface make no significant contribution to the integrals in (1.26). We have located the portions of the contours lying parallel to the surface deep enough (appreciably beyond one penetrationi depth) within the superconductor that the current is essentially zero there, as illustrated in Fig.1.2. Therefore, the $Q_1 - P_1$ and $P_2 - Q_2$ integrals may be neglected. What remains in (1.26) are the same two integrals that appear in (1.25), so we obtain

$$\phi(P) - \phi(Q) = \frac{2e}{\hbar}\Phi_y \tag{1.27}$$

The difference of the phase differences between two points along a junction is simply proportional to the magnetic flux passing through the junction between the points, including that in the pennetration depths of the superconductors.

It is useful to obtain a differential equation for the phase difference. Suppose the points P and Q are separated by a differential distance dz. The flux in that distance will be $B_y^0 dz(\lambda_1 + \lambda_2 + d)$, where B_y^0 is the flux density in the barrier, λ_1 and λ_2 are the penetration depths in the two superconductors, and d is the barrier thickness. Then, letting $d' = \lambda_1 + \lambda_2 + d$, (1.27) becomes

$$\frac{\partial\phi}{\partial y} = -\frac{2ed'}{\hbar}B_y^0 \tag{1.28}$$

where we have used partial-derivative notation to take account of the fact that there can also be

a component of $\overrightarrow{B}$ in the z direction leading to

$$\frac{\partial \phi}{\partial y} = -\frac{2ed'}{\hbar} B_z^0 \tag{1.29}$$

Combining (1.28) and (1.29) we can write the gradient of the phase difference in the plane of the junction as

$$\nabla \phi = \frac{2ed'}{\hbar} (\widehat{n} \times \overrightarrow{B}^0) \tag{1.30}$$

where $\widehat{n}$ is the unit vector directed from superconductor 1 toward superconductor 2.

Although the results of this section were derived in the context of tunnel junctions, they are equally applicable to the conductive barrier junctions as well. [9] This relationship between magnetic field on the junction and the gauge invariant phase indicates a dependance of maximum current at ZERO-voltage, the central spike in Fig.1.1(a), which is the critical current in magnetic field. Combining equation (1.9) and (1.30) one obtains

$$I_c(B^0) = I_c(0) \left| \frac{\sin(ed' LB^0/\hbar)}{ed' LB^0/\hbar} \right| \tag{1.31}$$

where L is the length of the junction and $I_c(0) = WLJ_c$ is the total critical current with zero magnetic field. Since the current source has only one polarity, $\phi(0)$ flips from $+\pi/2$ to $-\pi/2$ and back as necessary to keep $I_c(B^0)$ positive. We can put the above equation in another useful fform by noting that $e/\hbar = \pi/\Phi_0$, where Φ_0 is the flux quantum ($2.07 \times 10^{-15} Wb$) and expressing the total flux through the junction as $\Phi = d' LB^0$ to get

$$I_c(B^0) = I_c(0) \left| \frac{\sin(\pi\Phi/\Phi_0)}{\pi\Phi/\Phi_0} \right| \tag{1.32}$$

This equation will lead to an important superconducting quantum devices to be introduced in the next chapter.

Chapter 2

Superconducting quantum circuits

2.1 Introduction of Superconducting quantum circuits and superconducting quantum bits

In this Chapter, I am going to introduce the modeling of superconducting quantum circuit, following with its application to build quantum bits. Decoherence in superconducting circuits will briefly introduced as well. Then I am going to present two of my published papers. One is to propose a detector for scalar Aharonov-Bohm effect, supervised by professor Raymond Chiao and collaborated with professor Munoz, professor Douglas Singleton, professor Kyle Sundyst, and so on. The other is to engineer circuit to protect quantum coherence, supervised by professor Lin Tian.

2.1.1 Circuit Model of Josephson junction

The Josephson relations derived in Sec.1.2 apply to any junction between two superconductors with a sufficiently weak coupling between them. Equation 1.2-(1.28) and (1.29), upon integrating the current density over the junction cross section, become

$$I = I_c \sin\phi \tag{2.1}$$

$$\dot{\phi} = \frac{2e}{\hbar} V \tag{2.2}$$

In general, the critical current I_c depends on an applied magnetic field, as Eq.(1.32); in that case ϕ is the phase difference at the center of the junction if the junction characteristics are spatially uniform. The Josephson current relation reveals that Josephson junction includes a nonlinear inductance. This electron pair current is represented in the equivalent circuit model in Fig.2.1(a).

Capacitance: Besides the nonlinear inductance from Josephson junction, another component is the displacement current which flows between the adjacent superconducting electrodes and is represented in the circuit model by a capacitance. This would be easy to calculate in the case of a tunnel junction if the barrier thickness d and dielectric constant ε_r were know. In

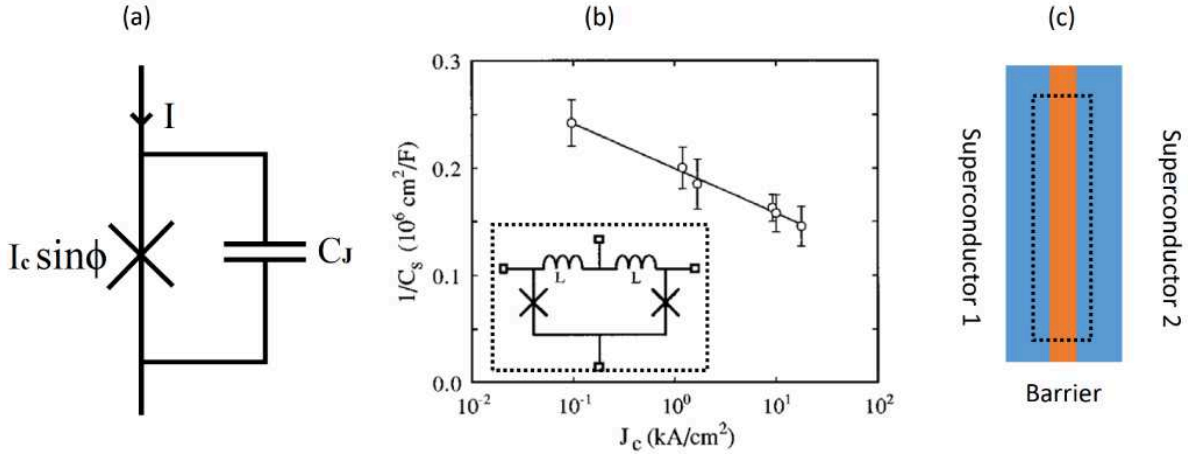

Figure 2.1: (a) Equivalent circuit model of a Josephson junction. Nonlinear inductor is connected parallelly with a capacitor. (b) Specific capacitance of Nb/AIO$_x$/Nb Josephson junctions. [15] Inset in dashed box is the circuit used in the experiment. (c) Two wide superconductors (blue) are connected with a long barrier (orange). The integrated loop along the dashed line can be modeled as the circuit in the inset of (b).

practice, these are only estimated and the capacitance used in modeling is obtained experimentally. The parallel-plane capacitance formula is assumed; $C = \varepsilon_0 \varepsilon_r A/d$ where A is junction area. Experimental evaluations have been published; a key result is shown in Fig.2.1(b), which gives the capacitance per unit area as a function of the Josephson current density for important niobium/aluminum oxide/niobium junctions. [16] Note that the dependence is weak, which reflects the fact that the tunneling current density is exponentially dependent on barrier thickness and capacitance is only linearly dependent. In semiconductor sandwich-form junctions, a reasonable estimate can be made since the thickness can be determined and the dielectric constant is usually known.

Conductance: The conductance element $G(V)$ in the equivalent circuit represents the quasiparticle current in the case of tunnel junctions. Its value is the slope of a line from the origin to the quasiparticle part of the I-V characteristic. In modeling of junctions for numerical computation, the conductance term is usually handled by piecewise-linear approximation. In some cases, analytic functions are fitted to the quasi-particle characteristic.

Other Issues in Modeling: For junctions long enough that the inductance of the electrodes is significant with respect to the Josephson inductance $L_J = \Phi_0/2\pi I_c$, as suggested in Fig.2.1(c), one should use a parallel set of circuits shown as two L's in Fig.2.1(b)'s inset, connected by inductance representing the electrodes. This issue becomes crucial for further discussion of superconducting quantum interference devices (SQUID).

2.1.2 Hamiltonian of Josephson junction

It should be noted that in many different kinds of junctions, the extrapolation downward of the linear part of the I-V characteristic (Fig.1.1(a)) found above the energy gap $V = 2\Delta/e$ does not always go to the origin. Often there is either so-called "excess current" or "deficit current" and the reasons are complex. [17] In this text, we simplify by assuming there is neither excess nor deficit in the analytic model and, in computer simulation, the actual shape can be modeled.

Based on the circuit model Fig.2.1(a), using ϕ as independent variable, we can write down Kirchhoff's current law for this Josephson junction

$$\frac{\hbar}{2e}C_J\ddot{\phi} + I_c \sin\phi = I_{net} \tag{2.3}$$

This is the motion of equation for the phase difference across Josephson junction. Correspondingly, the charge energy of the junction, as the kinetic part of ϕ is

$$\begin{aligned} K(\dot{\phi}) &= \frac{1}{2}C_J V^2 \\ &= \frac{C_J}{2}(\frac{\hbar}{2e})^2\dot{\phi}^2 \\ &= \frac{\hbar^2\dot{\phi}^2}{4E_c} \end{aligned} \tag{2.4}$$

where $E_c = \frac{1}{2}\frac{(2e)^2}{C_J}$ is the charging energy of one Cooper pair in the effective capacitor. The inductive energy of the junction, as the potential part

$$\begin{aligned} U(\phi) &= \frac{\hbar}{2e}\int_0^{\phi} I_c \sin\phi d\phi \\ &= \frac{\hbar}{2e}I_c(1-\cos\phi) \\ &= E_J(1-\cos\phi) \end{aligned} \tag{2.5}$$

where $E_J = \frac{\hbar}{2e}I_c$ is the Josephson energy of the junction. Therefore, without external field, the Hamiltonian of the junction is

$$H = \frac{\hbar^2\dot{\phi}^2}{4E_c} + E_J(1-\cos\phi) \tag{2.6}$$

Hence, the resonant frequency of JJ

$$\omega_J = \sqrt{\frac{2eI_c}{\hbar C_J}} \tag{2.7}$$

According to experimental data, [18, 19] this is at the order of GHz, same as radio frequency.

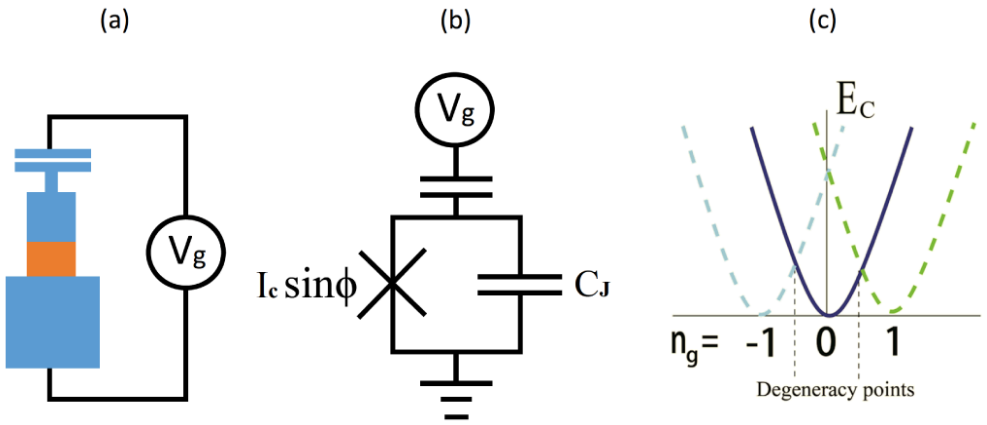

Figure 2.2: (a) A small superconducting island (small blue square) is connected to a big bulk of superconductor (blue) via a junction (Orange). Gate voltage V_g is used to bias the system energy. (b) Schematic circuit model of charge qubit. (c) Charge energy diagram.

We can see in the Hamiltonian (2.6) that phase difference ϕ behaves like position x in configuration space. So effective mass $m_E = \frac{\hbar^2}{2E_c}$, and canonical momentum $p = \frac{\hbar^2\dot{\phi}}{2E_c}$. In quantum limit, the quadratures $\widehat{\phi}$ and $\widehat{p}$ need to be quantized by applying quantum commutation rule

$$[\widehat{\phi}, \widehat{p}] = i\hbar \tag{2.8}$$

2.1.3 Coulomb blockade and charge qubit

When the area of junction is small, Fig.2.2(a)., tunneling rate is small so E_J is small and capacitance is also small enough so that charging energy of a Cooper pair in the Junction capacitor dominates the Hamiltonian, $E_c = \frac{1}{2}\frac{(2e)^2}{C_J} \gg E_J$. This means it costs too much energy for a Cooper pair to tunnel across the junction. As a result, they tends to stay where it was. This is called Coulomb blockade. Since number of Cooper pairs is

$$N = \frac{Q}{2e} = \frac{C_J V}{2e} = \frac{C_J}{2e}\frac{\hbar}{2e}\dot{\phi} = \frac{\hbar}{2E_c}\dot{\phi} = \frac{p}{\hbar} \tag{2.9}$$

where Q is total charge on the island. So we can use N as a quadrature. The commutator becomes

$$[\widehat{\phi}, \widehat{N}] = i \tag{2.10}$$

And the quantized Hamiltonian becomes

$$H = E_c\widehat{N} + E_J(1 - \cos\widehat{\phi}) \tag{2.11}$$

Since inductive energy now becomes a small term and the total energy mainly depends on charge energy, we move to number representation, where $\widehat{\phi} = i\widehat{N}$, and use take $\{|n\rangle\}$ as basis,

where n represents the number of pairs on superconducting island. Physically this indicates that the number of Cooper pairs on the island becomes a good quantum number. The energy diagram of this case is shown in Fig.2.2(c). At the crossings of different levels the degeneracy will be avoided due to Josephson tunneling energy E_J. This anti-crossings are called "degeneracy points" or "sweet points", in convention. The two quantum level structure at degeneracy points is usually used to build a qubit. In order to do so in the Coulomb blockade regime, we can apply an biasing gate voltage across the junction, taking the value $V_g = \frac{1}{2}\frac{N(2e)}{C_J}$. In this case, the canonical momentum becomes $(\widehat{N} - n_g)$ where n_g is half integer number of pairs due to bias. Recall that $\phi = i\dot{N}$ means ϕ displaces number N. So the Hamiltonian now becomes

$$\begin{aligned} H &= E_c(\widehat{N} - n_g) - E_J \cos\widehat{\phi} \\ &= E_c(n - n_g)\,|n\rangle\langle n| - \frac{E_J}{2}(|n\rangle\langle n+1| + |n+1\rangle\langle n|) \end{aligned} \tag{2.12}$$

Considering the lowest two levels $|0\rangle, |1\rangle$ and let $n_g = 1/2$, the Hamiltonian is simplified to be qubit form

$$\begin{aligned} H &= \frac{E_c}{2}(|1\rangle\langle 1| - |0\rangle\langle 0|) - \frac{E_J}{2}(|0\rangle\langle 1| + |1\rangle\langle 0|) \\ &= \frac{E_c}{2}\sigma_z - \frac{E_J}{2}\sigma_x \end{aligned} \tag{2.13}$$

where $\sigma_{x,y,z}$ are Pauli matrices. Since this Hamiltonian is in pair number picture, correspondingly electric charge on the SC island, people usually call it "Charge Qubit".

Note that in Coulomb blockade regime the superconducting island with small junction can be a electrometer to detect numbers of Cooper pairs, so charge qubit has also a name single Cooper pair transistor (SCT). This is similar to single electron transister (SET), whose island is not superconducting and the tunneling particle is single electron.

Two requirements must be met for Coulomb blockade to be clearly observed [8]: (1) E_c must exceed kT to avoid having its effects washed out by thermal fluctuations and (2) the resistance seen by the junction capacitance (i.e., the parallel combination of its internal tunneling resistance and any external shunting impedance) must exceed the quantum resistance $R_Q = h/4e^2$ to avoid having its effects washed out by quantum fluctuations.

2.1.4 Large junction and phase qubit

For a junction with large area and thin barrier, critical current is large and capacitance is large as well. Consequently, $E_J \gg E_c$. In this case, n is not a good quantum number any more. We need to return to phase representation and write down the Hamiltonian as

$$H = \frac{\hbar^2\dot{\phi}^2}{4E_c} - E_J\cos\phi \tag{2.14}$$

The dominant term becomes the inharmonic potential $-E_J\cos\phi$ where the energy levels are splitted in-equally. Though the bottom of the cosinusoidal potential well is still very close to a

harmonic potential, where the lowest level separations are too close to be a qubit.

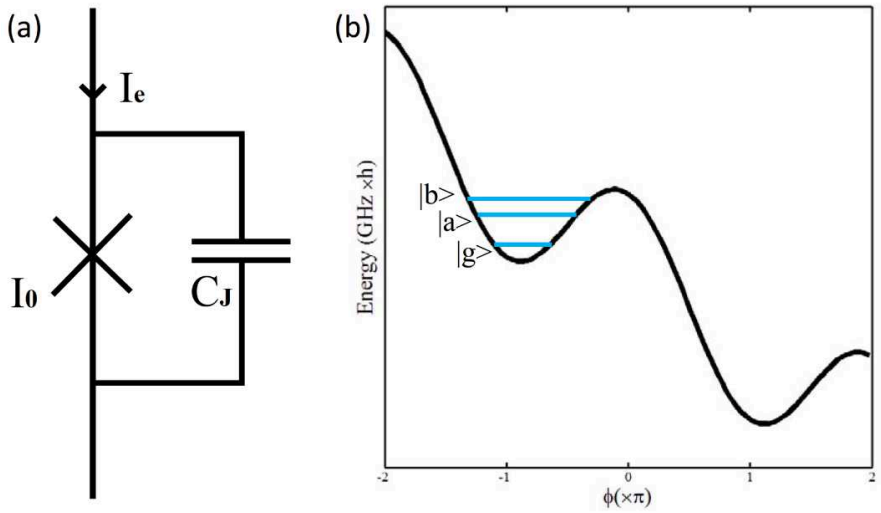

Figure 2.3: (a) Schematic circuit of DC current biased *Phase Qubit*. Cross stands for Josephson nonlinear inductor. (b) Washboard-like potential energy diagram of *Phase Qubit.* By adjusting I_e one can engineer each local potential well to include only three levels $|g\rangle$, $|a\rangle$, $|b\rangle$.

One way to enhance the inharmonicity is to apply a current bias I_e across the junction, as Fig.2.3(a) shows. Now the Hamiltonian becomes

$$H = \frac{\hbar^2 \dot{\phi}^2}{4E_c} - E_J \cos\phi - \frac{\hbar}{2e} I_e \phi \tag{2.15}$$

Defining $\sin\gamma_0 = I_e/I_c$, we can write down the potential term to be

$$\begin{aligned} U(\phi) &= -\frac{\hbar}{2e} I_c \cos\phi - \frac{\hbar}{2e} I_e \phi \\ &= -E_J(\cos\phi + \frac{I_e}{I_c}\phi) \\ &= -E_J(\cos\phi + \sin\gamma_0 \phi) \end{aligned} \tag{2.16}$$

Expand $\cos\phi$ around γ_0 up to third order to get the in-harmonic term

$$\cos\phi = \cos\gamma_0 - \sin\gamma_0(\phi - \gamma_0) - \frac{1}{2!}\cos\gamma_0(\phi-\gamma_0)^2 + \frac{1}{3!}\sin\gamma_0(\phi-\gamma_0)^3$$

Again neglecting constant terms, the potential term turns into

$$U(\phi) = \frac{E_J}{2!}\cos\gamma_0(\phi-\gamma_0)^2 - \frac{E_J}{3!}\sin\gamma_0(\phi-\gamma_0)^3 \tag{2.17}$$

The energy diagram is depicted in Fig.2.3(b). Adjusting external current bias I_e one can change

the portion of the quadratic term $\frac{\cos\gamma_0}{2}$ and the cubic term $\frac{\sin\gamma_0}{6}$ to change the inharmonicity. The lowest two levels in the local well can be used as qubit.

2.1.5 SQUID and tunable qubits

In superconductor, a loop of current gives integer numbers of flux quantum, i.e. fluxon. The existence of Josephson junction in the loop doesn't change magnetic screening property of superconductor as long as supercurrent dominates. [8] Let Φ_e be the external magnetic flux add into a loop of supercurrent. We have

$$\sum_i \phi_i + 2\pi\frac{\Phi_e}{\Phi_0} = 2n\pi \tag{2.18}$$

where Φ_0 is a fluxon. The first term in (2.18) sums over the phase difference across all the Junctions along the integral loop.

Flux qubit: If there is one JJ as Fig.2.4(a) shows, $\phi = 2n\pi - 2\pi\frac{\Phi_e}{\Phi_0} = 2n\pi - 2\pi\phi_e$, where ϕ_e is the gauge invariant phase factor due to external field. As mention in Sec.(2.1.1), when dealing with a loop of superconductor, the inductance on the electrodes needs to be considered. Therefore, an lindear inductor is connected in series with junction, Fig.2.4(b). The Hamiltonian can be written down as

$$H = \frac{\hbar^2\dot{\phi}^2}{4E_c} + E_J(1-\cos\phi) + \frac{E_L}{2}(\phi-\phi_e)^2 \tag{2.19}$$

where $E_L = \frac{\Phi_0^2}{(2\pi)^2 L} = \frac{\hbar^2}{(2e)^2 L}$ and L here is self-inductance. In large junction regime $E_J > E_c$, its potential energy diagram is depicted as Fig.2.4(c). With external field biased at $\phi_e = \frac{1}{2}\phi_0$, we obtain a double-well potential (dashed line) giving rise to two degenerate ground state $|left\rangle$ for clockwise supercurrent and $|right\rangle$ for counter-clockwise supercurrent, corresponding to magnetic flux in the loop going down and up. Because the finite barrier between the two wells, the degeneracy is lifted due to the overlap of ground state wavefunction. So at the sweet point the two actual lowest states are

$$\begin{cases} |\uparrow\rangle = |left\rangle + |right\rangle \\ |\downarrow\rangle = |left\rangle - |right\rangle \end{cases} \tag{2.20}$$

With these two flux states one can build a qubit, the so called "flux qubit". And this loop structure is sometimes called *rf-SQUID*. However, in real experiments, people usually shunt two large junctions and one small junction along the superconducting loop. [20] But the ground states have same physical meaning.

dc-SQUID: When there are two JJs along the loop, Fig.2.4(d), one needs two variables ϕ_1 and ϕ_2 as the phase difference across the two JJs. The superconducting loop now comes back to the form shown in Eq.(1.24). Coming with screening effect (2.18) one gets $\phi_1 + \phi_2 = 2n\pi - \phi_e$.

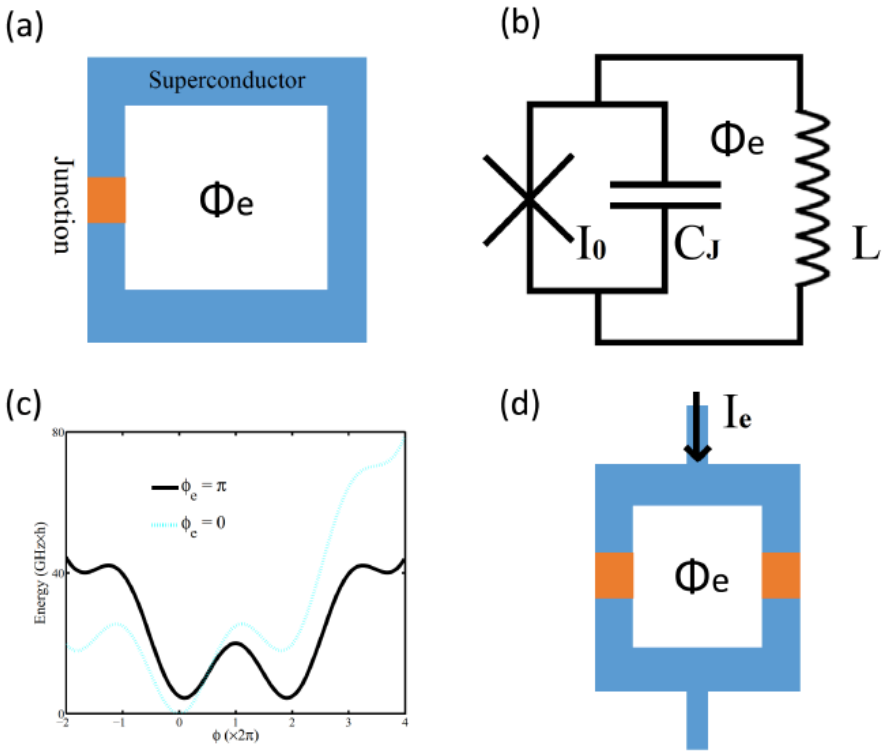

Figure 2.4: (a) A big superconductor loop (blue) embedded with a Josephson junction (orange). Magnetic flux Φ_e goes through the loop to adjust the phase difference across the junction. (b) Schematic circuit of one-junction SQUID. The superconductor loop is treated as an inductor that is connected with Josephson junction in series. (c) Potential energy diagram of the one-junction SQUID. When $\Phi_e = \pi$, it forms two degenerate double well system that can be used as a *Flux Qubit*. (d) Tunable dc SQUID.

The Hamiltonian now becomes

$$\begin{aligned} H &= \frac{\hbar^2(\dot{\phi_1}^2 - \dot{\phi_2}^2)}{4E_c} + E_J(1-\cos\phi_1) + E_J(1-\cos\phi_2) + \frac{E_L}{2}(\phi_1-\phi_2-\phi_e)^2 \\ &= \frac{\hbar^2(\dot{\phi_1}^2 - \dot{\phi_2}^2)}{4E_c} + 2E_J\cos\frac{\phi_1+\phi_2}{2}\cos\frac{\phi_1-\phi_2}{2} + \frac{E_L}{2}(\phi_1-\phi_2-\phi_e)^2 \\ &= \frac{\hbar^2\dot{\phi}^2}{2E_c} + 2E_J\cos\frac{\phi_e}{2}\cos\phi + \frac{E_L}{2}(\phi_1-\phi_2-\phi_e)^2 \end{aligned}$$

where the new variable $\phi = \frac{\phi_1-\phi_2}{2}$. Here I assumed the two junctions are identical so they have the same charge energy E_c and Josephson energy E_J. If the loop is small, the self-inductance L is too big so that energy E_L is negligible. With an external current across the SQUID, the

Hamiltonian becomes a phase qubit like form

$$H = \frac{\hbar^2 \dot{\phi}^2}{2E_c} + 2E_J \cos\frac{\phi_e}{2}\cos\phi - \frac{\hbar}{2e} I_e \phi \tag{2.21}$$

Comparing with (2.15) we can see in this dc-SQUID, the inductance energy term becomes tunable. So in large junction limit, this dc-SQUID is made as a tunable *phase qubit*.

Charge qubit: We replace the single junction in Sec.2.1.3 with a two-junction SQUID. The two junctions are in small junction limit $E_c \gg E_J$. Similar to the derivation in *dc-SQUID*, we just need to replace the Josephson energy in Eq.(2.13) with a tunable term $2E_J \cos\frac{\phi_e}{2}$, and get the Hamiltonian

$$\begin{aligned} H &= \frac{E_c}{2}(|1\rangle\langle 1| - |0\rangle\langle 0|) - \frac{E_J}{2}(|0\rangle\langle 1| + |1\rangle\langle 0|) \\ &= \frac{E_c}{2}\sigma_z - E_J \cos\frac{\phi_e}{2}\sigma_x \end{aligned} \tag{2.22}$$

As a summary, so far I have introduced some fundamental theory of superconducting circuit and superconducting qubits. This is an important ingredient of my research throughout these years.

In the following sections, I am going to show my published work based on this theoretical frame work of superconducting circuits.

2.2 Observability of the scalar Aharonov-Bohm effect inside a 3D Faraday cage with time-varying exterior charges and masses

2.2.1 Introduction

In the 19th century, Faraday showed that when the exterior of a large, enclosed cubical metallic cage (i.e., a "Faraday cage") is electrified at such a high voltage that sparks started to dart from the corners of the cage, he could still safely conduct many sensitive electrical experiments within the cage, such as sensitive electroscope measurements of the charge residing on the interior surface of the cage. He found the complete absence of any charges residing on the interior surface. Therefore in the special case of a spherical "Faraday cage" configuration, such as the one depicted in Figure 1, one would never expect any kind of electrical effects to be detectable inside the hollow spherical cavity which is carved out of this metallic sphere.

But what is impossible classically is sometimes possible quantum mechanically. For example, a 2D, cylindrical (i.e., tubular) Faraday cage was used in Aharonov and Bohm's original paper [21], in which they first proposed the electric (or "scalar") Aharonov-Bohm (AB) effect.[1] A metallic tube shielded an electron passing through the tube from any exterior electric fields. However, if a voltage pulse were to be applied to the *exterior* of the tube only when the electron wavepacket were to be deep in the *interior* of the tube, then the electron could not feel any

[1] We do not use the term "scalar" here to refer to neutron interferometry experiments that have been conducted in a uniform magnetic field, but reserve it to refer to the electric and gravitational AB effects.

forces during its passage through the tube. Nevertheless, the electron would pick up the scalar AB phase shift

$$\phi(t) = \frac{e}{\hbar} \int_0^t V(t')\, dt' \tag{2.23}$$

caused by the voltage pulse $V(t)$ applied to the tube whilst the electron was deep in the interior of the Faraday cage.

The scalar (electric) AB effect is less known than the vector (magnetic) version of the AB effect since it is harder to achieve the situation required for the electric AB effect where fields are vanishing while the potentials are non-zero. If one considers the fields and potentials for the cylindrical Faraday cage used in Aharonov and Bohm's original paper, then the electron will invariably pass through some region with a non-zero electric field, although the field may be extremely small. To have the electron pass *only* through regions where there is no field, one needs to switch the fields and potentials on and off completely, i.e., it is necessary to consider the time-dependent fields and potentials described by equation (2.23), where $V(t)$ is a function with compact support.

The existence of the scalar AB effect has been questioned (see for example the paper by Walstad [22]) exactly on the basis that some experimental confirmations of the effect [23] have the interfering electron passing through regions where the electric field is non-zero, and thus (potentially) one could explain the shift in an interference pattern in terms of classical forces rather than as a quantum phase effect.

In this paper we are proposing two variants of the scalar AB effect as two "thought experiments" which address these questions with setups where a quantum system that is influenced by potentials is *always* deep inside a field-free region of space. However, since both of these "thought experiments" involve time-dependent potentials which have no spatial gradients, the resulting effect on the system is not a *spatial* interference phenomenon, as in the vector (magnetic) AB effect, but rather a *temporal* interference phenomenon.

From equation (2.23) it can be seen that the phase in the case of the electric AB effect involves just an open time integration as opposed to the usual closed-path spatial line integral of the vector (magnetic) AB effect. This opens the possibility of setting up a scalar AB experiment where one does not split the system along different spatial paths, as in the vector AB setup, but instead the quantum system stays at a single location while the potential will be varying in time. Since we will not be spatially splitting and recombining our system, no *spatial* interference pattern will result, and therefore no shift in the *spatial* fringes as in the vector (magnetic) AB effect. However, we shall see below that there can still be a shift in the fringes of a purely *temporal* interference pattern, or a change of the frequency spectrum of the system.

Our proposal directly tests the scalar AB effect without any "loopholes" that would allow for the effect to be explained any other way. The basic setup involves a spherical metallic shell (i.e., a Faraday cage) that has an oscillating charge $Q(t)$ or mass $M(t)$ deposited on it. Inside the shell, the potential is spatially uniform, but is time-varying. The two systems that are placed inside this shell are a Josephson-circuit setup and a two-level atom. In both cases, the interior system does not move spatially and there is a complete absence of any field (electric or gravitational), but the system will experience a time-varying potential energy $U(t)$ which creates an observable AB effect.

2.2.2 An electric scalar AB effect via Josephson interferometry

We present here a method to observe the electric scalar AB effect by a superconducting artificial atom [18, 19]. In a bulk superconductor, phase factor in the order parameter has the form of scalar AB phase $\phi(t) = 2\frac{e}{\hbar}\int_0^t V(t)\,dt$, according to Josephson effect [7]. Another Josephson relation $I_s = I_c \sin\Delta\phi$ gives rise to zero-voltage tunneling current, where I_c is critical current of Josephson junction. This reveals a possibly observable physical effects only due to this scalar phase instead of electrical potential change, accordingly electric force. Consider an "atom", formed of Josephson junction circuit, confined within a Faraday cage, as shown in Figure 2.5. The cage has to be superconductive to rule out magnetic field within it due to Meissner effect, and to preserve the coherence of bulk phase factor from washing out by thermal fluctuations. Internal electric potential differences arise by sending rf-signals onto the surface of the cage, consequently to change the relative gauge invariant phase on surface. Asume the driving on surface is symmetric enough around the sphere. Because the skin effect on the surface of the superconducting cage doesn't affect the interior and the cage shields all external EM-field, communication between the exterior and interior can only be in way of the phase factor, in the limit of electrostatics equilibrium established instantly all over the whole Faraday cage. Note that this doesn't work for classical metal cage where phase factor is randomized. The indications of this internal effect can be measured from the external circuit by detecting the scattering signal from the interior.

This system can be modeled as the circuit shown in Figure 2.6. Neglecting possible readout circuit, we construct the Lagrangian using node potentials and phases $\{V_1, \phi_1; V_2, \phi_2\}$ in the standard way [24, 25]. Charge energy gives rise to kinetic energy in the circuit model

$$\mathcal{T} = \frac{C_{sph}}{2}V_1^2 + \frac{C'}{2}(V_1 - V_2)^2$$

And inductive energy plays the role of potential energy.

$$\begin{aligned}\mathcal{V} &= \frac{1}{2L}(\Phi_1 - \Phi_2)^2 - \frac{\hbar I_c}{2e}\cos\frac{2\pi}{\Phi_0}(\Phi_1 - \Phi_2) \\ &= \frac{1}{2L}\left(\frac{\hbar}{2e}\right)^2(\phi_1 - \phi_2)^2 - E_J\cos(\phi_1 - \phi_2)\end{aligned}$$

where $\Phi_0 = h/2e$ is flux quantum and $\phi_{1,2} = \frac{2\pi\Phi_{1,2}}{\Phi_0}$ are node phases. Josephson energy $E_J = \frac{\hbar I_c}{2e}$. Josephson effect Allowing quasiparticle tunneling current through Josephson junctions, node potentials are related to phases by $V_{1,2} = \frac{\hbar}{2e}\dot{\phi}_{1,2}$.

Omitting bias conditions, we find

$$\begin{aligned}\mathcal{L}\left(\phi_2, \dot{\phi}_2, t\right) &= \mathcal{T} - \mathcal{V} \\ &= \left(\frac{\hbar}{2e}\right)^2\left[\frac{C_{sph}}{2}\dot{\phi}_1^2 + \frac{C'}{2}\left(\dot{\phi}_2 - \dot{\phi}_1\right)^2 - \frac{1}{2L}(\phi_1 - \phi_2)^2 + E_J\cos(\phi_1 - \phi_2)\right] \qquad (2.24)\end{aligned}$$

An AC signal is introduced onto the sphere by charging its self-capacitance, so the electric

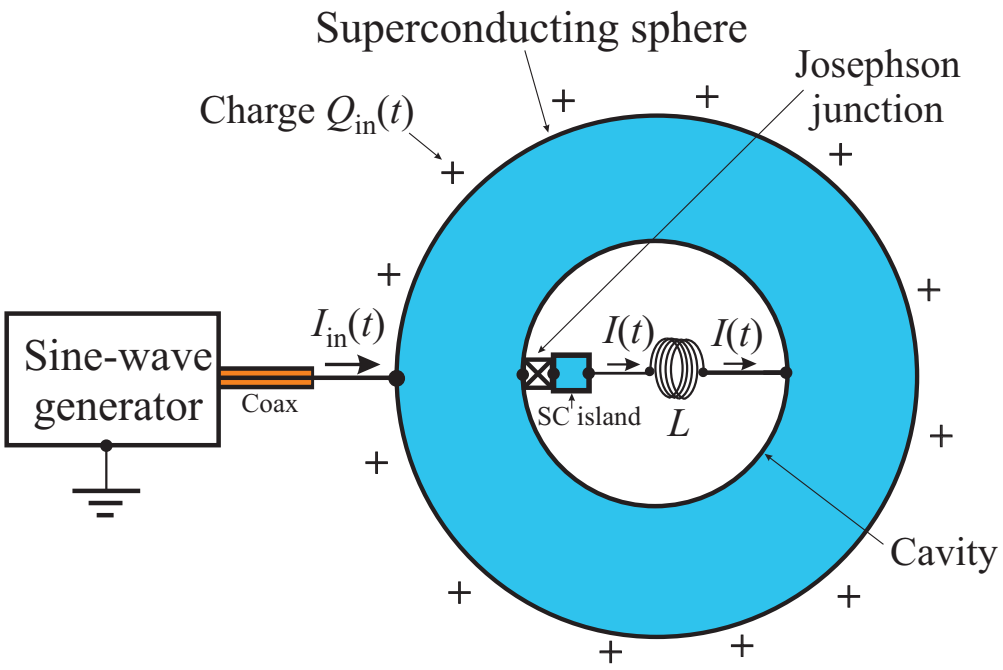

Figure 2.5: In the spherical superconducting (SC) shell, the SC artificial atom is formed with the hollow cavity and a superconducting wire on the horizontal axis. A SC island is connected to the cavity with a SC wire on one end and via a large Josephson junction on the other end. The effective inductance between the wire and cavity can be enhanced by increasing the number of switchbacks depicted as a solenoid. The spherical SC shell is made thick enough to prevent magnetic flux penetration into interior.

potential $V_1 = V_0 \sin \omega t$. For a superconductor subject to a voltage $V(t)$, a phase factor $\phi(t)$ develops within the order parameter of the Cooper pair condensate, $\Psi = \sqrt{\rho} e^{i\phi}$. The order parameter propagation to the interior gets retarded due to the junction. Hence a phase difference arises between the superconducting banks of the Josephson junction. This time-dependent difference drives a supercurrent according to the inverse AC Josephson effect, i.e. the Levinsen effect [13, 14].

We use new independent variables $\Delta\phi = \phi_2 - \phi_1$ and $\Delta\dot{\phi} = \dot{\phi}_2 - \dot{\phi}_1$. This allows us to obtain the following equation of motion out of the Lagrangian Eq.2.24.

$$0 = \Delta\ddot{\phi} + \omega_C^2 \Delta\phi + \left(\frac{2e}{\hbar}\right)^2 \frac{E_J}{C'} \sin \Delta\phi + \left(\frac{2e}{\hbar}\right)^2 \frac{C_{sph} V_0 \omega}{C'} \cos \omega t \tag{2.25}$$

where $\omega_C = \dfrac{1}{LC'}$. We adopt the following initial conditions, which assume an initial steady state throughout the system.

$$\begin{cases} \phi_2(t=0) = \phi_1(t=0) \\ \dot{\phi}_2(t=0) = \dot{\phi}_1(t=0) \end{cases} \tag{2.26}$$

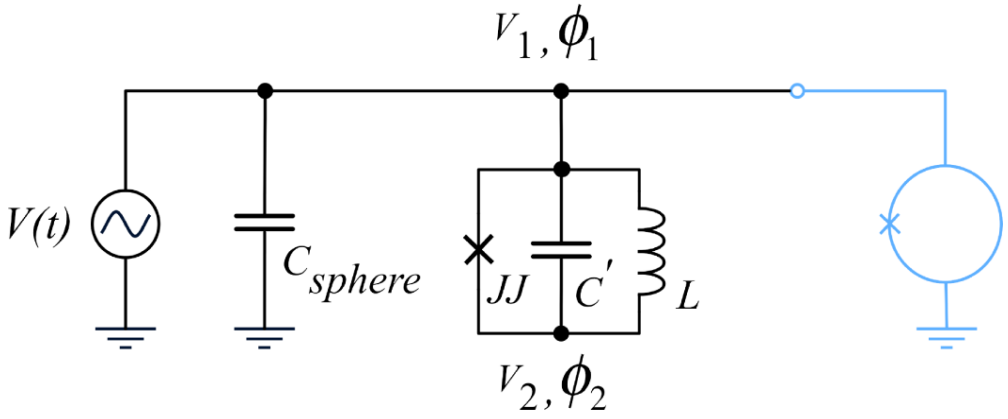

Figure 2.6: A simplified circuit includes three circuit loops that connected on node 1. In the leftmost loop, a signal generator drives the system. The next loop with the capacitor C_{sph} represents the spherical SC shell. C' and L are the effective capacitance and inductance of the SC island, respectively. The superconducting phase φ_2 on the central superconductor (node 2) and φ_1 on the sphere (node 1) are separated by a Josephson junction modeled with nonlinear inductance L_J and effective capacitance C_J. The right loop demonstrates a simple example of measurement, an rf-SQUID (light blue), although many possible variations of external low-noise readout exist to detect the change of φ_1 in time.

The first equation means initially the phases between interior and exterior are set to equal so that there is no current running across the junction. The second equation means initially the whole cage including inner circuit is in equipotential equilibrium. Numerical solution of $\Delta\phi$ is depicted in Fig.(2.7). When the floating circuit at node 2 is initially grounded and the internal circuit is cooled down to ground state, a AC signal at V_1 drives $\Delta\varphi$ starting at some moment according to the equation of motion (2.25). As mentioned at the beginning of this section, non-vanishing $\Delta\phi$ across the Josephson junction furthermore drives *zero voltage* supercurrent across the junction [7]. Hence the junction behaves as an *emf* only sensitive to phase changes. As a conclusion, with magnetic field and electric forces ruled out by the superconductive Faraday cage, this internal current is started by phase factor while the electric potential difference remains zero. Therefore, this will be the expected scalar AB effect.

Let's discuss the possibility of measurement here. The internal circuit absorbs driving signal, rf-photons, and turns into ac current. After the driving signal is turned off, the current maintains and change the phase ϕ_1. By connecting an rf-SQUID to the surface (light blue part in Figure 2.6) time dependent phase ϕ_1 is picked up and turns into current signal in the SQUID that can be detected. This process can be considered as some kind of scattering.

Also notice that the internal Josephson junction circuit, with the possible addition of current or flux biasing, reminds a similar circuit topology to phase or flux qubits, respectively [20, 26]. For large area Josephson junction, the anharmonic potential energy $U(\Delta\varphi) = \left(\frac{\hbar}{2e}\right)^2 \frac{1}{2L}(\Delta\varphi)^2 - E_J \cos(\Delta\varphi)$ dominates the dynamics. The wave function of the internal circuit

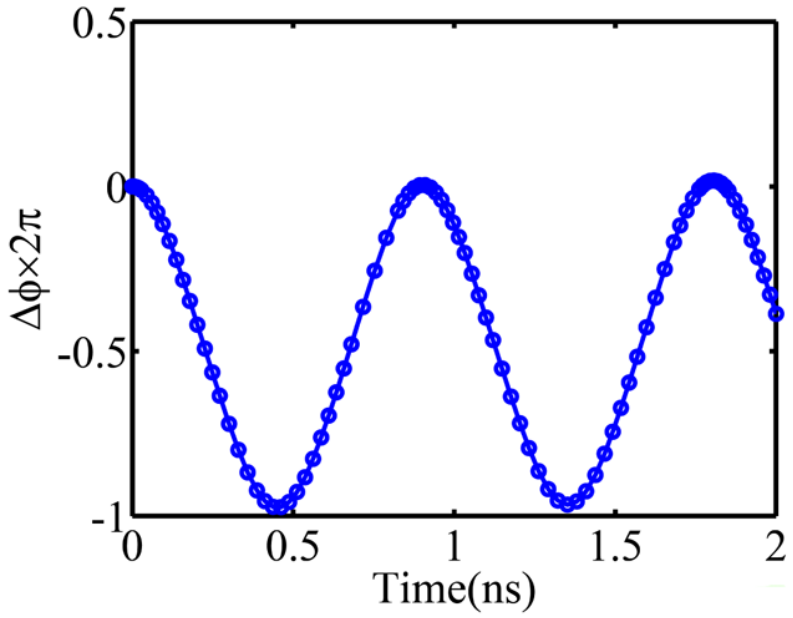

Figure 2.7: Phase difference across JJ $\Delta\varphi$ in terms of tme, solved from the Lagrangian equation of motion, when $\omega_0 \approx 8.5GHz, \alpha \approx 2 \times 10^{-15}Wb, V_0 = 1\mu V, \omega = 150MHz$.

is trapped in this potential. Energy is quantized into split levels, as depicted in Fig.(2.8). Similar to an atom occupying the local minimas of this periodic potential, for the ground state of this quantum circuit, the phase across the junction is trapped in the minimum of potential and becomes a good quantum number. This artificial "atom" in the cage, as we have just determined, can be affected by external AC signal. The phase difference $\Delta\varphi$ can be displaced from minimum of the potential well. If a 2π phase difference happens, a quanta of magnetic flux is generated in the cage, which now can treated as a cavity. Correspondingly in the energy vs phase diagram in Fig.(2.8), the "atom" jumps into secondary local minimum. After releasing the driving, the system may stay in the $\Delta\varphi = 2\pi$ state until there is a relaxation back to $\Delta\varphi = 0$ and emit AC signal to the surface of the cage. This signal can be detected via measurement of the rf-SQUID (rightmost loop in Figure 2.6). If the driving finishes one cycle from $\Delta\varphi = 0$ to $\Delta\varphi = 0$, the magnetic flux quantum comes back to *zero* in the cavity. Therefore, the internal magnetic flux becomes the consequence of a temporal scalar AB effect.

Here we make the following observations:

(1) The supercurrent arises when the voltage across the junction remains zero but a phase difference is increasing due to external signal. This doesn't have to be periodic AC field. Any change to the surface scalar AB phase can drive internal supercurrent, for example a single step wave signal will do.

(2) The scalar AB phase discussed here is only for a single Cooper pair instead of a bulk system. As pointed out earlier, the phase difference drives the supercurrent that in principle can be detected. Considering the bulk system, the AB phase factor should include the phase from all

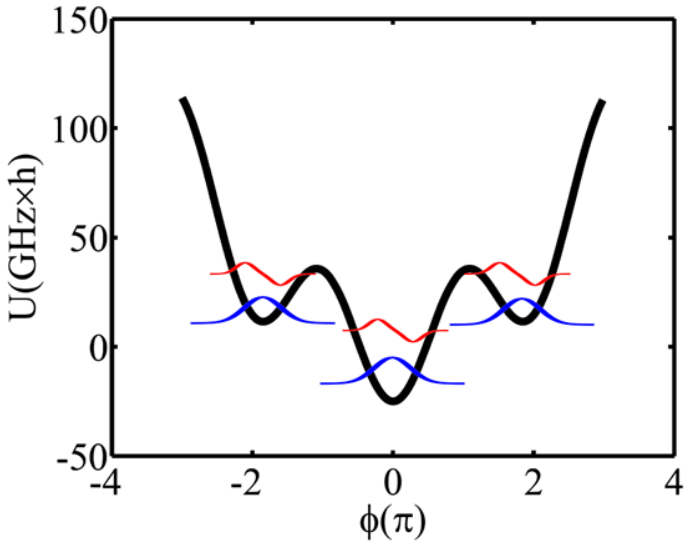

Figure 2.8: A plot of potential energy for $E_L = 1GHz \times h, E_J = 25GHz \times h$. Blue is the ground state for each well while red is the first excited state. Inter-well tunneling may occur, in which microwave photons may be emitted or absorbed.

Cooper pairs, $\varphi_{C.P.}(t) = \frac{2e}{\hbar}\int_0^t N_{C.P.}(t)\,V(t)\,dt$, and electrons, $\varphi_{els}(t) = \frac{e}{\hbar}\int_0^t N_{els}(t)\,V(t)\,dt$. Here $N_{C.P.}(t)$ is the total number of Cooper pairs (which is not conserved in principle) and $N_{els}(t)$ is the total number of electrons of the whole system. Also, AB phase factor from ionic lattice should be included as well $\varphi_{ion}(t) = \frac{-e}{\hbar}\int_0^t N_{ion}(t)\,V(t)\,dt$. For the case of this superconducting "atom" confined within the Faraday cage (see Figure 2.5), there will arise time-varying charge imbalances between the charge of the fixed ionic lattice and the charge of the mobile Cooper pairs on the SC island, which will give rise to a nonzero total AB phase developed in the internal circuit. The AB effect here merely drives the Cooper pair condensate and generates a magnetic field in the internal cavity. This is the physical reaction caused by the scalar AB phase that we expect here by theoretical analysis.

2.2.3 A gravitational AB phase shift observable as a time-dependent gravitational red shift

Here we consider the problem of a two-level atom that is undergoing a time-dependent gravitational red shift when the atom is placed inside a time-varying spherical mass shell $M(t)$ (see Figure 5) Again, as in the electric case, the gravitational scalar potential will be uniform everywhere within the interior of a mass shell, so that no gravitational force will be experienced by the atom. Nevertheless, there can in general arise a scalar AB phase [27], which arises from

the Newtonian gravitational scalar potential Φ

$$\varphi(t) = \frac{1}{\hbar}\int_0^t m(t')\,\Phi(t')\,dt' \tag{2.27}$$

where $m(t')$ is the time-varying rest mass of the quantum system that is acquiring this phase shift. The Newtonian gravitational scalar potential for a time-varying mass shell $M(t)$, such as that associated with the sinusoidally time-varying charge $Q(t)$ on the surface of the shell depicted in Figure 1, is given by

$$\begin{aligned}\Phi(t) &= -\frac{GM(t)}{r_0} \\ &= -\frac{G(M_0 + M_1\cos\omega t)}{r_0}\end{aligned} \tag{2.28}$$

where G is Newton's constant, r_0 is the radius of the mass shell, M_0 is the DC component of the mass shell, and M_1 is the amplitude of the AC component of the time-varying mass shell. It goes without saying that the mass-to-charge ratio of the electron is so tiny that the AC component associated with M_1 will be extremely small, so that there would be no hope for any practical laboratory experiment in connection with the Faraday cage configuration shown in Figure 5. However, we are concerned here with the problem of whether *in principle* the gravitational AB phase exists or not, so that a "thought experiment" would suffice here.

Nevertheless, there exist astrophysical situations, such as in the case of an exploding mass shell of a supernova, where the radius $r_0(t)$ is the time-dependent quantity rather than the mass $M(t)$. Then the gravitational AB phase shift may be large enough to be seen in practice. In any case, although the gravitational scalar potential may vary with time, nevertheless it must be independent of the position of the field point within the interior of the mass shell. This follows from Gauss's theorem. Therefore the atom within the mass shell experiences no classical forces. However, it can experience a nonzero quantum phase shift arising from the gravitational AB effect.

The rest mass of the excited state of an atom or of a nucleus will be larger than the rest mass of the ground state of this atom or nucleus. This follows from Einstein's equation

$$E = mc^2 \tag{2.29}$$

In quantum mechanics, Einstein's equation becomes

$$mc^2 = \langle\psi(t)|\, i\hbar\frac{\partial}{\partial t}\,|\psi(t)\rangle \tag{2.30}$$

Thus the rest mass m in relativity is the expectation value of the energy operator $i\hbar\partial/\partial t$ in quantum mechanics. For example, when an atom is in a stationary state $|\psi(t)\rangle = |\Psi_E\rangle\exp(-iEt/\hbar)$, it follows from (2.30) that

$$mc^2 = E\,\langle\Psi_E\,|\Psi_E\rangle = E \tag{2.31}$$

and thus we recover Einstein's equation (2.29). We shall assume that (2.30) holds in general

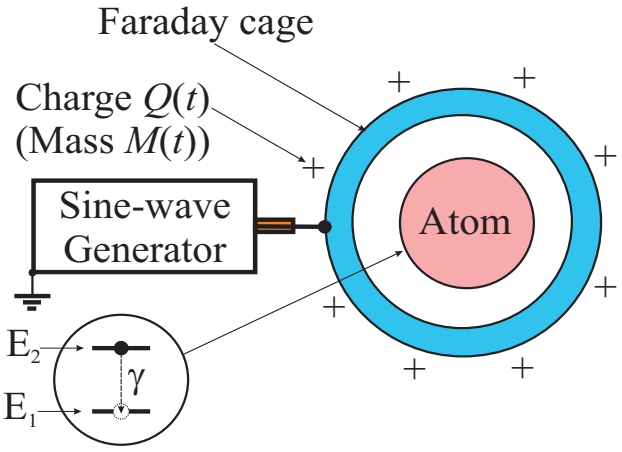

Figure 2.9: Two-level atom inside a spherical mass shell with a time-dependent mass $M(t)$ that arises from a time-dependent charge $Q(t)$. The mass $M(t)$ results a time-dependent gravitational redshift that leads to observable FM sidebands in the spectrum of the atom.

for open quantum systems, such as that of an atom inside a time-varying mass shell depicted in Figure 5.

Now from the expression for the gravitational AB phase (2.27), we expect that the atom in a stationary state with an energy E inside the mass shell will pick up an AB phase factor, so that

$$|\psi(t)\rangle = |\Psi_E\rangle \exp(-iEt/\hbar) \exp(-i\varphi(t)) \tag{2.32}$$

Substituting this into (2.30), we find

$$mc^2 = \langle\Psi_E| \{E + \hbar\dot{\varphi}\} |\Psi_E\rangle = E + \hbar\dot{\varphi} \tag{2.33}$$

which is an application of (2.30) to the case of a time-dependent environment, such as the time-varying mass shell. To find $\dot{\varphi}$, let us take the time derivative of the expression for the AB phase (2.27). Then one obtains the relationship

$$\dot{\varphi} = \frac{1}{\hbar} m(t) \Phi(t) \tag{2.34}$$

The physical meaning of this relationship is that the "instantaneous" frequency $\dot{\varphi}$ associated with the modulation of the phase of the atomic wavefunction due to an "instantaneous" change in the gravitational potential energy $m(t)\Phi(t)$ of the atom inside the mass shell, leads to an "instantaneous" energy change of the energy level of the atom given by

$$\delta E = \hbar\dot{\varphi} = m(t) \Phi(t) \tag{2.35}$$

Upon substitution of $\dot{\varphi}$ from (2.34) back into (2.33), it follows that

$$mc^2 = E + m(t) \Phi(t) \tag{2.36}$$

from which we infer that

$$E = mc^2\left(1 - \frac{\Phi}{c^2}\right) \tag{2.37}$$

which leads to the conclusion that the rest mass of quantum mechanical systems may be increased due to its external gravitational environment.

If we now take the difference in the upper and lower energy levels of the two-level atom and set it equal to the frequency of an emitted photon f_0 times Planck's constant h, we will find that

$$hf_0 = hf\left(1 - \frac{\Phi}{c^2}\right) \tag{2.38}$$

Since Φ is a negative quantity, this implies that the photon of energy hf as seen by an observer at infinity will be smaller in energy than the photon of energy hf_0 as seen by an observer near to the atom. Thus we have recovered Einstein's gravitational redshift starting from the gravitational AB phase shift.

Now if the potential Φ were to be time varying due to changes in the mass shell, the gravitational red shift would be changed by the time variation of Φ. If the time variation were to be sinusoidal, then we would expect the emission and absorption spectrum of the atom to undergo FM modulation. To see this, let us assume that the states of a two-level atom are represented by $|i\rangle$ for the initial state and by $|f\rangle$ for the final state. Then Fermi's Golden Rule states that the rate of transitions $w_{f\leftarrow i}$ between these two states will be given by the absolute square of the transition matrix element connecting the initial and final states, i.e.,

$$w_{f\leftarrow i} \propto \left|\langle f|\, H'\, |i\rangle\right|^2 \tag{2.39}$$

where H' is the time-dependent perturbation that causes the transitions to occur. (For the present purposes, we ignore the proportionality constant and the density of final states in Fermi's Golden Rule.)

Let us first consider the effect of the *electric* scalar AB effect on the transitions between the initial and final states of a *charged* atom, i.e., an ion, within the spherical shell of the Faraday cage. The electric AB phase is given by

$$\varphi_q(t) = \frac{q}{\hbar}\int_0^t V(t')\, dt' \tag{2.40}$$

where q is the charge of the ion. Since the initial and final states of the transition must have the same charge q (which follows from Wigner's charge superselection rule), it follows that the electric AB phase factors in the transition matrix elements in Fermi's Golden Rule must cancel out, i.e.,

$$\begin{aligned} w_{f\leftarrow i} &\propto \left|\langle f|\, e^{+i\varphi_q(t)} H' e^{-i\varphi_q(t)}\, |i\rangle\right|^2 \\ &= \left|\langle f|\, H'\, |i\rangle\right|^2 \end{aligned} \tag{2.41}$$

since $[H', V(t)] = 0$. From (2.41), we conclude that the electric AB effect cannot be observed

in the spectroscopy of any charged atomic system.

However, this is *not* true for the gravitational AB effect. This is because of the fact that the *rest mass* of an excited atom will be greater than the *rest mass* of the unexcited atom. (Recall that there exists no superselection rule for mass, unlike for the case of charge.)

Now from Einstein's equation (2.29), it follows that there exists a rest mass difference between the final and the initial states of the two-level atom, which is given by

$$\Delta m = \frac{\Delta E}{c^2} = \frac{E_f - E_i}{c^2} \tag{2.42}$$

where E_f is the energy level of the final state and E_i is the energy level of the initial state. Therefore from (2.27), we see that the difference in the gravitational AB phase picked up by the final state and the phase picked up the initial state will no longer vanish, but will differ by the amount

$$\begin{aligned} \Delta\varphi\left(t\right) &= \frac{\Delta m}{\hbar}\int_0^t \Phi\left(t'\right)dt' \\ &= \frac{E_f - E_i}{\hbar c^2}\int_0^t \Phi\left(t'\right)dt' \end{aligned} \tag{2.43}$$

where, to a a first approximation, the energy difference $E_f - E_i$ is independent of Φ.

As a simple example of how the difference in the gravitational AB phases in the initial and final states can lead to an observable AB interference effect, let us consider a superposition of the initial and final states which is initially given by

$$\left|\Psi\left(t=0\right)\right\rangle \propto \left|i\right\rangle + \left|f\right\rangle \tag{2.44}$$

After a time $t = T$, this superposition will evolve to pick up phase factors, viz.,

$$\begin{aligned} \left|\Psi\left(t=T\right)\right\rangle \propto \left|i\right\rangle e^{-\frac{i}{\hbar}E_i T} e^{-i\varphi_i T} \\ + \left|f\right\rangle e^{-\frac{i}{\hbar}E_f T} e^{-i\varphi_f T} \end{aligned} \tag{2.45}$$

where

$$\varphi_i\left(T\right) = \frac{E_i}{\hbar c^2}\int_0^T \Phi\left(t'\right)dt' \tag{2.46}$$

$$\varphi_f\left(T\right) = \frac{E_f}{\hbar c^2}\int_0^T \Phi\left(t'\right)dt' \tag{2.47}$$

are the gravitational AB phases picked up by the initial and final states, respectively. From (2.43) and (2.45) it follows that

$$\left|\Psi\left(t=T\right)\right\rangle \propto \left|i\right\rangle + \left|f\right\rangle e^{-\frac{i}{\hbar}\left(E_f - E_i\right)T} e^{-i\Delta\varphi T} \tag{2.48}$$

where $\Delta\varphi\left(T\right) = \varphi_f\left(T\right) - \varphi_i\left(T\right)$ is the difference of the two AB phases. From (2.27) and (2.28),

we see that

$$\varphi_i(T) = \alpha_i \sin \omega t \tag{2.49}$$

$$\varphi_f(T) = \alpha_f \sin \omega t \tag{2.50}$$

where $\alpha_i = GM_1 m_i/\hbar\omega r_0$ and $\alpha_f = GM_1 m_f/\hbar\omega r_0$ are the FM modulation parameters for the initial and final wavefunctions, respectively, of the two-level atom. The sinusoidal modulations of the phases given by (2.49) and (2.50) will lead to many FM harmonics of the frequency ω via the Jacobi-Anger expansion of the wavefunctions of the two-level atom (see Appendix 1). For large values of α_i and α_f, the dominant upper and lower FM sidebands of the FM-modulated wavefunctions of the atom will occur at the frequency shifts $\pm\alpha_i\omega$ and $\pm\alpha_f\omega$ away from their usual frequencies of $E_i/\hbar$ and $E_f/\hbar$.

It follows that the usual energy-conservation-enforcing delta function in the Fermi Golden rule will be modified from the usual two-level atom resonance condition not only by the usual gravitational red shift stemming from the DC component of the mass shell M_0, but it will also be modified due to the FM sidebands that arise from the AC component of the time-varying mass shell $M(t)$. The bottom line of this analysis is that the usual absorption or emission line of the two-level atom will be split into upper and lower FM sideband frequencies occurring on either side of the unsplit line of the atom with frequency shifts of $\pm(\Delta\alpha)\omega$, where

$$\begin{aligned} \Delta\alpha &= \left(\alpha_f - \alpha_i\right) \\ &= \frac{GM_1\left(m_f - m_i\right)}{\hbar\omega r_0} \end{aligned} \tag{2.51}$$

is the difference between the FM modulation parameters of the final state and the initial state that stems from the difference in their rest masses, $m_f - m_i$.

2.2.4 Conclusions

We conclude from the above two "counter-examples" that the claims of the non-existence of the scalar AB effect are false. Although these two "counter-examples" are by nature merely "thought experiments," they do establish the *existence* of the electric AB effect and the *existence* of the gravitational AB effect *in principle*. However, they may ultimately lead to actual experiments in the laboratory in the Josephson interferometry case, and to actual observational evidence in astrophysical settings in the gravitational redshift case.

Finally, we note that the magnetic (vector) AB effect as observed by Tonomura [28] using ferromagnetic toroids in electron interference experiments, are obviously topological in nature. However, the electric and gravitational (scalar) AB effects that are predicted to occur here inside the metallic shells of Figures 1 and 5, are obviously non-topological in nature.

2.3 Some further discussion on Scalar AB Effect with Professor Walstad

Scalar AB effect remains an open question so far. Professor Walstad published a paper in 2010 [22] criticizing observation experiments for scalar AB effect. Furthermore, he came to a conclusion that there is no physical reason for the existence of scalar AB phase. After submitting my paper, professor Walstad has some discussion with us. I am summarizing some important points and some further discussions for scalar AB effect in this section.

2.3.1 Where is the interference from?

Interference in AB effect comes from relative phase factor difference between two ways of electron, also it can be called coherence. If the relative phase difference becomes random, interference pattern disappears. The idea of the two way experiments are very similar for magnetic AB effect and scalar AB effect.

Equation (3) in literature [22] says the total wavefunction including the electron and apparatus in scalar AB effect experiment is

$$\begin{aligned}\Psi &= \Psi^p\Psi^s \\ &= e^{i\Delta Et/\hbar}\Psi^p e^{-i\Delta Et/\hbar}\Psi^s \\ &= \Psi^p\Psi^s \end{aligned} \tag{2.52}$$

where Ψ^p is wavefunction of electron and Ψ^s is wavefunction of the rest of the system. Prof. Walstad addressed this equation to show that because of energy conservation phase factor in the electron is eleminated, see the second line of the above equation, hence he concludes that interference due to scalar AB phase can't happen.

However, the problem is that Ψ^p can never be written into a single term as $e^{i\Delta Et/\hbar}\Psi^p$. As a typical "two way" experiment, the voltage between two paths generates an extra phase difference between two eigen states. The wavefunction of the electron should be a superposition of states corresponding to these two paths ($\Psi^{upp} + \Psi^{down}$). When the voltage is added only to the lower path a local phase factor appears. The wavefunction of electron becomes

$$\Psi^p = e^{i\Delta Et/\hbar}\Psi^{upp} + \Psi^{down}. \tag{2.53}$$

Or this form

$$\Psi^p = (e^{i\Delta Et/2\hbar}\Psi^{upp} + e^{-i\Delta Et/2\hbar}\Psi^{down}, \tag{2.54}$$

if the voltage is added between two paths. By taking probability of final state for both cases, one gets the interference term can be taken by

$$\Psi^p\Psi^{*p} = e^{i\Delta Et/\hbar}[\Psi^{upp}(\Psi^{down})^* + (\Psi^{upp})^*\Psi^{down}]. \tag{2.55}$$

so that

$$\left|\Psi^p\right|^2 = \cos(\Delta Et/\hbar)[\Psi^{upp}(\Psi^{down})^* + (\Psi^{upp})^*\Psi^{down}]. \tag{2.56}$$

It shows the origin of interference patterns.

Towards matrix formalism of this measurement, one can define Pauli matrix σ_x as the observable used to observe the interference pattern. Therefore the measurement operation can be formulated as

$$Tr(\rho\sigma_x) = \cos(\Delta Et/\hbar). \tag{2.57}$$

But if $Tr(\rho\sigma_x) = 0$ it means no interference pattern.

2.3.2 Is the apparatus classical or quantum mechanical?

Let's see what would happen if the apparatus is quantum mechanical. Due to the coupling between the capacitor and electron, capacitor reacts differently for electron's going different way. In other words, the apparatus is entangled with the electron and the total wavefunction should be as following:

$$\begin{aligned}\Psi = \Psi^p\Psi^s &= (e^{i\Delta Et/\hbar}\Psi^{upp}e^{-i\Delta Et/\hbar}\Psi_1^s + \Psi^{down}\Psi_2^s)/\sqrt{2} \\ &= (\Psi^{upp}\Psi_1^s + \Psi^{down}\Psi_2^s)/\sqrt{2}\end{aligned} \tag{2.58}$$

In this case the phase factor would be eleminated due to conservation of energy, as what Walstad concluded [22]. So the question is that should we include the entanglement? In other word, is the state of the apparatus a pure state or a mix state? A related question is that whether the observer (or apparatus) is entangled with the electron or not? Whether we should treat "apparatus + electron" as open quantum system or closed quantum system? If "apparatus + electron" is a closed quantum system, the observer is decoupled from the electron. So they are in a pure state. By tracing out apparatus subspace to measure the electron one gets no superposition in the electron state because it becomes a mix state, therefore the interference pattern is invisible.

However, when the electron is weakly coupled to the apparatus while the apparatus is much stronger coupled to observer, the phase factor in the apparatus will be averaged out taking classical approximation, and the coherence in electron will be preserved for longer. From this analysis, we conclude that there is a competition between two different total states: first, entanglement state between electron and apparatus

$$\begin{aligned}\Psi^{ent.} &= (e^{i\Delta Et/\hbar}\Psi^{upp}e^{-i\Delta Et/\hbar}\Psi_1^s + \Psi^{down}\Psi_2^s)/\sqrt{2} \\ &= (\Psi^{upp}\Psi_1^s + \Psi^{down}\Psi_2^s)/\sqrt{2};\end{aligned} \tag{2.59}$$

Second, product state between pure electron state and apparatus mix state

$$\Psi^{prod.} = \Psi^p\overline{\Psi}^s = (e^{i\Delta Et/\hbar}\Psi^{upp} + \Psi^{down})\overline{\Psi}^s, \tag{2.60}$$

where $\overline{\Psi}^s$ means classical treatment of the density matrix of apparatus. There is no phase factor in $\overline{\Psi}^s$. We can see that $\Psi^{ent.}$ doesn't include scalar AB phase while $\Psi^{prod.}$ does. Therefore, whether eAB effect exists or not, in this sense, depends on whether we treat apparatus/observer classically or quantum mechanically. Physically, it means whether we want to know the in-

terference result between the two paths or not. If we do, the apparatus couples to observer, otherwise it decouples to observer. However, it seems that a measurement apparatus should be always treated as classical because the reason one does measurement using an apparatus is to get the measurement result.

2.3.3 Cancellation of phase factor between electron and apparatus for magnetic AB effect?

Assume electron is strongly coupled to apparatus and the apparatus decohere slowly (weakly coupled to observer). Electon's going different ways also gives different torque on the solenoid. This gives rise to the coupling between electron and apparatus, from which observer knows the information of which way the electrons goes. If this information is not averaged out by treating apparatus to be classical, the apparatus will be entangled with electron and the phase factor will be canceled, because the motion of electron creates current hence magnetic flux on the solenoid, therefore it exerts the same amount of phase shift on solenoid. The entanglement state can be written down and one can see the same state as Equation.(2.59).

The phase difference the electron exerts on solenoid is

$$\Delta\varphi_{elect} = \frac{q\Phi_{elect.}}{\hbar}. \tag{2.61}$$

To simplify the calculation, we can assume the traveling electron has the same speed v_e as electrons in the solenoid. Also, we can assume the electrons goes around circumference of the solenoid. In order to simplify the calculation of the flux due to an electron, we treat the loop of electron as a single piece of solenoid so that $\Phi_{elect.} = \frac{B_{elect}}{2}A = \frac{\mu_0 I_{elect} nA}{2} = \frac{\mu_0 e v_e A}{2}$, where n is effective loop density N_{elect}/l_{elect} of the loop of electron and the $\frac{1}{2}$ is due to the edge effect of single electron solenoid. So the phase difference on solenoid due to two different paths of electron is

$$\begin{aligned}
\Delta\varphi_{elect} &= q_{solenoid}\frac{\Delta\Phi_{elect.}}{\hbar} \\
&= \frac{NI}{lv_e}\frac{\Delta\Phi_{elect.}}{\hbar} \\
&= \frac{NI}{lv_e}\frac{2\Phi_{elect.}}{\hbar} \\
&= \frac{NI}{lv_e}\frac{\mu_0 e v_e A}{\hbar} \\
&= e\frac{\mu_0 NI}{l}\frac{A}{\hbar} \\
&= e\frac{B_{solenoid}A}{\hbar} \\
&= e\frac{\Phi_{solenoid}}{\hbar}.
\end{aligned} \tag{2.62, 2.63}$$

Therefore,

$$\Delta\varphi_{elect} = \Delta\varphi_{solenoid} \tag{2.64}$$

which means the entanglement state between the electron and solenoid is

$$\begin{aligned}\Psi^{ent.} &= (e^{i\Delta\varphi_{elect}/2}\Psi^{upp}e^{-i\Delta\varphi_{solenoid}/2}\Psi_1^s + \\ &\quad e^{-i\Delta\varphi_{elect}/2}\Psi^{low}e^{i\Delta\varphi_{solenoid}/2}\Psi_2^s)/\sqrt{2} \\ &= (\Psi^{upp}\Psi_1^s + \Psi^{down}\Psi_2^s)/\sqrt{2}.\end{aligned} \tag{2.65}$$

From the above equation we see that the magnetic AB phase is canceled out as well for this case.

As an CONCLUSION, the apparatus/observer has to be CLASSICAL in order to see interference between two paths of electron!

2.3.4 Phase shift due to electric force?

In order to prove the physical reason of the existence of scalar AB phase, one has to demonstrate that the interference only comes from the difference of scalar AB phase instead of any other physical quantities. It is true that in Aharonov's original proposal, it is very hard to eliminate the interference due to electric force because of the geometric of the apparatus. However one doesn't have to eliminate electric force, because the electric force used to accelerate electrons can be, in principle, compensated by applying same electric field to both paths at the same time, to equalize the acceleration process in the two paths. An straight forward way to examine the effect due to electric force is depicted in Figure.(2.10). By scanning V_3 one can check how the force affect interference patter.

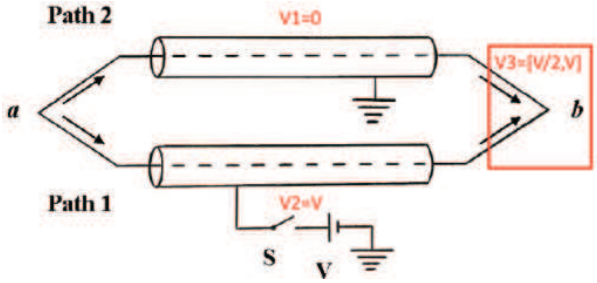

Figure 2.10: The red box represents another cylinder that covers the region in the box. V_3 is added to this part and it can be tuned between $V/2$ and V.

One can even go further. As Figure.(2.11) depicted, the cylinder in the upper part can be splitted into two sections, the first of which is added with $V_3 = V$. In this case the the issue due to electric force will be the same between upper and lower paths but the duration in two different cylinders are different, which give to different scalar AB phase $\phi^{upp,low} = \frac{e}{\hbar}\int_0^{t_{upp,low}} V(t')dt'$. Simply by choosing different length of the cylinders one gets $t_{upp} \neq t_{low}$ hence $\phi^{upp} \neq \phi^{low}$ and when the two paths join at b interference pattern emerges.

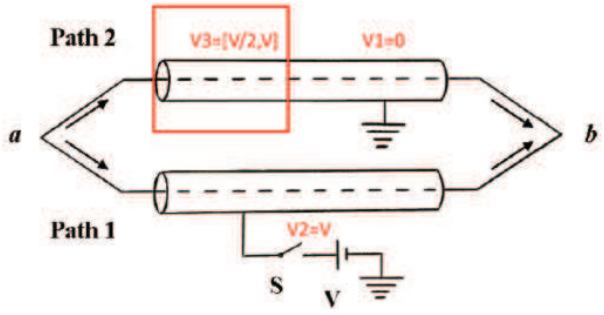

Figure 2.11: The upper cylinder is cut into two sections. One is grounded. Another is added with V_3.

2.3.5 Quantum measurement theory of AB effect

Without loss of generality, we can assume any AB effect appears as a relative phase factor $e^{i\phi}$ between two paths of electron. We now study how this phase factor affects measurement results due to different measurement schemes and treatments of the entire system.

If the electron is entangled with apparatus, as argued by Prof. Walstad, and they are decoupled from environment, which is classical, the total state of the closed quantum system is

$$\begin{aligned}\rho_{ea} &= \frac{1}{\sqrt{2}}(|\uparrow\rangle_e|\uparrow\rangle_a + e^{i\phi}|\downarrow\rangle_e|\downarrow\rangle_a)\frac{1}{\sqrt{2}}(\langle\uparrow|_e\langle\uparrow|_a + e^{-i\phi}\langle\downarrow|_e\langle\downarrow|_a) \\ &= \frac{1}{2}\begin{pmatrix} 1 & 0 & 0 & e^{-i\phi} \\ 0 & 0 & 0 & 0 \\ 0 & 0 & 0 & 0 \\ e^{i\phi} & 0 & 0 & 1 \end{pmatrix},\end{aligned} \tag{2.66}$$

where $e^{-i\phi}$ is the relative phase factor between $|\uparrow\rangle_e|\uparrow\rangle_a$ and $|\downarrow\rangle_e|\downarrow\rangle_a$. If the local phase factor isn't canceled out due to conservation of energy or other mechanisms, $e^{-i\phi} \neq 1$ and can be a controllable phase factor.

Let's study two different measurement schemes to check how one can observe interference pattern for this entangled system.

2.3.5.1 Local measurement on electron

According to equation.(2.57), local measurement on electron means total observable to the coupled system *electron* × *apparatus* is $M_{ea}^{(1)} = \sigma_x \otimes I$. The measurement gives output as

$$\begin{aligned} Tr[\rho_{ea} M_{ea}^{(1)}] &= Tr\left[\frac{1}{2}\begin{pmatrix} 1 & 0 & 0 & e^{-i\phi} \\ 0 & 0 & 0 & 0 \\ 0 & 0 & 0 & 0 \\ e^{i\phi} & 0 & 0 & 1 \end{pmatrix}\begin{pmatrix} 0 & 0 & 1 & 0 \\ 0 & 0 & 0 & 1 \\ 1 & 0 & 0 & 0 \\ 0 & 1 & 0 & 0 \end{pmatrix}\right] \\ &= Tr\left[\frac{1}{2}\begin{pmatrix} 0 & e^{-i\phi} & 1 & 0 \\ 0 & 0 & 0 & 0 \\ 0 & 0 & 0 & 0 \\ 0 & 1 & e^{i\phi} & 0 \end{pmatrix}\right] \\ &= 0, \end{aligned} \tag{2.67}$$

which indicates no interference pattern depending on the relative phase factor $e^{i\phi}$. To interpret more physically, this result means when the electron is entangled with apparatus and one locally measures the interference of electron, he sees no interference effect due to relative phase between two paths. Furthermore, according to Walstad's reasoning in his paper, if a magnetic AB phase exists when electron and solenoid are entangled (corresponding to a relative local phase in equation.(2.66), a local measurement on electron won't give any magnetic AB Effect! The question, whether magnetic AB phase between electron and solenoid get canceled or not, doesn't even need to be discussed.

The reason of losing the interference is that the phase factor will be hidden in the state of apparatus and get averaged out. Because the reduced interference observable matrix of apparatus:

$$\begin{aligned} M_a^{(1)} &= Tr_e[\rho_{ea} M_{ea}^{(1)}] \\ &= Tr_e\left[\frac{1}{2}\begin{pmatrix} 0 & e^{-i\phi} & 1 & 0 \\ 0 & 0 & 0 & 0 \\ 0 & 0 & 0 & 0 \\ 0 & 1 & e^{i\phi} & 0 \end{pmatrix}\right] \\ &= \frac{1}{2}\begin{pmatrix} 1 & 0 & 0 & 0 \\ 0 & 1 & 0 & 0 \end{pmatrix}\begin{pmatrix} 0 & e^{-i\phi} & 1 & 0 \\ 0 & 0 & 0 & 0 \\ 0 & 0 & 0 & 0 \\ 0 & 1 & e^{i\phi} & 0 \end{pmatrix}\begin{pmatrix} 1 & 0 \\ 0 & 1 \\ 0 & 0 \\ 0 & 0 \end{pmatrix} \\ &+ \frac{1}{2}\begin{pmatrix} 0 & 0 & 1 & 0 \\ 0 & 0 & 0 & 1 \end{pmatrix}\begin{pmatrix} 0 & e^{-i\phi} & 1 & 0 \\ 0 & 0 & 0 & 0 \\ 0 & 0 & 0 & 0 \\ 0 & 1 & e^{i\phi} & 0 \end{pmatrix}\begin{pmatrix} 0 & 0 \\ 0 & 0 \\ 1 & 0 \\ 0 & 1 \end{pmatrix} \\ &= \frac{1}{2}\begin{pmatrix} 0 & e^{-i\phi} \\ e^{i\phi} & 0 \end{pmatrix}. \end{aligned} \tag{2.68}$$

However, after measurement, the reduced density matrix of apparatus becomes a mix state density matrix.

$$\begin{aligned}
\rho_a &= Tr_e\left(\rho_{ea}\right) \\
&= \frac{1}{2}\begin{pmatrix} 1 & 0 & 0 & 0 \\ 0 & 1 & 0 & 0 \end{pmatrix}\begin{pmatrix} 1 & 0 & 0 & e^{-i\phi} \\ 0 & 0 & 0 & 0 \\ 0 & 0 & 0 & 0 \\ e^{i\phi} & 0 & 0 & 1 \end{pmatrix}\begin{pmatrix} 1 & 0 \\ 0 & 1 \\ 0 & 0 \\ 0 & 0 \end{pmatrix} \\
&+ \frac{1}{2}\begin{pmatrix} 0 & 0 & 1 & 0 \\ 0 & 0 & 0 & 1 \end{pmatrix}\begin{pmatrix} 1 & 0 & 0 & e^{-i\phi} \\ 0 & 0 & 0 & 0 \\ 0 & 0 & 0 & 0 \\ e^{i\phi} & 0 & 0 & 1 \end{pmatrix}\begin{pmatrix} 0 & 0 \\ 0 & 0 \\ 1 & 0 \\ 0 & 1 \end{pmatrix} \\
&= \frac{1}{2}\begin{pmatrix} 1 & 0 \\ 0 & 1 \end{pmatrix}.
\end{aligned} \tag{2.69}$$

Because $Tr\left(\rho_a\right) = 1$ and $Tr\left(\rho_a^2\right) < 1$, the state of apparatus ρ_a is a mix state. Therefore, the phase factor, in other word the interference information, disappears. In order to observe interference, one way to do is to make a joint measurement on the total entanglement state.

2.3.5.2 Joint measurement on the total entanglement state *electron* × *apparatus*

In this case, the total measurement observable is $M_{ea}^{(2)} = \sigma_x \otimes \sigma_x$. This measurement gives the results as

$$\begin{aligned}
Tr[\rho_{ea} M_{ea}^{(1)}] &= Tr\left[\frac{1}{2}\begin{pmatrix} 1 & 0 & 0 & e^{-i\phi} \\ 0 & 0 & 0 & 0 \\ 0 & 0 & 0 & 0 \\ e^{i\phi} & 0 & 0 & 1 \end{pmatrix}\begin{pmatrix} 0 & 0 & 0 & 1 \\ 0 & 0 & 1 & 0 \\ 0 & 1 & 0 & 0 \\ 1 & 0 & 0 & 0 \end{pmatrix}\right] \\
&= Tr\left[\frac{1}{2}\begin{pmatrix} e^{-i\phi} & 0 & 0 & 1 \\ 0 & 0 & 0 & 0 \\ 0 & 0 & 0 & 0 \\ 1 & 0 & 0 & e^{i\phi} \end{pmatrix}\right] \\
&= \cos\phi.
\end{aligned} \tag{2.70}$$

Therefore, by measuring interference terms, one sees patterns depending on relative local phase associated with different paths the electron goes. Note that, in joint measurement scheme, one has to measure σ_x on the entire closed quantum system and treat all the rest classically. The total state is $\rho_{ea} \otimes \rho_{enviroment}$.

In reality, the above analysis are too idealistic. First, there is hardly perfectly isolated quantum system as big as the apparatus discussed in AB Effect so the "closed quantum system" is just an assumption. Hence, energy conservation in the "closed" system is also just an assumption. Second, it is very hard to include all the small closed systems that is entangled with the electron. So when observer plans to measure the interference it is very hard to do

a total σ_x measurement to the entire entangled system. An easier treatment is to assume the apparatus is massive and strongly coupled to environment. So that the apparatus can be treated classically. In this case, although it is still coupled to electron but the energy or phase factor transferred from electron to apparatus will decohere very quickly to the environment, and energy in *electron*×*apparatus* system is not conserved! This also replies Prof. Walstad's argument "Scalar AB phase is canceled due to conservation of energy".

To simplify calculation, apparatus is included in the environment. And the total state is now a product state $\rho_{electron} \otimes \rho_{enviroment}$, where $\rho_{enviroment}$ is classical. The interference measurement theory can now be referred to Section.1-A.

And actually, the magnetic phase factors discussed before take different signs for electron and solenoid because this is a recoil effect. This means there is also a conservation rule in magnetic AB effect and the phase factor is canceled in the case when *electron* × *apparatus* system is a closed entanglement quantum system.

As a conclusion of the discussion in this section, whether interference effect exists or not depends on whether it is observed or not. When the interferometer is treated classically, spatial interference patterns emerges when observed, as Aharonov-Bhom predicted. When the interferometer is treated quantum mechanically and entangled with electron, interference pattern disappeared. However, temporal interference should be still observable with the quantum Faraday cage.

2.4 Decoherence in superconducting qubits

Superconducting qubits have macroscopic physical size, in some sense Schrödinger's cat, so they could be expected to be very sensitive to decoherence sources. One of my work is to study how to suppress decoherence due to $1/f$ noise using a universal quantum degeneracy point encoding technique, as discuss in the following section. So it is necessary to briefly introduce quantum decoherence in superconducting circuits in this section.

There are two process giving rise to decoherence rate $1/T_2$: relaxation, noted as relaxation rate $1/T_1$ to describe the time scale of a qubit relaxing from upper level to lower level and losing of energy; dephasing, noted as dephasing rate $1/\tau_\phi$ to describe the time scale of losing off-diagonal entries in density matrix due to low-frequency fluctuating noise. [18, 19, 29] The decoherence rate

$$\frac{1}{T_2} = \frac{1}{2T_1} + \frac{1}{\tau_\phi} \tag{2.71}$$

Imagine each type of qubit is described by a single degree of freedom ideally by eliminating all other degrees of freedom. Using John Clarke's way to distinguish two classes of decohering element: extrinsic and intrinsic. [19] Obvious extrinsic sources include external electromagnetic signals; these can generally be eliminated by using careful shielding and enough broadband filters. A more challenging extrinsic source is the local EM environment, e.g., circuit control signals. This type of decoherence can be well modeled using Amir Caldeira and Anthony Leggett's theory of quantum dissipation [30]. This theory maps any linear dissipation onto a bath of harmonic oscillators. The effects of these oscillators can be calculated from the Johnson–Nyquist noise that is generated by the complex impedance of the environment.

The main intrinsic limitation on the coherence of superconducting qubits results from low-frequency fluctuations in two level defects in Josephson junction devices. These two level defects come from three major sources. The first is critical-current fluctuations, which arise from fluctuations in the transparency of the junction caused by the trapping and untrapping of electrons in the tunnel barrier. The second source is charge fluctuations arising from the hopping of electrons between traps on the surface of the superconducting film or the surface of the substrate. The third source is magnetic-flux fluctuations due to the fluctuations of unpaired electron spins on the surface of the superconductor or substrate. Each defect produces random telegraph noise, and a superposition of such uncorrelated processes leads to a $1/f$ power spectrum. So the low frequency noise is also called $1/f$ noise.

2.5 Protect quantum coherence with Universal Quantum Degeneracy Point approach

2.5.1 Introduction

Decoherence due to the low-frequency noise is commonly considered as the major hurdle for implementing fault-tolerant quantum computing in superconducting qubits [18, 19, 31]. The low-frequency noise, often with $1/f$-type of spectrum [32, 33], is ubiquitous in Josephson junction devices [34–37]. In the past, extensive efforts have been devoted to study the microscopic origin of the low-frequency noise [38–44]. Most recently, theoretical and experimental researches suggested that one source of the low-frequency noise is the spurious two-level system fluctuators in the substrate or in the oxide layers of the Josephson junctions [45–49].

To protect the coherence of the superconducting qubits from the low-frequency noise, various approaches have been developed during the past few years, including the dynamic control technique, the quantum degeneracy point approach, the calibration of the qubit parameters by continuous measurement, and the design of novel quantum circuits and materials [46,50–62]. Among these approaches, the quantum degeneracy point approach [55–57] has been demonstrated to protect the qubit effectively from the low-frequency noise that couples with the qubit through the off-diagonal matrix elements, i.e. the transverse noise. The qubit decoherence time was increased by orders of magnitude by operating the qubit at its quantum degeneracy point, also called the optimal point or the "sweet spot", where the first order derivative of the qubit energy to the noise fluctuation is zero. This approach has already been applied to both the charge qubit and the flux qubit [63, 64].

Meanwhile, due to the diverse origins of the low-frequency noise in solid-state systems, the qubit can couple with either transverse or longitudinal low-frequency noise, where the longitudinal noise couples with the qubit in the diagonal elements and shifts the qubit energy. The simple quantum degeneracy point approach can only protect the qubit from transverse low-frequency noise. For longitudinal low-frequency noise, this approach can't reduce the decoherence of the qubit. For instance, in the quantronium qubit [55], when the low-frequency noise appears as a fluctuation in the Josephson energy, the qubit energy obtains an energy shift proportional to the noise, which generates qubit dephasing.

In this work, we propose a universal quantum degeneracy point (UQDP) scheme where

the encoded qubits can be protected from generic low-frequency noise. The physical qubits in this scheme are subject to transverse and (or) longitudinal low-frequency noises. We construct an encoded qubit in a subspace where the low-frequency noise only generates off-diagonal elements and can be effectively treated as transverse noise. We will show that universal quantum logic gates can be implemented in this architecture and are protected from the low-frequency noise as well. To test the analytical results, we numerically simulate the quantum logic gates in the presence of the low-frequency noise. The gate operations, protected by the encoding, demonstrate high fidelity in the simulation. Moreover, we will show that the proposed scheme is robust again small fabrication errors in the parameters of the Josephson junctions. The paper is organized as follows. In Sec. 2.5.2, we first present the UQDP scheme and the formation of the encoded qubits. Then, the decoherence of the encoded qubits under generic low-frequency noise is calculated analytically. In Sec. 2.5.6, we study the realization of the quantum logic gates on the encoded qubits. Numerical simulation of the quantum logic gates is also presented in this section. The discussions on the effects of the parameter spreads, different choices of the coupling between the physical qubits, and comparison with the Decoherence Free Subspace (DFS) approach are presented in Sec. 2.5.7 together with the conclusions.

2.5.2 Universal Quantum Degeneracy Point (UQDP)

The basic idea of the (simple) quantum degeneracy point approach is to use the finite energy separation between the two eigenstates of a qubit to protect the qubit from transverse low-frequency noise. Consider the qubit coupling with the transverse noise as

$$H_s = E_z\sigma_z + \delta V_x(t)\sigma_x \tag{2.72}$$

where the energy separation between the qubit states $|\uparrow\rangle$ and $|\downarrow\rangle$ is $2E_z$ and $\delta V_x(t)$ is the low-frequency noise with $|\delta V_x(t)| \ll E_z$. The noise couples with the qubit via the σ_x operator which provides a transverse coupling in the off-diagonal elements. Here, we treat $\delta V_x(t)$ as a classical noise for simplicity, but our results can be applied to quantum noises. The low-frequency nature of the noise determines that it can't resonantly (effectively) excite the qubit between its two states due to the large energy separation between the qubit states. Hence, the noise can be treated as static fluctuations. The qubit energy can be written as

$$H_s \approx (E_z + \delta V_x^2(t)/2E_z)\sigma_z \tag{2.73}$$

by second order perturbation approach, i. e. the qubit Hamiltonian adiabatically follows the time dependence of the noise via the second order term $\delta V_x^2(t)/2E_z$. The qubit dephasing is determined by this second order term and is hence significantly suppressed by a factor of $\sim |\delta V_x(t)/2E_z|^2$.

However, as we mentioned in Sec. 2.1, in real experiments, the qubit-noise coupling can be more complicated than that in Eq. 2.72. In this work, we consider a generic noise model with $\sum \delta V_\alpha(t)\sigma_\alpha$ including an arbitrary coupling with the qubits in all Pauli operators. We will show that an encoded subspace can be constructed in which the generic low-frequency noise can be converted to a transverse noise for the encoded qubit.

2.5.3 The encoded qubit

The encoded qubit can be constructed from two identical superconducting qubits connected by a coupling circuit. The form of the total Hamiltonian for the coupled qubits can be quite generally written as

$$H_0 = E_z(\sigma_{z1} + \sigma_{z2}) + \sum_{\alpha} E_{m\alpha}\sigma_{\alpha 1}\sigma_{\alpha 2} \tag{2.74}$$

where $\sigma_{\alpha j}$ are the Pauli operators of the j-th qubit and $\alpha = x, y, z$.

$$V_{\rm n} = \sum_{\alpha j} \delta V_{\alpha j}(t)\sigma_{\alpha j} \tag{2.75}$$

where $\delta V_{\alpha j}(t)$ accounts for the noise coupling with $\sigma_{\alpha j}$ of the j-th qubit. This Ising coupling is quite general for superconducting qubits in some sense, because cross terms like $\sigma_{x1}\sigma_{z2}$, corresponding to the interaction between the electric energy in the first qubit and the Josephson energy in the second qubit, are so small that they don't need to be considered. The total Hamiltonian including the system and the noise can be written as $H_{\rm en} = H_0 + V_{\rm n}$.

The coupling Hamiltonian in Eq.(2.74) can be realized in many circuits. For example, consider two charge qubits biased in their quantum degeneracy points with effective Josephson energy E_J, Josephson capacitance C_J, and gate capacitance C_g. We then have $E_z = E_J/2$. The qubits are connected by a superconducting quantum interference device (SQUID) with capacitance C_m and Josephson energy E_{J2} [18]. It can be derived that

$$E_{mx} = C_m e^2/[\Big(C_m + C_J + C_g\Big)^2 - C_m^2] \tag{2.76}$$

and $E_{my} = E_{mz} = -E_{\rm J2}/4$. Similar couplings can be derived for other superconducting qubits such as phase qubits and flux qubits.

The eigenstates of the Hamiltonian H_0 in Eq. (2.74) can be derived as

$$\begin{aligned}
|1\rangle &= -\sin\theta|\downarrow\downarrow\rangle + \cos\theta|\uparrow\uparrow\rangle, \\
|2\rangle &= \cos\theta|\downarrow\downarrow\rangle + \sin\theta|\uparrow\uparrow\rangle, \\
|3\rangle &= (-|\downarrow\uparrow\rangle + |\uparrow\downarrow\rangle)/\sqrt{2}, \\
|4\rangle &= (|\downarrow\uparrow\rangle + |\uparrow\downarrow\rangle)/\sqrt{2},
\end{aligned} \tag{2.77}$$

with

$$\cos\theta = 2E_z/\sqrt{4E_z^2 + E_m x^2} \tag{2.78}$$

and $\theta \in [0, \pi/2]$. The corresponding eigenenergies are $E_1 = -\sqrt{4E_z^2 + E_m x^2}$, $E_2 = \sqrt{4E_z^2 + E_m x^2}$, $E_3 = -E_m x$, and $E_4 = E_m x$ respectively. It can be shown that couplings in this general form can generate the encoded qubit under the condition: $E_{mx} \neq 0$ and (or) $E_{my} \neq 0$. In the following, we set $E_{my} = E_{mz} = 0$ with a finite E_{mx} for simplicity of discussion. So $E_m = E_{mx}$ The low-frequency noise coupled with the qubits have the general form We can rewrite the Pauli operators of the physical qubits in the eigenbasis in the order from $|1\rangle$ to $|4\rangle$. For example, in

the eigenbasis, we have

$$\sigma_{z1} = \begin{bmatrix} -\cos\theta & -\sin\theta & 0 & 0 \\ -\sin\theta & \cos\theta & 0 & 0 \\ 0 & 0 & 0 & -1 \\ 0 & 0 & -1 & 0 \end{bmatrix}, \tag{2.79}$$

and

$$\sigma_{y2} = i \begin{bmatrix} 0 & 0 & \cos\phi & \sin\phi \\ 0 & 0 & \sin\phi & -\cos\phi \\ -\cos\phi & -\sin\phi & 0 & 0 \\ -\sin\phi & \cos\phi & 0 & 0 \end{bmatrix}. \tag{2.80}$$

with the angle $\phi = \theta/2 + \pi/4$.

An interesting observation is that the diagonal elements of all the Pauli matrices in the subspace of the states $\{|3\rangle, |4\rangle\}$ are zero, i.e.

$$\langle 3| \sigma_{\alpha j} |3\rangle = \langle 4| \sigma_{\alpha j} |4\rangle = 0 \tag{2.81}$$

for $\alpha = x, y, z$ and $j = 1, 2$. The only non-zero matrix elements in this subspace are the off-diagonal elements $\langle 3|\sigma_{zj}|4\rangle$ and their conjugate elements. We know that the qubits couple with the low-frequency noise through the Pauli matrices as is given in Eq.(2.75). Hence, the noise only couples with this subspace through off-diagonal coupling elements. This coupling, however, will not generate effective excitation between the states $|3\rangle$ and $|4\rangle$ due to the low-frequency nature of the noise and the finite energy difference $2E_m$ between these two states. We thus select $\{|3\rangle, |4\rangle\}$ as the subspace for the encoded qubit and name the parameter point where the Hamiltonian has the form of Eq. (2.74) as the "universal quantum degeneracy point" (UQDP). Note that because of the generality of the form of the Hamiltonian, the UQDP may not be just one point, but can be a curve in the parameter space. At the UQDP, the subspace $\{|3\rangle, |4\rangle\}$ couples with all the noise $\delta V_{\alpha j}(t)$ transversely and suffers only quadratic dephasing. In addition, due to the same reasons that protect the encoded qubit from dephasing, the leakage from the encoded subspace to the redundant space of $\{|1\rangle, |2\rangle\}$ due to the perturbation of the noise is also prohibited in the lowest order. The matrix elements of σ_{xj} and σ_{yj} (hence the noise components $\delta V_{xj}(t)$ and $\delta V_{yj}(t)$ induce only virtual excitations between $\{|3\rangle, |4\rangle\}$ and $\{|1\rangle, |2\rangle\}$.

Note we only consider decoherence due to the low-frequency noise, notably '1/f noise', because it is the dominant source of decoherence for superconducting qubits [19]. High-frequency noises such as Johnson noise in the electric circuits can generate transitions between the encoded subspace. Relaxation between the two encoded levels is of high frequency noise too, because the energy spacing of UQDP is at the same order of magnitude as of common QDP schemes therefore is still great enough compared to noises. The relaxation rate is so low that high-frequency noises can be neglected [63].

2.5.4 Proposed circuit for superconducting qubits

We study the circuit in Fig. 2.12 as an example to show the derivation of coupling energy E_{mx} in Eq.5.

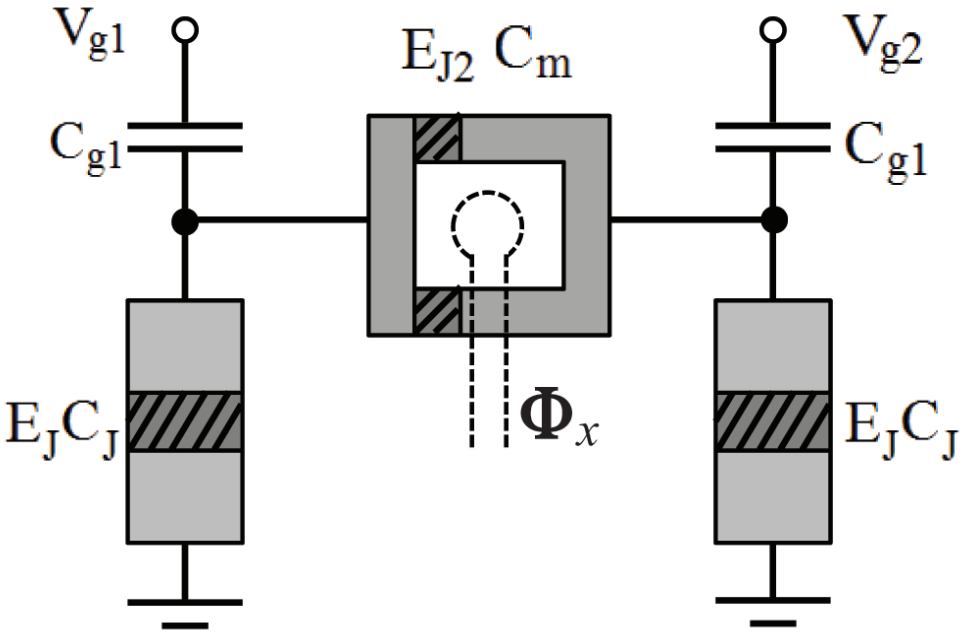

Figure 2.12: A circuit for coupled qubits.

Let $C_{g1} = C_{g2}, C_{J1} = C_{J2}$. The electric energy of this circuit is

$$E_c = \frac{1}{2}\sum_i C_i V_i^2 - Q_{g1}V_{g1} - Q_{g2}V_{g2}. \tag{2.82}$$

Here $i = J_1, J_2, m$, and $g1$ and $g2$.The last two terms substract the work done by the voltage source to give the available electric (free) energy. The voltage across each Josephson junction is given by the Josephson voltage-phase relation $V_i = (2e/\hbar)\dot{\varphi}_i$, where the over-dot indicates a partial time derivative. The ground in the circuit labels the zero of potential and is a virtual ground. The voltage across the gate capacitor $g1$ is $V_{Cg1} = V_{g1} - V_A$ and similarly for $V_{Cg1} = V_{g2} - V_B$, where V_A and V_B are the potentials at nodes A, B. The electric energy can then be written in terms of the time derivatives of the phases as

$$E_c = \frac{C_\Sigma}{2}\left(\frac{\hbar}{2e}\right)^2\left(\dot{\varphi}_1 + \dot{\varphi}_2\right) - C_m\left(\frac{\hbar}{2e}\right)^2\dot{\varphi}_1\dot{\varphi}_2, \tag{2.83}$$

where $C_\Sigma = \left(C_J + C_m + C_g\right)$ and constant term $-\frac{1}{2}C_g\left(V_{g1}^2 + V_{g2}^2\right)$ has been neglected.

The canonical momentum are

$$P_1 = \frac{\partial E_C}{\partial \dot{\varphi}_1} = \left(C_\Sigma\dot{\varphi}_1 - C_m\dot{\varphi}_2\right)/(2e/\hbar)^2 \tag{2.84}$$

$$P_2 = \frac{\partial E_C}{\partial \dot{\varphi}_2} = \left(C_\Sigma \dot{\varphi}_2 - C_m \dot{\varphi}_1\right) / (2e/\hbar)^2 \tag{2.85}$$

By solving equations (2.83), (2.84), (2.85) we get $E_c = \frac{(2e/\hbar)^2 C_\Sigma}{2\left(C_\Sigma^2 - C_m^2\right)} \left(P_1^2 + P_2^2\right) - \frac{(2e/\hbar)^2 C_m}{\left(C_\Sigma^2 - C_m^2\right)} P_1 P_2$. After quantization $P_i = -(i\hbar/2)\,\partial/\partial\varphi_i$, we notice only the coefficience of the term $P_1 P_2$ contributes to $\sigma_{x1}\sigma_{x2}$. So

$$E_{mx} = \frac{e^2 C_m}{\left(C_\Sigma^2 - C_m^2\right)}, \tag{2.86}$$

which is exactly the same as Eq.(2.76).

2.5.5 Dephasing of the encoded qubit

The dephasing of the encoded qubit can be calculated with perturbation theory. Without loss of generality, we assume that the noise contains only the x component $\delta V_{xj}(t)$ and the z component $\delta V_{zj}(t)$, both of which are Gaussian $1/f$ noises with the spectra

$$S_{xj}(\omega) = \int_{-\infty}^{\infty} \left\langle \delta V_{xj}(t) \delta V_{xj}(0) \right\rangle \frac{e^{i\omega t} dt}{2\pi} = \frac{A^2 \cos^2 \eta}{\omega} \tag{2.87}$$

$$S_{zj}(\omega) = \int_{-\infty}^{\infty} \left\langle \delta V_{zj}(t) \delta V_{zj}(0) \right\rangle \frac{e^{i\omega t} dt}{2\pi} = \frac{A^2 \sin^2 \eta}{\omega} \tag{2.88}$$

where the angle η is a parameter that describes the noise power distribution and A^2 is the total noise power. When $\eta = 0$, the low-frequency noise is a transverse noise with only the x (and y) component; When $\eta = \pi/2$, the low-frequency noise is a longitudinal noise with only the z component.

We introduce the Pauli operators for the encoded qubit as $X = |3\rangle\langle 4| + |4\rangle\langle 3|$, $Y = -i|3\rangle\langle 4| + i|4\rangle\langle 3|$, and $Z = |3\rangle\langle 3| - |4\rangle\langle 4|$. When projected to the encoded subspace of $\{|3\rangle, |4\rangle\}$, the effective Hamiltonian of the system coupling with the low-frequency noise can be written as

$$H_{\text{en}} = \left(-E_m - \frac{E_m (\sum_j \delta V_{xj}(t))^2}{2E_z^2} + \frac{(\sum_j \delta V_{zj}(t))^2}{2E_m} \right) Z \tag{2.89}$$

by applying second order perturbation. Here j=1,2. The noise enters this Hamiltonian in quadratic form. The dephasing of the encoded qubit due to arbitrary low-frequency noise hence only involves quadratic terms, similar to Eq.(2.73) for the simple quantum degeneracy point. Even the longitudinal noise δV_{zj} only contributes to the dephasing in quadratic terms.

To calculate the dephasing of the encoded qubit, we use the analytical results on dephasing due to Gaussian $1/f$ noise [65]. In the calculation, we assume the noises $\delta V_{\alpha j}(t)$ are not correlated with each other [66]. The parameters we choose are $E_z/2\pi\hbar = 5\,\text{GHz}$, $A = 2\times10^{-4} E_z$ with an infrared cutoff for the $1/f$ noise $\omega_{ir}/2\pi = 1\,\text{Hz}$. The dephasing times are plotted in Fig. 2.13 at different coupling ratio E_m/E_z. For the bare qubit, the decoherence time decreases rapidly by a few orders of magnitude as the noise distribution changes from transverse noise to

longitudinal noise. For the encoded qubit at $E_m/E_z = 1$, in contrast, the decoherence time only varies smoothly over the whole range of η.

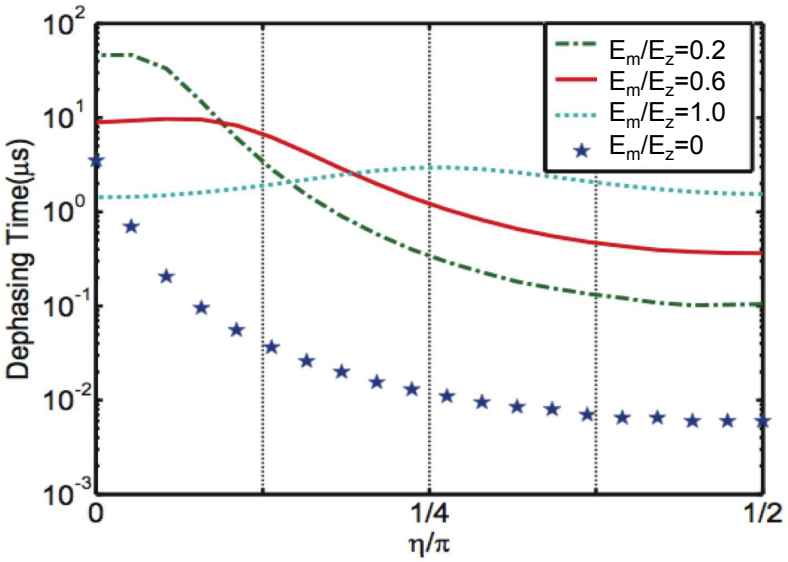

Figure 2.13: Dephasing time of the bare qubit (star) and the encoded qubit versus the noise power angle at different ratio E_m/E_z as is labelled in the plot (other curves). The decoherence times reach a maximum value around $\eta/\pi = 1/4$ for $E_m/E_z = 1$ because summation of the second and third terms in quation(13) gives a coefficient $cos2\eta$ to the amplitude of noise in the effective encoded hamiltonian, resulting in a minimum noise when $\eta = \pi/4$. The maximum value of decoherence time drifts to left with smaller η due to the change of the noise amplitude on x and y directions associating with the increasing ratio E_m/E_z.

2.5.6 Protected Quantum Logic Gates for Encoded Qubits

In the previous section, we showed that the encoded qubit is immune to arbitrary low-frequency noise to the first order of the coupling and the dephasing is dominated by quadratic terms derived from perturbation theory. As a result, the encoded qubit can be a highly-coherent quantum memory for storing quantum information. In this section, we will further show that universal quantum logic gates on the encoded qubits are also protected from the low-frequency noise with high fidelity. The gate operations require manipulations on the physical qubits. We will test our theoretical results for the gate operations with a numerical simulation. The numerical results give high gate fidelity for the UQDP.

2.5.6.1 Single-qubit gates

Quantum logic gates on single encoded qubit can be performed by manipulating the operators of individual physical qubits $\sigma_{\alpha i}$ or by manipulating the interaction terms between

two physical qubits $\sigma_{\alpha i}\sigma_{\alpha j}$. In the encoded space, the effective Hamiltonian of the encoded qubit is $H_0^{(e)} = -E_m Z$. When projected to this subspace, the operators σ_{z1} can be expressed as

$$P_e \sigma_{z1} P_e = -X \tag{2.90}$$

where P_e is the projection operator onto the subspace $\{|3\rangle, |4\rangle\}$. From Eq. (2.79), it can also be shown that the operator σ_{z1} generates no coupling between the encoded subspace and states in $\{|1\rangle, |2\rangle\}$. By pumping the first physical qubit with a pulse $H_X = 2\lambda \cos(2E_m t/\hbar)\sigma_{z1}$ for a duration of $\theta\hbar/2\lambda$, we can implement the X-rotation gate $U_x(\theta) = \exp(i\theta X/2)$.

Similarly, the operator $\sigma_{y1}\sigma_{y2} + \sigma_{z1}\sigma_{z2}$ can be expressed as

$$P_e(\sigma_{y1}\sigma_{y2} + \sigma_{z1}\sigma_{z2})P_e = -1 - Z \tag{2.91}$$

which generates a rotation in the Z-component of the encoded qubit. This operator can be realized in superconducting circuits. For example, for charge qubits connected by a coupling SQUID, this operator can be realized by varying the flux in the SQUID loop. By applying an ac pumping on the coupling SQUID with $H_Z = 2\lambda \cos(2E_m t/\hbar)(\sigma_{y1}\sigma_{y2} + \sigma_{z1}\sigma_{z2})$ for a duration of $\theta\hbar/2\lambda$, we have a Z-rotation gate $U_z(\theta) = \exp(i\theta Z/2)$. Combining the operations in Eq. (2.90) and Eq. (2.91), we achieve a complete $SU(2)$ generator set that generates arbitrary single-qubit quantum logic gates on the encoded qubit.

2.5.6.2 Controlled quantum logic gates

Two-qubit gates on the encoded qubits can be achieved by connecting the circuits of the encoded qubits as is shown in Fig. 2.14a. We consider two encoded qubits and use $\sigma_{\alpha j}$ as the Pauli operators for the first encoded qubit and $\tau_{\alpha j}$ as Pauli operators for the second encoded qubit. Assume that the lower physical qubits in each encoded qubit are connected with the coupling Hamiltonian

$$H_{\text{cgate}} = -2\lambda_c \cos(2(E_{m1} - E_{m2})t/\hbar)\sigma_{z2}\tau_{z2}. \tag{2.92}$$

The operators can be projected as

$$P_e \sigma_{z2} P_e = X_1 \tag{2.93}$$

$$P_e \tau_{z2} P_e = X_2 \tag{2.94}$$

onto the encoded subspaces. Hence, in the rotating frame the above coupling Hamiltonian can be written as

$$H_{\text{cgate}}^{(\text{rot})} = -\frac{\lambda_c}{2}(X_1 X_2 + Y_1 Y_2), \tag{2.95}$$

which provides a swap-like interaction between the encoded qubits. Combining this interaction with the single-qubit gates $U_x(\theta)$ and $U_z(\theta)$, we obtain a universal set of quantum logic operations for the encoded qubits. We can also design various geometries to connect arrays of encoded qubits. For example, in Fig. 2.14b, the lower physical qubits of the encoded qubits are connected to their nearest neighbors in a chain. In this case, the system can be viewed as a one-dimensional chain of qubits with nearest neighbor coupling. Universal quantum computation

can be implemented in this configuration.

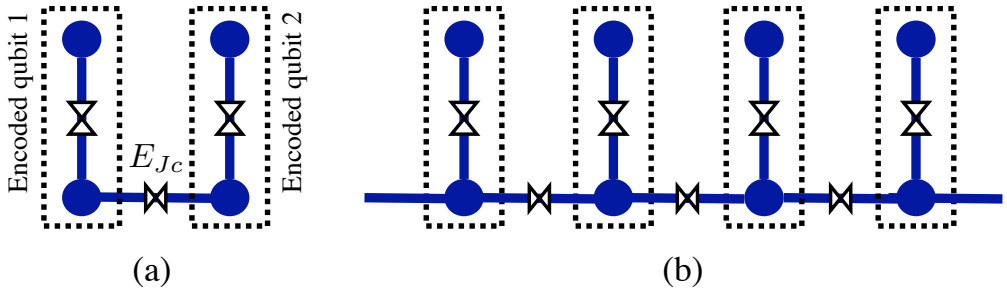

Figure 2.14: Encoded qubits connected with their nearest-neighbors. Blue dots mean physical qubit while the black crosses are tunable Josephson junctions.

For superconducting qubits, the above coupling Hamiltonian can be constructed using a tunable Josephson junction (a SQUID) that connects the physical qubits. For a SQUID with Josephson energy E_{Jc} and capacitive energy E_{cc}, we have

$$H_{\text{cgate}} = -\frac{E_{Jc}}{4}(\sigma_{z2}\tau_{z2} + \sigma_{y2}\tau_{y2}) + E_{cc}\sigma_{x2}\tau_{x2} \tag{2.96}$$

where both the Josephson energy and the capacitive energy can be tunable [67–70]. The coupling includes the extra terms $\sigma_{y2}\tau_{y2}$ and $\sigma_{x2}\tau_{x2}$, which only contain off-resonant leakage terms such as $|1\rangle_\sigma\langle 3| \otimes |3\rangle_\tau\langle 1|$. Under the time-dependent modulation $\cos(\omega_d t)$ by choosing proper pumping frequency, these terms can be neglected.

2.5.6.3 Numerical simulation

To test the analytical results in the previous subsections, we numerically calculated the fidelities of quantum logic gates. We simulated the evolution of the total time dependent hamiltonian containing gate operation and noise (2.97) with fourth-order Runge-Kutta method. This is repeated hundreds of times, randomly-generating $1/f$ noise for each time. Average gate fidelities were being tracked during the simulation and have been plotted as the figures shown in the paper.

In the simulation, we made the following assumptions on the $1/f$ noise: 1. all the physical qubits couple with the environmental noise in the form of $\delta V_{xj}(t)\sigma_{xj} + \delta V_{zj}(t)\sigma_{zj}$; 2. the noise power A^2 and the noise distribution angle η are the same for all physical qubits. The simulation of the $1/f$ noise can be implemented as

$$V_{\alpha j}(t) = \sum_{\omega=\omega_{ir}}^{\omega_{uv}} a_{\alpha j}(\omega)\cos(\omega t + \phi)\Delta\omega \tag{2.97}$$

where $a_{\alpha j}$ is a gaussian distribution with zero average and satisfies

$$\langle a_{\alpha x}(\omega_1)a_{\alpha x}(\omega_2)\rangle = A^2\cos^2(\eta)\delta(\omega_1 + \omega_2)/\omega_1 \tag{2.98}$$

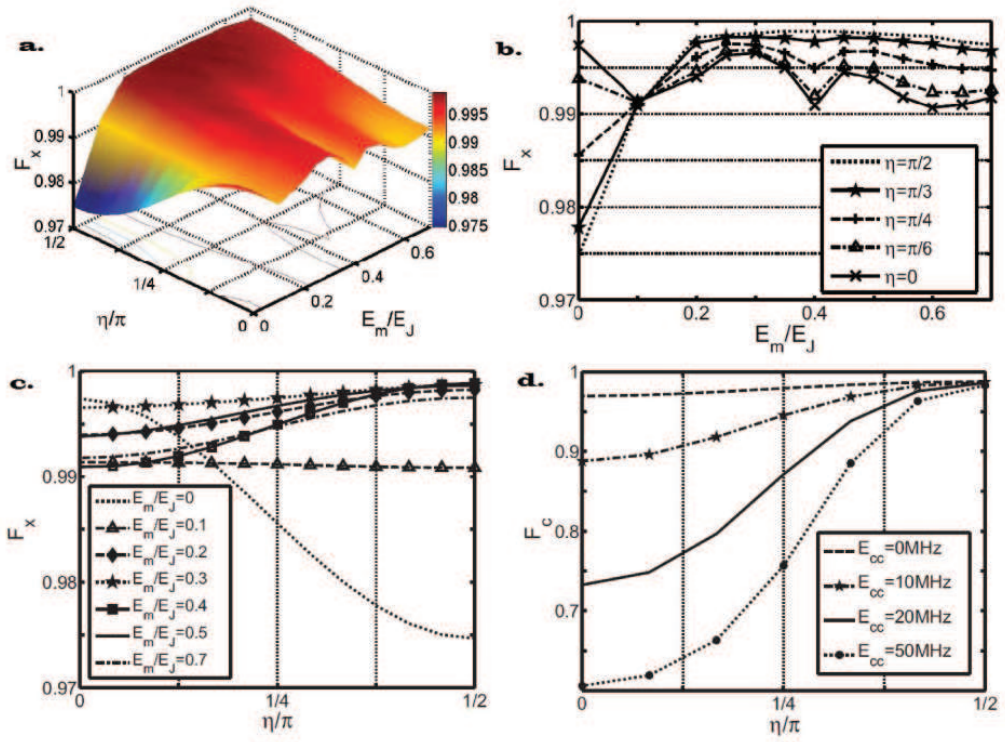

Figure 2.15: **a).** Gate fidelity F_x of single-qubit gate $U_x(\pi)$ versus η and E_m. Here, $E_J = 2E_z$. **b).** F_x versus E_m at various η as is labelled in the plot. **c).** F_x versus η at various E_m/E_z as is labelled in the plot. **d)**. The gate fidelity F_C of two-qubit gate U_C versus η at various $E_{cc}/2\pi\hbar$ as is labelled in the plot.

$$\langle a_{\alpha z}(\omega_1) a_{\alpha z}(\omega_2)\rangle = A^2 \sin^2(\eta)\delta(\omega_1+\omega_2)/\omega_1 \tag{2.99}$$

in connection with the definitions in Eq.(2.87) and Eq.(2.88). Here, discrete noise components are used to replace the continuous integral on the spectral density with $\Delta\omega/2\pi = 10^{-4}$ MHz. The phase ϕ is a random number with the uniform distribution between 0 and 2π. The parameters we choose for the physical qubits and the noise are $E_z/2\pi\hbar = 5$ GHz for the physical qubits, the infrared limit of the noise frequency $\omega_{ir}/2\pi = 1$ Hz, the upper bound of the noise frequency $\omega_{uv}/2\pi = 0.1$ MHz, and the noise power $A/E_z = 2\times 10^{-4}$ s/rad.

To simulate the effect of UQDP under one-qubit quantum operations, we use the following definition for the gate fidelity [71]

$$F_x = \frac{1}{2} + \frac{1}{12}\sum_{i=1,2,3} \mathrm{Tr}(U_x(\pi)\Sigma_i U_x^\dagger(\pi)\varepsilon(\Sigma_i)) \tag{2.100}$$

where $\Sigma_i = X, Y, Z$ for $i = 1, 2, 3$ are the Pauli operators for the encoded qubit and $\varepsilon(\Sigma_i) = P_e\mathcal{L}(\Sigma_i)P_e^\dagger$ is the projection of the final state onto the encoded subspace after applying the

quantum process on the initial density matrix Σ_i. The coupling constant is chosen to be $\lambda/2\pi\hbar = 300\,\text{MHz}$. The gate fidelity F_x of $U_x(\pi)$ versus η and E_m is plotted in Fig. 2.15**a, b, c**. For finite coupling E_m, where the encoded subspace is protected by the coupling, the fidelity only varies smoothly as the noise varies from transverse noise to longitudinal noise. While for $E_m = 0$, i.e. the uncoupled (bare) qubits, the fidelity decreases sharply as η increases to $\pi/2$. At fixed noise distribution η, the fidelity first rises rapidly when the coupling E_m increases from zero, then becomes saturated and even shows oscillatory behavior as E_m further increases. With $E_m \sim 0.4E_z$, F_x exceeds 0.997 for $\eta \in [0, \pi/2]$. In this regime, the optimal E_m for a particular η usually can be found within the range of $(0.4E_z,\ E_z)$.

For the two-qubit operation $U_C = \exp[-i\pi(X_1X_2 + Y_1Y_2)/4]$, the gate fidelity can be defined as [71]

$$F_C = \frac{1}{5} + \frac{1}{80}\sum_{i,j}\text{Tr}(U_C(\Sigma_i \otimes \Omega_j)U_C^\dagger \varepsilon(\Sigma_i \otimes \Omega_j)) \tag{2.101}$$

where $\Omega_i = X, Y, Z$ for $i = 1, 2, 3$ are the Pauli operators for the second encoded qubit and the super-operator gives $\varepsilon(\Sigma_i \otimes \Omega_j) = P_e\mathcal{L}(\Sigma_i \otimes \Omega_j)P_e^\dagger$. We choose the coupling of the first encoded qubit to be $E_{m1}/2\pi\hbar = 5\,\text{GHz}$ and the coupling of the second encoded qubit to be $E_{m2}/2\pi\hbar = 2\,\text{GHz}$. The operating Hamiltonian is given by Eq. (2.96) and is applied for a duration of $\pi\hbar/4\lambda_c$ with $\lambda_c/2\pi\hbar = 300\,\text{MHz}$. The gate fidelity F_c for U_C versus η is plotted in Fig. 2.15.**d** at various capacitive coupling E_{cc}. For zero E_{cc}, the gate U_C can be accomplished with high fidelity and shows only weak dependence on the distribution angle η, which proves the "universality" of our scheme. However, for non-zero E_{cc}, the fidelity drops quickly, and hence the implementation of the two-qubit gate requires the capacitive coupling to be small.

2.5.6.4 State preparation and detection

To implement the above quantum logic gates, we need to prepare the initial state of system in the encoded subspace. This can be achieved by letting the coupled qubits relax to their ground states $|1\rangle$ via thermalization. Then, an ac driving

$$H_{\text{prep}} = 2\lambda_p \cos\left[(E_1 - E_m)t/\hbar\right]\sigma_{x1} \tag{2.102}$$

can be applied on the first physical qubit, which generates a Rabi oscillation between the states $|1\rangle$ and $|3\rangle$ given the non-zero matrix element $\langle 3|\sigma_{x1}|1\rangle = -\sin(\theta/2 + \pi/4)$. After a period of $\pi/2\lambda_p \sin(\theta/2 + \pi/4)$, the state becomes $|3\rangle$ which is now in the encoded subspace.

State detection of the encoded qubits can be implemented with the assistance of single-qubit rotations as well. To measure the probability of an encoded qubit in the state $|3\rangle$ or $|4\rangle$, apply single-qubit gate $\exp[-i\pi X/4]$ as discussed above which converts the state $|3\rangle$ to the state $|\uparrow\downarrow\rangle$ and converts the state $|4\rangle$ to the state $|\downarrow\uparrow\rangle$. Then, measuring the physical qubits can give us information of the encoded states.

2.5.7 Discussions and Conclusions

The encoded qubit proposed above is made of two identical physical qubits with qubit energy E_z. For superconducting qubits, this parameter can be the Josephson energy E_J of

a charge qubit in the degeneracy point or the energy gap in the flux qubit. This parameter depends on the parameters of the Josephson junctions in the circuit. In real devices, the junction parameters usually have fabrication errors with an error spread on the order of 5%. Below we discuss the effect of the parameter error on the proposed scheme. We introduce a factor a_0 as the ratio between the energy of the second qubit and the energy of the first qubit with $|a_0 - 1| \ll 1$. The Hamiltonian in Eq. (2.74) becomes

$$H_{0\mathrm{n}} = E_z(\sigma_{z1} + a_0\sigma_{z2}) + E_m\sigma_{z1}\sigma_{z2}. \tag{2.103}$$

The eigenbasis of this Hamiltonian still includes the encoded subspace $\{|3\rangle, |4\rangle\}$, but with the new eigenstates and eigenenergies

$$\begin{array}{ll} |3\rangle_{\mathrm{n}} = \cos\varphi|3\rangle + \sin\varphi|4\rangle, & E_{3\mathrm{n}} = -E_{\mathrm{m,n}}; \\ |4\rangle_{\mathrm{n}} = -\sin\varphi|3\rangle + \cos\varphi|4\rangle, & E_{4\mathrm{n}} = E_{\mathrm{m,n}}; \end{array} \tag{2.104}$$

where $E_{\mathrm{m,n}} = \sqrt{(1-a_0)^2E_{\mathrm{J}}^2 + E_{\mathrm{m}}^2}$ and

$$\varphi = 1/2\sin^{-1}[(a_0 - 1)E_{\mathrm{z}}/E_{\mathrm{m,n}}] \tag{2.105}$$

respectively. The operators σ_{x1}, σ_{x2}, σ_{y1}, and σ_{y2} only contain non-vanishing matrix elements connecting $\{|1\rangle, |2\rangle\}$ and $\{|3\rangle, |4\rangle\}$. However, σ_{z1} and σ_{z2} now include non-trivial diagonal terms

$$\begin{array}{l} {}_{\mathrm{n}}\langle 3|\sigma_{z1}|3\rangle_{\mathrm{n}} = -{}_{\mathrm{n}}\langle 4|\sigma_{z1}|4\rangle_{\mathrm{n}} = \frac{-(1-a_0)E_{\mathrm{z}}}{E_{\mathrm{m,n}}}, \\ {}_{\mathrm{n}}\langle 3|\sigma_{z2}|3\rangle_{\mathrm{n}} = -{}_{\mathrm{n}}\langle 4|\sigma_{z2}|4\rangle_{\mathrm{n}} = \frac{(1-a_0)E_{\mathrm{z}}}{E_{\mathrm{m,n}}}, \end{array} \tag{2.106}$$

which induce residual longitudinal noises on the encoded qubit. The residual coupling can be derived as

$$V_{\mathrm{res}} \approx \frac{(a_0 - 1)E_{\mathrm{z}}}{E_{\mathrm{m,n}}}(\delta V_{z1} - \delta V_{z2})Z \tag{2.107}$$

in terms of the effective Pauli operator Z, which generates dephasing in first order terms of δV_{zj}. However, the residual coupling contains the ratio $|a_0 - 1|$ of the error spread which is less than 5% or even smaller with the advance of current technology. The dephasing by this term is hence reduced by a factor of $|a_0 - 1|^2 < 2 \times 10^{-3}$. Given the recent experimental measurement [56] of $|\delta V_{zj}/E_{\mathrm{z}}| < 10^{-2}$, the longitudinal dephasing due to the error spread can be comparable with or even lower than the quadratic dephasing due to the transverse noise in Eq. (2.89).

We would like to mention that the proposed scheme is different from the Decoherence Free Subspace (DFS) approach that has been widely studied in quantum information processing [72]. The DFS approach protects qubits from spatially correlated noises by choosing a subspace that is immune to such noises, i.e. the dephasing is suppressed by the noise correlation. While in our scheme, we explore the energy separation of the encoded subspace and the low-frequency nature of the noise (which can't excite transitions between states with large energy separation in the first order) to protect the quantum coherence.

In Sec. 2.5.2 and 2.5.6, we studied the encoded subspace and the gate operations using the coupling Hamiltonian with $E_{mx} = E_m$, $E_{my} = E_{mz} = 0$ for the simplicity of our discussions.

It can be shown that the UQDP approach can be applied to the general form of coupling given in Eq. (2.74) as far as either $E_{mx} \neq 0$ or $E_{my} \neq 0$ can be satisfied. As an example, consider the situation

$$E_{mx} = E_m,\ E_{my} = E_{mz} = b_0 E_m \tag{2.108}$$

with a coefficient b_0. In real system, this coupling can be obtained from a Josephson junction with energy E_{J2} that connects the two physical qubits and $b_0 = -\frac{E_{J2}}{4E_m}$. It can be found that the states $|3, 4\rangle$ defined in Eq. (2.77) still form the subspace for the encoded qubit. The energies of these states become $\epsilon_3 = -E_m - 2b_0 E_m$ and $\epsilon_4 = E_m$ including a shift due to the finite b_0. It can also be shown that the projections to the encoded subspace are $-P_e\sigma_{z1}P_e = P_e\sigma_{z2}P_e = X$ and $P_e\sigma_{xi}P_e = P_e\sigma_{yi}P_e = 0$. The encoded qubit is protected against any first order dephasing by the low-frequency noise. This observation shows that the UQDP scheme can be applied to various superconducting qubits such as flux qubits and phase qubits as far as we can construct the coupling in Eq.(2.74).

In conclusion, we have proposed a scheme of a universal quantum degeneracy point (UQDP) that can protect the superconducting qubits from generic low-frequency noise. Using coupled qubits to form the encoded qubits, we find a subspace where the low-frequency noise only affects the qubit dephasing to quadratic order. We have shown that universal quantum logic gates can also be performed on the encoded qubits with high fidelity. The scheme is robust again parameter spreads due to fabrication errors. The scheme can be applied to systems with very general form of couplings and provides a promising approach to protect superconducting qubits against low-frequency noise.

Chapter 3

Circuit QED

3.1 Introduction of superconducting circuit quantum electrical dynamics

In atomic quantum information devices, manipulation on qubit state can be enhanced by placing atoms into a cavity and hence coupled to coherent light. The dynamics is modeled as cavity quantum electrodynamics (CQED). Consider the qubit on a superconducting chip as an artificial "atom", AC signals propagating in the circuits as light. By coupling a superconducting qubit either capacitively or inductively to superconducting resonators, scientists have implement CQED method to manipulate quantum information on superconducting chips. Circuit QED is the formal terminology as the on-chip analogue of cavity QED. A key difference is that in circuit QED, the 'atom' does not move inside the "cavity", so the 'atom'–field interaction has time to act without losing the 'atom' and a trapping system is not needed. Together with the fact that the coupling strength is larger than the rate of photon lost from the cavity, which allows the strong coupling limit, even ultra-strong limit, of QED to be achieved in a relatively straightforward manner.

Fig.(3.1) shows schematic picture of charge qubit capacitively coupled to a transmission line resonator (TLR), as long as circuit model of the circuit QED system. [73] The Hamiltonian is

$$H = \hbar\omega^r(a^\dagger a + \frac{1}{2}) + \frac{\hbar\omega^q}{2}\sigma^z - e\frac{C_g}{C_\Sigma}\sqrt{\frac{\hbar\omega^r}{Lc}}(a^\dagger + a)(1 - 2n_g - \sigma^z\cos\theta + \sigma^x\sin\theta) \tag{3.1}$$

Here σ^x, σ^z are Pauli operators of the qubit, mixing angle $\theta = \arctan[E_J/4E_c(1-2n_g^{dc})]$ depends on dc bias charge n_g^{dc}, and the qubit energy splitting is $\hbar\omega^q = \sqrt{E_J^2 + [4E_c(1-2n_g^{dc})]^2}$. At the charge degeneracy point, $n_g^{dc} = 1/2$, $\theta = \pi/2$, Eq.(3.1) reduces to

$$H = \hbar\omega^r(a^\dagger a + \frac{1}{2}) + \frac{\hbar\omega^q}{2}\sigma^z + \hbar g\sigma^x(a^\dagger + a) \tag{3.2}$$

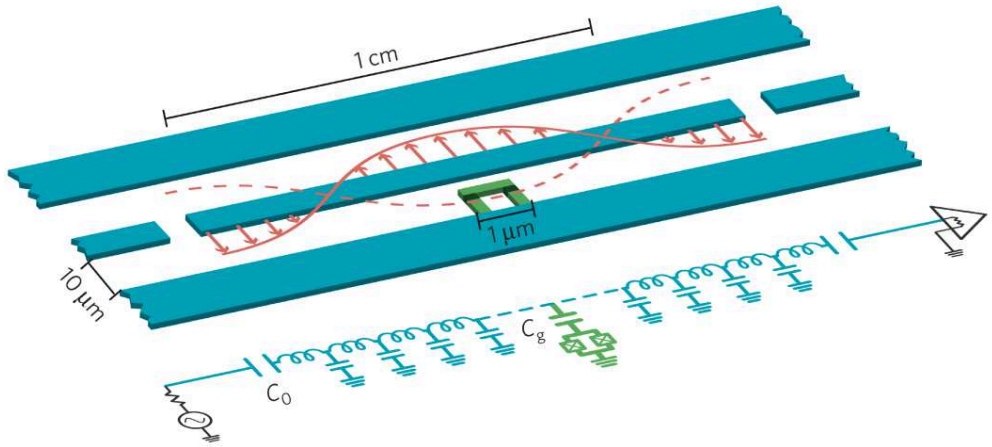

Figure 3.1: The upper part of the panel depicts a microstrip cavity (blue) that contains a charge qubit (green) placed at an antinode of the electric field. The microstripline can be used as a quantum bus. The lower part depicts this circuit in a lumped circuit representation. (Figure from Ref. [19]) C_0 is the capacitance of the coupling capacitor to the measurement electronics, and C_g is the capacitance of the coupling capacitor to the charge qubit.

Neglecting rapidly oscillating terms, Hamiltonian further reduces to

$$H = \hbar\omega^r(a^\dagger a + \frac{1}{2}) + \frac{\hbar\omega^q}{2}\sigma^z + \hbar g(a^\dagger\sigma^- + a\sigma^+) \tag{3.3}$$

where coupling strength $g = \frac{eC_g}{C_\Sigma}\sqrt{\frac{\omega^r}{\hbar L c}}$. This is the famous Jaynes-Cumming Hamiltonian used a lot in cavity QED. We note that we have omitted dampings for the moment. According to recent experimental results, ω^q and ω^r is in the range of $3-20GHz$, Q factor in superconducting resonators is up to 10^6 for on-chip TLR and 10^9 for 3D cavity. g can varies from $1-700MHz$, [74] which means circuit QED covers weak coupling, strong coupling and ultrastrong coupling regime, whereas, strong coupling is mostly studied so far.

Circuit QED can be operated in two distinct strong-coupling limits: the resonant regime, and the off-resonant dispersive regime. In the resonant regime, the qubit energy-level splitting is in resonance with the cavity frequency. While in off-resonant dispersive regime, qubit energy is off resonant with cavity. Dressed state, as combination of qubit excitation and cavity excitation, become the resultant state. Depending on whether qubit has bigger energy splitting or not, dressed states give rise to photon interaction in the cavity either repulsive or attractive. I will focus on the off-resonant dispersive regime in my thesis. In this case, the qubit and cavity eigenstates are not entangled, and the two systems cannot share excitations. The mutual energies, however, are still correlated, because the energy-level splitting of the qubit depends on the cavity state, and vice versa. Consequently, the cavity can be used to read out the qubit and to couple qubits to each other [74, 75].

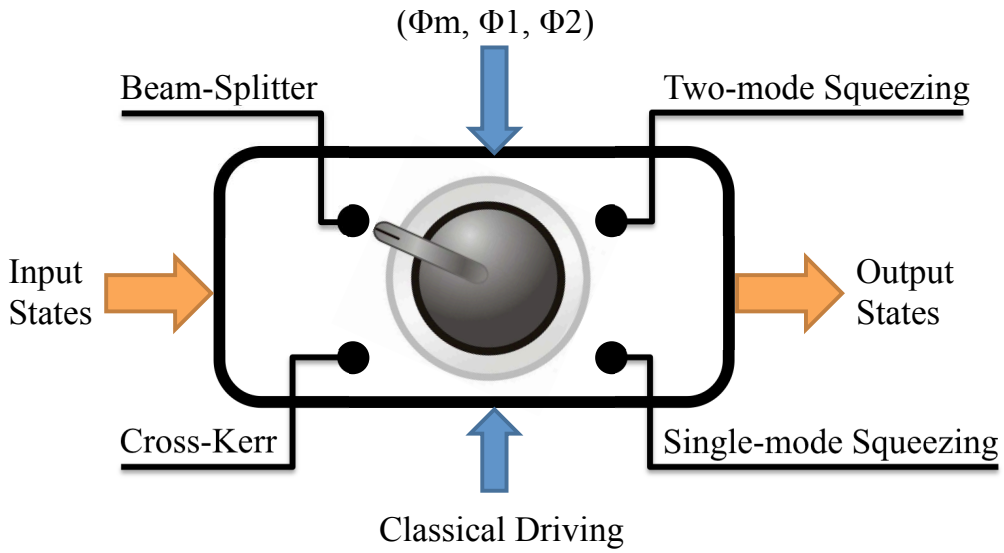

Figure 3.2: Illustration of dispersive FWM toolbox with controllable parameters Φ_m, Φ_1, Φ_2.

3.2 Parametric four-wave mixing toolbox for Circuit QED.

3.2.1 Introduction

Superconducting quantum circuits have been intensively studied as building blocks for quantum information processing. [19, 65, 76–86] Among these devices, superconducting microwave resonators have demonstrated relatively high quality factors and strong coupling with various superconducting qubits. [87] Various quantum optical phenomena and novel quantum many-body effects involving microwave photons, in particular, circuit quantum electrodynamics (CQED), have been observed in the superconducting resonators. [88]

The generation of non-classical states such as Fock states, entangled states, and NOON states in the superconducting resonators has been studied in recent experiments and theoretical proposals. [89–102] In most of these schemes, quantum state manipulation is achieved via the coupling between superconducting resonators and superconducting qubits. Several schemes have been proposed to generate unitary transformations on the microwave photons by engineering effective interaction Hamiltonians between the resonator modes, including Kerr and cross-Kerr interactions, beam-splitter operation, and squeezing operation. [70, 103–106] In all previous work, the proposed circuits can only realize specific quantum operation on the resonator modes.

Implementing quantum operations on superconducting resonators is crucial for realizing quantum information protocols in such devices. A basic set of quantum operations for both the discrete-state and the continuous variable quantum information protocols on the resonator modes include the Bogoliubov-linear operations such as the beam-splitter operation, the squeezing operation and the phase shifter, and nonlinear operations such as the cross-Kerr interaction. [107, 108] A discussion of these operations can be found in Appendix 2. In this work,

we present a scheme that can generate all of these operations within one single circuit. This toolbox is made of two superconducting qubits coupled with each other to form a quantum four-level system. Each qubit interacts with one superconducting resonator. By adjusting the parameters of the toolbox, we design dispersive four-wave mixing (FWM) processes to generate effective quantum operations on the resonator modes, as is illustrated in Fig. 3.2. During the operations, the quantum four-level system is always preserved in its quantum ground state by large detunings, and hence this scheme is a parametric scheme. Using numerical simulation, we show that high-fidelity quantum operations can be achieved with realistic circuit parameters. Compared with the previous schemes, [70,103–106] our results provide a switchable circuit that can generate all of the basic quantum operations by adjusting the parameters of the toolbox.

The paper is organized as the following. In Sec. 3.2.2, we present the general idea of the toolbox and illustrate the idea with a specific circuit made of two coupled superconducting charge qubits. In Sec. 3.2.3, we describe the dispersive FWM processes for generating effective Hamiltonians on the resonator modes using the toolbox. The realizations of four quantum operations are presented in detail in Sec. 3.2.4. In Sec. 3.2.5, we discuss the main sources of quantum errors in this scheme and present our numerical simulation of the quantum operations. Conclusions are given in Sec. 3.2.6. In Appendix 2, we briefly discuss all of the basic quantum operations and their roles in the quantum information processing for the resonator modes.

3.2.2 Circuit

The central element of the toolbox is a quantum four-level system that couples with the superconducting resonators and can be constructed in many ways. For the discussion in this paper, we will consider a circuit for the toolbox that is made of two superconducting qubits coupling with each other. The Hamiltonian for the total system has the form

$$H_{tot} = H_q + H_r + H_p, \tag{3.4}$$

which includes the Hamiltonian for the four-level system $H_q = \sum_j E_j|j\rangle\langle j|$ with eigenstates $|j\rangle$ and eigenenergies E_j ($j = a, b, c, d$), the Hamiltonian for the resonators and their couplings to the qubits

$$H_r = \sum_i \hbar\omega_{a_i}\hat{a}_i^\dagger\hat{a}_i + \hbar g_i\sigma_{xi}(\hat{a}_i^\dagger + \hat{a}_i), \tag{3.5}$$

with resonator frequencies ω_{a_i} and coupling constants g_i, and the Hamiltonian for the classical drivings on the qubits $H_p = \sum \hbar\Omega_i(t)\sigma_{xi}$ with driving amplitudes Ω_i. Without loss of generality, we have assumed that each resonator couples only with one qubit via the σ_{xi} operator and the classical driving is also on the σ_{xi} operator. Other forms of coupling and driving could also be considered for the toolbox.

The coupling terms in H_r (the driving terms in H_p) generate transitions between the eigenstates of the four-level system which involve absorption or emission of resonator photons (classical field). The transition matrix elements induced by these terms can be derived by projecting the σ_{xi} operator in the eigenbasis $|j\rangle$.

Superconducting qubits in various parameter regimes and circuit geometries have been studied, including flux qubit, phase qubit, charge qubit, transmon qubit, and *etc.*. [18, 19] The

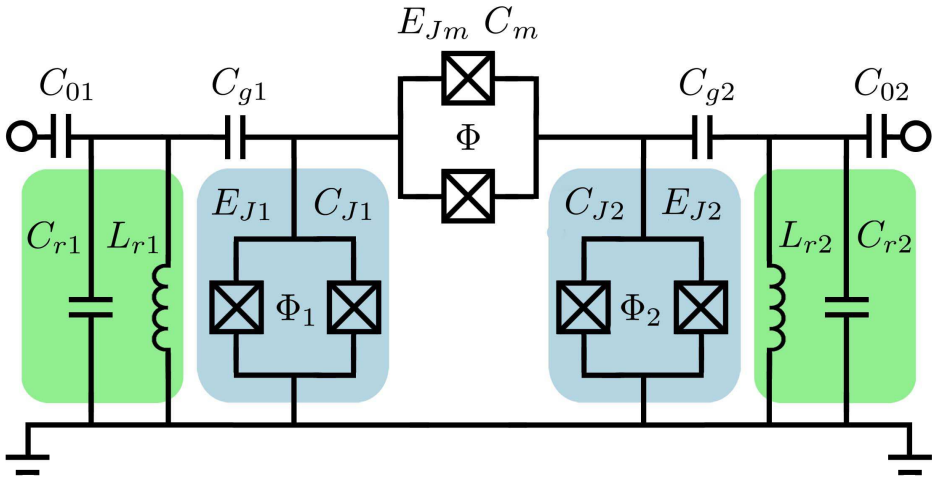

Figure 3.3: Schematic circuit for the toolbox. The resonators are labelled by capacitances C_{ri} and inductances L_{ri}.

qubits can be controlled by external electromagnetic fields such as the magnetic flux in the loop of a superconducting quantum interference device (SQUID) and the bias voltage on a superconducting island, depending on specific circuit design. Different coupling mechanisms between superconducting qubits have also been studied, such as capacitive coupling, Josephson coupling, and inductive coupling. [109–113] Decoherence in superconducting qubits has improved greatly in the past few years with $T_2^\star$ exceeding 95 μsec. recently observed. [59, 114–116]

To illustrate our scheme, we study a toolbox made of two superconducting charge qubits. [18] We want to emphasize, however, the FWM approach studied here is a general scheme that can be applied to other superconducting qubits with different forms of coupling. As shown in Fig. 3.3, the charge qubits couple with each other via a tunable Josephson junction and a capacitor where the effective Josephson energy E_{Jm} can be adjusted by varying the magnetic flux Φ in the loop. The Josephson energies E_{Ji} of the qubit junctions can be adjusted by changing the magnetic flux $\Phi_{1,2}$ in the qubit loops. The Hamiltonian for the coupled qubits can be derived using a Lagrangian approach with

$$H_q = (E_{J1}/2)\sigma_{z1} + (E_{J2}/2)\sigma_{z2} + H_{int} \tag{3.6}$$

$$H_{int} = E_{mx}\left(\sigma_{x1}\sigma_{x2} + b_0\sigma_{y1}\sigma_{y2} + b_0\sigma_{z1}\sigma_{z2}\right) \tag{3.7}$$

where E_{mx} is the capacitive coupling due to capacitance C_m and $b_0 = E_{Jm}/4E_{mx}$ is the ratio between the Josephson coupling and the capacitive coupling. Here, we assume the qubits are biased to have zero charging energy so that the qubit energies are the Josephson energies E_{Ji}. [117] We define the total capacitance connected to the superconducting island of the ith qubit as $C_{\Sigma i} = C_{Ji} + C_{gi} + C_m$ and the total capacitance connected to the ith resonator as $C_{\Sigma ri} = C_{ri} + C_{gi} + C_{0i}$, where C_{gi} is the capacitance that couples a resonator to its corresponding qubit, C_{Ji} is the Josephson capacitance, C_{ri} is the resonator capacitance, and C_{0i} is the capacitance that couples

to external circuit, as labeled in Fig. 3.3. With the capacitances satisfying $C_{\Sigma ri} \gg C_{\Sigma i} \gg C_m$, the capacitive coupling E_{mx} can be derived as

$$E_{mx} \approx C_m e^2 / \left[C_{\Sigma 1} C_{\Sigma 2} - C_m^2 \right]. \tag{3.8}$$

The eigenenergies of the Hamiltonian H_q are

$$E_a = E_{mx} b_0 - E_{s+}/2, \tag{3.9a}$$
$$E_b = -E_{mx} b_0 - E_{s-}/2, \tag{3.9b}$$
$$E_c = -E_{mx} b_0 + E_{s-}/2, \tag{3.9c}$$
$$E_d = E_{mx} b_0 + E_{s+}/2, \tag{3.9d}$$

where $E_{s\pm} = \sqrt{(E_{J1} \pm E_{J2})^2 + 4E_{mx}^2 (1 \mp b_0)^2}$ can be adjusted by varying the qubit energies E_{Ji} and the Josephson coupling E_{Jm}. The eigenstates are

$$|a\rangle = -\sin\theta_+ |0_1 0_2\rangle + \cos\theta_+ |1_1 1_2\rangle, \tag{3.10a}$$
$$|b\rangle = \cos\theta_- |0_1 1_2\rangle - \sin\theta_- |1_1 0_2\rangle, \tag{3.10b}$$
$$|c\rangle = \sin\theta_- |0_1 1_2\rangle + \cos\theta_- |1_1 0_2\rangle, \tag{3.10c}$$
$$|d\rangle = \cos\theta_+ |0_1 0_2\rangle + \sin\theta_+ |1_1 1_2\rangle, \tag{3.10d}$$

where $|0_i\rangle$ and $|1_i\rangle$ are the single-qubit eigenstates in the σ_{zi} basis and

$$\sin\theta_\pm = \sqrt{\left[E_{s\pm} \pm (E_{J1} \pm E_{J2})\right] / 2E_{s\pm}}.$$

The resonator-qubit coupling g_i for the ith resonator in Eq. (3.5) can also be derived using the Lagrangian approach with

$$g_i = \left(\frac{C_{gi} C_{\Sigma \bar{i}}}{C_{\Sigma 1} C_{\Sigma 2} - C_m^2} \right) \left(\frac{e^2}{2C_{\Sigma ri}} \hbar \omega_{a_i} \right)^{1/2} \tag{3.11}$$

where $C_{\Sigma \bar{i}}$ is the total capacitance of the $\bar{i}$th qubit with the index $\bar{i}$ referring to the qubit in the opposite side of the toolbox from the ith resonator. We also find that the ith resonator couples with the $\bar{i}$th qubit as well as the $\bar{i}$th resonator in the opposite side of the toolbox due to the cross-talk of the circuit elements. These indirect couplings have the forms of $\hbar g_i^{(2)} \sigma_{xi} (\hat{a}_{\bar{i}}^\dagger + \hat{a}_{\bar{i}})$ and $\hbar g^{(3)} (\hat{a}_1 + \hat{a}_1^\dagger)(\hat{a}_2 + \hat{a}_2^\dagger)$ with coupling constants much weaker than the dominant couplings g_i in Eq. (3.11), as will be discussed in Sec. 3.2.5.

Both the resonator-qubit coupling and the classical driving H_p are associated with the

qubit operators σ_{xi}. In the eigenbasis in Eqs. (3.10a, 3.10b, 3.10c, 3.10d), we have

$$\begin{aligned}\sigma_{x1} &= \cos(\theta_+ - \theta_-)(\sigma_{ab} + \sigma_{dc}) \\ &\quad + \sin(\theta_+ - \theta_-)(\sigma_{db} - \sigma_{ac}) + h.c. \qquad (3.12a)\\ \sigma_{x2} &= -\sin(\theta_+ + \theta_-)(\sigma_{ab} - \sigma_{dc}) \\ &\quad + \cos(\theta_+ + \theta_-)(\sigma_{ac} + \sigma_{db}) + h.c. \qquad (3.12b)\end{aligned}$$

where $\sigma_{ij} = |i\rangle\langle j|$ defines the transition operator connecting the eigenstates $|i\rangle$ and $|j\rangle$. From these expressions, it follows that each resonator (and classical driving) generally couples to four transitions. For example, the σ_{x1} term includes the σ_{ab}, σ_{dc} transitions with amplitude $g_1 \cos(\theta_+ - \theta_-)$ and the σ_{ac}, σ_{db} transitions with amplitude $\pm g_1 \sin(\theta_+ - \theta_-)$.

In the following sections, we will show how to engineer the energy levels of the quantum four-level system to have the resonators couple only with selected transitions by adjusting the circuit parameters.

3.2.3 Dispersive FWM scheme

The effective Hamiltonians to implement quantum operations on the resonators can be realized via the resonator-qubit coupling and classical driving in the circuit studied above. Here, we exploit four-photon processes, [118–123] in which single-photon transitions and two-photon processes are in the dispersive regime with large detunings while the designated four-photon processes are nearly at resonance. As an example, in Fig. 3.5a, consider a classical driving of frequency ω_1 generating the transition σ_{ac} with Rabi frequency Ω_1 and the resonator mode $\hat{a}_1$ generating the transition σ_{dc} with effective transition matrix element $\tilde{g}_1$. For the single-photon transition induced by the classical driving, the dispersive condition requires that $|\Delta_1| = |\omega_1 - E_{ca}/\hbar| \gg \Omega_1$; and for the single-photon transition induced by mode $\hat{a}_1$, it requires that $|\omega_{a_1} - E_{dc}/\hbar| \gg \tilde{g}_1\sqrt{n_1}$ with $E_{ij} = E_i - E_j$ and n_1 being the average photon number in $\hat{a}_1$. For the two photon process involving these two transitions, it requires that $|\Delta_1\delta| \gg \Omega_1\tilde{g}_1\sqrt{n_1}$ with $|\delta| = |\omega_1 + \omega_{a_1} - E_{da}/\hbar|$ being the two-photon detuning. Under the dispersive conditions, the dominant physical processes in this scheme are four-photon processes which can generate effective coupling between the resonator modes. Because the dispersive conditions prevent real transitions, the quantum four-level system is preserved in its ground state during the operation. The processes studied here are hence parametric schemes where the four-level system is subject to a "quantum" energy shift. [118]

To implement a quantum operation, we need to adjust the parameters of the superconducting circuit to find appropriate effective coupling constants and energy separations between the eigenstates. For the circuit in Fig. 3.3, we adopt two approaches to determine the circuit parameters. The first approach uses the relation in Eq. (3.12a, 3.12b) to tune the effective transition matrix elements by adjusting the angles $\theta_\pm$. By adjusting the circuit parameters E_{J1}, E_{J2}, b_0, the angles can be varied in a large range. The second approach exploits the controllability of the energy levels to engineer large detunings to suppress unwanted transitions. As an example, in Fig. 3.4, we plot the eigenenergies as functions of the ratio b_0 (defined in Sec. 3.2.2). As b_0 varies, the state $|a\rangle$ ($|c\rangle$) can be either above or below the state $|b\rangle$ ($|d\rangle$), which provides the

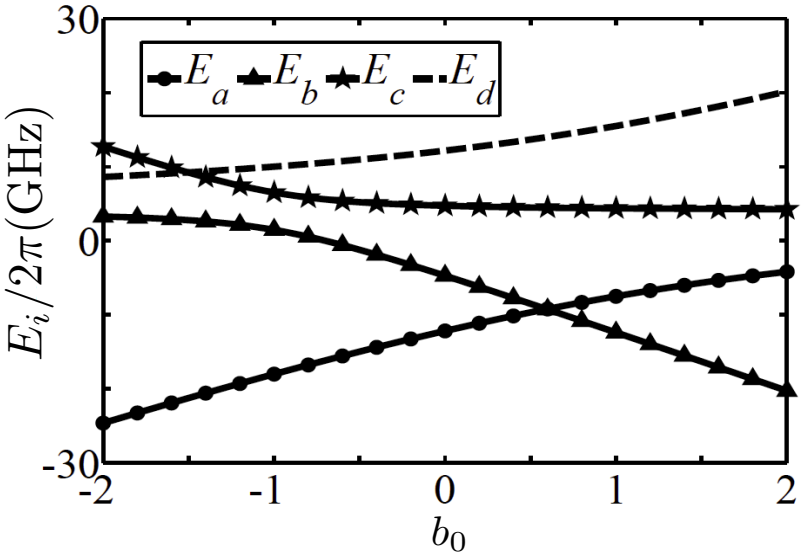

Figure 3.4: Eigenenergies of the four-level system at $E_{J1}/2\pi\hbar = 8.9\,\text{GHz}$, $E_{J2}/2\pi\hbar = 13.9\,\text{GHz}$, and $E_{mx}/2\pi\hbar = 4\,\text{GHz}$ (parameters used in the cross-Kerr operation in Sec. 3.2.4.2).

possibility to arrange both the order and the energy separation of the eigenstates. To make, e.g. the mode $\hat{a}_1$ only couples strongly to the σ_{ab} transition, we choose the parameters to have: (1) $\cos(\theta_+ - \theta_-) \gg \sin(\theta_+ - \theta_-)$ and (2) $|\omega_{a_1} - E_{ba}/\hbar| \ll |\omega_{a_1} - E_{dc}/\hbar|$. The first condition significantly reduces the effective coupling between $\hat{a}_1$ and the σ_{ac}, σ_{db} transitions and the second condition suppresses the $\hat{a}_1\sigma_{dc}$ term by large detuning. Now, mode $\hat{a}_1$ couples mainly with the σ_{ab} transition. In general, by combining the above two approaches, all quantum operations described in Appendix 2 can be realized with the FWM scheme within one single circuit.

3.2.4 Realization of operations

In this section, we present the realization of four quantum operations described in Appendix 2 using the quantum toolbox. The system parameters are chosen as the following: $\omega_{a_1}/2\pi = 10\,\text{GHz}$ and $\omega_{a_2}/2\pi = 16\,\text{GHz}$ for the resonator frequencies, $g_1/2\pi = g_2/2\pi = 0.3\,\text{GHz}$ for the coupling constants, and $E_{mx}/2\pi\hbar = 4\,\text{GHz}$ for the capacitive coupling defined in Eq. (3.8). The effective Josephson energies E_{J1}, E_{J2}, and E_{Jm} can be adjusted by tuning the magnetic flux Φ_1, Φ_2, and Φ respectively. The energy diagrams of the dispersive FWM schemes for the operations are shown in Fig. 3.5.

3.2.4.1 Beam-splitter operation

Consider the energy diagram in Fig. 3.5a, where the detunings are defined as $\Delta_1 = \omega_1 - E_{ca}/\hbar$, $\Delta_2 = \omega_2 - E_{ba}/\hbar$, and $\delta = \omega_1 + \omega_{a_1} - E_{da}/\hbar$ with ω_i being the frequency of the classical driving. In the energy diagram, the resonator modes only couple with the upper transitions σ_{db}, σ_{dc} and the classical drivings only couple with the lower transitions σ_{ab}, σ_{ac}.

The selection of these couplings can be achieved by choosing the adjustable parameters as $b_0 = -1$, $E_{J1}/2\pi\hbar = 13\,\text{GHz}$, and $E_{J2}/2\pi\hbar = 19\,\text{GHz}$ to generate highly asymmetric energy levels. Under these parameters and appropriate classical driving frequencies, the detunings for the desired single-photon and two-photon processes as labelled in the energy diagram are $\Delta_i/2\pi = -3.65\,\text{GHz}$ and $\delta/2\pi = -0.55\,\text{GHz}$. The detunings for the unwanted transitions, e.g. $\omega_{a_1} - E_{ba}/\hbar, \omega_{a_2} - E_{ca}/\hbar, \sim 13\,\text{GHz}$, are on a much larger scale, and hence the unwanted transitions are suppressed. These parameters also give $|\cos(\theta_+ - \theta_-)| \gg |\sin(\theta_+ - \theta_-)|$ so that the coupling between the mode $\hat{a}_1$ ($\hat{a}_2$) and the transition σ_{db} (σ_{dc}) is much weaker than the coupling between the mode $\hat{a}_1$ ($\hat{a}_2$) and the transition σ_{dc} (σ_{db}). As a result, the mode $\hat{a}_1$ mainly couples with the σ_{dc} transition. Similar arguments apply to other transitions in the energy diagram.

We divide the total Hamiltonian into two parts: $H_{tot} = H_0 + V$ where

$$H_0/\hbar = \omega_1\sigma_{cc} + \omega_2\sigma_{bb} + (\omega_1 + \omega_{a_1})\sigma_{dd} + \sum_i \omega_{a_i}\hat{a}_i^\dagger\hat{a}_i, \tag{3.13}$$

$\sigma_{ii} = |i\rangle\langle i|$, and V includes all remaining terms in the total Hamiltonian. Here, the ground state energy is set to zero. The Hamiltonian in the interaction picture of H_0 can be written as $e^{iH_0t/\hbar}Ve^{-iH_0t/\hbar} \approx H_{I0} + V_I$ under the rotating wave approximation with $H_{I0}/\hbar = -\Delta_1\sigma_{cc} - \Delta_2\sigma_{bb} - \delta\sigma_{dd}$ and

$$V_I/\hbar = \Omega_1\sigma_{ca} + \Omega_2\sigma_{ba} + \tilde{g}_1\hat{a}_1\sigma_{dc} + \tilde{g}_2e^{i\Delta_F t}\hat{a}_2\sigma_{db} + h.c.. \tag{3.14}$$

The effective couplings $\tilde{g}_1 = g_1\cos(\theta_+ - \theta_-)$ and $\tilde{g}_2 = g_2\cos(\theta_+ + \theta_-)$ are derived from Eqs. (3.12a, 3.12b). And, $\Delta_F = \omega_1 + \omega_{a_1} - \omega_2 - \omega_{a_2}$ is a small detuning for the four-photon process designed to balance the extra terms in the effective Hamiltonian for the resonators.

Given the dispersive conditions discussed in Sec. 3.2.3, we treat V_I as a perturbation to the Hamiltonian H_{I0}. Assume that the toolbox is initially prepared in its ground state $|a\rangle$. It can be shown that the dominant correction to H_{I0} by the perturbation V_I is a fourth-order term that generates a "quantum" energy shift in the ground state in the form of $\sigma_{aa}H_{\text{bm}}$ where

$$H_{\text{bm}}/\hbar = \sum_i \delta\epsilon_i^{\text{bm}}\hat{a}_i^\dagger\hat{a}_i + \left(\chi^{\text{bm}}\hat{a}_1^\dagger\hat{a}_2e^{i\Delta_F t} + h.c.\right) \tag{3.15}$$

with the energy shifts $\delta\epsilon_i^{\text{bm}} = \Omega_i^2\tilde{g}_i^2/\Delta_i^2\delta$, the effective coupling constant

$$\chi^{\text{bm}} = \Omega_1\Omega_2\tilde{g}_1\tilde{g}_2/\Delta_1\Delta_2\delta, \tag{3.16}$$

and the four-photon detuning $\Delta_F = \delta\epsilon_2^{\text{bm}} - \delta\epsilon_1^{\text{bm}}$. The small four-photon detuning is chosen to balance the effect of the mode shifts $\delta\epsilon_i^{\text{bm}}$. The above effective Hamiltonian performs the beam-splitter operation on the resonators while the toolbox is preserved in the ground state during the operation. The beam-splitter operation can perform the swap gate on the resonators after applied for a gate time of $\pi/2\chi^{\text{bm}}$. [107] With the parameters given above and with $\Omega_i/2\pi = 1\,\text{GHz}$, the effective coupling is $|\chi^{\text{bm}}|/2\pi = 11.6\,\text{MHz}$ and the swap gate has a gate time of 21.6 nsec..

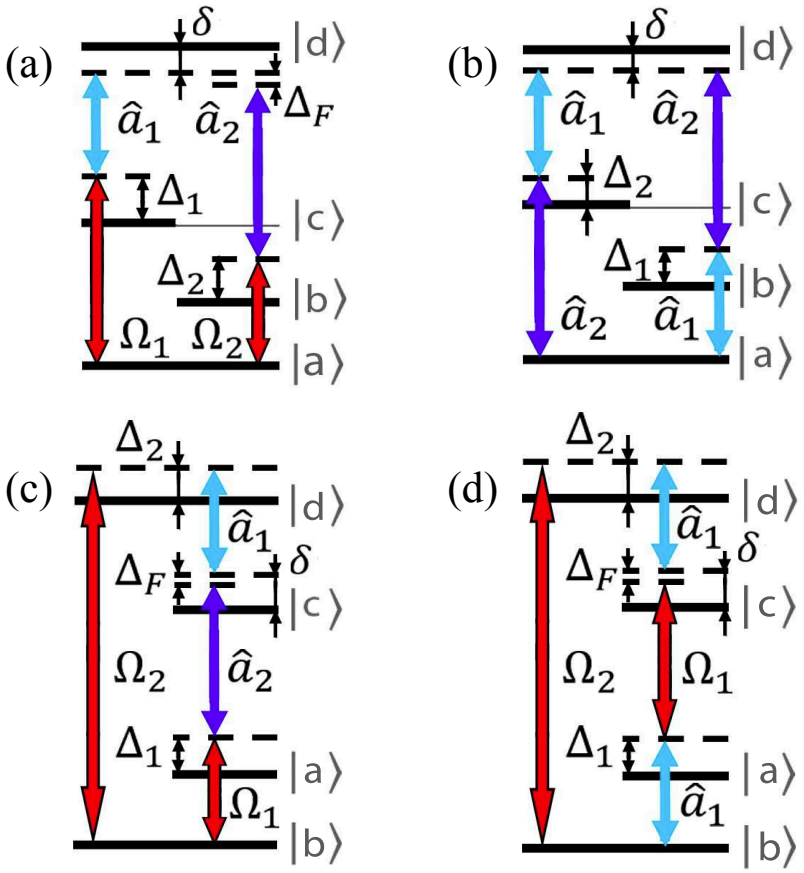

Figure 3.5: (Color online) Energy diagram for the FWM schemes of (a) beam-splitter operation, (b) cross-Kerr interaction, (c) two-mode squeezing, and (d) single-mode squeezing. The labels are: detuning Δ_i for single-photon transition, detuning δ for two-photon process, detuning Δ_F for four-photon process, Rabi frequency Ω_i for classical driving (red arrows), and operator $\hat{a}_i$ for resonator mode (light and dark blue arrows).

3.2.4.2 Cross-Kerr nonlinearity

The energy diagram for the cross-Kerr operation is shown in Fig. 3.5b with the detunings defined as $\Delta_1 = \omega_{a_1} - E_{ba}/\hbar$, $\Delta_2 = \omega_{a_2} - E_{ca}/\hbar$, and $\delta = \omega_{a_1} + \omega_{a_2} - E_{da}/\hbar$. Compared with the beam-splitter operation, the asymmetry in the energy levels is reduced and no classical driving needs to be applied. The parameters are chosen to be $b_0 = -0.6$, $E_{J1}/2\pi\hbar = 8.9\,\text{GHz}$, and $E_{J2}/2\pi\hbar = 13.9\,\text{GHz}$, which give $\Delta_1/2\pi = -4.9\,\text{GHz}$, $\Delta_2/2\pi = -4.8\,\text{GHz}$, and $\delta/2\pi = -0.12\,\text{GHz}$. Under these parameters, the effective coupling constants for the desired couplings $\hat{a}_1\sigma_{dc}, \hat{a}_1\sigma_{ab}$ are $\tilde{g}_1/2\pi \approx 0.3\,\text{GHz}$. While the unwanted couplings $\hat{a}_1\sigma_{db}, \hat{a}_1\sigma_{ac}$ are strongly suppressed with $\tilde{g}_1/2\pi \approx 0.01\,\text{GHz}$. The unwanted coupling $\hat{a}_2\sigma_{dc}$ has a detuning of $|\omega_{a_2} - E_{dc}/\hbar|/2\pi \approx 11\,\text{GHz}$ and is suppressed by the large detuning.

We divide the total Hamiltonian as $H_{tot} = H_0 + V$ with

$$H_0/\hbar = \omega_{a_1}\sigma_{bb} + \omega_{a_2}\sigma_{cc} + \omega_t\sigma_{dd} + \sum_i \omega_{a_i}\hat{a}_i^\dagger\hat{a}_i \tag{3.17}$$

and $\omega_t = \omega_{a_1} + \omega_{a_2}$. The Hamiltonian in the interaction picture of H_0 is $e^{iH_0t/\hbar}Ve^{-iH_0t/\hbar} \approx H_{I0} + V_I$ under the rotating wave approximation where $H_{I0}/\hbar = -\Delta_1\sigma_{bb} - \Delta_2\sigma_{cc} - \delta\sigma_{dd}$ and

$$V_I/\hbar = \tilde{g}_1\hat{a}_1(\sigma_{dc} + \sigma_{ba}) + \tilde{g}_2\hat{a}_2(\sigma_{db} + \sigma_{ca}) + h.c. \tag{3.18}$$

with the effective couplings $\tilde{g}_1 = g_1\cos(\theta_+ - \theta_-)$ and $\tilde{g}_2 = g_2\cos(\theta_+ + \theta_-)$. With the same perturbation theory approach as used in the previous subsection, we derive the fourth-order perturbation correction to the ground state energy $\sigma_{aa}H_{\rm ck}$. Here,

$$H_{\rm ck}/\hbar = \sum_i \delta\epsilon_i^{\rm ck}\hat{a}_i^\dagger\hat{a}_i + \chi^{\rm ck}\hat{a}_1^\dagger\hat{a}_2^\dagger\hat{a}_2\hat{a}_1, \tag{3.19}$$

with the energy shifts $\delta\epsilon_i^{\rm ck} = \tilde{g}_i^2/\Delta_i$ and the effective coupling

$$\chi^{\rm ck} = (1/\Delta_1 + 1/\Delta_2)^2\left(\tilde{g}_1^2\tilde{g}_2^2/\delta\right). \tag{3.20}$$

With the above parameters, $|\chi^{\rm ck}|/2\pi = 8.4\,\text{MHz}$ which generates the controlled phase gate with a gate time of 59.5 nsec..

3.2.4.3 Two-mode squeezing

In Fig. 3.5c, we present an energy diagram that can realize the two-mode squeezing operation with the detunings defined as $\Delta_1 = \omega_1 - E_{ab}/\hbar$, $\Delta_2 = \omega_2 - E_{db}/\hbar$, and $\delta = \omega_2 - \omega_{a_1} - E_{cb}/\hbar$. Here, the order of the eigenstates is switched with $E_a > E_b$, i.e. the state $|b\rangle$ is the ground state of the toolbox. The circuit parameters are chosen to be $b_0 = 0.8$, $E_{J1}/2\pi\hbar = 4\,\text{GHz}$ and $E_{J2}/2\pi\hbar = 22\,\text{GHz}$. Under these parameters, we tune the classical driving frequencies to have $\Delta_i/2\pi = 3\,\text{GHz}$ and $\delta/2\pi = 0.9\,\text{GHz}$. The classical drivings generate the σ_{ab}, σ_{db} transitions in the energy diagram. It can also be shown that the mode $\hat{a}_1$ mainly couples with the σ_{dc} transition and the mode $\hat{a}_2$ mainly couples with the σ_{ac} transition.

Using the approach in the previous subsections with

$$H_0/\hbar = \omega_1\sigma_{aa} + \omega_s\sigma_{cc} + \omega_2\sigma_{dd} + \sum_i \omega_{a_i}\hat{a}_i^\dagger\hat{a}_i, \tag{3.21}$$

and $\omega_s = \omega_2 - \omega_{a_1}$, we derive that $H_{I0}/\hbar = -\Delta_1\sigma_{aa} - \Delta_2\sigma_{dd} - \delta\sigma_{cc}$ and

$$V_I/\hbar = \Omega_1\sigma_{ab} + \Omega_2\sigma_{db} + \tilde{g}_1\hat{a}_1\sigma_{dc} + \tilde{g}_2e^{i\Delta_F t}\hat{a}_2\sigma_{ac} + h.c. \tag{3.22}$$

with the effective couplings $\tilde{g}_1 = g_1\cos(\theta_+ - \theta_-)$ and $\tilde{g}_2 = g_2\cos(\theta_+ + \theta_-)$, and a small four-photon detuning $\Delta_F = \omega_2 - \omega_1 - \omega_{a_1} - \omega_{a_2}$. The fourth-order perturbation correction to the

ground state energy is $\sigma_{aa}H_{\rm sq}$ with

$$H_{\rm sq}/\hbar = \sum_i \delta\epsilon_i^{\rm sq}\hat{a}_i^\dagger\hat{a}_i + \left(\chi^{\rm sq}\hat{a}_1^\dagger\hat{a}_2^\dagger e^{i\Delta_F t} + h.c.\right), \tag{3.23}$$

where the energy shifts are $\delta\epsilon_i^{\rm sq} = \Omega_{\bar{i}}^2\tilde{g}_{\bar{i}}^2/\Delta_{\bar{i}}^2\delta$ with the index $\bar{i}$ referring to the circuit elements in the opposite side of the ith resonator (e.g. for $i = 1, \bar{i} = 2$), the effective coupling is

$$\chi^{\rm sq} = \Omega_1\Omega_2\tilde{g}_1\tilde{g}_2/\Delta_1\Delta_2\delta, \tag{3.24}$$

and the four-photon detuning is $\Delta_F = -\delta\epsilon_1^{\rm sq} - \delta\epsilon_2^{\rm sq}$. The nonzero four-photon detuning balances the effect of the energy shifts and makes the squeezing operation possible. With the parameters given above and with $\Omega_i/2\pi = 1$ GHz, we have $|\chi^{\rm sq}|/2\pi = 9.7$ MHz.

3.2.4.4 Single-mode squeezing

The single-mode squeezing operation can be realized with the energy diagram in Fig. 3.5d with the detunings defined as $\Delta_1 = \omega_{a_1} - E_{ab}/\hbar$, $\Delta_2 = \omega_2 - E_{db}/\hbar$, and $\delta = \omega_2 - \omega_{a_1} - E_{cb}/\hbar$. The circuit parameters are chosen to be $b_0 = 1.25$, $E_{J1}/2\pi\hbar = 8$ GHz and $E_{J2}/2\pi\hbar = 24$ GHz. Tuning the frequencies of the classical drivings, we can have $\Delta_1/2\pi = 4$ GHz, $\Delta_2/2\pi = -3.5$ GHz, and $\delta/2\pi = 0.5$ GHz. We adjust the circuit parameters to increase the energy separation between the states $|a\rangle$ and $|b\rangle$ to be close to the frequency of the mode $\hat{a}_1$ so that $\hat{a}_1$ couples strongly with the σ_{ab} transition as well as with the σ_{dc} transition. Meanwhile, the energy levels are adjusted so that the frequency of the mode $\hat{a}_2$ is largely detuned from all possible transitions and is effectively decoupled from the toolbox. The classical drivings generate the σ_{ac}, σ_{db} transitions.

With the Hamiltonian

$$H_0/\hbar = \omega_{a_1}\sigma_{aa} + \omega_s\sigma_{cc} + \omega_2\sigma_{dd} + \sum_i \omega_{a_i}\hat{a}_i^\dagger\hat{a}_i, \tag{3.25}$$

and $\omega_s = \omega_2 - \omega_{a_1}$, we have $H_{I0}/\hbar = -\Delta_1\sigma_{aa} - \Delta_2\sigma_{dd} - \delta\sigma_{cc}$ and

$$V_I/\hbar = \Omega_1\sigma_{ca}e^{i\Delta_F t} + \Omega_2\sigma_{db} + \tilde{g}_1\hat{a}_1(\sigma_{dc} + \sigma_{ab}) + h.c. \tag{3.26}$$

with the effective coupling constant $\tilde{g}_1 = g_1\cos(\theta_+ - \theta_-)$ and the four photon detuning $\Delta_F = \omega_2 - \omega_1 - 2\omega_{a_1}$. Then, we derive the fourth-order perturbation correction to the ground state energy $\sigma_{aa}H_{\rm sq1}$ with

$$H_{\rm sq1}/\hbar = \delta\epsilon_1^{\rm sq1}\hat{a}_1^\dagger\hat{a}_1 + \left(\chi^{\rm sq1}\hat{a}_1^\dagger\hat{a}_1^\dagger e^{-i\Delta_F t} + h.c.\right) \tag{3.27}$$

where the energy shifts are

$$\delta\epsilon_1^{\rm sq1} = \left(\delta/\Delta_1 + \Omega_1^2/\Delta_1^2 + \Omega_2^2/\Delta_2^2\right)\left(\tilde{g}_1^2/\delta\right), \tag{3.28}$$

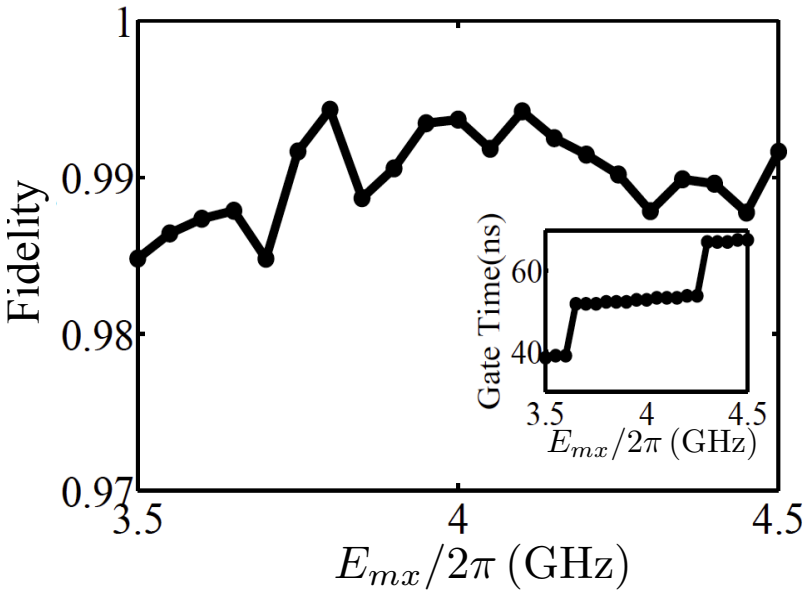

Figure 3.6: Fidelity and gate time versus E_{mx} for the controlled phase gate using the scheme and parameters in Sec. 3.2.4.2

the effective coupling constant is

$$\chi^{\mathrm{sq1}} = \Omega_1\Omega_2\tilde{g}_1^2/\Delta_1\Delta_2\delta, \tag{3.29}$$

and the four-photon detuning is $\Delta_F = 2\delta\epsilon_1^{\mathrm{sq1}}$. With the parameters given above and with $\Omega_i/2\pi = 1$ GHz, we find that $|\chi^{\mathrm{sq1}}|/2\pi = 11.1$ MHz.

3.2.5 Error sources

Quantum errors can affect the effective quantum operations on the superconducting resonators. In our system, the main sources of quantum errors include (1) unwanted transitions induced by resonator-qubit coupling and classical driving, (2) indirect coupling due to the cross-talk between different circuit elements, and (3) decoherence of the qubits and resonators.

We first study the effect of unwanted transitions on the effective quantum operations. In the schemes discussed in the previous section, the circuit parameters can be adjusted to either reduce the coupling matrix element of the unwanted transitions or vary the energy levels to produce large detuning to suppress the unwanted transitions. To test the effectiveness of our approach, we numerically simulate the quantum operations using the full Hamiltonian in Eq. (3.4) which includes all coupling terms. In Fig. 3.6, we show the simulation results for the controlled quantum phase gate on Fock states. This gate is realized with the cross-Kerr operation which applies the operator $\exp(-i\chi^{\mathrm{ck}}t)$ to the states. [107] This gate generates a π phase on the states after a gate time of π/χ^{ck} when both resonators are in state $|1\rangle$. For the initial state $(|0_1\rangle+|1_1\rangle)(|0_2\rangle+|1_2\rangle)/2$, the target final state is $(|0_1 0_2\rangle+|0_1 1_2\rangle+|1_1 0_2\rangle-|1_1 1_2\rangle)/2$. In our

simulation, we calculate the fidelity of this gate for $E_{mx}/2\pi \in (3.5, 4.5)$ GHz. For each value of E_{mx}, we search for a set of parameters E_{Ji} and b_0 that yields high gate fidelity. At $E_{mx}/2\pi = 4$ GHz with the parameters in the previous section, the fidelity exceeds 0.99. Our results show that high fidelity can be achieved for this operation by choosing appropriate parameters.

Another source of quantum errors is the circuit cross-talk between different circuit elements. In Eqs. (3.5, 3.11), the direct coupling between the resonator and its neighboring qubit is presented. However, due to the cross-talk, each resonator also couples with the qubit in the opposite side of the circuit in the form of $\hbar g_i^{(2)} \sigma_{xi} (\hat{a}_{\bar{i}}^\dagger + \hat{a}_{\bar{i}})$. The coupling constant for this indirect coupling is

$$g_i^{(2)} = \left(\frac{C_{gi} C_m}{C_{\Sigma 1} C_{\Sigma 2} - C_m^2} \right) \left(\frac{e^2}{2 C_{\Sigma ri}} \hbar \omega_{a_i} \right)^{1/2} \tag{3.30}$$

with $g_i^{(2)}/g_i = C_m / C_{\Sigma \bar{i}} \ll 1$. Another indirect coupling is the coupling between the two resonators in the form of $g^{(3)}(a_1 + a_1^\dagger)(a_2 + a_2^\dagger)$ with the coupling constant

$$g^{(3)} = \frac{\sqrt{C_{g1} C_{g2}} C_m}{C_{\Sigma 1} C_{\Sigma 2} - C_m^2} \sqrt{\frac{C_{g1} C_{g2}}{4 C_{\Sigma r1} C_{\Sigma r2}}} \sqrt{\hbar \omega_{a_1} \hbar \omega_{a_2}}. \tag{3.31}$$

It can be shown that

$$g^{(3)}/g_i \sim \frac{C_m}{C_{\Sigma \bar{i}}} \sqrt{\frac{C_{gi}}{4 C_{\Sigma ri}}} \sqrt{\frac{\hbar \omega_{a_i}}{e^2/2 C_{gi}}} \ll 1. \tag{3.32}$$

These indirect coupling terms can hence be neglected.

Decoherence of the superconducting qubits and resonators is one of the key barriers for scalable quantum computing and has been intensively studied. The superconducting resonators have relatively high Q-factors. With Q exceeding 10^6, it corresponds to a damping time of $\sim 100\,\mu$sec.. In recent experiments, the decoherence time of superconducting qubits has been significantly improved and $T_2^\star$ can reach $95\,\mu$sec.. [114, 116] Meanwhile, for the dispersive FWM schemes studied in this work, the quantum toolbox is preserved in its ground state during the quantum operations and is not affected by the decoherence of the qubits. Our study in the previous section also shows that the time scale for the quantum operations - $\sim \pi/\chi^\alpha$ for operation α - is well below 100 nsec. which is shorter than the decoherence time by $2-3$ orders of magnitudes. Hence, decoherence has very weak effect on our schemes.

3.2.6 Conclusions

To conclude, we presented a superconducting quantum toolbox that can perform various quantum operations on superconducting resonators in one single circuit. The scheme exploits the dispersive FWM approach to generate effective couplings between the resonator modes. By adjusting the circuit parameters, the energy levels and coupling constants can be varied to generate specific quantum operation. We discussed the main error sources in the schemes and numerically simulated the controlled phase gate on Fock states. Our results showed that high-fidelity quantum operations can be achieved in this circuit. One advantage of this scheme is that nearly all quantum operations for both discrete-state and continuous-variable quantum protocols

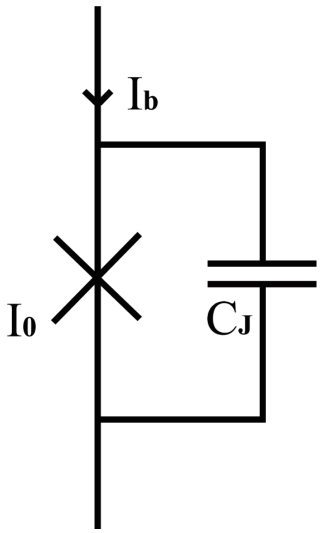

Figure 3.7: Schematic circuit diagram of phase qubit.

can be realized in one single circuit. [107,108,124] Our scheme can advance the implementation of quantum information processing on the microwave modes in the superconducting circuits.

3.3 Three wave-mixing scheme with phase qubit

3.3.1 Parametric three-level artificial atom

The three-level structure is implemented with a phase qubit. A single junction phase qubit, with current bias, can be modeled as Fig.(3.7) by parallelly connecting a nonlinear inductor and a capacitor with current $I_c \sin\phi$ and $\frac{\hbar}{2e}C\ddot{\phi}$ respectively. Using Kerchhoff's Law a classical equation of motion for ϕ yields:

$$\frac{\hbar}{2e}C\ddot{\phi} + I_c \sin\phi = I_e, \tag{3.33}$$

Potential energy term is $U(\phi) = E_J(1-\cos\phi) - I_e\phi$,where $E_J = \frac{\hbar I_c}{2e}$. Kinetic energy term $K(\dot{\phi}) = \frac{1}{2}(\frac{\hbar}{2e})^2 C\dot{\phi}^2, m_\phi = (\frac{\hbar}{2e})^2 C$, single eletron charging energy $E_c = \frac{e^2}{2C}$, being the dual operator of phase difference the number operator $n = \frac{\hbar C}{(2e)^2}\dot{\phi}, K(\dot{\phi}) = 4E_c n^2$. So hamiltonian for phase qubit becomes

$$H_{qb} = 4E_c n^2 + E_J(1-\cos\phi) - \frac{\hbar}{2e}I_e\phi = 4E_c n^2 + E_J[(1-\cos\phi) - \frac{I_e}{I_c}\phi], \tag{3.34}$$

For potential $U(\phi)$, considering the bottom part, it can be treated as a simple harmonic potential $U(\phi)_{SHO} \approx E_J \cos\phi_0(\phi-\phi_0)^2/2$,where $\sin\phi_0 = I_e/I_c$ corresponds to potential minimum, with

the plasma frequency $\omega_p = (\frac{2e}{\hbar C})^{1/2}[I_c^2 - I_e^2]^{1/4} = \sqrt{8E_cE_J\cos\phi_0}$. Barrier height $\Delta U = U_{\max} - U_{\min} = \frac{\hbar}{2e}[I_e(2\sin^{-1}\frac{I_e}{I_c} - \pi) + 2\sqrt{I_c^2 - I_e^2}] = E_J[\sin\phi_0(2\phi_0 - \pi) + 2\cos\phi_0]$. Then, we can adjust the barrier height in order to keep only three levels in the well.

In order to quantize energy levels in the well, we need to do some approximation to $U(\phi)$. Considering biasing with dc-current I_e close to I_c, we have $I_e = I_c\sin\phi_0$. Expanding to third order of $(\phi - \phi_0)$ because the forth order term has very small coefficient $\cos\phi_0/4!$ considering I_e is usually close to I_c,

$$U(\phi) = E_J[(1 - \cos\phi) - \frac{2e}{\hbar}\phi\sin\phi_0] \tag{3.35}$$

$$= E_J[1 - \frac{2e}{\hbar}\phi_0\sin\phi_0 - \cos(\phi - \phi_0)\cos\phi_0 + \sin(\phi - \phi_0)\sin\phi_0 - (\phi - \phi_0)\sin\phi_0] \tag{3.36}$$

$$\approx E_J[(\phi - \phi_0)^2\frac{\cos\phi_0}{2} - (\phi - \phi_0)^3\frac{\sin\phi_0}{6}], \tag{3.37}$$

Constant terms have been neglected in the last step. This result shows the well potential of phase qubit can be treated as cubic potential.

Now the hamiltonian turns into $H_{phase} = 4E_cn^2 + (\phi - \phi_0)^2 E_J\frac{\cos\phi_0}{2} - (\phi - \phi_0)^3\frac{E_J\sin\phi_0}{6}$. In order to solve energy levels, we firstly transform H_{phase} with

$$a = (\frac{1}{2\hbar})^{1/2}(\frac{E_J\cos\phi_0}{8E_c})^{1/4}(\phi - \phi_0) + i(\frac{1}{2\hbar})^{1/2}(\frac{8E_c}{E_J\cos\phi_0})^{1/4}n, \tag{3.38}$$

$$a^+ = (\frac{1}{2\hbar})^{1/2}(\frac{E_J\cos\phi_0}{8E_c})^{1/4}(\phi - \phi_0) - i(\frac{1}{2\hbar})^{1/2}(\frac{8E_c}{E_J\cos\phi_0})^{1/4}n, \tag{3.39}$$

so that,

$$H_{qb} = \hbar\omega_p(a^\dagger a + \frac{1}{2}) - \zeta(a + a^+)^3, \tag{3.40}$$

where $\zeta = 1/\sqrt{54N_s}$ and $N_s = \frac{2^{3/4}}{3}(\frac{E_J}{E_c})^{1/2}(1 - \sin\phi_0)^{5/4}$ meaning the number of harmonic oscillator states. Solving eigenvalues of this cubic potential energy requires perturbation theory and recursion Method [125, 126]. For $\frac{E_c}{E_J} \ll 1$, to the fourth order:

$$E_0(\phi_0) = \hbar\omega_p(\frac{1}{2} - \frac{11}{8}\zeta(\phi_0)^2 - \frac{465}{32}\zeta(\phi_0)^4), \tag{3.41}$$

$$E_1(\phi_0) = \hbar\omega_p(\frac{3}{2} - \frac{71}{8}\zeta(\phi_0)^2 - \frac{5625}{32}\zeta(\phi_0)^4), \tag{3.42}$$

$$E_2(\phi_0) = \hbar\omega_p(\frac{5}{2} - \frac{191}{8}\zeta(\phi_0)^2 - \frac{23475}{32}\zeta(\phi_0)^4). \tag{3.43}$$

Figure-1 shows the energy levels of E_0, E_1, E_2.

And figure-2 shows dependance of ζ on bias current $\sin\phi_0$.

In order to satisfy perturbative condition, ζ needs to be at least one order of magnitude smaller than ζ^2, to which order the perturbation terms will be neglected.(see following) By tuning current bias $\sin\phi_0$, we can adjust the energy splitting between different levels.

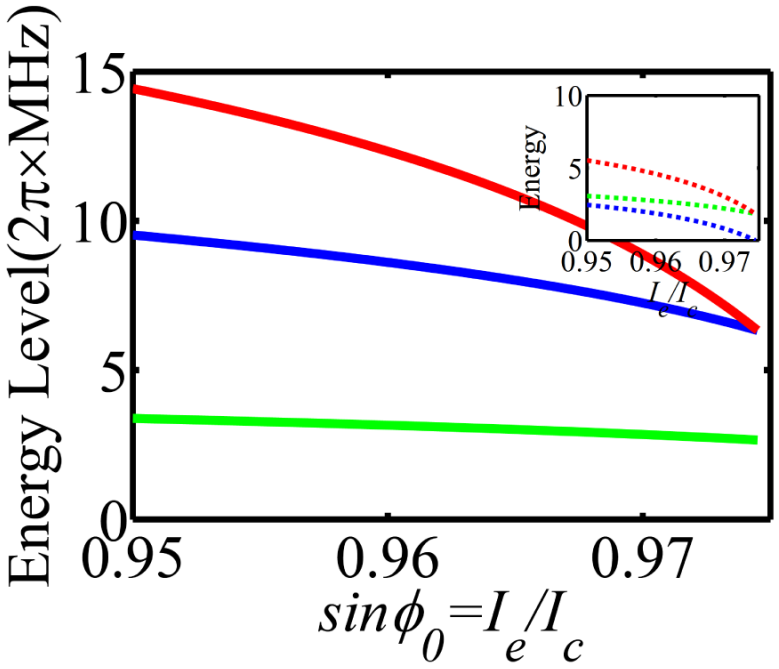

Figure 3.8: Energy levels are shown in terms of bias $\sin\phi_0$. Inset is for photon energy in resonance with possible transitions among these three levels.

$$\Delta E_{10}(\phi_0) = E_1 - E_0 = \hbar\omega_p(1 - \frac{15}{2}\zeta(\phi_0)^2 - \frac{5160}{32}\zeta(\phi_0)^4), \tag{3.44}$$

$$\Delta E_{21}(\phi_0) = E_2 - E_1 = \hbar\omega_p(1 - \frac{30}{2}\zeta(\phi_0)^2 - \frac{17850}{32}\zeta(\phi_0)^4), \tag{3.45}$$

$$\Delta E_{20}(\phi_0) = E_2 - E_0 = \hbar\omega_p(2 - \frac{45}{2}\zeta(\phi_0)^2 - \frac{23010}{32}\zeta(\phi_0)^4). \tag{3.46}$$

Eigenstates(un-normalized) for the first three levels $|g\rangle, |a\rangle, |b\rangle$ to the second order is approximated as

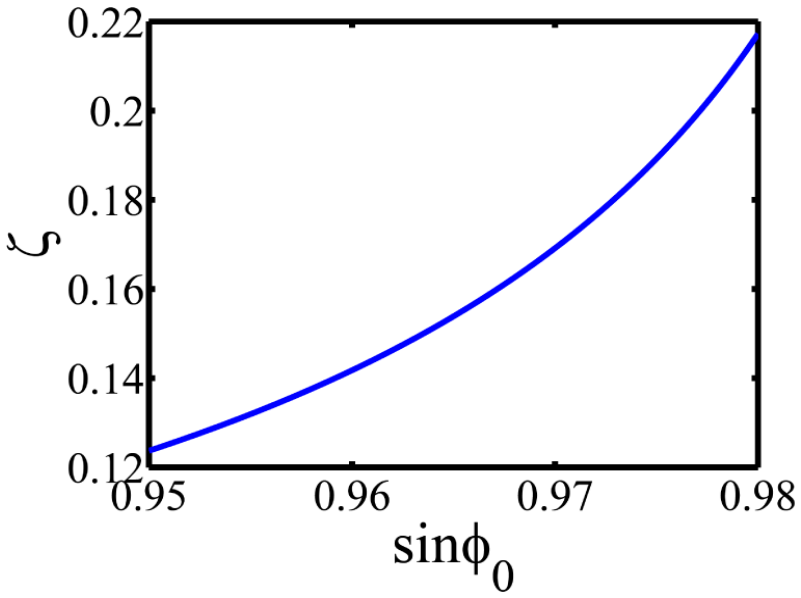

Figure 3.9: ζ in terms of bias current rate is plotted.

$$|g\rangle = |0\rangle + \zeta(\frac{3}{2\sqrt{2}}|1\rangle + \frac{1}{2\sqrt{3}}|3\rangle) + \zeta^2(\frac{27\sqrt{2}}{16}|2\rangle + \frac{7\sqrt{6}}{16}|4\rangle + \frac{2\sqrt{5}}{24}|6\rangle), \tag{3.47}$$

$$|a\rangle = |1\rangle + \zeta(-\frac{3}{2\sqrt{2}}|0\rangle + 3|2\rangle + \frac{\sqrt{3}}{3}|4\rangle) + \zeta^2(\frac{67\sqrt{6}}{16}|3\rangle + \frac{11\sqrt{30}}{16}|5\rangle + \frac{\sqrt{35}}{12}|7\rangle), \tag{3.48}$$

$$|b\rangle = |2\rangle + \zeta(-3|1\rangle + \frac{9\sqrt{3}}{2\sqrt{2}}|3\rangle + \frac{\sqrt{15}}{3\sqrt{2}}|5\rangle) + \zeta^2(-\frac{9\sqrt{2}}{16}|0\rangle + \frac{121\sqrt{3}}{8}|4\rangle + \frac{45\sqrt{10}}{16}|6\rangle + \frac{\sqrt{465}}{18}|8\rangle). \tag{3.49}$$

Since a and $a^\dagger$ are annihilation and creation operators for basis $\{|0\rangle, |1\rangle, |2\rangle, ...\}$,

$$\langle g|a|a\rangle = 1 + 04.83\zeta^2 + 51.66\zeta^4, \tag{3.50}$$

$$\langle a|a|g\rangle = 3.75\zeta^2 + 353.47\zeta^4, \tag{3.51}$$

$$\langle g|a|b\rangle = -1.5\zeta + 40.09\zeta^3, \tag{3.52}$$

$$\langle b|a|g\rangle = 0.5\zeta + 1.26\zeta^3, \tag{3.53}$$

$$\langle b|a|a\rangle = 36.86\zeta^2 + 232.16\zeta^4, \tag{3.54}$$

$$\langle a|a|b\rangle = 1.414 + 33\zeta^2 + 639.48\zeta^4, \tag{3.55}$$

$$\langle g|\, a^{+}\, |a\rangle = 0.13\zeta^2 + 343.65\zeta^4, \tag{3.56}$$
$$\langle a|\, a^{+}\, |g\rangle = 1 + 4.82\zeta^2 + 51.66\zeta^4, \tag{3.57}$$
$$\langle g|\, a^{+}\, |b\rangle = 0.5\zeta + 0.42\zeta^3, \tag{3.58}$$
$$\langle b|\, a^{+}\, |g\rangle = -1.5\zeta + 20.34\zeta^3, \tag{3.59}$$
$$\langle b|\, a^{+}\, |a\rangle = 1.414 + 33\zeta^2 + 625.42\zeta^4, \tag{3.60}$$
$$\langle a|\, a^{+}\, |b\rangle = 10.61\zeta^2 + 232.15\zeta^4, \tag{3.61}$$

$$\langle g|\, (a - a^{+})\, |a\rangle = 1 + 4.70\zeta^2 - 291.99\zeta^4, \tag{3.62}$$
$$\langle a|\, (a - a^{+})\, |g\rangle = -1 - 1.08\zeta^2 + 301.81\zeta^4, \tag{3.63}$$
$$\langle g|\, (a - a^{+})\, |b\rangle = -2\zeta + 39.67\zeta^3, \tag{3.64}$$
$$\langle b|\, (a - a^{+})\, |g\rangle = 2\zeta - 19.08\zeta^3, \tag{3.65}$$
$$\langle b|\, (a - a^{+})\, |a\rangle = -1.41 + 3.86\zeta^2 - 111.49\zeta^4, \tag{3.66}$$
$$\langle a|\, (a - a^{+})\, |b\rangle = 1.41 + 22.39\zeta^2 + 407.3\zeta^4, \tag{3.67}$$

$$\langle g|\, (a + a^{+})\, |a\rangle = 1 + 4.96\zeta^2 + 295.69\zeta^4, \tag{3.68}$$
$$\langle a|\, (a + a^{+})\, |g\rangle = 1 + 8.58\zeta^2 + 401\zeta^4, \tag{3.69}$$
$$\langle g|\, (a + a^{+})\, |b\rangle = -1\zeta + 40.5\zeta^3, \tag{3.70}$$
$$\langle b|\, (a + a^{+})\, |g\rangle = -1\zeta + 21.6\zeta^3, \tag{3.71}$$
$$\langle b|\, (a + a^{+})\, |a\rangle = 1.41 + 69.9\zeta^2 + 857\zeta^4, \tag{3.72}$$
$$\langle a|\, (a + a^{+})\, |b\rangle = 1.41 + 43.6\zeta^2 + 971.6\zeta^4, \tag{3.73}$$

By taking average,

$$\langle g|\, a^{+}\, |a\rangle = 0.13\zeta^2 + 293.84\zeta^4, \tag{3.74}$$
$$\langle a|\, a^{+}\, |g\rangle = 1 + 4.82\zeta^2 + 201.10\zeta^4, \tag{3.75}$$
$$\langle g|\, a^{+}\, |b\rangle = 0.5\zeta + 0.42\zeta^3, \tag{3.76}$$
$$\langle b|\, a^{+}\, |g\rangle = -1.5\zeta + 20.34\zeta^3, \tag{3.77}$$
$$\langle b|\, a^{+}\, |a\rangle = 1.414 + 33\zeta^2 + 625.42\zeta^4, \tag{3.78}$$
$$\langle a|\, a^{+}\, |b\rangle = 10.61\zeta^2 + 282.15\zeta^4. \tag{3.79}$$

To the first order of perturbation

$$a^{\dagger} \equiv \begin{bmatrix} 0 & 0 & 0.5\zeta \\ 1 & 0 & 0 \\ -1.5\zeta & 1.414 & 0 \end{bmatrix}, a \equiv \begin{bmatrix} 0 & 1 & -1.5\zeta \\ 0 & 0 & 1.414 \\ 0.5\zeta & 0 & 0 \end{bmatrix}. \tag{3.80}$$

we can see the perturbation approach have good agreement for different cases.

3.3.2 Phase qubit coupled to a resonator

3.3.2.1 Hamiltonian

Consider two transmission line resonators with hamiltonian $H_{tlr1,2} = \hbar\omega_{1,2}b_{1,2}b^{+}_{1,2}$, where $\omega_{1,2} = \frac{2\pi}{L_{1,2}\sqrt{lc}}$ and l, c are capacitance per unit length of transmission line. The phase qubit is capacitively connected to them leading to electrostatic energy on coupling capacitor C_{g1} and C_{g2}. So coupling hamiltonian can be derived as following

$$H_{coupling} = \frac{1}{2}C_{g1}(\widetilde{V}_1 - V)^2 + \frac{1}{2}C_{g2}(\widetilde{V}_2 - V)^2 \tag{3.81}$$

$$= \frac{1}{2}(C_{g1} + C_{g2})V^2 - C_{g1}V\widetilde{V}_1 - C_{g2}V\widetilde{V}_2 + \frac{1}{2}C_{g1}\widetilde{V}_1^2 + \frac{1}{2}C_{g1}\widetilde{V}_1^2 \tag{3.82}$$

where $\widetilde{V}_1, \widetilde{V}_2, V$ are voltage over C_{g1} C_{g2} and phase qubit. Quantized cavity field arises $\widetilde{V}_{1,2} = V_{1,2}(b^{+}_{1,2}+b_{1,2})$, where V_1 and V_2 are amplitudes depending on location. And $V_{1,2} = \sqrt{\frac{\omega_{1,2}}{lc}}\cos(\frac{2\pi x}{L_{1,2}})$, x is the position to couple the phase qubit on TLR. Notice that the second and third term of the previous hamiltonian means interaction between phase qubit and TLRs. So interaction hamiltonian would be

$$H_{int} = -C_{g1}V\widetilde{V}_1 - C_{g2}V\widetilde{V}_2 \tag{3.83}$$

$$= -2eV_1\frac{C_{g1}}{C}n(b_1^{+} + b_1) - 2eV_2\frac{C_{g2}}{C}n(b_2^{+} + b_2) \tag{3.84}$$

Using transform in equation3.38,

$$H_{int} = ig_1(a - a^{+})(b_1^{+} + b_1) + ig_2(a - a^{+})(b_2^{+} + b_2) \tag{3.85}$$

where coupling strengths $g_{1,2} = eV_{1,2}\frac{C_{g1,2}}{C}(\frac{1}{2\hbar})^{-1/2}(\frac{8E_c}{E_J\cos\phi_0})^{-1/4}$.

3.3.2.2 Transition matrices

In order to realize three wave-mixing, we need to adjust the barrier height to allow only three levels in the well. Assume the ground state, first excited state and second excited state are $|g\rangle, |a\rangle, |e\rangle$, corresponding to $|\Psi_0\rangle, |\Psi_1\rangle, |\Psi_2\rangle$ in the discussion of phase qubit.

Represents $(a - a^+)i$ in the eigen-states yields: transission selection rules

$$\sigma_{ag}/i = \langle g|\,(a - a^+)\,|a\rangle = 1 + 4.70\zeta^2 - 291.99\zeta^4, \tag{3.86}$$
$$\sigma_{ga}/i = \langle a|\,(a - a^+)\,|g\rangle = -1 - 1.08\zeta^2 + 301.81\zeta^4, \tag{3.87}$$
$$\sigma_{bg}/i = \langle g|\,(a - a^+)\,|b\rangle = -2\zeta + 39.67\zeta^3, \tag{3.88}$$
$$\sigma_{gb}/i = \langle b|\,(a - a^+)\,|g\rangle = 2\zeta - 19.08\zeta^3, \tag{3.89}$$
$$\sigma_{ab}/i = \langle b|\,(a - a^+)\,|a\rangle = -1.41 + 3.86\zeta^2 - 111.49\zeta^4, \tag{3.90}$$
$$\sigma_{ba}/i = \langle a|\,(a - a^+)\,|b\rangle = 1.41 + 22.39\zeta^2 + 407.3\zeta^4, \tag{3.91}$$

The small asymmetric between two conjugate elements is due to perturbation cut-off. Assume $E_J = 50E_c$ and $\sin\phi_0 = 0.9$, which means I_e is very close to I_c. This is a usual bias case in phase qubit experiment(ref.). Then perturbation parameter $\zeta \approx 0.2$. We can keep the lowest terms

$$\sigma_{ag} = \sigma_{ga}^+ = \langle g|\,i(a - a^+)\,|a\rangle = i, \tag{3.92}$$
$$\sigma_{bg} = \sigma_{gb}^+ = \langle g|\,i(a - a^+)\,|b\rangle = -0.62i, \tag{3.93}$$
$$\sigma_{ab} = \sigma_{ba}^+ = \langle b|\,i(a - a^+)\,|a\rangle = -1.41i, \tag{3.94}$$

These Pauli matrices are the transission matrices when the phase qubit is capacitively coupled to cavities.

3.3.3 Three wave-mixing approach

Now we have a three level artificial atom coupled to two cavities. And all the possible transissions are coupled to cavity modes. We are going to discuss a general case of three wave-mixing approach using perturbation theory. Considering frequency selection rules similar to atom system, we neglect large detunings and leave small detunings remaining in the dispersive regime to avoid real excitation. Using RWA we get the following effective hamiltonian

$$\begin{aligned}\frac{H_{int}}{\hbar} =& g_\alpha\left(\sigma_{ae}c_1^+ e^{i\Delta_\alpha t} + \sigma_{ea}c_1 e^{-i\Delta_\alpha t}\right) + \\ & g_\beta\left(\sigma_{ga}c_2^+ e^{i\Delta_\beta t} + \sigma_{ag}c_2 e^{-i\Delta_\beta t}\right) + \\ & g_p\left(\sigma_{eg}c_3 e^{-i\Delta_p t} + \sigma_{ge}c_3^+ e^{i\Delta_p t}\right).\end{aligned} \tag{3.95}$$

where coupling strengths to each transission have been rewrited as g_α, g_β, g_p respectively and c_1, c_2, c_3 corresponds to three photon modes.

By performing transformation $T = \exp i\left[\left(-\Delta_\alpha + \Delta_p\right)\sigma_{aa} + \Delta_p\sigma_{ee}\right]t$ we obtain following

Hamiltonian

$$\frac{H}{\hbar} = \left(\Delta_\alpha - \Delta_p\right)\sigma_{aa} - \Delta_p\sigma_{ee} + g_p\left(\sigma_{eg}c_3 + \sigma_{ge}c_3^+\right) \tag{3.96}$$

$$+ g_\alpha\left(\sigma_{ae}c_1^+ + \sigma_{ea}c_1\right) + g_\beta\left(\sigma_{ga}c_2^+ e^{i\Delta_F t} + \sigma_{ag}c_2 e^{-i\Delta_F t}\right). \tag{3.97}$$

where

$$\Delta_F \equiv \Delta_\alpha + \Delta_\beta - \Delta_p \tag{3.98}$$

Assuming that system in the three-photon resonance $\Delta_F = 0$ the Hamiltonian became time-independent. Using third-order perturbation theory to solve this hamiltonian we have zero-order energies $E_g^0 = 0$, $E_a^0 = \Delta_\alpha - \Delta_p$, $E_e^0 = -\Delta_p$, and perturbation potential

$$V = g_\alpha\left(\sigma_{ae}c_1^+ + \sigma_{ea}c_1\right) + g_\beta\left(\sigma_{ga}c_2^+ + \sigma_{ag}c_2\right) + g_p\left(\sigma_{eg}c_3 + \sigma_{ge}c_3^+\right). \tag{3.99}$$

Then we have perturbation terms $E_n^1 = \left\langle \Psi_n^0 \right| V \left| \Psi_n^0 \right\rangle = 0$, $E_g^2 = \frac{g_\beta^2 c_2 c_2^+}{\Delta_\beta} + \frac{g_p^2 c_3 c_3^+}{\Delta_p}$, $E_a^2 = \frac{g_\beta^2 c_2^+ c_2}{\Delta_\alpha - \Delta_p} + \frac{g_\alpha^2 c_1 c_1^+}{\Delta_a}$, $E_e^2 = \frac{g_\alpha^2 c_1^+ c_1}{-\Delta_a} + \frac{g_p^2 c_3^+ c_3}{-\Delta_p}$, $E_g^3 = \frac{1}{\Delta_p\Delta_\beta}\left[g_\beta g_\alpha g_p c_3 c_1^+ c_2^+ + g_p g_\alpha g_\beta c_3^+ c_1 c_2\right]$. In order to avoid transition from the ground state the following conditions have to be fulfilled.

$$\frac{g_\beta\sqrt{n_\beta}}{\left|\Delta_\beta\right|} << 1, \frac{g_p\sqrt{n_p}}{\left|\Delta_p\right|} << 1, \frac{g_\alpha g_p\sqrt{n_\alpha n_p}}{\left|\Delta_p\Delta_\beta\right|} << 1, \frac{g_\beta g_\alpha\sqrt{n_\beta n_\alpha}}{\left|\Delta_p\Delta_\beta\right|} << 1. \tag{3.100}$$

Effective Hamiltonian becomes:

$$\frac{H_{eff}}{\hbar} = \frac{g_\beta^2 c_2 c_2^+}{\Delta_\beta} + \frac{g_p^2 c_3 c_3^+}{\Delta_p} + \frac{g_p g_\alpha g_\beta}{\Delta_p\Delta_\beta}\left[c_3 c_1^+ c_2^+ + c_3^+ c_1 c_2\right] \tag{3.101}$$

3.3.4 Electricmagnetical Induced Transparence(EIT)

By adjusting current bias on phase qubit to $\sin\phi = 0.963$, $\zeta = 0.14$, $\left(E_a - E_g\right) \simeq 5.2GHz$, $(E_b - E_a) \simeq 3.2GHz$. Capacitively drive the phase qubit at resonance between E_a and E_b. The capacitive transition matrix $(a^\dagger + a) = \begin{bmatrix} 0 & 1 & -0.14 \\ 1 & 0 & 1.414 \\ -0.14 & 1.414 & 0 \end{bmatrix}$, in which case transition between g and b is so small that it can be treated as dipole forbiden. $(a^\dagger + a) \approx \begin{bmatrix} 0 & 1 & 0 \\ 1 & 0 & 1.414 \\ 0 & 1.414 & 0 \end{bmatrix}$. Capacitively couple a transmission line resonator, detuned from $\left(E_a - E_g\right)$ with Δ, to phase qubit. Δ can vary within domain $[-1.5GHz, 1.5GHz]$. The diagram shows as:

And numerical simulation of EIT is shown as:

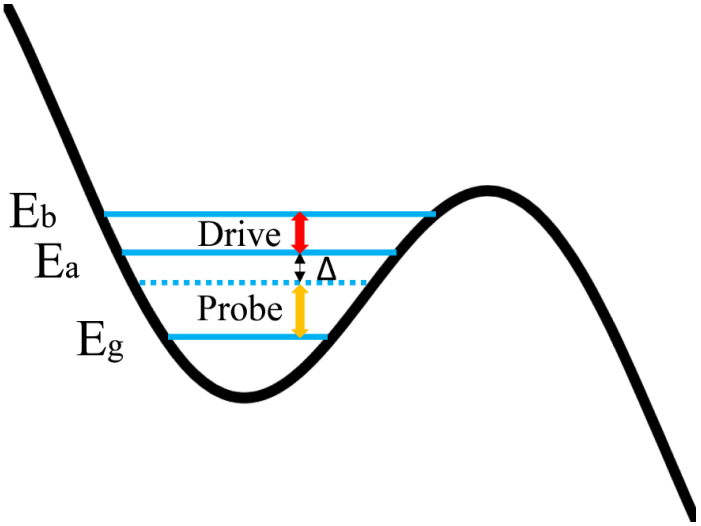

Figure 3.10: Energy diagram of EIT.

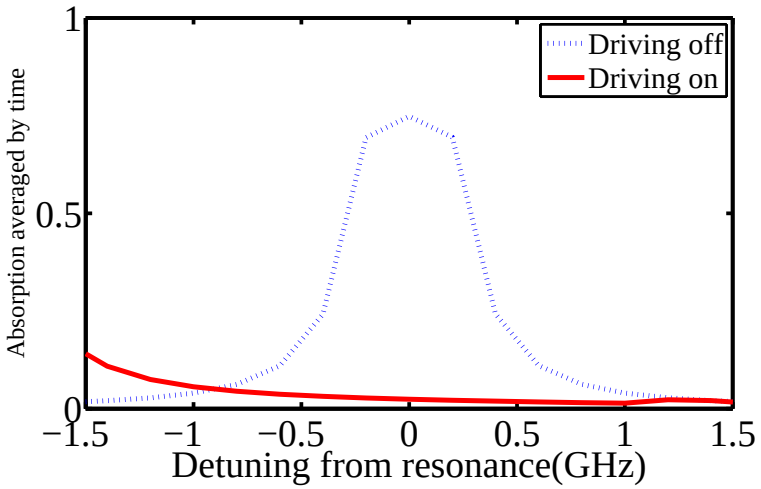

Chapter 4

Quantum simulation using superconducting quantum circuits

4.1 Introduction of quantum simulation

> ”Nature isn’t classical, dammit, and if you want to make a simulation of nature, you’d better make it quantum mechanical... Let the computer itself be built of quantum mechanical elements which obey quantum mechanical laws.—-Feynman”

The simulation of quantum systems in general remains a extremely difficult, if not impossible, task for classical computers, even for latest and most powerful supercomputers. [6] Quantum state of a large physical system is described by a number of parameters that proliferates exponentially with the system size, which is generally defined as the number of particles or degrees of freedom in the system. Furthermore, simulating the temporal evolution of the system requires a number of operations that also increases exponentially with the size of the system. This exponential explosion is unavoidable, unless approximation methods (e.g.,Monte Carlo methods) are used. However, depending on the specifics of the problemunder study, good approximations are not always available or they also face some limitations. Quantum simulation fights fire with fire, in a manner of speaking, employing a controlled quantum-mechanical device to mimic and investigate other quantum systems. The advantage of quantum simulators over classical devices is that, being quantum systems themselves, they are capable of storing large amounts of information in a relatively small amount of physical space. For example, the storage capacity of N qubits is exponentially larger than that of N classical bits. The quantum state of $N = 40$ spin-$1/2$ particles, which would require a 4TB classical memory register, [6] can be represented by a 40-qubit (i.e., 5-quantum-byte) register.

Quantum simulation is not tied to any particular physical implementation. [4–6] The idea of a quantum simulator can be illustrate as Fig.(4.1).

The alternative simulation method initially proposed by Feynman, i.e., quantum simulation, can be loosely defined as simulating a quantum system by quantum mechanical means. This very general definition allows us to include three types of simulation: [6] 1) Digital quantum simulation; 2) Analog quantum simulation; 3) Quantum-information-inspired algorithms

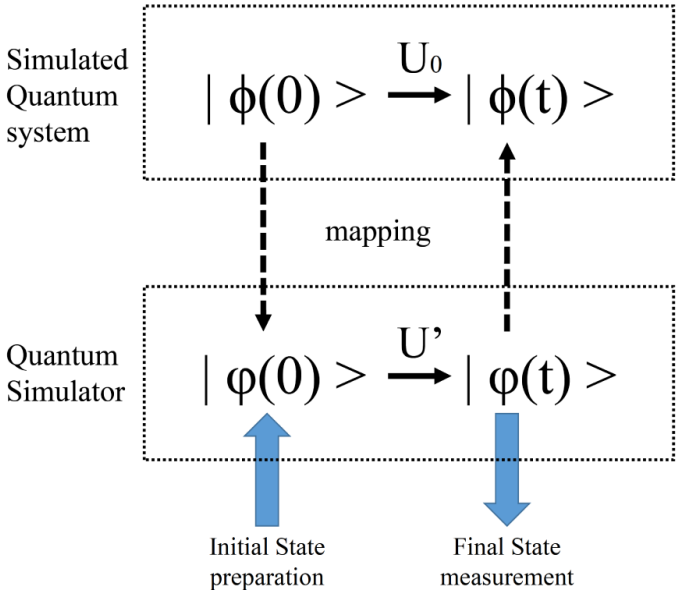

Figure 4.1: A quantum system with state ϕ and evolution U_0 is mapped to a quantum simulator with state φ and simulative evolution U'. Initial state preparation, simulating evolution operator, and final state measurement are the fundamental three steps of doing quantum simulation. [6]

for the classical simulation of quantum systems.

The realizations of systems exhibiting these characteristics range from ultracold atoms in traps and optical lattices, measurement-based linear optics, and trapped ions, to Josephson-junction arrays, electrons in quantum-dot arrays and on the surface of liquid helium, etc, and recently experimentally-realized digital superdoncuting computer. [127] In this Chapter, I am going to present my results of using superconducting quantum circuit to simulate Bosonic and Fermionic many body physics. Sec.4.2 presents a paper simulating Bose-Hubbard Model (BHM) with site-wise manipulation induced phase transition, which is published on Phys.Rev.B.. Sec.4.3 presents my recent result to demonstrate the cooling scheme proposed in Sec.4.2. Sec.?? presents my continuous work on the simulation of Hubbard model that is going to be submitted very soon.

4.2 Sitewise manipulations and Mott insulator-superfluid transition of interacting photons using superconducting circuit simulators

4.2.1 Introduction

Intensive research has been focused on simulating complex matter using well-controlled quantum systems in order to better understand their behavior and create useful analogues [6, 128–132]. Successful examples include cold atoms trapped in optical potentials [128], trapped

ions [129, 130], spins in defects in diamonds [131], photonic arrays [132], etc. Recently, another class of quantum simulators based on superconducting circuits opens more opportunities [133–137], which is made possible due to progresses in fabricating well-designed circuits on chips. In those superconducting circuits, dissipation and decoherence have been suppressed significantly [133, 138]. Moreover, interacting superconducting qubits and resonators can be fabricated on a chip, where quantum error-correction encoding and high fidelity operations have been realized [139, 140]. Various designs of couplers for connecting different qubits or resonators with wide tuning ranges have also been demonstrated [141–143]. Those progresses in superconducting circuits provide a promising perspective of scalable superconducting circuits as quantum simulators for many-body systems, which may be bosonic [134, 144–146] or fermionic [147, 148] in nature.

The Bose-Hubbard Model (BHM) has been a paradigm in many-body theories, and the Mott insulator-superfluid (MI-SF) phase transition associated with the BHM has been of broad interest [128, 149]. This transition was observed unambiguously in cold atoms trapped in optical lattices and can be probed with single-atom resolutions [150, 151]. On the other hand, a theoretical framework for obtaining the BHM using the Jaynes-Cummings Hubbard Model has been established [152, 153]. Simulating this general model in cavity arrays has been proposed [123, 152, 154, 155]. One may envision that introducing inhomogeneity into the BHM parameters can lead to richer physics, some of which has been explored in Refs. [156, 157]. Simulating those phenomena requires tunability of single-site parameters, which could be hard in current available simulators [6, 128–131].

As a candidate of quantum simulators, superconducting circuit has the following additional features [6, 65, 134]: (I) The circuit can be manipulated by applying voltages, currents and/or magnetic flux. Hence useful classical circuit techniques can be introduced in similar ways. (II) Circuit manipulations can be implemented locally to a single site/unit or globally to the whole system. (III) The circuit can be tailored to certain characteristic frequency, interaction strength, etc., and the circuit geometry can be fabricated in desired patterns. Furthermore, according to recent reports the decoherence time of superconducting qubits based on different superconducting circuits is approaching 0.1 ms [114–117]. The Q factor of an on-chip transmission line resonator [62] can even go beyond 10^5. A 3D superconducting resonator [116, 138] can have a quality factor up to 10^9, which implies that the life time of photons in superconducting resonators may approach 10 ms. This is good enough to allow one to practically consider the photon number as a conserved quantity in the circuit if compared to the operation frequency in the circuit typically in the range of 100 MHz−10 GHz [19, 65, 133, 158].

Having those features of superconducting circuit in mind, we propose a scheme to simulate the BHM with controllable inhomogeneous parameters. To demonstrate some interesting features, we consider how the phase transition between the delocalized SF and localized Mott insulator can be induced by manipulating the parameters of one single site. In conventional setups, global parameters such as the overall density or interaction drive the system across this transition, and here we propose that in superconducting-circuit simulators, one may observe this transition with a single-site manipulation by exploiting the sensitivity to the commensurate filling close to the transition. The details of our proposed scheme are verified by the exact diagonalization method [159], which already shows signatures of this transition in moderate-size

systems. Thus this proposed scheme should be feasible in experiments.

Here the simulator is based on an array of superconducting transmission line resonators (TLRs). The goal is to simulate the BHM [149]

$$H = -\sum_i \mu_i n_i + \sum_i \frac{U_i}{2} n_i(n_i - 1) - \sum_i t_i (b_i^\dagger b_{i+1} + b_i b_{i+1}^\dagger). \tag{4.1}$$

Here μ_i is the on-site energy and plays the role of the chemical potential, U_i is the on-site interaction, and t_i is the nearest-neighbor hopping coefficient. In cold atoms one can control the filling and motion of a single atom [150], but manipulations of the energy and interaction on each site remain a challenge.

A superconducting TLR with a length in the range of centimeters can support a microwave resonant frequency corresponding to the oscillations of the electric potential and magnetic flux from the standing waves of the Cooper pair density. Those microwaves are referred to as the photons in the TLR [73]. The quantum electrodynamics (QED) framework can then be applied to the TLR-qubit system to get the so-called circuit QED [73]. A single site of the system is modeled by the Jaynes-Cummings (JC) model [160] while an array of circuit QED systems, as schematically shown in Figure 4.2, can be described by the Jaynes-Cummings Hubbard model [161]

$$\begin{aligned} H = &\sum_n [\hbar\omega_n^c a_n^\dagger a_n + \hbar\omega^q \sigma_n^z + g_n(a_n\sigma_n^+ + a_n^\dagger \sigma_n^-)] \\ &+ \sum_n J_n(a_n^\dagger a_{n+1} + a_n a_{n+1}^\dagger), \end{aligned} \tag{4.2}$$

where ω_n^c is the cavity frequency, ω^q is the qubit frequency, g_n is the coupling strength between the cavity and qubit, and J_n is the effective hopping coefficient between cavities.

When the qubit is close to resonance with the cavity, they are co-excited and the excitation on a single site has the form of a polariton. Simulating polaritonic many-body behavior has been studied recently based on various physical systems [144, 145, 162]. Here we consider a different regime in the parameter space to take advantage of the tunability of superconducting quantum circuits. We focus on the dispersive regime [153], where the excitation is limited in the TLR while the qubit stays in its ground state. Hence the on-site excitation becomes photonic. In this regime, a perturbation calculation shows that the system can simulate the BHM. To make connections to experiments, feasible controlling and probing methods of the quantum phase transition between localized and delocalized states will be discussed. The exact diagonalization (ED) [159] method is used to numerically demonstrate the details of the phase transition.

4.2.2 Architecture of the simulator

As illustrated in Figure 4.2, the proposed simulator is a one dimensional (1D) array of superconducting circuit elements. One site is formed by a TLR capacitively coupled to a superconducting charge qubit [19, 65, 133, 158], which is labeled as SQUID-A, and the qubit energy is tunable. The TLRs on different sites are connected via the SQUID-B, which leads to tunable

couplings between nearest neighbor sites. Here a derivation of how the Bose-Hubbard Hamiltonian (4.1) can be simulated by the superconducting circuit will be presented. Here we will use Hz×2π as the unit of energy and set $\hbar \equiv 1$.

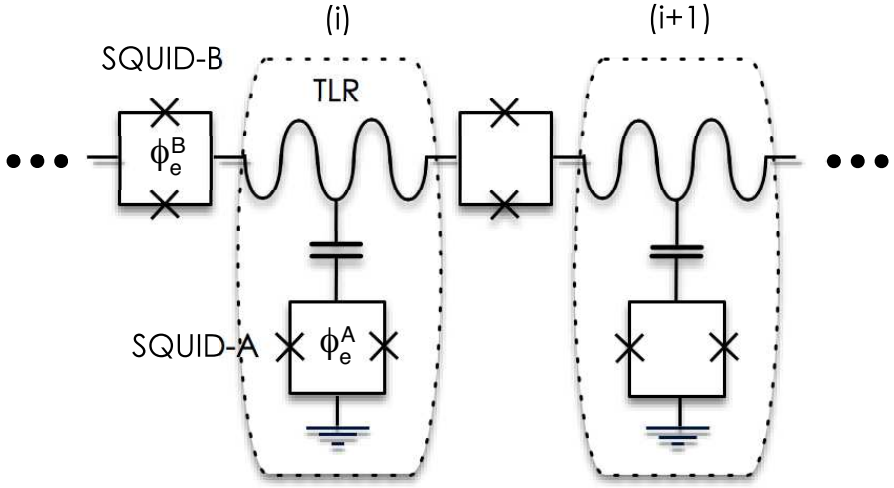

Figure 4.2: Schematic plot of the 1D TLR array. SQUID-A as a tunable charge qubit is capacitively coupled to the center of a TLR. Nearest neighbor sites are connected by SQUID-B. The external magnetic flux ϕ_e^A and ϕ_e^B through SQUID A and B can be used to tune their Josephson energies.

4.2.2.1 TLR as a lattice element

The qubit-TLR system is an analogue of an atom-cavity system. In the strong coupling regime the dynamics of the latter system can be modeled by the Jaynes-Cummings Hamiltonian [73]. Our superconducting circuit Hamiltonian can be derived following the work of circuit-QED in Refs. [73, 81, 163]. The Hamiltonian of a single lattice site is

$$H^{site} = H^{TLR} + H^{qubit}. \tag{4.3}$$

The TLR with length D could be treated as a cavity with a single mode of the first harmonic. The excitation in the TLR is modeled as

$$H^{TLR} = \omega^c a^\dagger a. \tag{4.4}$$

The cavity frequency is $\omega^c = \frac{2\pi}{\sqrt{C^c L^c}} = 2\pi\sqrt{E_c^c E_L^c}$, where the net capacitance and inductance of the TLR are C^c and L^c, and the charge and inductive energies of the cavity are $E_c^c = \frac{(2e)^2}{C^c}$ and $E_L^c = \frac{1}{L^c(2e)^2}$. For the first harmonic, the spatial distribution [73] of N peaks at $x = -\frac{D}{2}, 0, \frac{D}{2}$. The node charge number and node flux at the maxima correspond to $N = \sqrt{\omega^c/E_c^c}(a^\dagger + a)$ and $\phi^c = -i\sqrt{\omega^c/E_L^c}(a^\dagger - a)$.

Since the qubit consists of two Josephson junctions in a superconducting loop, its Hamiltonian is

$$H^{qubit} = E_c^A(n - n_g)^2 + 2E_J^A \cos(\frac{\phi_e^A}{2})(1 - \cos\phi). \tag{4.5}$$

Here $n = C_\Sigma^A V_J/2e$ and $n_g = C_g^A V_g/2e$ are the numbers of Cooper pairs on the island and the gate, respectively. The capacitance between the qubit and TLR is C_g^A. $E_c^A = \frac{(2e)^2}{2C_\Sigma^A}$ with C_Σ^A being the total effective capacitance in the qubit. The Josephson tunneling energy is E_J^A and the phase ϕ displaces the number of Cooper pairs. Because of the giant Kerr effect due to the Josephson junction, the energy difference between the lowest two levels $|0\rangle$ and $|1\rangle$ is separated from the other energies. Therefore SQUID-A in Fig. 4.2 behaves like a superconducting qubit [65] with the Hamiltonian $H^{qubit} = E_c^A \frac{1-2n_g}{2}\widetilde{\sigma}^z + 2E_J^A \cos(\frac{\phi_e^A}{2})\widetilde{\sigma}^x$, where $\widetilde{\sigma}^x = |0\rangle\langle 1| + |1\rangle\langle 0|$ and $\widetilde{\sigma}^z = -|0\rangle\langle 0| + |1\rangle\langle 1|$. Furthermore, $n_g = n^{dc} + C_g^A\sqrt{\omega^c/E_c^c}(a^\dagger + a)$ by investigating the gate voltage V_g at the point of the TLR where the qubit couples to, which includes the DC gate voltage on the qubit and a quantum mode of the TLR: $V_g = V^{dc} + \widehat{V^{ac}}$. As Figure 4.2 shows, the qubit is coupled to the center of the TLR so $\widehat{V^{ac}} = \sqrt{2}eN/C^c = \sqrt{\omega^c/2C^c}(a^\dagger + a)$ for the fundamental mode.

Here we focus on the case when the DC gate voltage bias is at the degeneracy point, $n^{dc} = \frac{1}{2}$. Then by introducing $|\uparrow\rangle = (|0\rangle + |1\rangle)/\sqrt{2}$ and $|\downarrow\rangle = (|0\rangle - |1\rangle)/\sqrt{2}$ with $\sigma^x = |\uparrow\rangle\langle\downarrow| + |\downarrow\rangle\langle\uparrow|$ and $\sigma^z = -|\downarrow\rangle\langle\downarrow| + |\uparrow\rangle\langle\uparrow|$ and dropping constant terms, the one-site Hamiltonian becomes

$$H^{site} = \omega^c a^\dagger a - \frac{\omega^q \sigma^z}{2} + g^q \sigma^x (a^\dagger + a), \tag{4.6}$$

where $\omega^q = 4E_J^A \cos(\frac{\phi_e^A}{2})$ and $g^q = 2e\frac{C_g^A}{C_\Sigma^A}\sqrt{\omega^c C^c}$. We define $H_0 = \omega^c(a^\dagger a - \sigma^z/2)$ and $V = \Delta\sigma_z/2 + g^q\sigma^x(a^\dagger + a)$ with $\Delta = \omega^c - \omega^q$ being the detuning between the cavity and qubit frequencies. Thus $H^{site} = H_0 + V$ and V is treated as a perturbation.

The qubit frequency and cavity frequency are in the same range of about 10GHz, so it is natural to apply the rotating wave approximation (RWA). Then $\Delta \ll \omega^c + \omega^q$. Moving into the interaction picture and rotating frame one gets the Jaynes-Cummings interaction $g^q(\sigma_+ e^{i\omega^q t} + \sigma_- e^{-i\omega^q t})(a^\dagger e^{i\omega^c t} + a e^{-i\omega^c t}) \overset{RWA}{\approx} g^q(\sigma_- a^\dagger e^{i\Delta t} + \sigma_+ a e^{-i\Delta t})$, where $\sigma_\pm$ are the ladder operators. Moving back to the non-rotating frame we get an effective interaction $g^q(\sigma^- a^\dagger + \sigma^+ a)$. Here we consider the dispersive regime [153, 164] so $\Delta \gg g^q$ and there is virtually no excitation from $|\uparrow\rangle$ to $|\downarrow\rangle$. Applying standard perturbation theory with $E_\uparrow^{(0)} = 0$, $E_\downarrow^{(0)} = \Delta$, $V_{\uparrow\uparrow} = V_{\downarrow\downarrow} = 0$, $V_{\uparrow\downarrow} = g^q a^\dagger = V_{\uparrow\downarrow}^\dagger$ and going up to the fourth order, the quartic Kerr term gives rise to an effective on-site interaction.

Going back to the Schrodinger picture, the single-site Hamiltonian becomes

$$H^{site} = \omega^{c,eff} a^\dagger a + \frac{\omega^q}{2}\sigma^z + (\frac{g^q}{\Delta})^3 g^q a^\dagger a(a^\dagger a - 1). \tag{4.7}$$

The charge qubit could be either a single Cooper-pair transistor or a transmon [19, 59, 65, 158] whose qubit frequency can be tuned by changing the magnetic flux bias through a SQUID

loop in the qubit circuit. $\omega^{c,eff} = \omega^c - \frac{g^{q2}}{\Delta} + (\frac{g^q}{\Delta})^3 g^q$ is the effective onsite frequency and the quartic term is the effective on-site interaction of the photons. Those two terms are functions of the controllable parameter Δ. Assuming $g^q = 120\text{MHz}\times 2\pi$ [19, 158], $\Delta \geq 0.9\text{GHz}\times 2\pi$ so $\left(\omega^c - \omega^{c,eff}\right) \in [-0.1, 0.1]\text{GHz}\times 2\pi$. We remark that the case $\Delta \sim g^q$, where the excitations are polaritons rather than photons, has been discussed in the literature [145].

4.2.2.2 Tunable TLR array

Different architectures for implementing a tunable coupler between two superconducting TLRs have been realized and discussed in Refs. [100, 100, 109, 113, 142, 143, 165]. Here we present a basic design. As shown in Figure 4.2, SQUID B with different size and energy from those of SQUID A is coupled adjacent TLRs. The coupling Hamiltonian is

$$H^B = \sum_{i=upp,low} [\frac{C_J^B}{2}\left(\dot{\phi}_i^{jj}\right)^2 + E_J^B(1 - \cos\phi_i^{jj})], \tag{4.8}$$

where $\phi_{i=upp,low}^{jj}$ are the phase differences across the upper and lower Josephson junctions of SQUID B (see Fig. 4.2). The two Josephson junctions in SQUID B are assumed to be uniform with the same capacitance C_J^B and Josephson energy E_J^B. The external magnetic flux bias through SQUID B is $\phi_e^B = \phi_{upp}^{jj} + \phi_{low}^{jj}$ and $\dot{\phi}_{upp}^{jj} + \dot{\phi}_{low}^{jj} = \dot{\phi}_e^B = 0$. Here we introduce $\phi_{1,2}^c$ on the two ends connecting to TLR 1 and 2 as the node phases and $N_{1,2}$ as the numbers of Cooper pairs on the node. According to the geometry of the SQUIDs, $\phi_1^c - \phi_2^c = \frac{1}{2}(\phi_{upp}^{jj} - \phi_{low}^{jj})$. Josephson equations then give $\frac{C_J^B}{2}\left(\dot{\phi}_{1,2}^c\right)^2 = \frac{1}{2}\frac{(2e)^2}{C_J^B}N_{1,2}^2 = E_c^B N_{1,2}^2$. Therefore, the charge-energy term of H^B becomes $2E_c^B N_1^2 - 4E_c^B N_1 N_2 + 2E_c^B N_2^2$. Meanwhile, the Josephson energy is approximated by $E_J^B \cos(\frac{\phi_e^B}{2})[(\phi_1^c)^2 - 2\phi_1^c\phi_2^c + (\phi_2^c)^2]$, where higher-order terms are negligible because the phase difference across SQUID B $\left(\phi_{upp}^{jj} - \phi_{low}^{jj}\right)$ can initially be set to zero by shorting both sides. It will be shown that $2E_J^B\cos(\frac{\phi_e^B}{2})$ can be tuned to the same order of magnitude as the on-site interaction term $(\frac{g^q}{\Delta})^3 g^q$ in Eq. (4.7), which is needed to place the system near the MI-SF phase transition.

The Hamiltonian for SQUID B, after those manipulations, becomes

$$\begin{aligned} H^B = &\sum_{i=1,2}[2E_c^B N_i^2 + E_J^B\cos(\frac{\phi_e^B}{2})(\phi_i^c)^2] \\ &- [4E_c^B N_1 N_2 + 2E_J^B\cos(\frac{\phi_e^B}{2})\phi_1^c\phi_2^c], \end{aligned} \tag{4.9}$$

Here the simple harmonic terms inside the summation give an additional frequency shift to the TLR Hamiltonian in Eq. (4.4), which becomes $H_{net,i}^{TLR} = \frac{1}{2}E_c^{c*}N_i^2 + \frac{1}{2}E_L^{c*}(\phi_i^c)^2$ with $E_c^{c*} = E_c^c + 4E_c^B$ and $E_L^{c*} = E_L^c + 2E_J^B\cos(\frac{\phi_e^B}{2})$. This corresponds to a dressed cavity frequency

$$\omega^{c*} = 2\pi\sqrt{E_c^{c*}E_L^{c*}} \tag{4.10}$$

as the TLRs are connected into an array with those SQUID Bs. The cross term in H^B leads to a coupling Hamiltonian $H^{coup} = -g^{cap}(a_1^\dagger + a_1)(a_2^\dagger + a_2) + g^{ind}(a_1^\dagger - a_1)(a_2^\dagger - a_2)$ with $g^{cap} = \omega^c E_c^B / E_c^{c*}$ and $g^{ind} = \omega^c 4E_J^B \cos(\frac{\phi_e^B}{2})/E_L^{c*}$. A similar coupling Hamiltonian can be found in Ref. [165], which is supported by experiments [141]. By considering two identical resonators $\omega_1^{c*} = \omega_2^{c*}$ and applying RWA and conservation of the photon number, one obtains

$$H_{12}^{coup} \simeq -(g^{cap} + g^{ind})(a_1^\dagger a_2 + a_1 a_2^\dagger). \tag{4.11}$$

We define $g = g^{cap} + g^{ind}$, which gives rise to the effective hopping J_n in Eq. (4.2).

For the simulator discussed here, typical values [19, 133] of $E_c^B = 300\text{MHz}\times 2\pi$, $E_J^B = 500\text{MHz}\times 2\pi$, $E_c^{c*} = 10\text{GHz}\times 2\pi$, $E_L^{c*} = 10\text{GHz}\times 2\pi$ will be considered. Note that ϕ_e^B can be tuned within $[0, 2\pi]$, so $g^{ind} \in [2, -2]\text{GHz}\times 2\pi$. The net coupling strength is $g = -(g^{cap} + g^{ind}) \in [-2.3, 1.7]\text{GHz}\times 2\pi$. Since the perturbation approach is applied to the on-site Hamiltonian, in order to keep H^{coup} with the same order of magnitude as the highest order term in Eq. (4.7), the coupling strength g has to fulfill the condition $g < g^q$. By biasing the system in the range ϕ_e^B around π, one should be able to get a smaller range of $g \in [-30, 30]$ MHz$\times 2\pi$.

4.2.2.3 Superconducting-circuit simulator of the BHM

Collecting all terms we obtain a many-body Jaynes-Cummings Hubbard Hamiltonian:

$$H^{JCHM} = \sum_i H_i^{site} + \sum_{\langle ij \rangle} H_{ij}^{coup}, \tag{4.12}$$

where $\langle ij \rangle$ denote nearest-neighbor pairs. In the dispersive regime, where our perturbation approach is applicable, the qubit does not get excitations and stays in its ground state. Therefore the qubit term $\sum_i \omega_i^q \sigma_i^z$ does not contribute to the many-body energy. In this case, the Jaynes-Cummings Hubbard model can be mapped to the Bose Hubbard model [153] by treating the photons in the TLR as interacting bosons.

When compared to Eq. (4.1), the on-site energy, on-site interaction, and hopping terms are

$$\mu_i = -[\omega_i^{c*} - (\frac{g_i^q}{\Delta_i})g_i^q + (\frac{g_i^q}{\Delta_i})^3 g_i^q] \tag{4.13}$$

$$\frac{U_i}{2} = (\frac{g_i^q}{\Delta_i})^3 g_i^q \tag{4.14}$$

$$t_i = (g_i^{cap} + g_i^{ind}) = g_i. \tag{4.15}$$

As discussed previously, Δ_i and g_i can be tuned by a magnetic flux bias, so they are the independent variables in this model. One may recall that $|t| = |g| \in [0, 30]\text{MHz}\times 2\pi$ from previous discussions. In the dispersive regime $|\Delta| \in [0.35, 1.0]\text{GHz}\times 2\pi$ should give reasonable values [19, 133] of $g^q = 120\text{MHz}\times 2\pi$. Hence $U \in [0.0024, 10]$ MHz$\times 2\pi$. To meet the traditional treatment of BHM, we analyze parameters in the unit of t. Thus $g^q/t \in [4, +\infty)$, $|\Delta/t| \in [10, +\infty)$, $U/t \in (0, +\infty)$, which implies that the range of U/t in this simulator should

cover the MI-SF transition. To avoid going beyond the valid range of our approximation, the parameters are chosen in the range $|\Delta/t| \in [30, 10^3]$.

In this simulation scheme the on-site energy μ_i, interaction strength U_i, and hopping coefficient t_i can be explicitly made site-dependent, which leads to a versatile simulator of the BHM, especially if phenomena due to spatial inhomogeneity are of interest. When compared to ultracold atoms in optical lattices, this superconducting circuit simulator has some additional features. The interacting bosons in the simulator is confined inside the TLRs so there is no need for background trapping potentials, which is common in cold-atom systems. Various geometries can be studied by fabricating the elements accordingly. In addition, open boundary conditions (OBCs) with hard walls can be introduced by terminating the coupling SQUID at the ends of the superconducting TLR array. Even in the presence of stray weak capacitive couplings, a high Q factor can still be maintained [62]. On the other hand, periodic boundary conditions (PBCs) can be realized by fabricating a loop structure so bulk properties can be studied with a relatively small number of sites. The examples given in the following section will illustrate those features.

We remark that the wide range of U/t, which covers the SF-MI transition, is a consequence of the independent tunability of t and U in this simulator. Other interesting phenomena, such as the hardcore boson exhibiting nontrivial scaling behavior [166, 167] may be beyond the scope of this simulator because the t needs to remain finite as U goes to infinity. Such a regime requires $g^q/\Delta \to \infty$ so it is outside the dispersive regime investigated here.

4.2.3 Single-site manipulations of the MI-SF transition

Here we present one interesting application of this superconducting circuit simulator, where the MI-SF transition of the BHM can be induced by single-site manipulations. Other possible applications will be discussed later. To concentrate on the underlying physics, we consider a 1D array of N sites. The main idea is to exploit the commensurability of the BHM close to the MI-SF transition.

The parameters of a selected site (called site 1) is tuned by external magnetic flux through the charge qubit coupled to the TLR of this site. One may consider, for site 1, a shift of the onsite energy by δ and a shift of the onsite coupling constant by η. The choice of which site to be manipulated is not important since the conclusions remain the same for the case with PBC. According to Eq. (4.13), when the detuning energy between the qubit and TLR on site 1, Δ_1, is different from the detuning energy on the other sites $\Delta_i = \Delta_0$, $i = 2, \cdots, N$, the BHM parameters of site 1 are different form those on the other sites. Thus the BHM Hamiltonian of this 1D array with manipulations of site 1 is rewritten as

$$\begin{aligned} H = {} & [\delta n_1 + \eta n_1(n_1 - 1)] - \mu \sum_{i=1}^{N} n_i \\ & + \frac{U}{2} \sum_{i=1}^{N} n_i(n_i - 1) - t \sum_{i}^{N'} (b_i^\dagger b_{i+1} + b_{i+1}^\dagger b_i). \end{aligned} \tag{4.16}$$

The first two terms summarize the effects of a different detuning on site 1. Here

$$\begin{cases} \delta = -g_q^2(\frac{1}{\Delta_1} - \frac{1}{\Delta_0}) + g_q^4\left[(\frac{1}{\Delta_1})^3 - (\frac{1}{\Delta_0})^3\right] \\ \eta = g_q^4\left[(\frac{1}{\Delta_1})^3 - (\frac{1}{\Delta_0})^3\right] \end{cases} . \tag{4.17}$$

A diagram of δ and η as a function of Δ_1 is shown in Figure 4.3, which gives an estimation of the BHM parameters in the presence of a single-site manipulation. $N' = N - 1$ for the OBC and $N' = N$ for the PBC in the upper limit. We keep $t_i = t$ the same in the whole lattice because it does not depend on Δ_1. The unit of energy will be t. The value of U is fixed by Δ_0 and g_q.

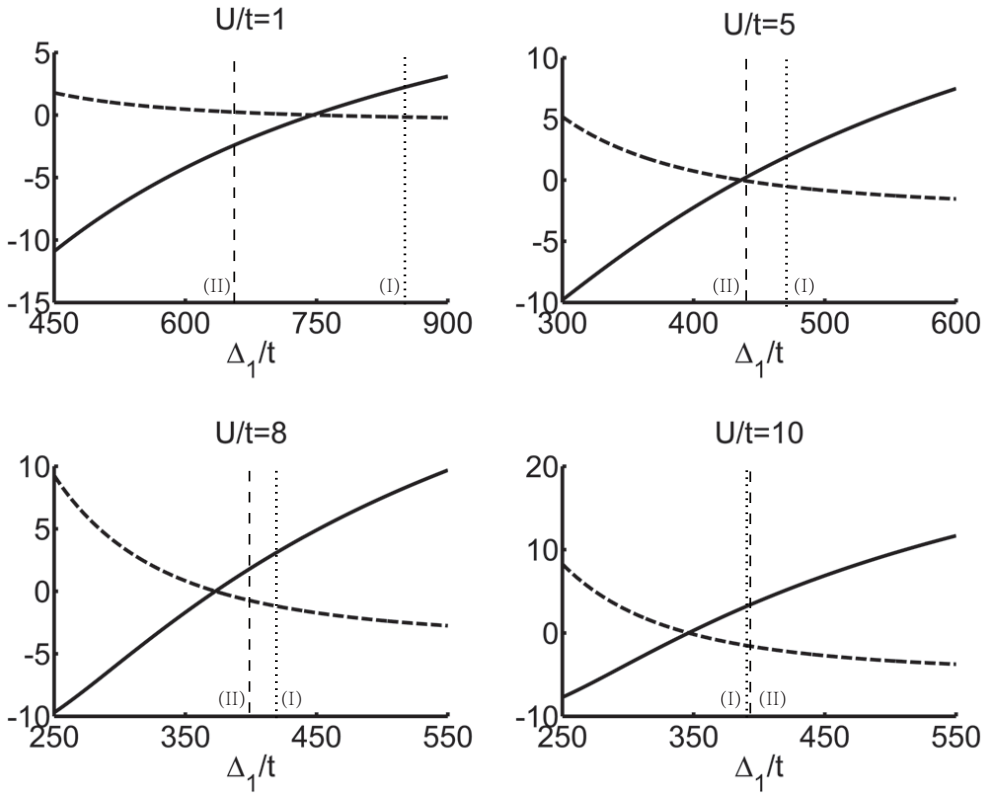

Figure 4.3: δ (solid lines) and η (dashed lines) as functions of Δ_1 for $U/t = 1, 5, 8, 10$ and $g_q = 120\text{MHz}\times 2\pi$. As Eq. (4.16) shows, δ and η are the displacements of the on-site energy and on-site interaction of the first site. The vertical lines (I) and (II) indicate the mean-field critical values of the two cases discussed in Sec. 4.2.3.

We vary Δ_1/t as an independent variable. The advantages of this protocol are: (1) The qubit energy is intact away from the manipulated site. (2) Particles are conserved in the whole system. We define the particle density ρ as the ratio between the photon number and site number. In the following we consider the phase transition due to this single-site manipulation when $\rho < 1$ and $\rho = 1$. For $\rho = (N-1)/N$ the system is a delocalized SF state in the absence of manipulations and a single-site push leads to a localized MI state, which is shown schematically

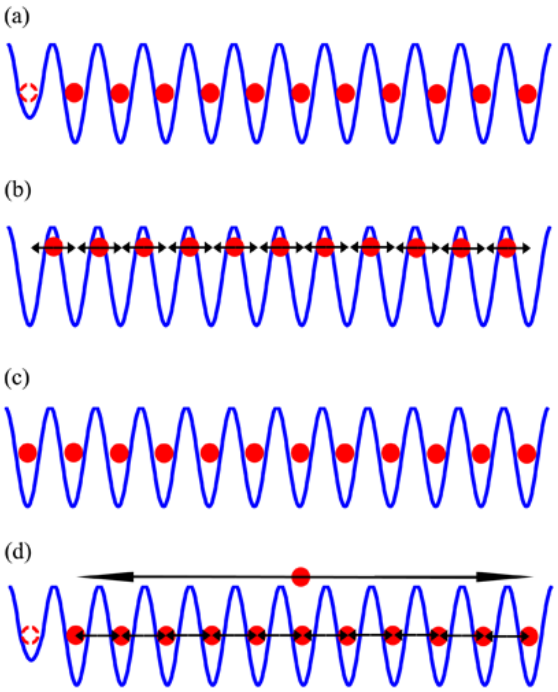

Figure 4.4: (Color online) Illustration of single-site manipulations of the Mott insulator to superfluid transition for $N-1$ bosons with strong repulsion in N sites ((a) and (b)) and for N bosons with strong repulsion in N sites ((c) and (d)). (a) The on-site energy of site-1 is increased and the system is pushed into a localized Mott insulator. The dashed circle implies that the first site is virtually empty. (b) The system becomes a delocalized superfluid as the on-site energy is lowered. (c) The system is a localized Mott insulator when the onsite energy of site 1 is small. (d) By increasing the on-site energy of site 1, photons are pushed into the bulk and form a delocalized superfluid.

in Fig. 4.4(a)(b). The second case with $\rho = 1$ is illustrated by Fig. 4.4(c)(d), where the system is in an MI state without manipulations and becomes an SF after a single-site push.

To characterize those single-site manipulated transitions and to identify where the transitions take place, we analyze a useful quantity called the fidelity metric, which has been shown to capture quantum phase transitions or sharp quantum crossovers in fermion Hubbard model [167, 168] and other model Hamiltonians [169, 170]. Given a Hamiltonian of the form $H(\lambda) = H_0 + \lambda H_1$, the fidelity is defined as the overlap between two (renormalized) ground states obtained with a small change $\delta\lambda$ in the parameter λ:

$$F(\lambda, \delta\lambda) = \langle \Phi_0(\lambda) | \Phi_0(\lambda + \delta\lambda) \rangle. \tag{4.18}$$

However, the fidelity has been shown to be an extensive quantity that scales with the system

size [170, 171]. Therefore, the fidelity metric is induced as [167, 170, 172]

$$g(\lambda, \delta\lambda) = (2/N)(1 - F(\lambda, \delta\lambda))/\delta\lambda^2, \tag{4.19}$$

whose limit as $\delta\lambda \to 0$ is well defined away from the critical points and standard perturbation theories apply. More precisely,

$$\lim_{\delta\lambda \to 0} g(\lambda, \delta\lambda) = \frac{1}{N} \sum_{\alpha \neq 0} \frac{|\langle \Phi_\alpha(\lambda) | H_1 | \Phi_0(\lambda) \rangle|^2}{[E_0(\lambda) - E_\alpha(\lambda)]^2}. \tag{4.20}$$

The fidelity metric measures how significantly the ground-state wave function changes as the parameter λ changes. A dramatic increase of the fidelity metric as a function of the varying parameter indicates a quantum phase transition or sharp quantum crossover [169].

4.2.3.1 Case 1: $\rho < 1$

When there are $(N - 1)$ photons in an array of N sites, the ground state should be delocalized due to the incommensurate filling if all the sites have the same on-site energy and interaction energy. As will be shown in Figure 4.5 and Figure 4.6, non-uniform distributions of n_i and stronger fluctuations of the on-site photon density, quantified by the variance $\sigma_i = \left\langle \left\langle n_i^2 \right\rangle - \langle n_i \rangle^2 \right\rangle$, in the small Δ_1/t regime indicates delocalization of the photons with interactions up to $U = 10t$. By increasing the on-site energy of site 1, which can be performed by increasing Δ_1, a transition to a localized MI state of the remaining $N - 1$ sites occurs. The setup is summarized in Figure 4.4(a)(b). Based on current experimental technology [134–136, 173], the size of the lattice in our exact diagonalization are chosen as $N = 4, 8, 12$. An estimation of the phase transition point can be obtained from a mean-field approximation.

For a homogeneous 1D array of N sites, the $(N - 1)$ photons are not localized if the hopping coefficient is finite. By increasing the on-site energy of the first site, it becomes unfavorable if any particle hops into it. If the repulsive interactions between the bosons exceed the critical value of the MI-SF transition ($U_c/t \approx 3.28$ in 1D [174, 175]), the ground state for the rest $N - 1$ sites becomes a Mott insulator with a wavefunction in Fock space as $|\varphi_1\rangle = |0, 1, 1, ..., 1\rangle$. From the Hamiltonian (4.16), one gets the ground state energy $E_1 = \langle \varphi_1 | H | \varphi_1 \rangle = -\mu(N - 1)$.

Then we estimate the ground state of a SF to determine where the transition occurs when Δ_1 is varied. In our mean-field approximation, a simplified trial ground state with no double (or higher) occupancy is used, which is appropriate for the case $U \gg t$. The trial ground state is $|\varphi_2\rangle = \frac{1}{\sqrt{N}}(|0, 1, 1, ..., 1\rangle + |1, 0, 1, ..., 1\rangle + |1, 1, 0, ..., 1\rangle + ... + |1, 1, 1, ..., 0\rangle)$. The ground state energy is $E_2 = \langle \varphi_2 | H | \varphi_2 \rangle \approx \delta + \eta - 2t - \mu(N - 1)$. The energy difference between the two ground states is

$$\Delta E = E_1 - E_2 \approx 2t - (\delta + \eta). \tag{4.21}$$

A phase transition occurs at the crossing point $\Delta E = 0$, or $(\delta + \eta) = 2t$. Thus the system forms a Mott insulator by emptying the first site. From Eqs. (4.17) and (4.21) we obtain an estimation of the phase transition point at $\Delta_1 \approx 390t$ for $U = 10t$. The mean-field estimations are shown on Fig. 4.3. To check this prediction and provide more accurate estimations, we

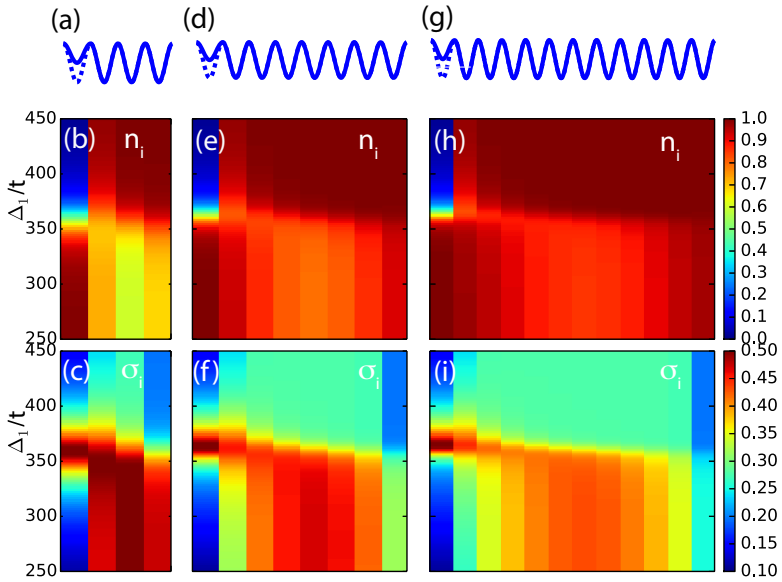

Figure 4.5: (Color online) Exact diagonalization results of the density n_i and its variance σ_i as a functions of Δ_1 for Case-1 with OBC. Site 2 to N are uniform and $U = 10t$. (a)-(c) show the results for a 4-site array with 3 photons. In (a) the dashed line and solid line on the first site correspond to the two schemes shown in Fig. 4.4. (d)-(f) correspond to the case of 8 sites with 7 photons. (g)-(i) correspond to 12 sites with 11 photons.

implement the ED method for several moderate-size systems. Figures 4.5 and 4.6 show ground state properties including n_i and σ_i on different sites as Δ_1 varies. The energy gap of the first excited state, shown in Figure 4.6(a), verifies the existence of the SF (gapless) and MI (gapped) states.

The fidelity metric shown in Figures 4.6(b) and 4.7 captures and locates the critical regime when the on-site energy of site 1 is manipulated. In Figure 4.5, above $\Delta_1/t \approx 365$, the density is uniform away from site 1. The variance σ_i is also suppressed in the bulk. Thus the system is in the MI regime. Below $\Delta_1/t \approx 365$, the photons tend to congregate at the two ends of the array, but the variance is small. At the center of the array, the photon density is smaller with a larger variance. This corresponds to a delocalized state. The density n_i thus captures the main conclusion of our mean-field analysis, and shows corrections from finite-size effects.

The critical values in the numerical results are close to the mean-field estimations. The location of the critical point does not change much as N changes, but the MI features become more prominent when N increases. Due to finite-size and boundary effects, the edge of the Mott insulator is distorted but the bulk indeed exhibits features such as an integer filling and suppressed fluctuations σ_i. Boundary effects can also be observed on the neighbors of the manipulated site as their values of n_i deviate from the bulk. Those observations are also valid in Figure 4.6(a)(b), where site 1 is connected to site 2 and site 12 due to PBC.

For small U/t, as shown in Figure 4.6 and the insets of Figure 4.7, the SF state dominates

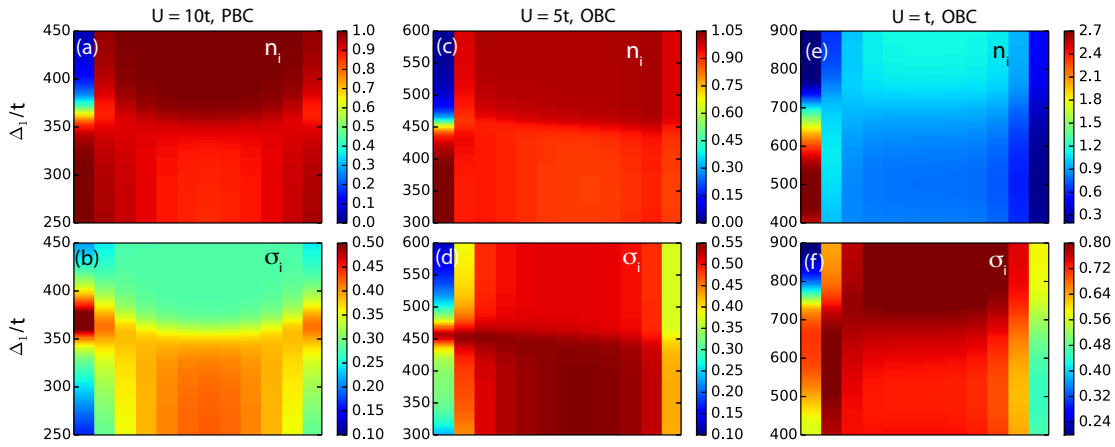

Figure 4.6: (Color online) Photon density profiles and its variance for selected values of U and boundary conditions. (a) and (b): $U/t = 10$ and PBC. In this case, the photons in site 2 and N can both tunnel to site 1. Hence the photon density on site 2 and N are different from the bulk value due to boundary effects. (c) and (d): $U/t = 5$ and OBC. (e) and (f): $U/t = 1$ and OBC. The non-uniform density and its significant variance of the last case indicate that there is no Mott insulator in this setting. Here $N = 12$ with 11 photons.

the whole parameter space explored in our ED calculations, which confirms that no artifact is induced if the system is in the SF regime. In the insets of Figure 4.7, the results of a broader range of Δ_1 for the case of $U = t$ is shown and the small smooth gap through out the range of Δ_1 is consistent with a SF state of the case $U = t$ in Figure 4.6(e)(f).

Figure 4.7 shows another signature of the phase transition as $\Delta_1/t \approx 365$ for $U = 10t$ when $N = 4, 8$, and 10, as indicated by a minimum in the energy gap followed by a rapid rise. For different values of U/t, Δ_i in the bulk are different according to Eq. (4.14). Hence the critical point shifts in the Δ_1/t axis according to Eqs. (4.17) and (4.21) and this is consistent with the results shown in Figure 4.7.

4.2.3.2 Case 2: $\rho = 1$

As illustrated in Figure 4.4(c)(d), here we consider N photons placed in an N-site array. If U/t is large, the system is in a Mott insulator state. As the on-site energy of site 1 increases, the boson in that site is expected to be pushed to the bulk and this should lead to a delocalized state because of the extra boson. Following a similar procedure, we estimate the critical value of Δ_1 that controls δ and η for this case.

The localized MI ground state can be written as $|\varphi_1\rangle = |1, 1, 1, ..., 1\rangle$, with the ground state energy $E_1 = \langle\varphi_1| H |\varphi_1\rangle = \delta - N\mu$. We consider a trial delocalized trial ground state $|\varphi_2\rangle = \frac{1}{\sqrt{N-1}}(|0, 2, 1, ..., 1\rangle + |0, 1, 2, ..., 1\rangle + ... + |0, 1, 1, ..., 2\rangle)$, whose ground state energy is

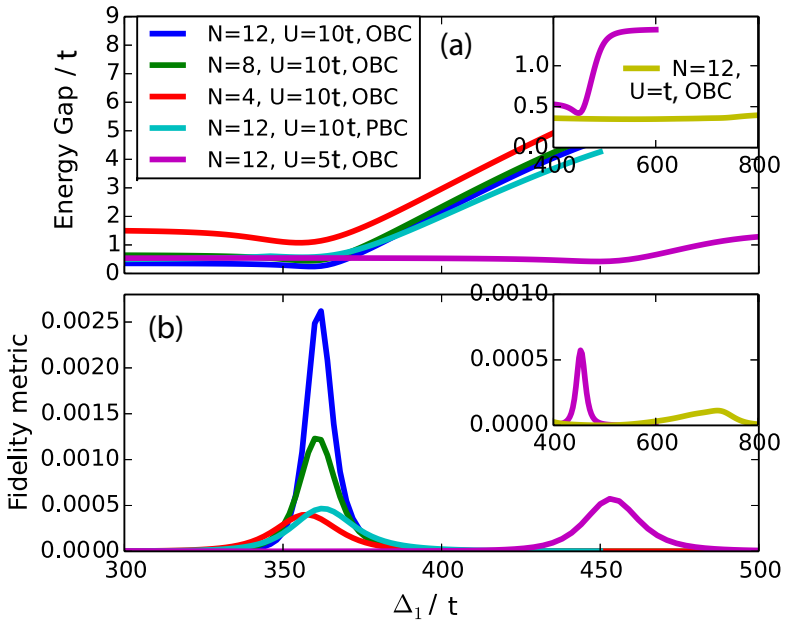

Figure 4.7: (Color online) (a) Energy gap for different values of U and N. The inset shows a regime when $U = t$, in yellow, for $N = 12$ with OBC compared to $U = 5t$ from the main figure. (b) The peaks of the fidelity metric indicate the critical points. When N varies, the location of the critical point remains intact. However, varying the on-site interaction U changes the location of the critical point, which is consistent with the analysis in Sec. 4.2.3. Note that PBC gives the same critical point as OBC.

$E_2 = \langle\varphi_2| H |\varphi_2\rangle \approx -N\mu + \frac{U}{2} - 2t$. Thus the energy difference is

$$\Delta E = E_1 - E_2 \approx \delta - \frac{U}{2} + 2t. \tag{4.22}$$

The MI-SF phase transition occurs when $\Delta E = 0$, and one may notice that the critical point depends explicitly on U, which is in contrast to the U-independent critical point in the mean-field analysis of case 1. For case 2 we obtain that the critical points are $\delta = 3t, \Delta_1 \approx 390t$ for $U/t = 10$ and $\delta = 0.5t, \Delta_1 \approx 445t$ for $U/t = 5$. The mean-field predictions are also shown in Fig. 4.3.

Numerical results from the ED method for this case are shown in Figure 4.9. As shown in panels (a) and (b), below the critical point $\Delta_1 \sim 470t$, the system is an MI with one photon per site and above $\Delta_1 \sim 470t$ the system becomes an SF with significant σ_i in the bulk. The fidelity metric shown in panel (d) verifies that the critical point is close to the estimation from our mean-field analysis. These results verify the feasibility of inducing and observing those transitions in moderate-sized systems.

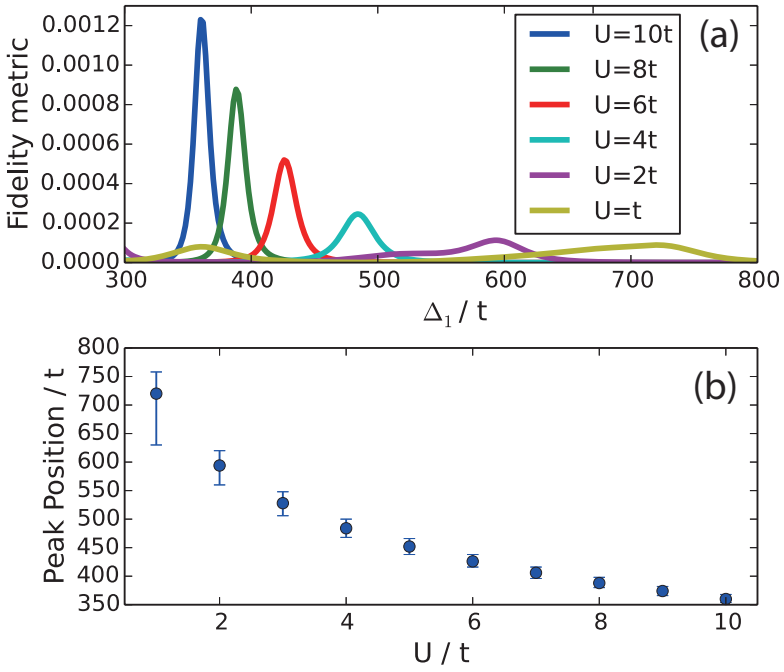

Figure 4.8: (Color online) (a) Fidelity metric as a function of Δ_1 for different values of U for $N = 8$ and 7 photons. (b) Peak position of Fidelity metric as a function of U/t. The full width at half maximum (FWHM) is shown as the bar spanning across each point.

4.2.4 Implications for experimental realization

State Preparation: In the MI regime, the particle density on each site is an integer. One may prepare an arbitrary n-photon state in each site, including $n = 0, 1$ that are of interest, by adiabatically swapping the qubit state to the TLR [89, 176]. This single site preparation can be performed simultaneously on all the sites. Then starting from the MI regime, one can transform it to the many-body ground state for different cases. For example, in case 1 in Sec.III, the ground state in the MI regime is $|0, 1, 1, 1, ...\rangle$. Recent work also proposes a scheme of a N photon state preparation in a superconducting TLR array supported by numerical results [162].

Cooling: Solid state simulators based on superconducting circuits including the one we propose here contain many degrees of freedom, which not only provide great tunability but also introduce relatively strong couplings to external fields. To experimentally implement the simulator proposed here, cooling such a complex system can be a great challenge. We suggest the following three stages. In stage 1, the whole system is kept in the superconducting phase and thermal excitations in the superconducting circuits and Josephson junctions should be suppressed [19, 65, 88, 133, 158]. They are also associated with suppression of dissipation and decoherence. As mentioned in the introduction, the life time of the photons at this stage is already much longer than the operation time of the superconducting circuit by a factor about 10^7.

In stage 2, cooling of the TLR-qubit single site system should be performed before con-

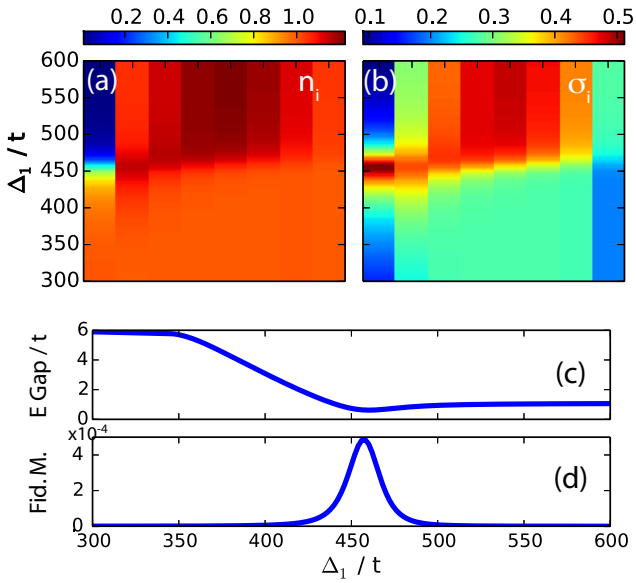

Figure 4.9: (Color online) Exact diagonalization results for Case 2 with $N = 8$ and 8 photons. Here $U = 10t$. (a) and (b) show the density profile in the array and the density variance. The energy gap (E Gap) and fidelity metric (Fid. M.) in (c) and (d) clearly exhibit signatures of the MI-SF transition.

necting the whole array. This is associated with the state preparation of the TLR array and a different degree of freedom from that of stage 1 needs to be dealt with. The quantum computation community has been making significant progresses related to the cooling at this stage [88]. Inspired by ideas from optical systems, Sisyphus cooling and side-band cooling of superconducting systems have successfully cooled a qubit to its ground state [177–179].

In stage 3, once a multi-site array is connected by turning on the hopping between adjacent sites, the desired many-body Hamiltonian follows. In order to simulate and observe the quantum phase transition discussed here, one needs to constantly cool the system and keep the number of photons conserved during the operation. This is more challenging than cooling just a single site, especially inhomogeneity of the on-site energies is present. Applying a bias or other manipulations can cause excitations as well and need to be performed quasi-adiabatically. Moreover, to take out the heat from the multi-site system when operating near the critical regime leads to yet another issue. Advanced schemes for cooling a single site have been available while cooling a multi-site array like the one studied here has not been reported so far. Development of such technologies is important for realizing the proposed simulator. Based on current ground-state preparations and state-manipulation technologies developed in coupled superconducting cavity systems [90, 180], it is promising that photon-number-conserving cooling processes may be realized by scaling up the cooling methods for those coupled systems.

Detection of the phase transition: Since the single-site manipulations of the MI-SF transition exhibit strong signatures in the density distribution, we briefly discuss a direct measurement of the photon numbers and number fluctuations on each site. Interestingly, the mea-

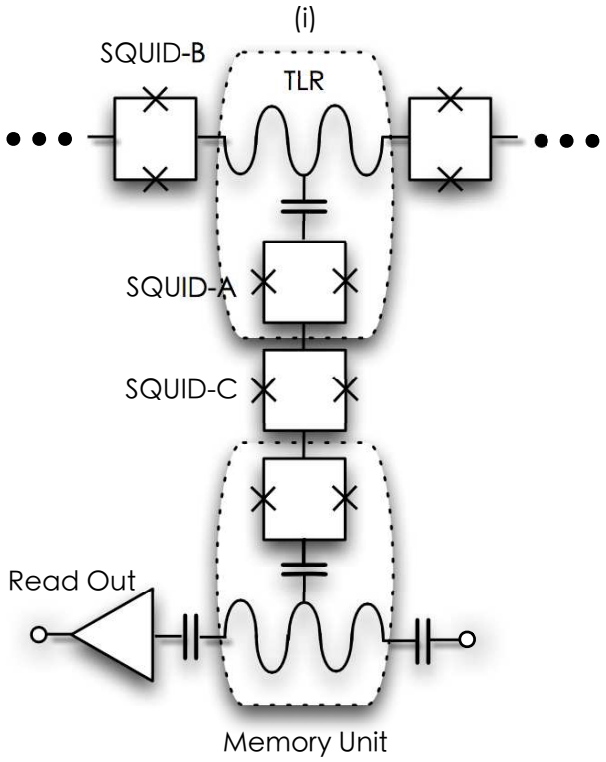

Figure 4.10: Measuring the photons in the simulator: Each site of the simulator is connected to a memory unit formed by another qubit-TLR system via a tunable SQUID (labeled as SQUID C) acting as a switch. Measurements of the photon number in the memory unit can be applied [181–183]. This memory unit can also serve as a circuit for preparing the initial state by manipulating SQUID-C and SQUID-B.

surement can be turned on and off when needed to minimize the coupling of simulator to those external circuits. As shown in Figure 4.10, each site can be coupled to a memory TLR via the additional circuit. The central SQUID-C is used to switch the coupling between the on-site unit and the measurement unit [184] for controlling the memorizing window. This is possible by changing the bias flux through SQUID-C (labeled on Figure 4.10), ϕ_m. A fast photon state SWAP between the two TLRs can be applied by a four-wave mixing scheme proposed in Ref. [164] to get $|n_{on-site}0_{measure}\rangle \rightarrow |0_{on-site}n_{measure}\rangle$, so that the photons in the TLR of the simulator are transferred and stored into the measurement TLR. Fast measurements of single-photon states can be applied to measure photon numbers in the memory TLR with technologies developed in circuit QED recently [83, 84, 106, 181–183]. By repeating the measurement one gets the average photon number $\langle n_i \rangle$ and variation $\langle \sigma_i \rangle$ as depicted in Figure 4.5 for detecting different quantum phases in the TLR array.

The conservation of photon numbers is important in realizing the single-site induced MI-SF transitions. The circuit may lose or gain photons due to couplings to external circuits or the AC control signals in the circuit. Recent progresses in superconducting quantum circuits has extended the lifetime of photons in each site with a TLR coupled to a qubit to milliseconds [62, 116, 138], which is long enough compared to the manipulations and measurements that are on the order of nano-seconds [19, 65, 133, 158]. Furthermore, the couplers, SQUID-B, can have very different energy scale from that of the photons in the simulator to avoid trapping photons. Therefore, the photon numbers in the TLRs can be treated as constants. The manipulations, in particular those due to the couplers between sites, can be introduced in an adiabatic fashion and minimize photon loss. Even in driven systems single photon can be transferred faithfully among multiple TLRs [90], which predicts a promising perspective for photon-conserving manipulations in quantum circuits. Other theoretical work [185–187] for number-conserving manipulations of photon excitations in superconducting circuits also provide exciting alternatives. Moreover, stabilizing photon coherent states in driven systems has been experimentally demonstrated [188]. Those progresses hint the feasibility of the proposed simulator based on superconducting circuits.

4.2.5 Conclusion

A versatile quantum simulator of interacting bosons based on a tunable superconducting TLR-SQUID array has been presented. The BHM with tunable parameters on each site can be studied using the photons in this simulator. We have demonstrated the feasibility of inducing the MI-SF transition by manipulating only one single site. Our results are further supported by the exact diagnolization method, and details of the transition with realistic parameters are presented. The fidelity metric, energy gap, and on-site photon number show signatures of the phase transition. We also discussed possible schemes for state preparation, cooling, and detection of the phase transition for this proposed simulator.

Besides the manipulations of the phase transition discussed here, this quantum simulator is also capable of demonstrating topological properties in the BHM with superlattice structures and should exhibit the topological properties, edge states, and topological phase transitions studied in Refs. [156, 157, 189]. Moreover, quantum quenches [190, 191] and their associated dynamics may also be simulated by this superconducting circuit simulator as well. For example, similar to Ref. [192] one can separate the TLR array into two sections by turning off the hopping between the two sections. Then different photon numbers are prepared in the two sections. By switching on the hopping between the two sections, photons are expected to slosh back and forth between the two sections, which should be detectable with similar measurement methods. Thus the superconducting circuit simulator adds more excitement to the physics of interacting bosons and complements other available simulators.

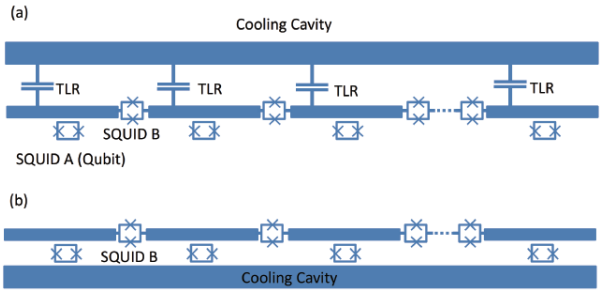

Figure 4.11: Schematic circuit of the cooling scheme. (a) A low Q cavity is capacitively coupled to every site of the TLR array. (b) A low Q cavity is capacitively coupled to each on-site SQUID.

4.3 Side-band cooling of an array of TLRs

4.3.1 Motivation and circuit

Simulator of Bose-Hubbard Model has been intensively studied recently with superconducting quantum circuits (SCQC). But cooling of the many body state of an array of SCQC remains un-developed. I studied a quantum simulator of BHM and briefly mentioned cooling of the simulatorin [193]. In this section, I am going to detailed theory to study the cooling mechanism of an array of TLR. We can start with a simple scheme where a big cooling cavity is coupled to all the sites of this array, via two different coupling ways: 1. cooling cavity directly capacitively coupled to on-site TLR (see Figure.4.11-(a)); 2. cooling cavity coupled to on-site qubits (see Figure.4.11-(b)). The theoretical treatments for these two schemes are slightly different. So we discuss it separately as following.

Physics of the cooling approach is referred to Fig.4.12.(a). One sends in a red-detuned driving signal ω_d into the cavity with resonant frequency ω_c, where $\Delta_\beta = \omega_d - \omega_c < 0$. If there is any energy separation in the collective state of the TLR array close to the detuned frequency Δ_β, it will form a 3-wave mixing scheme. The cavity absorbs a collective excitation quantum from the array and gains one resonant photon out of a driving photon. The photons in the cavity will decay eventually then the array keeps getting lower levels of collective state.

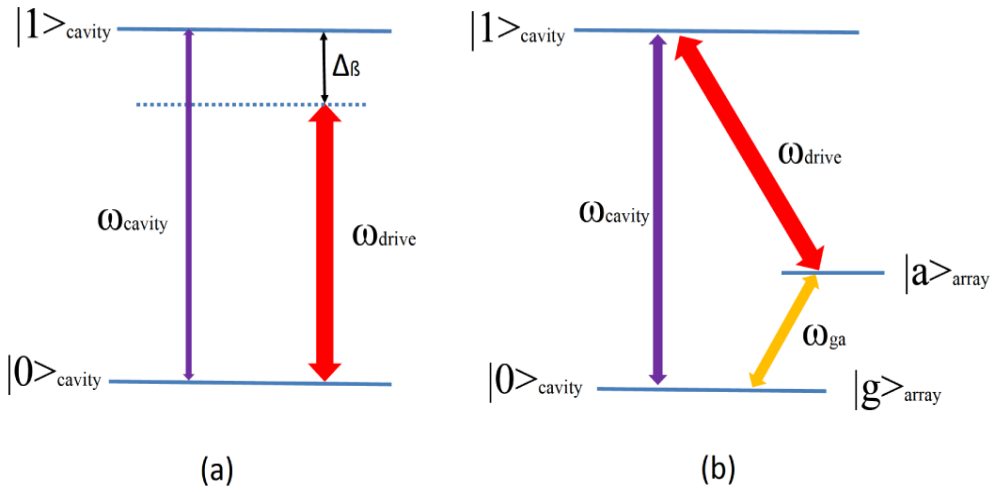

Figure 4.12: The three-wave mixing transition diagram of cooling process. ω_{drive} is the frequency of driving signal. ω_{cavity} is the resonant frequency of cooling cavity. $\Delta_\beta = \omega_d - \omega_c$ is the detuning. Here it shows red-detune. $|n\rangle_{\text{cavity}}$ is the photon state of cavity, while, in (b), $|g\rangle_{\text{array}}$ $|a\rangle_{\text{array}}$ are ground state and one of the excited state of the array, whose energy separation is ω_{ga}.

4.3.2 Cooling Cavity directly coupled to on-site TLRs

4.3.2.1 Modelling the circuit

The total Hamiltonian of this system is

$$\begin{aligned} H &= \omega^c a^\dagger a + \sum_i g_i (b_i a^\dagger + b_i^\dagger a) \\ &+ \sum_i \omega_i^{TLR} b_i^\dagger b_i + J \sum_i (b_i b_{i+1}^\dagger + b_i^\dagger b_{i+1}) \\ &+ \sum_i \omega_i^q c_i^\dagger c_i + \sum_i g_i^q \sigma_{x,i} (b_i^\dagger + b_i) \\ &+ \epsilon(t)(a^\dagger e^{-i\omega_d t} + a e^{i\omega_d t}) \end{aligned} \tag{4.23}$$

where a, b, c are annihlation operators of cooling cavity, on-site TLR and on-site qubit, and ω^c is the cooling cavity frequency, g is the coupling between on-site TLR mode with cooling cavity, ω^{TLR} is the on-site TLR frequency, J is the coupling between different sites of TLRs, ω^q is on-site qubit frequency, g^q is coupling between on-site qubit and on-site TLR, σ^x is Pauli operator of on-site qubit, $\epsilon(t)$ is the amplitude of pumping field, ω^d is pumping frequency. Tuning and biasing circuit parameters to selectively stay in the regime $(\omega_i^{TLR} - \omega_i^q) \gg g_i^q \gg J$, one gets Bose-Hubbard Model Hamiltonian [193] from the second and third line of the total Hamiltonian

in equation (4.23) using fourth order perturbation theory. The total Hamiltonian becomes

$$H = \omega^c a^\dagger a + \sum_i g_i(b_i a^\dagger + b_i^\dagger a) + \sum_i \omega_i^p b_i^\dagger b_i + J\sum_i (b_i b_{i+1}^\dagger + b_i^\dagger b_{i+1}) + \frac{\alpha}{2}\sum_i b_i^\dagger b_i^\dagger b_i b_i + \epsilon(a^\dagger e^{-i\omega_d t} + a e^{i\omega_d t}) \tag{4.24}$$

where α is on-site photon interaction strength and ω^p is effective on-site photon frequency. In this case g is at the same magnitude as J, which is around $5MHz$, so that the pertubative treat is applied up to the same order as g and J.

Move to rotating frame of following the unitary transformation $U = \exp\{i\omega^d t(a^\dagger a + \sum_i b_i^\dagger b_i)\}$, and the total Hamiltonian follows the transformation $\widetilde{H} = UHU^\dagger - iU\dot{U}^\dagger$. Use Baker-Campbell-Hausdor formula

$$e^X H e^{-X} = H + [X, H] + \frac{1}{2!}[X, [X, H]] + \frac{1}{3!}[X, [X, [X, H]]] + ...$$

where $X = i\omega^d t(a^\dagger a + \sum_i b_i^\dagger b_i)$. Because $[a^\dagger a, a] = -a$, $[a^\dagger a, a^\dagger] = a^\dagger$ and $[b^\dagger b, b] = -b$, $[b^\dagger b, b^\dagger] = b^\dagger$,

$$\begin{aligned}
[X, \omega^c a^\dagger a] &= 0 \\
[X, g_i(b_i a^\dagger + b_i^\dagger a)] &= 0 \\
[X, \omega_i^p b_i^\dagger b_i] &= 0 \\
[X, J\sum_i (b_i b_{i+1}^\dagger + b_i^\dagger b_{i+1})] &= 0 \\
[X, \frac{\alpha}{2}\sum_i b_i^\dagger b_i^\dagger b_i b_i] &= 0.
\end{aligned} \tag{4.25}$$

And,

$$\begin{aligned}
U a e^{i\omega_d t} U^\dagger &= a \\
U a^\dagger e^{-i a^\dagger \omega_d t} U^\dagger &= a^\dagger,
\end{aligned}$$

so

$$U\epsilon(a^\dagger e^{-i\omega_d t} + a e^{i\omega_d t})U^\dagger = \epsilon(a^\dagger + a). \tag{4.26}$$

Also,

$$i\dot{U}U^\dagger = iU[-i\omega^d(a^\dagger a + \sum_i b_i^\dagger b_i)]U^\dagger = \omega^d(a^\dagger a + \sum_i b_i^\dagger b_i). \tag{4.27}$$

Therefore, we get the transformed Hamiltonian as

$$\begin{aligned}\widetilde{H} &= (\omega^c - \omega^d)a^\dagger a + \sum_i g_i(b_i a^\dagger + b_i^\dagger a) + \sum_i (\omega_i^p - \omega^d) b_i^\dagger b_i \\ &+ J\sum_i (b_i b_{i+1}^\dagger + b_i^\dagger b_{i+1}) + \frac{\alpha}{2}\sum_i b_i^\dagger b_i^\dagger b_i b_i + \epsilon(a^\dagger + a) \\ &= \Delta^c a^\dagger a + \sum_i g_i(b_i a^\dagger + b_i^\dagger a) + \sum_i \Delta_i^p b_i^\dagger b_i \\ &+ J\sum_i (b_i b_{i+1}^\dagger + b_i^\dagger b_{i+1}) + \frac{\alpha}{2}\sum_i b_i^\dagger b_i^\dagger b_i b_i + \epsilon(a^\dagger + a),\end{aligned} \tag{4.28}$$

where $\Delta^c = \omega^c - \omega^d$ is the detuning between driving signal and cooling cavity, $\Delta^p = \omega^p - \omega^d$ is the detuning between driving signal and photon frequency.

4.3.2.2 Diagonalization of the total Hamiltonian

Consider a four-site array, which is the smallest size example in Ref. [193]. Without the driving term and nonlinear terms, the Hamiltonian on five-component vector $C = (a, b_1, b_2, b_3, b_4)$ can be written as $\widetilde{H}_0 = C^\dagger \widetilde{\mathcal{H}}_0 C$, where

$$\widetilde{\mathcal{H}}_0 = \begin{bmatrix} \Delta^c & g_1 & g_2 & g_3 & g_4 \\ g_1 & \Delta_1^p & J & 0 & 0 \\ g_2 & J & \Delta_2^p & J & 0 \\ g_3 & 0 & J & \Delta_3^p & J \\ g_4 & 0 & 0 & J & \Delta_4^p \end{bmatrix}. \tag{4.29}$$

For simplified Hamiltonian

$$\widetilde{\mathcal{H}}_0 = \begin{bmatrix} \Delta^c & g & g & g & g \\ g & \Delta^p & J & 0 & 0 \\ g & J & \Delta^p & J & 0 \\ g & 0 & J & \Delta^p & J \\ g & 0 & 0 & J & \Delta^p \end{bmatrix}.$$

The eigenvalues of this Hamiltonian are

$$\begin{cases} \lambda_0 = \frac{1}{2}(-J - \sqrt{5}J + 2\Delta^p) \\ \lambda_1 = \frac{1}{2}(-J + \sqrt{5}J + 2\Delta^p) \\ \lambda_2 = x_1 \\ \lambda_3 = x_2 \\ \lambda_4 = x_3 \end{cases} \tag{4.30}$$

where x_1, x_2, x_3 are the solutions of polynomial equation

$$\begin{aligned}&(-2g^2J + 4g^2\Delta^p + J^2\Delta^c - J\Delta^p\Delta^c - \Delta^{p,2}\Delta^c)\\&+ (J\Delta^p + \Delta^{p,2} + J\Delta^c + 2\Delta^p\Delta^c - 4g^2 - J^2)x\\&- (J + 2\Delta^p + \Delta^c)x^2 + x^3\\&= 0.\end{aligned} \tag{4.31}$$

Because $\widetilde{\mathcal{H}}_0$ is hermitian matrix, the three roots of this polynomial equation are real. Their values can be solved numerically with Cardano's formula (citation). For the general 5×5 dimensional lindear Hamiltonian from equation.(4.29) The diagonalized linear Hamiltonian can be written as $\widetilde{H}_0^{diag.} = N\widetilde{H}_0N^{-1}$ with unitary transformation N. The new basis becomes $D = NC = (A, B_1, B_2, B_3, B_4)$ given by

$$\begin{cases} A = N_{00}a + \sum_{j=1}^{4} N_{0j}b_j \\ B_i = N_{i0}a + \sum_{j=1}^{4} N_{ij}b_j \end{cases}$$

Define $M = N^{-1}$. Correspondingly the original basis can be written into polynomial of new basis

$$\begin{cases} a = M_{00}A + \sum_{j=1}^{4} M_{0j}B_j \\ b_i = M_{i0}A + \sum_{j=1}^{4} M_{ij}B_j \end{cases}$$

with eigenvalues $(\lambda_0, \lambda_1, \lambda_2, \lambda_3, \lambda_4)$. The entries of M and N are function for Δ^c, Δ^p, g, and J. However the analytical solutions for these are complicated. Numerical solutions can be made instead. But in this article I have skipped this step because theses formulas doesn't affect the principle of cooling. It only affects the magnitude of cooling rate, so the details of matrices M and N will be studied in the near future.

In this new basis, the linear Hamiltonian is diagonlized as

$$\widetilde{H}_0 = \lambda_0 A^\dagger A + \sum_{i=1}^{4} \lambda_i B_i^\dagger B_i. \tag{4.32}$$

The driving term

$$\epsilon(a^\dagger + a) = \epsilon[M_{00}(A^\dagger + A) + \sum_{j=1}^{4} M_{0j}(B_j^\dagger + B_j)]. \tag{4.33}$$

In the regime $g_i/\Delta_i^p \ll 1$, one gets $M_{0j}/M_{00} \ll 1$. So driving term can be approximated with

$$\epsilon(a^\dagger + a) \approx \epsilon M_{00}(A^\dagger + A). \tag{4.34}$$

The on-site interaction term

$$\frac{\alpha}{2}\sum_{i=1}^{4} b_i^\dagger b_i^\dagger b_i b_i = \frac{\alpha}{2}\sum_{i=1}^{4}[(M_{i0}A^\dagger + \sum_{j=1}^{4} M_{ij}B_j^\dagger)(M_{i0}A^\dagger + \sum_{k=1}^{4} M_{ik}B_k^\dagger)$$
$$(M_{i0}A + \sum_{m=1}^{4} M_{im}B_m)(M_{i0}A + \sum_{n=1}^{4} M_{in}B_n)]$$
$$\overset{RWA}{\approx} \frac{\alpha}{2}\sum_{i=1}^{4}\{M_{i0}^4 A^\dagger A^\dagger AA + \sum_{j,k,m,n=1}^{4}(M_{ij}M_{ik}M_{im}M_{in})B_j^\dagger B_k^\dagger B_m B_n$$
$$+ 4M_{i0}^2 A^\dagger A \sum_{m,n=1}^{4}(M_{im}M_{in})B_m^\dagger B_n\}. \tag{4.35}$$

Here, the fast rotating terms $A^\dagger B_i^\dagger B_j B_k$, $A^\dagger B_i^\dagger B_j^\dagger B_k$ and their conjugate terms are neglected due to RWA. Look at different terms in equation.(4.35) we got three nonlinear terms in the total Hamiltonian:

(1) Self-Kerr correction in the cooling cavity

$$\begin{aligned} V^c &= \frac{\alpha}{2}(\sum_{i=1}^{4} M_{i0}^4)A^\dagger A^\dagger AA \\ &= \frac{\alpha}{2}\Pi_0 A^\dagger A^\dagger AA \end{aligned} \tag{4.36}$$

where $\Pi_0 = \sum_{i=1}^{4} M_{i0}^4$.

(2) Self-Kerr correction in the on-site TLR

$$\begin{aligned} V^{TLR} &= \frac{\alpha}{2}\sum_{j,k,m,n=1}^{4}(\sum_{i=1}^{4} M_{ij}M_{ik}M_{im}M_{in})B_j^\dagger B_k^\dagger B_m B_n \\ &= \frac{\alpha}{2}\sum_{j,k,m,n=1}^{4}\mu_{jkmn}B_j^\dagger B_k^\dagger B_m B_n, \end{aligned} \tag{4.37}$$

where $\mu_{jkmn} = \sum_{i=1}^{4} M_{ij}M_{ik}M_{im}M_{in}$.

(3) Photon number correlation term (Cross-Kerr) between cooling cavity and TLRs

$$\begin{aligned} V^{couple} &= 2\alpha \sum_{i=1}^{4} M_{i0}^2 A^\dagger A \sum_{m,n=1}^{4} (M_{im} M_{in}) B_m^\dagger B_n \\ &= 2\alpha A^\dagger A \sum_{m,n=1}^{4} \eta_{mn} B_m^\dagger B_n, \end{aligned} \tag{4.38}$$

where $\eta_{mn} = \sum_{i=1}^{4} M_{i0}^2 M_{im} M_{in}$.

Therefore, the total Hamiltonian in this new basis D becomes

$$\begin{aligned} \widetilde{H}^D &= \lambda_0 A^\dagger A + \sum_{i=1}^{4} \lambda_i B_i^\dagger B_i + \frac{\alpha}{2} \Pi_0 A^\dagger A^\dagger A A \\ &+ \frac{\alpha}{2} \sum_{j,k,m,n=1}^{4} \mu_{jkmn} B_j^\dagger B_k^\dagger B_m B_n + 2\alpha A^\dagger A \sum_{m,n=1}^{4} \eta_{mn} B_m^\dagger B_n + \epsilon M_{00} (A^\dagger + A). \end{aligned} \tag{4.39}$$

Again, in the large detuning regime between the cooling cavity and TLRs, $M_{0j} \ll M_{ij}$ with $ij \neq 0$. Hence, $\Pi_0 \ll \eta_{jkmn} \ll \mu_{jkmn}$, which means self-Kerr effect of on-site TLR is much stronger than cross-Kerr effect between cooling cavity and TLRs, and cross-Kerr is much stronger than self-Kerr effect in cooling Cavity.[1]

4.3.2.3 Obtaining cooling term

Notice that the fock state in cooling cavity will be a mixture of classical field and quantum field. The cavity operator A now includes a classical part and a quantum part:

$$\begin{aligned} A &= \overline{A}(t) + \Lambda \\ A^\dagger &= \overline{A}^*(t) + \Lambda^\dagger. \end{aligned} \tag{4.40}$$

So unitary operator $U_\Lambda = \exp\{\overline{A}(t) A^\dagger - \overline{A}^*(t) A\}$ becomes displacement operator on A, because

$$\begin{aligned} U_\Lambda A U_\Lambda^\dagger &= \exp\{\overline{A}(t) A^\dagger - \overline{A}^*(t) A\} A \exp\{\overline{A}^*(t) A - \overline{A}(t) A^\dagger\} \\ &= A - \overline{A}(t) \\ &= \Lambda \end{aligned} \tag{4.41}$$

Applying U_Λ on total Hamiltonian $\widetilde{H}^D$ to separate classical field from quantum field, one

[1] Part of the derivation in the first circuit model are learned through personal communication with Claudia Grandi from prof. Girvin's group at Yale University.

gets...

$$\begin{aligned}
\widetilde{H}^{\Lambda} &= U_{\Lambda}\widetilde{H}^{D}U_{\Lambda}^{\dagger} - iU_{\Lambda}\dot{U}_{\Lambda}^{\dagger} \\
&= \lambda_0[\left|\overline{A}\right|^2 + (\overline{A}\Lambda^{\dagger} + \overline{A}^{*}\Lambda) + \Lambda^{\dagger}\Lambda] + \sum_{i=1}^{4}\lambda_i B_i^{\dagger}B_i + \epsilon M_{00}(A^{\dagger} + A) \\
&+ \frac{\alpha}{2}\sum_{j,k,m,n=1}^{4}\mu_{jkmn}B_j^{\dagger}B_k^{\dagger}B_mB_n + \frac{\alpha}{2}\Pi_0[\Lambda^{\dagger}\Lambda^{\dagger}\Lambda\Lambda + 4\left|\overline{A}\right|^2\Lambda^{\dagger}\Lambda \\
&+ \left|\overline{A}\right|^4 + 2(\overline{A}^{*}\overline{A}^{2}\Lambda^{\dagger} + \overline{A}\overline{A}^{*2}\Lambda) + \overline{A}^{*2}\Lambda\Lambda + \overline{A}^{2}\Lambda^{\dagger}\Lambda^{\dagger} + 2(\overline{A}^{*}\Lambda^{\dagger}\Lambda\Lambda + \overline{A}\Lambda^{\dagger}\Lambda^{\dagger}\Lambda)] \\
&+ 2\alpha[\left|\overline{A}\right|^2 + (\overline{A}\Lambda^{\dagger} + \overline{A}^{*}\Lambda) + \Lambda^{\dagger}\Lambda]\sum_{m,n=1}^{4}\eta_{mn}B_m^{\dagger}B_n - i(\dot{\overline{A}}\Lambda^{\dagger} - \dot{\overline{A}}^{*}\Lambda). \qquad (4.42)
\end{aligned}$$

For a constant classical driving field $\dot{\overline{A}} = 0$, hence

$$\begin{aligned}
\widetilde{H}^{\Lambda} &= \lambda_0[\left|\overline{A}\right|^2 + (\overline{A}\Lambda^{\dagger} + \overline{A}^{*}\Lambda) + \Lambda^{\dagger}\Lambda] + \sum_{i=1}^{4}\lambda_i B_i^{\dagger}B_i \\
&+ \frac{\alpha}{2}\sum_{j,k,m,n=1}^{4}\mu_{jkmn}B_j^{\dagger}B_k^{\dagger}B_mB_n + \epsilon M_{00}(A^{\dagger} + A) \\
&+ \frac{\alpha}{2}\Pi_0[\Lambda^{\dagger}\Lambda^{\dagger}\Lambda\Lambda + 4\left|\overline{A}\right|^2\Lambda^{\dagger}\Lambda + \left|\overline{A}\right|^4 + 2(\overline{A}^{*}\overline{A}^{2}\Lambda^{\dagger} + \overline{A}\overline{A}^{*2}\Lambda) \\
&+ \overline{A}^{*2}\Lambda\Lambda + \overline{A}^{2}\Lambda^{\dagger}\Lambda^{\dagger} + 2(\overline{A}^{*}\Lambda^{\dagger}\Lambda\Lambda + \overline{A}\Lambda^{\dagger}\Lambda^{\dagger}\Lambda)] \\
&+ 2\alpha[\left|\overline{A}\right|^2 + (\overline{A}\Lambda^{\dagger} + \overline{A}^{*}\Lambda) + \Lambda^{\dagger}\Lambda]\sum_{m,n=1}^{4}\eta_{mn}B_m^{\dagger}B_n. \qquad (4.43)
\end{aligned}$$

$(\overline{A}\Lambda^{\dagger} + \overline{A}^{*}\Lambda)$ in the last term of above Hamiltonian exchanges energy between TLR array and cooling cavity. Notice that in cooling cavity quantum field decohere very fast, so $< \Lambda >= 0$. The last term of above Hamiltonian becomes

$$2\alpha[\left|\overline{A}\right|^2 + \overline{A}\Lambda^{\dagger} + \Lambda^{\dagger}\Lambda]\sum_{m,n=1}^{4}\eta_{mn}B_m^{\dagger}B_n \qquad (4.44)$$

where $\overline{A}\Lambda^{\dagger}$ indicates that driving signal keeps turning into higher energy photons. The additional energy comes from the TLR array hence cooling process is induced! Also $\sum_{m,n=1}^{4}\eta_{mn}B_m^{\dagger}B_n$ conserves total photon numbers in the array. Therefore, we conclude that this scheme gives rise to a photon-conserving side band cooling.

4.3.3 Cooling Cavity capacitively coupled TLRs via on-site SQUID

4.3.3.1 Modelling the circuit

The total Hamiltonian of this system is

$$\begin{aligned} H = {} & \omega^c a^\dagger a + \sum_i g_i^{qc} \sigma_i^x (a^\dagger + a) \\ & + \sum_i \omega_i^q \sigma_i^z + \sum_i g_i^{qTLR} \sigma_i^x (b^\dagger + b) \\ & + \sum_i \omega_i^{TLR} b_i^\dagger b_i + \sum_i J_i (b_i b_{i+1}^\dagger + b_i^\dagger b_{i+1}) \\ & + \epsilon(t)(a^\dagger e^{-i\omega_d t} + a e^{i\omega_d t}) \end{aligned} \tag{4.45}$$

where a, b, c are annihlation operators of cooling cavity, on-site TLR and on-site qubit, and ω^c is the cooling cavity frequency, g^{qc} is the coupling strength between qubit and cooling cavity, g^{qTLR} is the coupling strength between qubit and on-site TLR, ω^{TLR} is the on-site TLR frequency, J is the coupling between different sites of TLRs, ω^q is on-site qubit frequency, σ^x is Pauli operator of on-site qubit, $\epsilon(t)$ is the amplitude of pumping field, ω^d is pumping frequency. Tuning and biasing circuit parameters to selectively stay in the dispersive regime, without loss of generality we assume $\Delta = (\omega^c - \omega_i^q) = (\omega_i^{TLR} - \omega_i^q) \gg g_i^{qTLR} = g_i^{qc} \gg J$, one gets Bose-Hubbard Model Hamiltonian [193] from the second and third line of the total Hamiltonian in equation (4.45), using fourth order perturbative treatment with on-site interaction between qubit and TLR. The total Hamiltonian becomes $\frac{\alpha}{2} \sum_i b_i^\dagger b_i^\dagger b_i b_i$

$$\begin{aligned} H = {} & \omega^c a^\dagger a + \sum_i g_i^{qc} (\sigma_i^- a^\dagger + \sigma_i^+ a) + \sum_i (\omega_i^{TLR} b_i^\dagger b_i + \omega_i^q \sigma_i^z) \\ & + \sum_i g_i^{qTLR} (\sigma_i^- b_i^\dagger + \sigma_i^+ b_i) + \sum_i J_i (b_i b_{i+1}^\dagger + b_i^\dagger b_{i+1}) + \epsilon(t)(a^\dagger e^{-i\omega_d t} + a e^{i\omega_d t}) \end{aligned} \tag{4.46}$$

$$\begin{aligned} = {} & \omega^c a^\dagger a + \sum_i (\omega_i^{TLR} b_i^\dagger b_i + \omega_i^q \sigma_i^z) + \sum_i g_i [\sigma_i^- (a^\dagger + b_i^\dagger) + \sigma_i^+ (a + b_i)] \\ & + \sum_i J_i (b_i b_{i+1}^\dagger + b_i^\dagger b_{i+1}) + \epsilon(t)(a^\dagger e^{-i\omega_d t} + a e^{i\omega_d t}) \end{aligned} \tag{4.47}$$

Separate the Hamiltonian into three terms

$$H = H^0 + V + D \tag{4.48}$$

The on-site interaction term

$$V = \sum_{i=1}^{N} g_i [\sigma_i^- (a^\dagger + b_i^\dagger) + \sigma_i^+ (a + b_i)] + J_i (b_i b_{i+1}^\dagger + b_i^\dagger b_{i+1}), \tag{4.49}$$

and driving term

$$D = \epsilon(t)(a^{\dagger}e^{-i\omega_d t} + ae^{i\omega_d t}), \tag{4.50}$$

while

$$H^0 = \omega^c a^{\dagger}a + \sum_i \omega_i^{TLR} b_i^{\dagger} b_i$$

In interaction picture

$$V^{int} = e^{jH^0 t} V e^{-jH^0 t}$$

The evolution operator in interaction picture can be expand into Dyson series as following

$$\begin{aligned}
U(t) = 1 &- j\int_0^t dt_1 \sum_{m,n} \left\langle m \left| V^{int} \right| n \right\rangle e^{-j(E_n - E_m)t_1} \left| m \right\rangle \left\langle n \right| \\
&- \int_0^t dt_1 \int_0^{t_1} dt_2 \sum_{m,n,q} e^{-j(E_n - E_m)t_1} \left\langle m \left| V^{int} \right| n \right\rangle \left\langle n \left| V^{int} \right| q \right\rangle e^{-j(E_q - E_n)t_2} \left| m \right\rangle \left\langle q \right| \\
&+ j\int_0^t dt_1 \int_0^{t_1} dt_2 \int_0^{t_2} dt_3 \sum_{m,n,q,p} e^{-j(E_n - E_m)t_1} e^{-j(E_q - E_n)t_2} e^{-j(E_p - E_q)t_3} \\
&\left\langle m \left| V^{int} \right| n \right\rangle \left\langle n \left| V^{int} \right| q \right\rangle \left\langle q \left| V^{int} \right| p \right\rangle \left| m \right\rangle \left\langle p \right| \\
&+ \int_0^t dt_1 \int_0^{t_1} dt_2 \int_0^{t_2} dt_3 \int_0^{t_3} dt_4 \sum_{m,n,q,p,k} e^{-j(E_n - E_m)t_1} e^{-j(E_q - E_n)t_2} e^{-j(E_p - E_q)t_3} e^{-j(E_k - E_p)t_4} \\
&\left\langle m \left| V^{int} \right| n \right\rangle \left\langle n \left| V^{int} \right| q \right\rangle \left\langle q \left| V^{int} \right| p \right\rangle \left\langle p \left| V^{int} \right| k \right\rangle \left| m \right\rangle \left\langle k \right| \\
&+ ...
\end{aligned} \tag{4.51}$$

To evaluate different terms of $U(t)$, two following assumptions are going to be made as well. (1) The array of TLRs are uniform, which means all TLR frequencies, qubits and coupling terms are the same; (2) All qubits are in ground state which means all σ^z terms gives only -1 value.

The *first* order term gives three different species:

1) Cooling cavity $\leftrightarrow$ on-site qubit (q_i)

$$\begin{aligned}
U^{cq(1)} &= -\frac{g^c}{\Delta^c} e^{-j\Delta^c t} \sum_{i,n^c} [\sqrt{n^c} \left| n^c \downarrow_i^q n_i^{TLR} \right\rangle \left\langle (n^c - 1) \uparrow_i^q n_i^{TLR} \right| + h.c.] \\
&= -\frac{g^c}{\Delta^c} e^{-j\Delta^c t} \sum_i (\sigma_i^+ a + \sigma_i^- a^{\dagger})
\end{aligned} \tag{4.52}$$

where $\Delta_i^c = \omega_i^q - \omega^c$, $\Delta_i = \omega_i^{TLR} - \omega_i^q$.

2) on-site qubit ↔ TLR

$$U^{Tq(1)} = -\frac{g^{TLR}}{\Delta^c} e^{-j\Delta^{TLR}t} \sum_{i,n^c} [\sqrt{n^{TLR}} \left| n^c \uparrow_i^q (n_i^{TLR} - 1) \right\rangle \left\langle n^c \downarrow_i^q n_i^{TLR} \right| + h.c.]$$
$$= -\sum_i \frac{g^c}{\Delta_i^c} e^{-j\Delta^c t} (\sigma_i^- b_i^\dagger + \sigma_i^+ b_i) \tag{4.53}$$

3) $\text{TLR}_i \leftrightarrow \text{TLR}_{i+1}$

$$U^{TT(1)} = jtJ \sum_i (b_i b_{i+1}^\dagger + b_i^\dagger b_{i+1}) \tag{4.54}$$

The *second* order term gives
1) Cooling cavity ↔ on-site qubit ↔ TLR

$$U^{cqT(2)} = \sum_i \frac{g_i^c g_i^T}{\Delta_i(\Delta_i + \Delta_i^c)} e^{-jt(\Delta_i + \Delta_i^c)} (a^\dagger \sigma_i^- \sigma_i^+ b_i + b_i^\dagger \sigma_i^- \sigma_i^+ a)$$
$$\overset{(1)}{=} \frac{g^c g^T}{\Delta(\Delta + \Delta^c)} e^{-jt(\Delta + \Delta^c)} \sum_i \frac{1 - \sigma_i^z}{2} (b_i a^\dagger + b_i^\dagger a)$$
$$\overset{(2)}{=} \frac{g^c g^T}{\Delta(\Delta + \Delta^c)} e^{-jt(\Delta + \Delta^c)} \sum_i (b_i a^\dagger + b_i^\dagger a) \tag{4.55}$$

Notice that when $(\Delta + \Delta^c) = 0$, $\frac{e^{-jt(\Delta+\Delta^c)}}{(\Delta+\Delta^c)} = -jt$, hence

$$U^{cqT(2)} = -jt \frac{g^c g^T}{\Delta} \sum_i (b_i a^\dagger + b_i^\dagger a) \tag{4.56}$$

2) on-site qubit ↔ $\text{TLR}_i \leftrightarrow \text{TLR}_{i+1}$

$$U^{qTT(2)} = -\sum_i \frac{g_i^T J_i}{\Delta_i^2} (1 + j\Delta_i t) e^{-j\Delta_i t} (b_{i+1}^\dagger b_i b_i^\dagger \sigma_i^- + \sigma_i^+ b_i b_i^\dagger b_{i+1})$$
$$= -\sum_i \frac{g_i^T J_i}{\Delta_i^2} (1 + j\Delta_i t) e^{-j\Delta t} (\sigma_i^- b_{i+1}^\dagger + \sigma_i^+ b_{i+1}) b_i b_i^\dagger$$
$$\approx -\sum_i \frac{g_i^T J_i}{\Delta_i^2} e^{j\Delta t} e^{-j\Delta t} (\sigma_i^- b_{i+1}^\dagger + \sigma_i^+ b_{i+1}) b_i b_i^\dagger$$
$$\overset{(1)}{=} -\frac{g^T J}{\Delta^2} \sum_i (\sigma_i^- b_{i+1}^\dagger + \sigma_i^+ b_{i+1})(b_i^\dagger b_i + 1) \tag{4.57}$$

3) Cooling cavity $\leftrightarrow$ q_i $\leftrightarrow$ Cooling cavity

$$\begin{aligned} U^{cqc(2)} &= jt \sum_i \frac{g_i^{c,2}}{\Delta_i^c} a^\dagger \sigma_i^- \sigma_i^+ a \\ &= jt a^\dagger a \sum_i \frac{g_i^{c,2}}{\Delta_i^c} \frac{1-\sigma_i^z}{2} \\ &\overset{(1)}{=} jt \frac{g^{c,2}}{\Delta^c} a^\dagger a \sum_i \frac{1-\sigma_i^z}{2} \\ &\overset{(2)}{=} jt \frac{g^{c,2}}{\Delta^c} N a^\dagger a \end{aligned} \tag{4.58}$$

4) TLR_i $\leftrightarrow$ q_i $\leftrightarrow$ TLR_i

$$\begin{aligned} U^{TqT(2)} &= -jt \sum_i \frac{g_i^{T,2}}{\Delta_i} b_i^\dagger b_i \frac{1-\sigma_i^z}{2} \\ &\overset{(1)}{=} -jt \frac{g^{T,2}}{\Delta} \sum_i b_i^\dagger b_i \frac{1-\sigma_i^z}{2} \\ &\overset{(2)}{=} -jt \frac{g^{T,2}}{\Delta} \sum_i b_i^\dagger b_i \end{aligned} \tag{4.59}$$

5) TLR_i $\leftrightarrow$ TLR_{i+1}/TLR_{i-1} $\leftrightarrow$ TLR_i

$$\begin{aligned} U^{TTT(2)} &= -\frac{1}{2} t^2 2 \sum_i J_i^2 b_i^\dagger b_i \\ &= -t^2 J^2 \sum_i b_i^\dagger b_i \end{aligned} \tag{4.60}$$

The *third* order term gives
1) Cooling cavity $\rightarrow$ q_i $\rightarrow$ TLR_i $\rightarrow$ q_i

$$\begin{aligned} U^{cqTq(3)} &= \sum_i \frac{g_i^c g_i^{T,2}}{\Delta_i^{c,2}(\Delta_i + \Delta_i^c)} e^{-jt\Delta_i^c} \sigma_i^+ b_i b_i^\dagger \sigma_i^- \sigma_i^+ a \\ &= \sum_i \frac{g_i^c g_i^{T,2}}{\Delta_i^{c,2}(\Delta_i + \Delta_i^c)} e^{-jt\Delta_i^c} \sigma_i^+ a (b_i^\dagger b_i + 1) \frac{1-\sigma_i^z}{2} \\ &\overset{(1)}{=} \frac{g^c g^{T,2}}{\Delta^{c,2}(\Delta + \Delta^c)} e^{-jt\Delta^c} \sum_i \sigma_i^+ a (b_i^\dagger b_i + 1) \frac{1-\sigma_i^z}{2} \\ &\overset{(2)}{=} \frac{g^c g^{T,2}}{\Delta^{c,2}(\Delta + \Delta^c)} e^{-jt\Delta^c} \sum_i \sigma_i^+ a (b_i^\dagger b_i + 1) \end{aligned} \tag{4.61}$$

2) $q_i \rightarrow TLR_i \rightarrow q_i \rightarrow$ Cooling cavity

$$\begin{aligned} U^{cqTq(3)} &= \sum_i \frac{g_i^c g_i^{T,2}}{\Delta_i \Delta_i^c}(-1+jt)e^{jt\Delta_i^c} a^\dagger \sigma_i^- (b_i^\dagger b_i + 1)\frac{1+\sigma_i^z}{2} \\ &\overset{(1)}{=} \frac{g^c g^{T,2}}{\Delta\Delta^c}(-1+jt)e^{jt\Delta^c} \sum_i a^\dagger \sigma_i^- (b_i^\dagger b_i + 1)\frac{1+\sigma_i^z}{2} \\ &\overset{(2)}{=} 0 \end{aligned} \tag{4.62}$$

3) Cooling cavity $\rightarrow q_i \rightarrow TLR_i \rightarrow TLR_{i+1}$

$$\begin{aligned} U^{cqTT(3)} &= \sum_i \frac{J_i g_i^c g_i^T}{\Delta_i^c(\Delta_i+\Delta_i^c)^2} e^{-jt(\Delta_i+\Delta_i^c)} b_{i+1}^\dagger b_i b_i^\dagger \sigma_i^- \sigma_i^+ a \\ &= \sum_i \frac{J_i g_i^c g_i^T}{\Delta_i^c(\Delta_i+\Delta_i^c)^2} e^{-jt\Delta_i^c} b_{i+1}^\dagger a(b_i^\dagger b_i + 1)\frac{1-\sigma_i^z}{2} \\ &\overset{(1)}{=} \frac{Jg^c g^T}{\Delta^c(\Delta+\Delta^c)^2} e^{-jt\Delta^c} \sum_i b_{i+1}^\dagger a(b_i^\dagger b_i + 1)\frac{1-\sigma_i^z}{2} \\ &\overset{(2)}{=} \frac{Jg^c g^{T,2}}{\Delta^c(\Delta+\Delta^c)^2} e^{-jt\Delta^c} \sum_i b_{i+1}^\dagger a(b_i^\dagger b_i + 1) \end{aligned} \tag{4.63}$$

4) Cooling cavity $\leftarrow q_i \leftarrow TLR_i \leftarrow TLR_{i+1}$

$$\begin{aligned} U^{TTqc(3)} &= \sum_i \frac{J_i g_i^c g_i^T}{\Delta_i^c(\Delta_i+\Delta_i^c)^2} e^{-jt(\Delta_i+\Delta_i^c)} a^\dagger \sigma_i^- \sigma_i^+ b_i b_i^\dagger b_{i+1} \\ &= \sum_i \frac{J_i g_i^c g_i^T}{\Delta_i^c(\Delta_i+\Delta_i^c)^2} e^{-jt\Delta_i^c} b_{i+1}^\dagger a(b_i^\dagger b_i + 1)\frac{1-\sigma_i^z}{2} \\ &\overset{(1)}{=} \frac{Jg^c g^T}{\Delta^c(\Delta+\Delta^c)^2} e^{-jt\Delta^c} \sum_i b_{i+1}^\dagger a(b_i^\dagger b_i + 1)\frac{1-\sigma_i^z}{2} \\ &\overset{(2)}{=} \frac{Jg^c g^{T,2}}{\Delta^c(\Delta+\Delta^c)^2} e^{-jt\Delta^c} \sum_i b_{i+1}^\dagger a(b_i^\dagger b_i + 1) \end{aligned} \tag{4.64}$$

5) $q_i \leftrightarrow TLR_i \leftrightarrow TLR_{i+1} \leftrightarrow q_{i+1}$

$$\begin{aligned}
U^{qTTq(3)} &= \sum_i \frac{J_i g_i^T g_{i+1}^T}{\Delta_i^2 \Delta_{i+1}} e^{jt(\Delta_i - \Delta_{i+1})} \sigma_{i+1}^+ b_{i+1} b_{i+1}^\dagger b_i b_i^\dagger \sigma_i^- \\
&= \sum_i \frac{J_i g_i^T g_{i+1}^T}{\Delta_i^2 \Delta_{i+1}} e^{jt(\Delta_i - \Delta_{i+1})} \sigma_{i+1}^+ \sigma_i^- b_{i+1} b_{i+1}^\dagger b_i b_i^\dagger \\
&\overset{(1)}{=} -jt \frac{J g^{T,2}}{\Delta^2} \sum_i \sigma_{i+1}^+ \sigma_i^- b_{i+1} b_{i+1}^\dagger b_i b_i^\dagger \\
&\overset{(2)}{=} 0
\end{aligned} \tag{4.65}$$

For the *fourth* order terms, because they are very small already, so we just need to analyse non-oscillating elements. There are following cases:

1) $TLR_i \leftrightarrow q_i \leftrightarrow$ Cooling cavity $\leftrightarrow q_i \leftrightarrow TLR_i$

$$\begin{aligned}
U^{T_i q c q T_i(4)} &= jt \sum_i \frac{g_i^{c,2} g_i^{T,2}}{\Delta_i^2 (\Delta_i + \Delta_i^c)} b_i^\dagger \sigma^- \sigma^+ a a^\dagger \sigma^- \sigma^+ b_i \\
&= jt \sum_i \frac{g_i^{c,2} g_i^{T,2}}{\Delta_i^2 (\Delta_i + \Delta_i^c)} \frac{1 - \sigma_i^z}{2} b_i^\dagger a a^\dagger b_i \\
&\overset{(1)}{=} jt \frac{g^{c,2} g^{T,2}}{\Delta^2 (\Delta + \Delta^c)} \sum_i (\frac{1 - \sigma_i^z}{2}) b_i^\dagger b_i (a^\dagger a + 1) \\
&\overset{(2)}{=} jt \frac{g^{c,2} g^{T,2}}{\Delta^2 (\Delta + \Delta^c)} \sum_i b_i^\dagger b_i (a^\dagger a + 1)
\end{aligned} \tag{4.66}$$

2) $TLR_i \leftrightarrow q_i \leftrightarrow$ Cooling cavity $\leftrightarrow q_k \leftrightarrow TLR_k$

$$\begin{aligned}
U^{T_i q c q T_k(4)} &= \sum_{i \neq k} \frac{g_i^c g_i^T g_k^c g_k^T e^{-j(\Delta_i + \Delta_i^c - \Delta_k - \Delta_k^c)t}}{\Delta_i (\Delta_i + \Delta_i^c)(\Delta_i + \Delta_i^c - \Delta_k)(\Delta_i + \Delta_i^c - \Delta_k - \Delta_k^c)} \\
&\quad (b_k^\dagger \sigma^- \sigma^+ a a^\dagger \sigma^- \sigma^+ b_i + b_i^\dagger \sigma^- \sigma^+ a a^\dagger \sigma^- \sigma^+ b_k) \\
&= \sum_{i \neq k} \frac{g_i^c g_i^T g_k^c g_k^T e^{-j(\Delta_i + \Delta_i^c - \Delta_k - \Delta_k^c)t}}{\Delta_i (\Delta_i + \Delta_i^c)(\Delta_i + \Delta_i^c - \Delta_k)(\Delta_i + \Delta_i^c - \Delta_k - \Delta_k^c)} \\
&\quad \frac{1 - \sigma_i^z}{2} (b_k^\dagger b_i + b_i^\dagger b_k) a a^\dagger \\
&\overset{(1)}{=} jt \frac{g^{c,2} g^{T,2}}{\Delta^2 (\Delta + \Delta^c)} (a^\dagger a + 1) \sum_{i \neq k} \frac{1 - \sigma_i^z}{2} (b_i^\dagger b_k + b_i b_k^\dagger) \\
&\overset{(2)}{=} jt \frac{g^{c,2} g^{T,2}}{\Delta^2 (\Delta + \Delta^c)} (a^\dagger a + 1) \sum_{i \neq k} (b_i^\dagger b_k + b_i b_k^\dagger)
\end{aligned} \tag{4.67}$$

3) $\mathrm{TLR}_i \leftrightarrow \mathrm{q}_i \leftrightarrow \mathrm{TLR}_i \leftrightarrow \mathrm{q}_i \leftrightarrow \mathrm{TLR}_i$

$$\begin{aligned} U^{TqTqT(4)} &= jt \sum_i \frac{g_i^{T,4}}{\Delta_i^3} b_i^\dagger \sigma_i^- \sigma_i^+ b_i b_i^\dagger \sigma_i^- \sigma_i^+ b_i \\ &= jt \sum_i \frac{g_i^{T,4}}{\Delta_i^3} \frac{1-\sigma_i^z}{2} b_i^\dagger b_i b_i^\dagger b_i \\ &\overset{(1)}{=} jt \frac{g_i^{T,4}}{\Delta_i^3} \sum_i \frac{1-\sigma_i^z}{2} b_i^\dagger b_i b_i^\dagger b_i \\ &\overset{(2)}{=} jt \frac{g_i^{T,4}}{\Delta_i^3} \sum_i b_i^\dagger b_i b_i^\dagger b_i \end{aligned} \tag{4.68}$$

Again, under the above assumptions (1) and (2), pick up the diagonal terms

$$\begin{aligned} \mathrm{img}\{U^{diag}\} = {} & jt \frac{g^{c,2}}{\Delta^c} N a^\dagger a - jt \frac{g^{T,2}}{\Delta} \sum_i b_i^\dagger b_i \\ & + jt \frac{g^{c,2} g^{T,2}}{\Delta^2(\Delta+\Delta^c)} \sum_i b_i^\dagger b_i (a^\dagger a + 1) + jt \frac{g_i^{T,4}}{\Delta_i^3} \sum_i b_i^\dagger b_i b_i^\dagger b_i \end{aligned} \tag{4.69}$$

and

$$\mathrm{real}\{U^{diag}\} = -t^2 J^2 \sum_i b_i^\dagger b_i \tag{4.70}$$

and coupling terms with oscillation frequency $\omega \ll \min\{\Delta_i, \Delta_i^c\}$,

$$\begin{aligned} \mathrm{img}\{U^{osc}\} = {} & jtJ \sum_i (b_i b_{i+1}^\dagger + b_i^\dagger b_{i+1}) + \frac{g^c g^T}{\Delta(\Delta+\Delta^c)} e^{-jt(\Delta+\Delta^c)} \sum_i (b_i a^\dagger + b_i^\dagger a) \\ & + jt \frac{g^{c,2} g^{T,2}}{\Delta^2(\Delta+\Delta^c)} (a^\dagger a + 1) \sum_{i \neq k} (b_i^\dagger b_k + b_i b_k^\dagger) \end{aligned} \tag{4.71}$$

and

$$\mathrm{real}\{U^{osc}\} = -\frac{g^T J}{\Delta^2} \sum_i (\sigma_i^- b_{i+1}^\dagger + \sigma_i^+ b_{i+1})(b_i^\dagger b_i + 1). \tag{4.72}$$

Collecting the imaginary terms to get effective Hamiltonian without driving

$$
\begin{aligned}
V^{eff} &= \frac{g^{c,2}}{\Delta^c} N a^\dagger a + \frac{g^{T,2}}{\Delta} \sum_i b_i^\dagger b_i + J \sum_i (b_i b_{i+1}^\dagger + b_i^\dagger b_{i+1}) \\
&+ \frac{g^{c,2} g^{T,2}}{\Delta^2(\Delta+\Delta^c)} \sum_i b_i^\dagger b_i (a^\dagger a + 1) + \frac{g^c g^T}{\Delta(\Delta+\Delta^c)} e^{-jt(\Delta+\Delta^c)} \sum_i (b_i a^\dagger + b_i^\dagger a) \\
&+ \frac{g^{c,2} g^{T,2}}{\Delta^2(\Delta+\Delta^c)} (a^\dagger a + 1) \sum_{i \neq k} (b_i^\dagger b_k + b_i b_k^\dagger) + \frac{g_i^{T,4}}{\Delta_i^3} \sum_i b_i^\dagger b_i b_i^\dagger b_i. \qquad (4.73)
\end{aligned}
$$

Now the total effective Hamiltonian

$$
\begin{aligned}
H^{eff} &= H^0 + V^{eff} + D \\
&= (\omega^c + \frac{g^{c,2}}{\Delta^c} N) a^\dagger a + (\omega^T + \frac{g^{T,2}}{\Delta}) \sum_i b_i^\dagger b_i \\
&+ J \sum_i (b_i b_{i+1}^\dagger + b_i^\dagger b_{i+1}) + \frac{g^{c,2} g^{T,2}}{\Delta^2(\Delta+\Delta^c)} (a^\dagger a + 1) \sum_{i \neq k} (b_i^\dagger b_k + b_i b_k^\dagger) \\
&+ \frac{g^{c,2} g^{T,2}}{\Delta^2(\Delta+\Delta^c)} \sum_i b_i^\dagger b_i (a^\dagger a + 1) + \frac{g_i^{T,4}}{\Delta_i^3} \sum_i b_i^\dagger b_i b_i^\dagger b_i \\
&+ \frac{g^c g^T}{\Delta(\Delta+\Delta^c)} e^{-jt(\Delta+\Delta^c)} \sum_i (b_i a^\dagger + b_i^\dagger a) \\
&+ \epsilon(t)(a^\dagger e^{-i\omega^d t} + a e^{i\omega^d t}) \qquad (4.74)
\end{aligned}
$$

Move into rotating frame using unitary transformation $U = \exp\{j\omega^d t(a^\dagger a + \sum_i b_i^\dagger b_i)\}$, we gets

$$
\begin{aligned}
\widetilde{V}^{eff} &= \Delta^{cd} a^\dagger a + \Delta^{Td} \sum_i b_i^\dagger b_i + \frac{g^{c,2} g^{T,2}}{\Delta^2(\Delta+\Delta^c)} \sum_i b_i^\dagger b_i \\
&+ J \sum_i (b_i b_{i+1}^\dagger + b_i^\dagger b_{i+1}) + \frac{g^{c,2} g^{T,2}}{\Delta^2(\Delta+\Delta^c)} (a^\dagger a + 1) \sum_{i \neq k} (b_i^\dagger b_k + b_i b_k^\dagger) \\
&+ \frac{g^{T,4}}{\Delta^3} \sum_i b_i^\dagger b_i b_i^\dagger b_i + \frac{g^{c,2} g^{T,2}}{\Delta^2(\Delta+\Delta^c)} a^\dagger a \sum_i b_i^\dagger b_i \\
&+ \frac{g^c g^T}{\Delta(\Delta+\Delta^c)} e^{-jt(\Delta+\Delta^c)} \sum_i (b_i a^\dagger + b_i^\dagger a) + \epsilon(t)(a^\dagger + a) \qquad (4.75)
\end{aligned}
$$

(Check if there are only $-\omega^d$ in the first two terms) where $\Delta^{cd} = \omega^c + \frac{g^{c,2}}{\Delta^c} N - \omega^d$ and $\Delta^{Td} = \omega^T + \frac{g^{T,2}}{\Delta} - \omega^d$. Different terms in this Bose-Hubbard Hamiltonian are photons in cooling cavity, photons in TLRs, hopping between neighbour sites of TLRs, fourth order correction to photon

numbers in TLRs, fourth order coupling between different sites of TLRs (not necessarily to be neighbors), interaction between on-site photons, cross-Kerr term between cooling cavity and TLRs.

Simplify the interaction Hamiltonian,

$$\begin{aligned}\widetilde{V}^{eff} &= \Delta^{cd} a^\dagger a + \Gamma_{ik} \sum_{i,k} (b_i^\dagger b_k + b_i b_k^\dagger) + \Upsilon_{ik} a^\dagger a \sum_{i,k} b_i^\dagger b_k \\ &+ \Theta_i \sum_i b_i^\dagger b_i b_i^\dagger b_i + \epsilon(t)(a^\dagger + a) + \Omega e^{-jt(\Delta+\Delta^c)} \sum_i (b_i a^\dagger + b_i^\dagger a) \end{aligned} \tag{4.76}$$

where

$$\begin{aligned}\Gamma_{ik} &= \begin{cases} \left(\Delta^{Td} + \frac{g^{c,2} g^{T,2}}{\Delta^2(\Delta+\Delta^c)}\right)/2, \text{ when } i = k \\ \left(J + \frac{g^{c,2} g^{T,2}}{\Delta^2(\Delta+\Delta^c)}\right), \text{ when } i \neq k \end{cases} \\ \Upsilon_{ik} &= \frac{g^{c,2} g^{T,2}}{\Delta^2(\Delta+\Delta^c)} \\ \Theta &= \frac{g^{T,4}}{\Delta^3} \\ \Omega &= \frac{g^c g^T}{\Delta(\Delta+\Delta^c)}. \end{aligned}$$

Asume the photon in the LRC circuit decays fast, so resonant photon number in cooling cavity $N^c = \left\langle a^\dagger a \right\rangle = 0$. Hence the cross-Kerr term in the effective Hamiltonian is eliminated

$$\begin{aligned}\widetilde{H}^{eff} &= \Gamma_{ik} \sum_{i \neq k} (b_i^\dagger b_k + b_i b_k^\dagger) + \frac{g_i^{T,4}}{\Delta_i^3} \sum_i b_i^\dagger b_i b_i^\dagger b_i \\ &+ \epsilon(t)(a^\dagger + a) + \Omega e^{-jt(\Delta+\Delta^c)} \sum_i (b_i a^\dagger + b_i^\dagger a) \end{aligned} \tag{4.77}$$

This Hamiltonian has the same form as equation (4.28) following the same method as the first circuit, by separating $a^\dagger$ into a summation of quantum $\Lambda^\dagger$ and classical term $\overline{A}$, we get cooling term $\overline{A}\Lambda^\dagger \sum_{m,n=1}^4 \eta_{mn} B_m^\dagger B_n$ out of the Hamiltonian (4.77). Again, the physical meaning of $\overline{A}\Lambda^\dagger \sum_{m,n=1}^4 \eta_{mn} B_m^\dagger B_n$ is that driving signal turns into resonant photon in cooling cavity by absorbing energy from the array of TLRs and meanwhile maintain the total photon numbers in TLR array. Note that the rotating factor $e^{-jt(\Delta+\Delta^c)}$ can be eliminated by choosing appropriate detunings. And advantage of the second scheme is that the effective coupling between TLR and cooling cavity can be controlled via tunable qubit energy. This may be a better experimental design to optimize cooling rate!

It is necessary to point out that that we have asumed the coupling strength between the cooling cavity and all the on-site SQUIDs are uniform. This is hard for a long array of TLRs. But we can take the advantage of the tunability of SQUID and compensate the periodicity of coupling strength by changing magnetic bias on each SQUID. Further, we are going to discuss

the case when only the two ending sites are coupled to the cooling cavity, which is much easier to realize by putting these two site at simmetric location in the cavity.

4.3.4 Work To Do for the next step

4.3.4.1 A more accurate theory to obtain cooling term

Notice that the approach we get here has made a lot of assumptions, including critical ones

$$\epsilon(a^\dagger + a) \approx \epsilon M_{00}(A^\dagger + A) \tag{4.78}$$

$$\left\langle a^\dagger a \right\rangle = 0 \tag{4.79}$$

For the first assumption, a direrct three-wave mixing derivation will be present to obtain the cooling term $\varkappa\Lambda^\dagger\overline{A}\Xi$, where Ξ is the creation operator of collective mode of the TLR array and $\varkappa$ is the cooling rate. The second assumption is actually not true because in a cavity-assisted cooling, the cooling cavity has a high quality factor. However referring to steady photon state in the cooling cavity, one can define a relative photon operator $\alpha = a - \langle a \rangle$, therefore the fluctuations of photon number in the cooling cavity $\left\langle \alpha^\dagger \alpha \right\rangle = 0$. We can expect the fundamental physics doesn't change but a different form of cooling strength might be obtained for the second scheme. Hence, a further adjustment using $\alpha = a - \langle a \rangle$ to the derivation the cooling rate will be made.

4.3.4.2 Numerical estimation of cooling rate

Fermion golden rule will be applied to solve for analytical form of cooling rate. Experimental parameters will be applied. I will need to play with different values of quality factor Q and detuning Δ^c in order to optimize cooling rate.

4.4 Simulator of a spin-1 array

4.4.1 XX coupling

Notice that by adjusting bias current on phase qubit, we can make $\zeta \to 0$ and the same time keep three levels in the washboard potential, so that the capacitive coupling matrix becomes $(a^\dagger + a) \approx \begin{bmatrix} 0 & 1 & 0 \\ 1 & 0 & 1.414 \\ 0 & 1.414 & 0 \end{bmatrix}$ (see EIT section). Define it as S_x. Suppose that there is a chain

of phase qubits coupled with capacitors, hamiltonian of which is:

$$\frac{H_{XX}}{\hbar} = \sum_{j=1}^{N} \sum_{n=g,a,b} \omega_n^j a^{j\dagger} a^j + g_c \sum_{j=1}^{N-1} (a^{j\dagger} + a^j)(a^{j+1\dagger} + a^{j+1}) \tag{4.80}$$

$$= \sum_{j=1}^{N} \sum_{n=g,a,b} \omega_n^j S_n^j + g_c \sum_{j=1}^{N-1} S_x^j S_x^{j+1}. \tag{4.81}$$

Here capacitive coupling strength between two sites $g_c = e^2/C_1C_2E_c$. The first term is from on-site three level phase qubit, which can be treated as spin {-1,0,1} respectively.

$$S_g^j = \begin{bmatrix} -1 & 0 & 0 \\ 0 & 0 & 0 \\ 0 & 0 & 0 \end{bmatrix}, S_a^j = \begin{bmatrix} 0 & 0 & 0 \\ 0 & 1 & 0 \\ 0 & 0 & 0 \end{bmatrix}, S_b^j = \begin{bmatrix} 0 & 0 & 0 \\ 0 & 0 & 0 \\ 0 & 0 & 1 \end{bmatrix}, \tag{4.82}$$

and $\omega_{ga} = \omega_a - \omega_g, \omega_{ab} = \omega_b - \omega_a$ are defined as previous sections. Let $S_z^j = \begin{bmatrix} -1 & 0 & 0 \\ 0 & 0 & 0 \\ 0 & 0 & 1-s \end{bmatrix}$, where s is a nonlinear factor $s = (\omega_{ab} - \omega_{ga})/\omega_{ga}$. In this case, the hamiltonian can be simplified as

$$\frac{H_{XX}}{\hbar} = \sum_{j=1}^{N} \sum_{n=-1,0,1} \omega_0^j S_z^j + g_c \sum_{j=1}^{N-1} S_x^j S_x^{j+1}. \tag{4.83}$$

It has to be noted that S_x and S_z don't satisfy Lie Group's commutator rules.(more math-

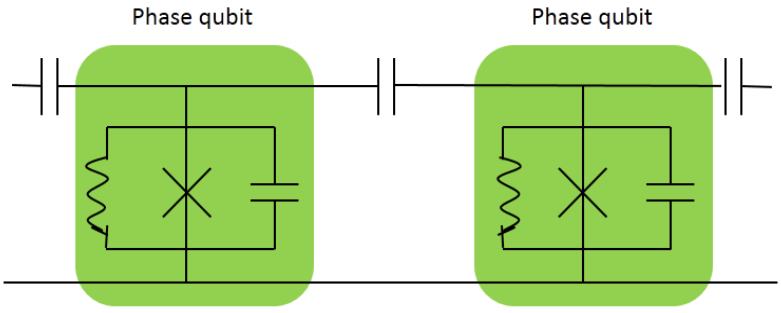

Figure 4.13: A chain of phase qubits coupled with capacitors.

4.4.2 XXZ coupling

Replace the capacitor with a loop SQUID and get a coupling hamiltonian $H^{j,j+1}_{couple}/\hbar = g_c(a^{j\dagger}+a^{j})(a^{j+1\dagger}+a^{j+1}) - g_i(a^{j\dagger}-a^{j})(a^{j+1\dagger}-a^{j+1})$,where $g_i = 4E_J\cos(\frac{\phi_e}{2})$ is inductive coupling strength between two sites and can be tuned by controlling the magnetic bias ϕ_e. Rewrite the hamiltonian into $\{S^{j}_{x,y,z}\}$ form.

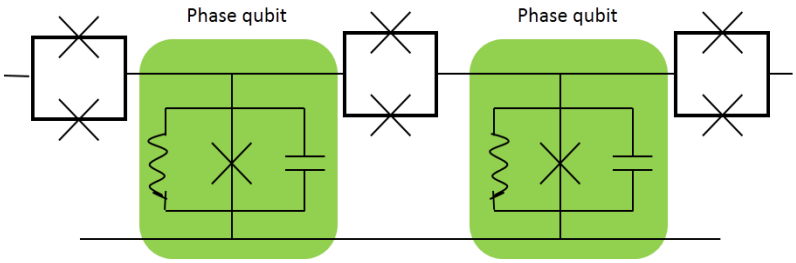

Figure 4.14: A chain of phase qubits coupled with SQUID

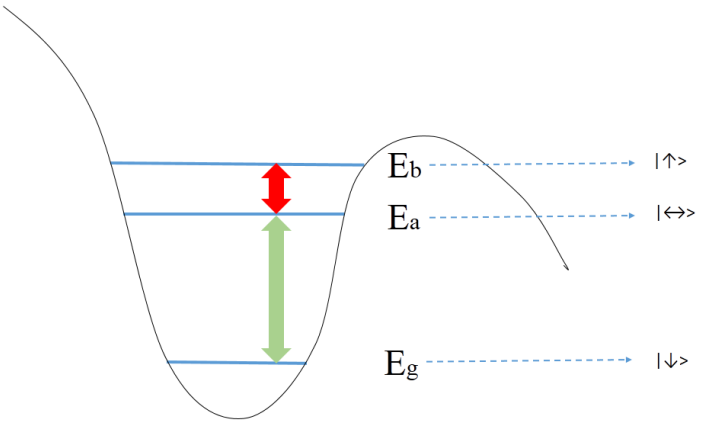

Figure 4.15: Three level structure of a phase qubit is shown. The three levels can be treated as Spin 1,0,-1 states respectively.

Chapter 5

Superconducting resonator coupled to other oscillators

In this Chapter, I am going to explore the theory of a superconducting resonator coupled to different types of AC signal, including electrical, flux and mechanical oscillators. Hamiltonians are derived. The general formalism give rises to different regime of physical effect which reconcile with reported experiments. The initial motivation of this work was to study a parametric amplifier of gravitational wave in quantum limit, using superconducting circuit. The theory derived in this chapter, however, works for various system. Some future research could be pursued based on the formalism established here.

5.1 Parametric oscillator in superconducting cavity

In Chapter 3, we introduced superconducting transmission line resonator (TLR). When the two ends of TLR are capacitively coupled to external leads, one gets boundary condition for time independent solution are $V(0) = V(D)$ and $\frac{\partial}{\partial x}V(x)\mid_{x=0} = \frac{\partial}{\partial x}V(x)\mid_{x=D}$. Here D is effective electrical length of the TLR. By solving Schrödinger equation, we get the static solutions with separate energy levels, [73] which means standing waves of Cooper pair density arises in TLR. The time independent part is depicted in Fig.5.1(a). This generates standing wave of radio frequency photons between TLR and substrates, and becomes one dimensional cavity. Only considering fundamental mode with resonant frequency ω_0^r, TLR has quantized Hamiltonian

$$H_0 = \omega_0^r(a^\dagger a + \frac{1}{2}) \tag{5.1}$$

Assuming the capacitance and inductance per unit length of the resonator are c and l, we get $\omega_0^r = \frac{2\pi}{D\sqrt{cl}}$. The reason we use unit length values of capacitance and inductance instead of net values is based on the assumption that the mechanical motion at one end doesn't change the bulk property of the circuit.

Let's now consider a transmission line resonator with one end electrically coupled to a small AC voltage signal, so the amplitude of electric potential at that end $V(D) = V_d \cos\omega t$,

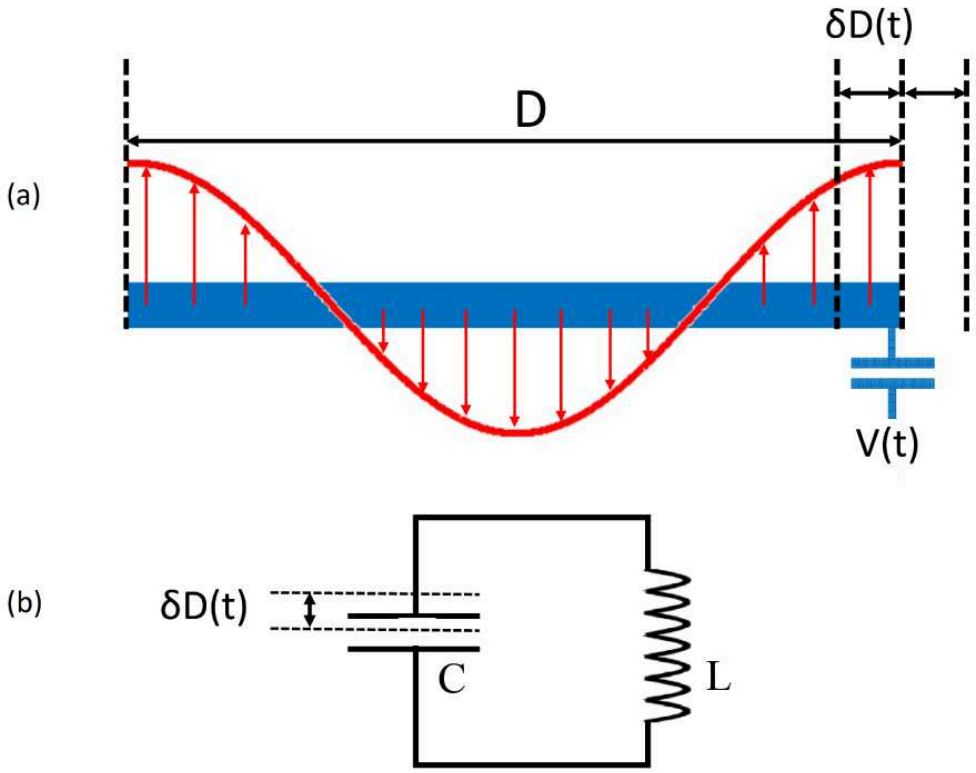

Figure 5.1: (a) A transmission line resonator with one end coupled to an AC signal. (b) An schematic LC circuit. The upper plate of the capacitor is movable and driven by mechanical motion $\delta D(t)$.

see Fig.5.1(a). The driving signal changes the potential value at one end, equivalently changes TLR's effective electrical length $D \to D + \delta D(t)$. Hence the boundary condition under driving takes the new form

$$\begin{cases} V(0) = V(D + \delta D) \\ \frac{\partial}{\partial x} V(x) \mid_{x=0} = \frac{\partial}{\partial x} V(x) \mid_{x=D+\delta D} = 0 \end{cases}$$

Because what changes here is effective boundary condition but the TLR doesn't change mechanically, so the capacitance and inductance per unit length of TLR stays the same. Asume the driving is slow $\omega \ll \omega_0^r$, we have following consequences. The first is that driving signal is too slow to change TLR's static ground state, so we can expect at every instance, the amplitude of electrical potential at the end D takes this form

$$V(D) = V_0 - |V_d \cos \omega t| \tag{5.2}$$

Let $V(D) = V_0 - V_0 \sin \theta(t)$, where V_0 is the voltage amplitude of the ground state standing wave

in TLR. Instant phase at the end D

$$\theta(t) = 2\pi\frac{\delta D(t)}{D} \tag{5.3}$$

and $\theta \in [-\frac{\pi}{2}, \frac{\pi}{2}]$. Without loss of generality, we can assume $\omega t \in [-\frac{\pi}{2}, \frac{\pi}{2}]$ to get rid of the absolute sign in Eq.(5.2), hence

$$\theta(t) = \sin^{-1}(\frac{V_d}{V_0}\cos\omega t) \tag{5.4}$$

Note that the instant resonant frequency $\omega^r(t)$ is a function for electrical length

$$\begin{aligned}\omega^r(t) &= \frac{2\pi}{D\sqrt{cl}}\frac{1}{1+\delta D(t)/D} \\ &= \frac{2\pi}{D\sqrt{cl}}[1-\frac{\delta D(t)}{D}+O(\frac{\delta D^2(t)}{D^2})]\end{aligned}$$

In the weak signal regime, $V_d \ll V_0$, $\delta D/D \ll 1$, we keep the lowest order of $\frac{\delta D(t)}{D}$ and $\sin\theta(t) \approx \theta(t)$. Plug in with Eq.(5.3) and (5.4) we get

$$\begin{aligned}\omega^r(t) &\approx \omega_0^r(1-\frac{V_d\cos\omega t}{2\pi V_0}) \\ &= \omega_0^r - \omega_0^r\frac{V_d}{2\pi V_0}\cos\omega t \\ &= \omega_0^r - \frac{\omega_0^r}{4\pi V_0}V_d(e^{i\omega t}+e^{-i\omega t}) \\ &= \omega_0^r - \frac{\omega_0^r}{4\pi V_0}(\widetilde{V}_d+\widetilde{V}_d^*)\end{aligned}$$

where $\widetilde{V}_d = V_d e^{i\omega t}$. When the AC signal is in quantum limit classical variable $\widetilde{V}_d$ needs to be quantized and replaced with operator $\widehat{V}_d^\dagger = d^\dagger e^{i\omega_d t}$. So the instant resonant frequency is a function of AC signal

$$\begin{aligned}\omega^r(t) &= \omega_0^r - \frac{\omega_0^r}{4\pi V_0}(\widehat{V}_d^\dagger+\widehat{V}_d) \\ &= \omega_0^r - \frac{\omega_0^r}{4\pi V_0}(d^\dagger e^{i\omega_d t}+de^{-i\omega_d t})\end{aligned} \tag{5.5}$$

Plug this instant resonant frequency into TLR Hamiltonian Eq.(5.1), we obtain the TLR Hamil-

tonian with coupling to small AC signal as following

$$\begin{aligned} H &= \omega_0^r[1 - \frac{V_d}{2\pi V_0}(de^{-i\omega t} + d^\dagger e^{i\omega t})]a^\dagger a \\ &= \omega_0^r a^\dagger a - \frac{\omega_0^r V_d}{2\pi V_0} a^\dagger a(de^{-i\omega t} + d^\dagger e^{i\omega t}) \\ &= H_0 + H_{int}. \end{aligned}$$

The interaction between transmission line and driving

$$H_{int} = \chi a^\dagger a(de^{-i\omega_d t} + d^\dagger e^{i\omega_d t}) \tag{5.6}$$

where coupling strength $\chi = -\frac{\omega_0^r V_d}{2\pi V_0}$. Since number operator $n = a^\dagger a$, so interaction hamiltonian has a classical form as $H_{int}\tilde{}QV$, which can be interpreted as electrical potential energy.

ω_0^r for a TLR is usually in the range of GHz, since $\omega \ll \omega_0^r$, we can expect ω to be in the range of KHz to MHz. We know that mechanical oscillation could be in this range (citation). Hence we can expect that if red-detuned driving field is sent into the resonator, it will absorb the low frequency AC signal and turns into resonant photon in the cavity. In this way, weak low frequency signal ω can be detected in a three wave mixing way. Alternatively, sideband cooling, squeezing or heating up the signal source can be implemented.

It's worthful to note that this formalism works not only for a cavity but also works for LC circuit which has fundamental mode with resonant frequency ω_0^r. Also, the physical cause of small AC signal can be an capacitive antenna or inductive antenna, where the signal becomes magnetic flux $\phi(t) = \phi_d \cos \omega t$. This AC flux signal is just going to change the boundary condition like the way electrical signal does. Modeling of an AC signal at one end of the resonator has been examined by experiment. [194]

5.2 Superconducting cavity coupled to mechanical oscillator

5.2.1 Quantum LC circuit coupled to acoustic mode

Now we consider another configuration which is showed in K. W. Lehnert's paper [195]. Now we consider the circuit shown in Fig.5.1(b), instead of a cavity, a superconducting LC resonator is formed of a big inductance connected to a capacitor, one plate of which is movable. The typical frequency of the mechanical motion of this plate is from KHz to MHz. Let's study the Hamiltonian formalism of the quantum system including electrical oscillation in the superconducting LC circuit and mechanical oscillation on the moving plate of the capacitor. For simplicity and without loss of generality, we treat the capacitor as two parallel plates, so $C = \frac{\varepsilon A}{D}$, where D is the distance between two plates and A is the plate area. The mechanical vibration causes change of $\delta D(t)$, so the modulated capacity $C = \frac{\varepsilon A}{D+\delta D}$, and the resonant frequency of the LC circuit $\omega_0 = \frac{2\pi}{\sqrt{LC}}$. Assume vibration is small compare to the total distance between the two plates $\delta D \ll D$, so we can expand modulated frequency ω_{mod} in terms of $\Delta_d = \delta D/D$ and keep

the first order term

$$\begin{aligned}\omega_{\text{mod}}(t) &= \frac{2\pi}{\sqrt{LC(t)}} \\ &= \frac{2\pi}{\sqrt{L\frac{\varepsilon A}{D}}}\sqrt{1+\Delta_d} \\ &= \omega_0[1+\frac{1}{2}\Delta_d + O(\Delta_d^2)] \\ &\approx \omega_0(1+\Delta_d/2) \end{aligned} \tag{5.7}$$

Without loss of generality we can assume the mechanical vibration is cosinusoidal $\Delta_d(t) = 2\Delta\cos(\omega_m t)$. Consequently, the hamiltonian of the LC circuit becomes

$$H = \omega_{r0}(a^\dagger a + \frac{1}{2})(1+\Delta\cos(\omega_m t)) \tag{5.8}$$

Furthermore, the quantized Hamiltonian is

$$\begin{aligned} H &= \omega_{r0}(a^\dagger a + \frac{1}{2})[1+\Delta(d^\dagger e^{i\omega_m t} + de^{-i\omega_m t})] \\ &= \omega_{r0}(a^\dagger a + \frac{1}{2}) + \Delta\omega_{r0}a^\dagger a(d^\dagger e^{i\omega_m t} + de^{-i\omega_m t}) \end{aligned} \tag{5.9}$$

The second term $\Delta\omega_{r0}a^\dagger a(d^\dagger e^{i\omega_m t} + de^{-i\omega_m t})$ indicates a interaction Hamiltonian similar as Eq.(5.6) in previous section.

5.2.2 General theory of Superconducting cavity coupled to mechanical oscillator

Again, the mechanical oscillator is coupled to the the capacity of a superconducting cavity. This can be achieved in different ways, such as the way in previous subsection, or as the way in Fig.5.2(a), where one end of a 3D superconducting cavity is a movable piston connected with a mechanical oscillator, etc. The idea is to make the mechanical oscillator modulates collective capacitance of the cavity. Without loss of generality, the capacitance can be always modeled as a double plate capacitor and the effective circuit hence can be modeled again as Fig.5.1(b). In this subsection we proceed the theory to general case in cluding different frequency regions of the mechanical signal.

We start with a general Hamiltonian of the quantum LC circuit before quantization

$$H = \frac{C}{2}\dot{\phi}^2 + \frac{1}{2L(2e)^2}\phi^2 \tag{5.10}$$

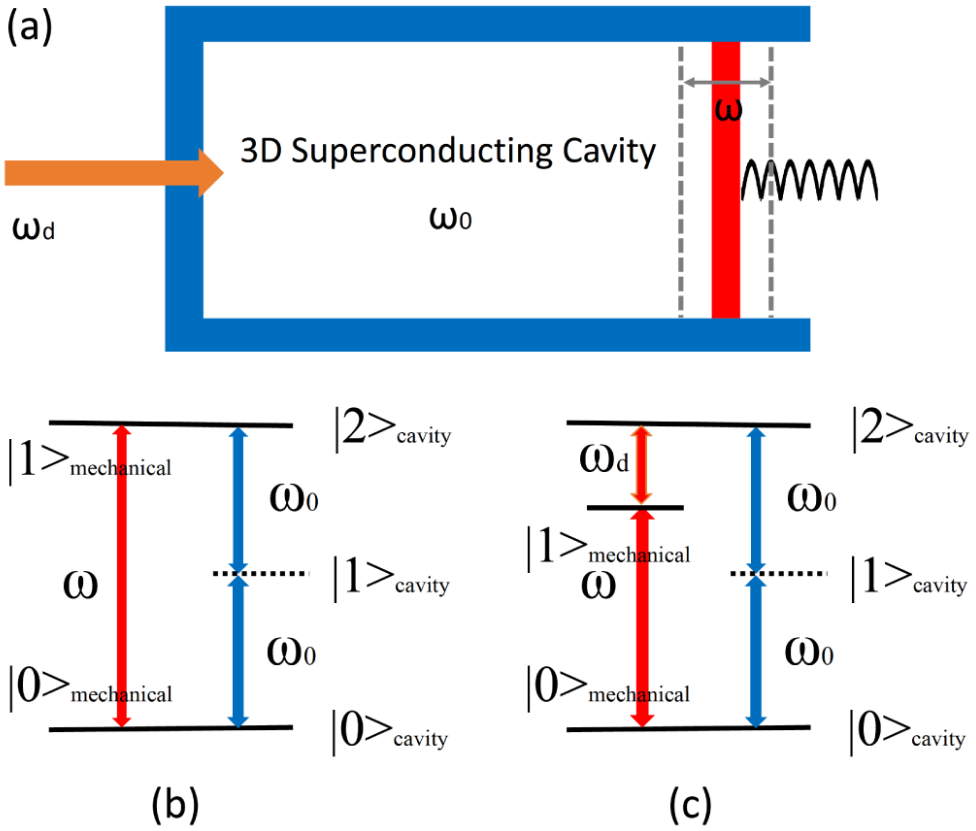

Figure 5.2: (a) A 3D superconducting cavity with one end coupled to mechanical oscillator. (b) Three wave mixing scheme when $\omega = 2\omega^0$. (c) Four wave mixing scheme when $\omega \neq 2\omega^0$.

By quantizing the Hamiltonian using Cooper pair number operator $N = C^2\dot{\phi}^2/(2e)^2$,

$$H^0 = \frac{(2e)^2}{2C}N^2 + \frac{1}{2L(2e)^2}\phi^2 \tag{5.11}$$

$$= \frac{1}{2}E_cN^2 + \frac{1}{2}E_L\phi^2 \tag{5.12}$$

where charge energy $E_c = \frac{(2e)^2}{C}$ and inductive energy $E_L = \frac{1}{L(2e)^2}$. Because capacitor is coupled to mechanical oscillator, the movable plate gives rise to a modulated distance between two plates $D(t) = D(1 + \Delta_d \cos\omega t)$. The capacitive energy becomes

$$E_c(t) = \frac{(2e)^2}{C} = \frac{(2e)^2}{\varepsilon A/D(t)} = \frac{(2e)^2}{\varepsilon A/D}(1 + \Delta_d \cos\omega t) = E_c(1 + \Delta_d \cos\omega t) \tag{5.13}$$

Hence, capacitively coupling to a mechanical oscillator, the Hamiltonian (5.11) becomes

$$\begin{aligned} H &= \frac{1}{2}E_c(1+\Delta_d\cos\omega t)N^2 + \frac{1}{2}E_L\phi^2 \\ &= \frac{1}{2}E_cN^2 + \frac{1}{2}E_L\phi^2 + \frac{1}{2}E_c\Delta_d\cos\omega t N^2 \\ &= H^0 + \frac{1}{2}E_c\Delta_d\cos\omega t N^2 \end{aligned} \tag{5.14}$$

Replacing with creation and annihlation operators

$$\begin{cases} N = \sqrt{\frac{\omega_0}{E_c}}(a+a^\dagger) \\ \phi = i\sqrt{\frac{\omega_0}{E_L}}(a-a^\dagger) \end{cases}$$

and quantized mechanical oscillator $\cos\omega t = d^\dagger + d$, we get

$$H = \omega^0(aa^\dagger + a^\dagger a) + \frac{1}{2}\omega^0\Delta_d(d^\dagger+d)(a^\dagger+a)^2 \tag{5.15}$$

$$= H^0 + H^{int} \tag{5.16}$$

where resonant frequency in the cavity $\omega^0 = 2\pi\sqrt{E_cE_L}$, interaction part $H^{int} = \frac{\chi}{2}(d^\dagger+d)(a^\dagger+a)^2$, and for convenience $\hbar$ has been set to 1. In order to study different coupling regime we need to expand H^{int}

$$\begin{aligned} H^{int} &= \chi(d^\dagger+d)(a^\dagger+a)^2 \\ &= \chi(d^\dagger a^{\dagger 2} + d^\dagger aa^\dagger + d^\dagger a^\dagger a + d^\dagger a^2 + da^{\dagger 2} + daa^\dagger + da^\dagger a + da^2) \\ &= \chi(d^\dagger a^{\dagger 2} + d^\dagger aa^\dagger + d^\dagger a^\dagger a + d^\dagger a^2 + h.c.) \end{aligned} \tag{5.17}$$

Write it in Heisenburg picture with $d \to de^{-i\omega t}$ and $a \to ae^{-i\omega^0 t}$

$$\widetilde{H}^{int} = \chi[e^{i(\omega+2\omega^0)t}d^\dagger a^{\dagger 2} + e^{i\omega t}d^\dagger aa^\dagger + e^{i\omega t}d^\dagger a^\dagger a + e^{i(\omega-2\omega^0)t}d^\dagger a^2 + h.c.] \tag{5.18}$$

For any frequency regime, with rotating wave approximation the fast rotating terms with frequency $(\omega + 2\omega^0)$ are always negligible.

$$\widetilde{H}^{int} \approx \chi[e^{i\omega t}d^\dagger(aa^\dagger + a^\dagger a) + e^{i(\omega-2\omega^0)t}d^\dagger a^2 + h.c.] \tag{5.19}$$

For acoustic mechanical oscillator $\omega \ll \omega^0$, rotating terms with frequency $(2\omega^0 - \omega)$ are fast rotating terms so they can be neglected. The Hamiltonian now becomes

$$H^{int} \approx \chi[d^\dagger(aa^\dagger + a^\dagger a) + h.c.] \tag{5.20}$$

which is exactly as the form (5.6) in previous discussion.

For high frequency mechanical oscillation when ω is at the order GHz. If $(\omega - 2\omega^0) \ll \omega$,

terms with frequency ω are fast rotating terms and hence negligible. The Hamiltonian now is

$$H^{int} \approx \chi[d^{\dagger}a^2 + da^{\dagger 2}] \tag{5.21}$$

In this Hamiltonian $da^{\dagger 2}$ indicates squeezing effect. If $\omega = 2\omega^0$, there arises three-wave mixing, where one mechanical phonon is mixed with two photons, and a mechanical quantum turns into two radio wave photons in superconducting cavity, as Fig.5.2(b). in this scheme, dynamical Casimir effect (citation) arises if starting from vacuum in the cavity. If $\omega \neq 2\omega^0$, one can send in a driving signal with frequency $\omega^d = |\omega - 2\omega^0|$, there arises a four wave mixing process, where with compensation of driving field, a phonon is turned into two photons in the cavity, as Fig.5.2(c).

5.3 Superconducting cavity coupled to EM wave via SQUID

Connect one end of the transmission line resonator with a SQUID as Fig.5.3(a). AC magnetic field is sent into SQUID $\phi_e(t) = \phi_d \sin \omega t$, which modulates boundary condition at this end, so it is expected to get similar effect as discussed in previous section. The interaction Hamiltonian can be obtained in a similar way but now it is the inductive part of Hamiltonian that is coupled to modulating signal. Consider the schematic circuit show in Fig.5.3(b). A LC quantum circuit connected with a SQUID giving a Hamiltonian

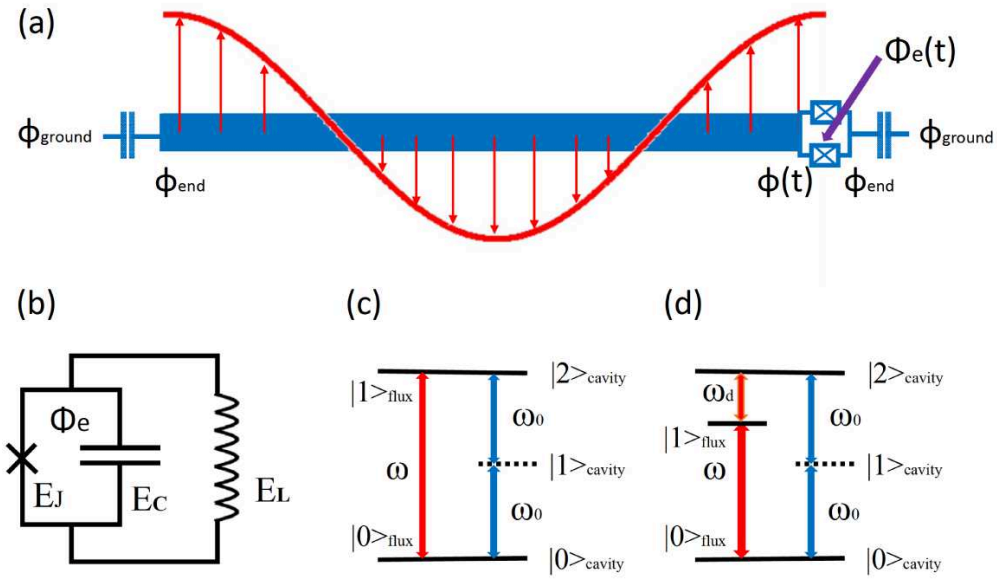

Figure 5.3: (a) A TLR has a SQUID at right end, with both sides open. Magnetic flux $\Phi_e(t)$ is sent into SQUID loop. Variable $\phi(t)$ is the gauge invariant phase at the left edge of SQUID. (b) Schematic circuit of (a). (c) Three wave mixing. (d) Four wave mixing.

$$
\begin{aligned}
H &= \frac{(C+C_J)}{2}\dot{\phi}^2 + 2E_J\cos\phi_e(1-\cos\phi) + \frac{1}{2L(2e)^2}\phi^2 \\
&= \frac{1}{2}E_c'N^2 + \frac{1}{2}E_L\phi^2 - 2E_J\cos\phi_e\cos\phi \\
&= \frac{1}{2}E_c'N^2 + \frac{1}{2}E_L\phi^2 - 2E_J\cos\phi_e[1-\frac{\phi^2}{2}+\frac{\phi^4}{4!}+O(\phi^4)] \\
&= \frac{1}{2}E_c'N^2 + \frac{1}{2}(E_L + 2E_J\cos(\phi_d\sin\omega t))\phi^2 - \frac{2}{4!}E_J\cos\phi_e\phi^4 + O(\phi^4)
\end{aligned} \tag{5.22}
$$

where $E_c' = \frac{(2e)^2}{C+C_J}$. Now from the generating function for Bessel functions, one obtains the Jacobi-Anger expansion

$$
\cos(\phi_d\sin\omega t) = \sum_{n=-\infty}^{\infty} J_n(\phi_d)\cos(n\omega t) \tag{5.23}
$$

where Bessel functions of the first kind $J_n(\phi_d) = \sum_{m=0}^{\infty}\frac{(-1)^m}{m!\Gamma(m+n+1)}(\frac{\phi_d}{2})^{2m+n}$. For weak driving, ϕ is trapped near the minimum $\phi \sim 0$, also $\phi_d/2\pi \ll 1$, so we can truncate $\cos\phi$ to second order and $\cos(\phi_d\sin\omega t)$ to

$$
\begin{aligned}
\cos(\phi_d\sin\omega t) &\approx \sum_{n=-\infty}^{\infty}(\frac{\phi_d}{2})^n\cos(n\omega t) \\
&\approx 1 + \frac{\phi_d}{2}\cos(\omega t)
\end{aligned} \tag{5.24}
$$

Therefore, the Hamiltonian becomes

$$
\begin{aligned}
H &= \frac{1}{2}E_c'N^2 + \frac{1}{2}[E_L + 2E_J + E_J\phi_d\cos(\omega t)]\phi^2 \\
&= \frac{1}{2}E_c'N^2 + \frac{1}{2}(E_L+2E_J)\phi^2 + \frac{1}{2}E_J\phi_d\cos(\omega t)\phi^2 \\
&= \frac{1}{2}E_c'N^2 + \frac{1}{2}E_L'\phi^2 + |g|\cos(\omega t)\phi^2 \\
&= \frac{1}{2}E_c'N^2 + \frac{1}{2}E_L'\phi^2 + (g^*e^{-i\omega t} + ge^{i\omega t})\phi^2
\end{aligned} \tag{5.25}
$$

where $E_L' = E_L + 2E_J$, $g = \frac{1}{2}E_J\phi_d$. Quantizing phase ϕ, N and AC signal $\cos(\omega t)$ as previous section

$$
\begin{aligned}
H &= \frac{1}{2}E_c'N^2 + \frac{1}{2}E_L'\phi^2 + g(d^\dagger + d)\phi^2 \\
&= \omega^0 a^\dagger a - \frac{1}{2}\omega_0\frac{E_J}{E_L}\phi_d(d^\dagger+d)(a^\dagger+a)^2 \\
&= \omega^0 a^\dagger a - \chi'(d^\dagger+d)(a^\dagger+a)^2
\end{aligned} \tag{5.26}
$$

where $\omega_0' = 2\pi\sqrt{E_c' E_L'}$, $\chi' = \frac{1}{2}\omega_0 \frac{E_J}{E_L'}\phi_d$. We get the same interaction as previous section. We apply rotating wave approximation to discuss different regimes.

Neglecting fast rotating terms with frequency $(\omega + 2\omega^0)$

$$\widetilde{H}^{int} \approx \chi'[d^\dagger(aa^\dagger + a^\dagger a) + d^\dagger a^2 + h.c.] \tag{5.27}$$

For low frequency signal, e.g. the time dependent AC circuit giving rise to AC magnetic field, $\omega \ll \omega^0$, rotating terms with frequency $(2\omega^0 - \omega)$ are fast rotating terms so they can be neglected. The Hamiltonian now becomes

$$H^{int} \approx \chi[d^\dagger(aa^\dagger + a^\dagger a) + h.c.] \tag{5.28}$$

This is not interesting for magnetic signal.

For microwave ω is at the order GHz. If $(\omega - 2\omega^0) \ll \omega$, terms with frequency ω are fast rotating terms and hence negligible. The Hamiltonian now is

$$H^{int} \approx \chi[d^\dagger a^2 + d a^{\dagger 2}] \tag{5.29}$$

In this Hamiltonian $da^{\dagger 2}$ indicates squeezing effect. If $\omega = 2\omega^0$, there arises three-wave mixing, where one mechanical phonon is mixed with two photons, and a mechanical quantum turns into two radio wave photons in superconducting cavity, as Fig.5.2(c). in this scheme, dynamical Casimir effect arises if starting from vacuum in the cavity. And actually Wilson, et al, has done an experiment [196] to verify dynamical Casimir effect based on this scheme. In order to enhance this nonlinearity, Lähteenmäki, et al., accomplished to couple a transmission line resonator with an array of dc-SQUIDs and observed dynamical Casimir effect. [194] Same interaction Hamiltonian was obtained in their paper. If $\omega \neq 2\omega^0$, one can send in a driving signal with frequency $\omega^d = |\omega - 2\omega^0|$, there arises a four wave mixing process, where with compensation of driving field, a phonon is turned into two photons in the cavity, as Fig.5.2(d).

Note that the coupling strength $\chi' = \frac{1}{2}\omega_0 \frac{E_J}{E_L'}\phi_d$ is not limited to $300MHz$, which is a typical coupling strength in latest circuit QED experiments. [73,81] This means that ultra-strong coupling beyond Jaynes-Cummings model can be studied in this type of system by directly connecting a superconducting resonator with Josephson junction devices, such as dc-SQUID.

Chapter 6

Summary and Future Work

In this dissertation, I have applied quantum circuit theory to model superconducting device. With the circuit model, I am able to study different designs and applications of superconducting circuit. Relating with qubits and decoherence, I have worked on an encoding method based on a universal quantum degeneracy point (UQDP). Working on UQDP, the encoded qubit is coupled to generic noise up to second order and the first order coupling is suppressed. Numerical simulation of the qubit in a noisy environment has demonstrate a two order of magnitude longer decoherence time and high fidelity for one-qubit and two-qubit gates. A possible implementation using superconducting circuit is discussed. This piece of work is covered in chapter 2. The UQDP with superconducting circuit includes a typical circuit geometry that gives rise to tunable four-level structure as an artificial atom. Connecting this structure with two different TLR and applying four-wave mixing method, I am able to get a parametric toolbox processing photon states of these two TLRs and implement circuit QED. Potentially, this scheme can be used to implement universal quantum computation by processing on-chip photons. The parametric toolbox includes universal set of two mode operations. This piece of work is covered in chapter 3. By coupling many sites of TLR with SQUID into an array, quantum computation or quantum simulation can be implemented. In chapter 4, I have studied sitewise manipulation induced Mott-insulator to superfluid transition using a quantum simulator based on this type of superconducting circuit. The critical point in microcanonical ensemble, solved with exact diagnolization numerical method, satisfies our mean field estimation. This type of coupling can be extended to 2D or 3D array. A photon preserving cooling scheme is proposed to study ground state of collective ground state in this simulator. In light of the quantum nature of a mesocopic or macroscopic size, one can use superconducting devices to detect and amplify weak quantum signals. In chapter 1, I proposed a superconducting Faraday cage to observe interference effect only due to scalar AB phase. External AC signal can drive internal circuit in a superconducting Faraday cage. Quantum jump in the internal state can be detected from the exterior surface in order to observe and demonstrate scalar AB effect. And in chapter 5, I studied parametric amplifier of mechanical signals using superconducting cavity. Using the same mechanism, dynamical Casimir effect has been observed.

Some future work based on my study during these years is summarized as following:

Flat band states simulator using 2D array of superconducting quantum circuit

We have demonstrated using circuit can simulate a two dimensional Bose-Hubbard model. We have also study different phases of two interacting photons in a saw-tooth type 2D lattice. Our numerical simulation of this system has shown flat band states. Also, this is robust against small un-uniformity of on-site energy and hopping strength between different sites. Same circuit topology can be applied to simulate Fermi-Hubbard model and obtain flat band states of fermions. The circuit ingredients are different from previous case. We borrowed reference [127]'s idea to encode Fermions with X-mon qubits and managed to engineer the total Hamiltonian of the simulated system to be encoded with X-mon qubits. This piece of work is being written and going to be submitted soon.

Cavity-assisted sideband cooling of an array of TLRs

The first step of this theory is present in Chapter 4. However, further work need to be done, for example, to apply Fermi-golden rule to obtain cooling rate and numerical estimations of cooling rate for different cooling schemes based on experimental parameters. This further work needs to be collaborated with an experimental group.

Also, I have made assumptions

$$\epsilon(a^\dagger + a) \approx \epsilon M_{00}(A^\dagger + A)$$
$$\left\langle a^\dagger a \right\rangle = 0$$

in the derivation of cooling. For the first assumption, a direrct three-wave mixing derivation will be present to obtain the cooling term $\varkappa \Lambda^\dagger \overline{A} \Xi$, where Ξ is the creation operator of collective mode of the TLR array and $\varkappa$ is the cooling rate. The second assumption is actually not true because in a cavity-assisted cooling, the cooling cavity has a high quality factor. However referring to steady photon state in the cooling cavity, one can define a relative photon operator $\alpha = a - \langle a \rangle$, therefore the fluctuations of photon number in the cooling cavity $\left\langle \alpha^\dagger \alpha \right\rangle = 0$. We can expect the fundamental physics doesn't change but a different form of cooling strength might be obtained for the second scheme. Hence, a further adjustment using $\alpha = a - \langle a \rangle$ to the derivation the cooling rate will be made.

Quantum simulator of spin-1 array

As the theory presented in the last section of Chapter 4, spin-1 atom can be simulated with phase qubits. Different types of coupling can be implemented as well. Therefore, one can build an array of these "atom"s or use them as coupler between spin-1/2 "atom"s, such as charge qubits, to get a universal quantum simulator.

Chapter 7

Appendix

7.1 Bloch's theorem for scalar potentials that are periodic in time

Consider the general case in which the potential energy inside the Faraday cages depicted in Figures 1 and 5 satisfy the periodicity condition in time

$$U(t+T) = U(t) \tag{7.1}$$

where the period $T = 2\pi/\omega$ is that of an arbitrary periodic waveform generator that replaces the sine-wave generators in Figures 1 and 5. Then it is apparent that this temporal periodicity condition is mathematically identical to the spatial periodicity condition

$$U(x+a) = U(x) \tag{7.2}$$

that applies to a 1D crystalline lattice with a lattice constant a.

Bloch's theorem [197] then tells us that the wavefunction inside the 1D crystalline lattice is given by

$$\psi(x) = e^{ipx/\hbar} u_p(x) \tag{7.3}$$

where p is the "crystal momentum" or "quasi-momentum", and where

$$u_p(x+a) = u_p(x) \tag{7.4}$$

is a periodic function of x within the spatial crystalline lattice.

Similarly, the temporal version of Bloch's theorem (also known as "Floquet's theorem") is given by

$$\psi(t) = e^{-iEt/\hbar} u_E(t) \tag{7.5}$$

where E is the "crystal energy" or "quasi-energy" [198] [199], and where

$$u_E(t+T) = u_E(t) \tag{7.6}$$

is a periodic function of t within a certain "temporal crystalline lattice." [200] (We have sup-

pressed the spatial dependence of the wavefunction $\psi(t)$ and of the periodic function $u_E(t)$ as being understood in (7.5). This also applies to all of the following expressions for $\psi(t)$ and $u_E(t)$). Both the "crystal momentum" and the "crystal energy" are *physically observable quantities* that obey *conservation laws*, because of the discrete translational symmetry of the crystalline systems in x and in t, respectively, which follow from the translational symmetry of (7.1) and (7.2).

Since $u_E(t)$ is a periodic function of time with a period T, it can be expanded by Fourier's theorem into a Fourier series expansion

$$u_E(t) = \sum_{n=-\infty}^{+\infty} c_n \exp(-in\omega t) \tag{7.7}$$

where c_n are the Fourier coefficients of $u_E(t)$, and where $\omega = 2\pi/T$ is the frequency of periodic charge waveform $Q(t)$ that is being injected onto the surface of the Faraday cage in Figures 1 and 5 by the arbitrary periodic waveform generator. Substituting (7.7) into (7.5), one finds that

$$\begin{aligned} \psi(t) &= \sum_{n=-\infty}^{+\infty} c_n \exp(-i(E + n\hbar\omega)t/\hbar) \\ &= \sum_{n=-\infty}^{+\infty} c_n \exp(-iE_n t/\hbar) \end{aligned} \tag{7.8}$$

so that we conclude that

$$E_n = E + n\hbar\omega \tag{7.9}$$

which describes the "quasi-energy" levels [198] of any charged quantum system inside the cavity of a Faraday cage which is being driven by an arbitrary periodic waveform.

Note that this derivation of the spectrum of quasi-energy levels (7.9) applies to the case of *any* periodic potential energy function $U(t)$. However, let us now consider the important special case of a *sinusoidal* time variation of $U(t)$.

The wavefunction of a quantum system inside the Faraday cage such as the ones depicted in Figures 1 and 5, will be phase modulated by the time-varying potential energy in accordance with the time-dependent Schrödinger equation

$$i\hbar\frac{\partial\psi}{\partial t} = H\psi = (H_0 + U(t))\psi \tag{7.10}$$

where the H is the total Hamiltonian, H_0 is the unperturbed Hamiltonian, and $U(t)$ is the potential energy of the quantum system inside the spherical shell, which results, for example, from the injection of the charge $Q(t)$ onto the surface of the spherical metallic shell (i.e., Faraday cage) in Figure 1. Note that $U(t)$ will be independent of the position of any field point in the volume within the shell. Thus

$$U(t) = U_0 \cos\omega t \tag{7.11}$$

for the case of an oscillating charge $Q(t) = Q_0 \cos\omega t$ which is *exterior* to the Faraday cage. However, any field arising from the spatial gradients of $U(t)$ *interior* to the space containing

the quantum system is zero.

Now we shall assume that the quantum system is initially in an unperturbed eigenstate of the unperturbed Hamiltonian H_0, i.e.,

$$H_0\psi = E\psi \tag{7.12}$$

where E is the unperturbed energy level of the system. Since $[H_0, U(t)] = 0$, it follows that the solution to the time-dependent Schrödinger equation is

$$\begin{aligned}\psi(t) &= \psi(0)\, e^{-\frac{i}{\hbar}\left(Et+\int_0^t U(t')dt'\right)} \\ &= \psi(0)\, e^{-\frac{i}{\hbar}Et} e^{-i\varphi(t)}\end{aligned} \tag{7.13}$$

where $\varphi(t)$ is the phase shift of the wavefunction of the system which is associated with the scalar AB effect, i.e.,

$$\varphi(t) = \frac{1}{\hbar}\int_0^t U(t')\, dt' \tag{7.14}$$

in agreement with (2.23). Using the explicit functional form of (7.11) in order to evaluate this integral, we find that

$$\varphi(t) = \alpha \sin \omega t \tag{7.15}$$

where the "FM depth of modulation" α parameter is defined as follows:

$$\alpha = \frac{U_0}{\hbar\omega} \tag{7.16}$$

Thus we find that the wavefunction of the system in the presence of the *interior* potential energy $U(t)$, which is caused, for example, by the *exterior* charge $Q(t)$, will have the form

$$\psi(t) = \psi(0)\, e^{-\frac{i}{\hbar}Et} e^{-i\alpha \sin \omega t} \tag{7.17}$$

Now from the generating function for Bessel functions, one obtains the Jacobi-Anger expansion [201]

$$e^{-i\alpha \sin \omega t} = \sum_{n=-\infty}^{\infty} J_n(\alpha)\, e^{-in\omega t} \tag{7.18}$$

where $J_n(\alpha)$ is the n^{th} order Bessel function of the argument α. The meaning of the index n is that it denotes the n^{th} harmonic sideband of the phase modulated wavefunction, which will end up modifying the quasi-energy level structure of the quantum system. Positive values of n will correspond to upshifted-frequency sidebands, and negative values of n to downshifted-frequency sidebands in the quasi-energy spectrum.

Substituting the Jacobi-Anger expansion into the wavefunction (7.17), we conclude that

$$\begin{aligned}\psi(t) &= \psi(0)\, e^{-\frac{i}{\hbar}Et} \sum_{n=-\infty}^{\infty} J_n(\alpha)\, e^{-in\omega t} \\ &= \psi(0) \sum_{n=-\infty}^{\infty} J_n(\alpha)\, e^{-\frac{i}{\hbar}(E+n\hbar\omega)t} \\ &= \psi(0) \sum_{n=-\infty}^{\infty} J_n(\alpha)\, e^{-\frac{i}{\hbar}E_n t}\end{aligned} \tag{7.19}$$

where the quasi-energy levels E_n are once again given by the expression

$$E_n = E + n\hbar\omega \tag{7.20}$$

7.2 Basic quantum operations for the photon modes

Quantum information processing with photons has been widely studied either with discrete states or continuous variable states. [107, 108] Here, we briefly summarize the basic quantum operations for the photon modes. [124] Two categories of quantum operations are considered: the Bogoliubov-linear operations and the nonlinear interactions. The photon modes are represented by the annihilation (creation) operators $\hat{a}_1$ and $\hat{a}_2$ ($\hat{a}_1^\dagger$ and $\hat{a}_2^\dagger$).

7.2.1 Bogoliubov-linear operations

The Bogoliubov-linear operations perform the following transformation

$$\hat{a}_i \to \sum_j \left(A_{ij}\hat{a}_j + B_{ij}\hat{a}_j^\dagger\right) + C_i \tag{7.21}$$

with coefficients A_{ij}, B_{ij} C_i. An arbitrary Bogoliubov-linear operation can be constructed using the basic elements: the beam-splitter operation, the squeezing operation, and the phase shifter.

The beam-splitter operation can be realized by $H_{\rm bm} = \hbar\chi^{\rm bm} e^{i\phi}\hat{a}_1^\dagger\hat{a}_2 + h.c.$ with coupling amplitude $\chi^{\rm bm}$. Under this Hamiltonian, the operators evolve as

$$\begin{pmatrix} \hat{a}_1(t) \\ \hat{a}_2(t) \end{pmatrix} = \begin{pmatrix} \cos\varphi & -e^{i\phi}\sin\varphi \\ -e^{-i\phi}\sin\varphi & \cos\varphi \end{pmatrix} \begin{pmatrix} \hat{a}_1(0) \\ \hat{a}_2(0) \end{pmatrix} \tag{7.22}$$

with $\varphi = \chi_{\rm bm} t$. At $\varphi = \pi/2$, the beam-splitter operation swaps the states of the two modes up to a phase factor. In discrete-state quantum computing schemes, this operation can generate single-qubit Hadamard gate.

The squeezing operation can be realized by $H_{\rm sq} = i\hbar\chi^{\rm sq}\hat{a}_1^\dagger\hat{a}_2^\dagger + h.c.$ with coupling ampli-

tude $\chi^{\rm sq}$. Under this Hamiltonian, the operators evolve as

$$\begin{pmatrix} \hat{a}_1(t) \\ \hat{a}_2^\dagger(t) \end{pmatrix} = \begin{pmatrix} \cosh\varphi & \sinh\varphi \\ \sinh\varphi & \cosh\varphi \end{pmatrix} \begin{pmatrix} \hat{a}_1(0) \\ \hat{a}_2^\dagger(0) \end{pmatrix} \tag{7.23}$$

with $\varphi = \chi^{\rm sq} t$, which describes the parametric amplification process that generates two-mode squeezing. [124] When applied to the vacuum state, it generates the so-called continuous-variable EPR states. When combined with the beam-splitter operation, it can generate squeezing on individual mode. A related operation is the single-mode squeezing operation which can be generated by $H_{\rm sq1} = i\hbar\chi^{\rm sq1}(\hat{a}^\dagger)_i^2 + h.c.$ on mode $\hat{a}_i$.

The phase shifter operation can be realized by $H_{\rm ph} = \hbar\Delta^{\rm ph}\hat{a}_i^\dagger\hat{a}_i$ which creates a shift in the resonator frequency. The above quantum operations can be combined to generate arbitrary linear transformations in Eq. (7.21).

7.2.2 Cross-Kerr nonlinearity

One nonlinear operation is the cross-Kerr interaction given by $H_{\rm ck} = \hbar\chi^{\rm ck}\hat{a}_1^\dagger\hat{a}_1\hat{a}_2^\dagger\hat{a}_2$ between two modes with interaction amplitude $\chi^{\rm ck}$. This interaction can lead to controlled gates on photon qubits. [107] For continuous-variable schemes, this operation together with the linear operations can generate operations that are arbitrary polynomials of the quadrature variables. [107, 108, 118] This operation can also be exploited for quantum nondemolition measurement on photon states.

7.3 Acknowlegements

For the project scalar AB effect discussed in Chapter 2, we thank Profs. Dan Stamper-Kurn and Chih-Chun Chien for helpful discussions.

The work about the universal quantum degeneracy point, discussed in Chapter 2, is supported by the National Science Foundation under Grant No. NSF-CCF-0916303 and NSF-DMR-0956064. XHD is partially supported by Scholarship from China.

For the project about four-wave mixing toolbox in Chapter 3, we would like to thank Prof. A. N. Korotkov and Prof. A. Lupaşcu for valuable comments on the manuscript. This work is supported by the projects NSF-CCF-0916303 and NSF-DMR-0956064. XHD is partially supported by a CSC Scholarship.

For the project about quantum simulation of sitewise manipulation induced Mott-Superfluid transition discussed in Chapter 4, we thank Lin Tian and Raymond Chiao for valuable advice on this work and Anton Sharybov, Yong Hu, Kevin Mitchell and Jay Sharping for useful discussions. The computations were performed using the resources of the National Energy Research Scientific Computing Center (NERSC) supported by the U.S. Department of Energy, Office of Science, under Contract No. DE-AC02-05CH11231.

Bibliography

[1] M. Johnson, M. Amin, S. Gildert, T. Lanting, F. Hamze, N. Dickson, R. Harris, A. Berkley, J. Johansson, P. Bunyk, et al., Quantum annealing with manufactured spins, Nature 473 (7346) (2011) 194–198.

[2] M. A. Nielsen, I. L. Chuang, Quantum computation and quantum information, Cambridge university press, 2010.

[3] E. G. Rieffel, D. Venturelli, B. OGorman, M. B. Do, E. M. Prystay, V. N. Smelyanskiy, A case study in programming a quantum annealer for hard operational planning problems, Quantum Information Processing 14 (1) (2015) 1–36.

[4] I. Buluta, F. Nori, Quantum simulators, Science 326 (5949) (2009) 108–111.

[5] S. Lloyd, et al., Universal quantum simulators, SCIENCE-NEW YORK THEN WASHINGTON- (1996) 1073–1077.

[6] I. Georgescu, S. Ashhab, F. Nori, Quantum simulation, Reviews of Modern Physics 86 (1) (2014) 153.

[7] B. Josephson, Possible new effects in superconductive tunnelling, Physics Letters 1 (7) (1962) 251 – 253. doi:http://dx.doi.org/10.1016/0031-9163(62)91369-0.
URL http://www.sciencedirect.com/science/article/pii/0031916362913690

[8] M. Tinkham, Introduction to Superconductivity: Second Edition, Dover Books on Physics, Dover Publications, 2004.
URL http://books.google.com/books?id=k6AO9nRYbioC

[9] R. Parks, Superconductivity: Part 1 (In Two Parts), Superconductivity, Taylor & Francis, 1969.
URL http://books.google.com/books?id=jndkBOJhDKQC

[10] T. Van Duzer, C. W. Turner, Principles of superconductive devices and circuits.

[11] M. D. Fiske, Temperature and magnetic field dependences of the josephson tunneling current, Reviews of Modern Physics 36 (1) (1964) 221.

[12] C. Hamilton, Frequency dependence of the josephson current, Physical Review B 5 (3) (1972) 912.

[13] S. Shapiro, Josephson currents in superconducting tunneling: The effect of microwaves and other observations, Physical Review Letters 11 (2) (1963) 80.

[14] M. Levinsen, R. Chiao, M. Feldman, B. Tucker, An inverse ac josephson effect voltage standard, Applied Physics Letters 31 (11) (1977) 776–778.

[15] M. Maezawa, M. Aoyagi, H. Nakagawa, I. Kurosawa, S. Takada, Specific capacitance of nb/alox/nb josephson junctions with critical current densities in the range of 0.1–18 ka/cm2, Applied physics letters 66 (16) (1995) 2134–2136.

[16] E. Tarte, G. Wagner, R. Somekh, F. Baudenbacher, P. Berghuis, J. Evetts, The capacitance of bicrystal josephson junctions deposited on srtio/sub 3/substrates, Applied Superconductivity, IEEE Transactions on 7 (2) (1997) 3662–3665.

[17] A. Kleinsasser, Excess currents and voltages in superconducting junctions, Applied physics letters 62 (2) (1993) 193–195.

[18] Y. Makhlin, G. Schön, A. Shnirman, Quantum-state engineering with josephson-junction devices, Rev. Mod. Phys. 73 (2001) 357–400. doi:10.1103/RevModPhys.73.357.
URL http://link.aps.org/doi/10.1103/RevModPhys.73.357

[19] J. Clarke, F. K. Wilhelm, Superconducting quantum bits, Nature 453 (7198) (2008) 1031–1042.

[20] J. Mooij, T. Orlando, L. Levitov, L. Tian, C. H. Van der Wal, S. Lloyd, Josephson persistent-current qubit, Science 285 (5430) (1999) 1036–1039.

[21] Y. Aharonov, D. Bohm, Significance of electromagnetic potentials in the quantum theory, Physical Review 115 (3) (1959) 485.

[22] A. Walstad, A critical reexamination of the electrostatic aharonov-bohm effect, International Journal of Theoretical Physics 49 (11) (2010) 2929–2934.

[23] A. Van Oudenaarden, M. H. Devoret, Y. V. Nazarov, J. Mooij, Magneto-electric aharonov–bohm effect in metal rings, Nature 391 (6669) (1998) 768–770.

[24] B. Yurke, J. S. Denker, Quantum network theory, Physical Review A 29 (3) (1984) 1419.

[25] M. H. Devoret, Quantum fluctuations in electrical circuits, Les Houches, Session LXIII.

[26] J. M. Martinis, M. H. Devoret, J. Clarke, Energy-level quantization in the zero-voltage state of a current-biased josephson junction, Physical review letters 55 (15) (1985) 1543.

[27]

[28] A. Tonomura, N. Osakabe, T. Matsuda, T. Kawasaki, J. Endo, S. Yano, H. Yamada, Evidence for aharonov-bohm effect with magnetic field completely shielded from electron wave, Physical Review Letters 56 (8) (1986) 792.

[29] M. E. Flatté, et al., Manipulating quantum coherence in solid state systems, Vol. 244, Springer Science & Business Media, 2007.

[30] A. Caldeira, A. J. Leggett, Quantum tunnelling in a dissipative system, Annals of Physics 149 (2) (1983) 374–456.

[31] J. You, F. Nori, Superconducting circuits and quantum information, arXiv preprint quant-ph/0601121.

[32] P. Dutta, P. Horn, Low-frequency fluctuations in solids: 1 f noise, Reviews of Modern physics 53 (3) (1981) 497.

[33] M. Weissman, 1 f noise and other slow, nonexponential kinetics in condensed matter, Reviews of modern physics 60 (2) (1988) 537.

[34] O. Astafiev, Y. A. Pashkin, Y. Nakamura, T. Yamamoto, J. Tsai, Quantum noise in the josephson charge qubit, Physical review letters 93 (26) (2004) 267007.

[35] K. Kakuyanagi, T. Meno, S. Saito, H. Nakano, K. Semba, H. Takayanagi, F. Deppe, A. Shnirman, Dephasing of a superconducting flux qubit, arXiv preprint cond-mat/0609564.

[36] D. Van Harlingen, T. Robertson, B. Plourde, P. Reichardt, T. Crane, J. Clarke, Decoherence in josephson-junction qubits due to critical-current fluctuations, Physical Review B 70 (6) (2004) 064517.

[37] Y. Yu, S.-L. Zhu, G. Sun, X. Wen, N. Dong, J. Chen, P. Wu, S. Han, Quantum jumps between macroscopic quantum states of a superconducting qubit coupled to a microscopic two-level system, Physical review letters 101 (15) (2008) 157001.

[38] A. Zorin, F.-J. Ahlers, J. Niemeyer, T. Weimann, H. Wolf, V. Krupenin, S. Lotkhov, Background charge noise in metallic single-electron tunneling devices, Physical Review B 53 (20) (1996) 13682.

[39] F. Wellstood, C. Urbina, J. Clarke, Flicker (1/f) noise in the critical current of josephson junctions at 0.09–4.2 k, Applied physics letters 85 (22) (2004) 5296–5298.

[40] O. Astafiev, Y. A. Pashkin, Y. Nakamura, T. Yamamoto, J. Tsai, Temperature square dependence of the low frequency 1/f charge noise in the josephson junction qubits, Physical review letters 96 (13) (2006) 137001.

[41] H. Paik, S. Dutta, R. Lewis, T. Palomaki, B. Cooper, R. Ramos, H. Xu, A. Dragt, J. Anderson, C. Lobb, et al., Decoherence in dc squid phase qubits, Physical Review B 77 (21) (2008) 214510.

[42] R. H. Koch, D. P. DiVincenzo, J. Clarke, Model for 1/f flux noise in squids and qubits, Physical review letters 98 (26) (2007) 267003.

[43] M. Constantin, C. Y. Clare, Microscopic model of critical current noise in josephson junctions, Physical review letters 99 (20) (2007) 207001.

[44] T. Lanting, A. Berkley, B. Bumble, P. Bunyk, A. Fung, J. Johansson, A. Kaul, A. Kleinsasser, E. Ladizinsky, F. Maibaum, et al., Geometrical dependence of the low-frequency noise in superconducting flux qubits, Physical Review B 79 (6) (2009) 060509.

[45] I. Martin, L. Bulaevskii, A. Shnirman, Tunneling spectroscopy of two-level systems inside a josephson junction, Physical review letters 95 (12) (2005) 127002.

[46] J. M. Martinis, K. Cooper, R. McDermott, M. Steffen, M. Ansmann, K. Osborn, K. Cicak, S. Oh, D. Pappas, R. Simmonds, et al., Decoherence in josephson qubits from dielectric loss, Physical Review Letters 95 (21) (2005) 210503.

[47] A. D. OConnell, M. Ansmann, R. C. Bialczak, M. Hofheinz, N. Katz, E. Lucero, C. McKenney, M. Neeley, H. Wang, E. M. Weig, et al., Microwave dielectric loss at single photon energies and millikelvin temperatures, Applied Physics Letters 92 (11) (2008) 112903.

[48] M. Neeley, M. Ansmann, R. C. Bialczak, M. Hofheinz, N. Katz, E. Lucero, A. Oconnell, H. Wang, A. Cleland, J. M. Martinis, Process tomography of quantum memory in a josephson-phase qubit coupled to a two-level state, Nature Physics 4 (7) (2008) 523–526.

[49] M. Constantin, C. Y. Clare, J. M. Martinis, Saturation of two-level systems and charge noise in josephson junction qubits, Physical Review B 79 (9) (2009) 094520.

[50] Y. Nakamura, Y. A. Pashkin, T. Yamamoto, J. Tsai, Charge echo in a cooper-pair box, Physical review letters 88 (4) (2002) 047901.

[51] K. Shiokawa, D. Lidar, Dynamical decoupling using slow pulses: Efficient suppression of 1/f noise, Physical Review A 69 (3) (2004) 030302.

[52] H. Gutmann, F. K. Wilhelm, W. M. Kaminsky, S. Lloyd, Compensation of decoherence from telegraph noise by means of an open-loop quantum-control technique, Physical Review A 71 (2) (2005) 020302.

[53] G. Falci, A. DArrigo, A. Mastellone, E. Paladino, Dynamical suppression of telegraph and 1/ f noise due to quantum bistable fluctuators, Physical Review A 70 (4) (2004) 040101.

[54] L. Faoro, L. Viola, Dynamical suppression of 1/f noise processes in qubit systems, Physical review letters 92 (11) (2004) 117905.

[55] D. Vion, A. Aassime, A. Cottet, P. Joyez, H. Pothier, C. Urbina, D. Esteve, M. H. Devoret, Manipulating the quantum state of an electrical circuit, Science 296 (5569) (2002) 886–889.

[56] G. Ithier, E. Collin, P. Joyez, P. Meeson, D. Vion, D. Esteve, F. Chiarello, A. Shnirman, Y. Makhlin, J. Schriefl, et al., Decoherence in a superconducting quantum bit circuit, Physical Review B 72 (13) (2005) 134519.

[57] Y. MAKHLIN, A. SHNIRMAN, Dephasing of solid-state qubits at optimal points, Physical review letters 92 (17) (2004) 178301–1.

[58] L. Tian, Correcting low-frequency noise with continuous measurement, Physical review letters 98 (15) (2007) 153602.

[59] J. Koch, M. Y. Terri, J. Gambetta, A. A. Houck, D. Schuster, J. Majer, A. Blais, M. H. Devoret, S. M. Girvin, R. J. Schoelkopf, Charge-insensitive qubit design derived from the cooper pair box, Physical Review A 76 (4) (2007) 042319.

[60] J. Schreier, A. A. Houck, J. Koch, D. I. Schuster, B. Johnson, J. Chow, J. M. Gambetta, J. Majer, L. Frunzio, M. H. Devoret, et al., Suppressing charge noise decoherence in superconducting charge qubits, Physical Review B 77 (18) (2008) 180502.

[61] V. E. Manucharyan, J. Koch, L. I. Glazman, M. H. Devoret, Fluxonium: Single cooper-pair circuit free of charge offsets, Science 326 (5949) (2009) 113–116.

[62] H. Wang, M. Hofheinz, J. Wenner, M. Ansmann, R. Bialczak, M. Lenander, E. Lucero, M. Neeley, A. OConnell, D. Sank, et al., Improving the coherence time of superconducting coplanar resonators, Applied Physics Letters 95 (23) (2009) 233508.

[63] J. Schrie, Dekoharenz in josephson quantenbits, Ph.D. thesis,.

[64] F. Yoshihara, K. Harrabi, A. Niskanen, Y. Nakamura, J. Tsai, Decoherence of flux qubits due to 1/f flux noise, Physical review letters 97 (16) (2006) 167001.

[65] Y. Makhlin, G. Schön, A. Shnirman, Quantum-state engineering with josephson-junction devices, Reviews of modern physics 73 (2) (2001) 357.

[66] Y. Hu, Z.-W. Zhou, J.-M. Cai, G.-C. Guo, Decoherence of coupled josephson charge qubits due to partially correlated low-frequency noise, Physical Review A 75 (5) (2007) 052327.

[67] J. You, J. Tsai, F. Nori, Scalable quantum computing with josephson charge qubits, Physical review letters 89 (19) (2002) 197902.

[68] D. Averin, C. Bruder, Variable electrostatic transformer: controllable coupling of two charge qubits, Physical review letters 91 (5) (2003) 057003.

[69] S. Saito, T. Meno, M. Ueda, H. Tanaka, K. Semba, H. Takayanagi, Parametric control of a superconducting flux qubit, Physical review letters 96 (10) (2006) 107001.

[70] L. Tian, M. Allman, R. Simmonds, Parametric coupling between macroscopic quantum resonators, New Journal of Physics 10 (11) (2008) 115001.

[71] M. A. Nielsen, A simple formula for the average gate fidelity of a quantum dynamical operation, Physics Letters A 303 (4) (2002) 249–252.

[72] D. A. Lidar, I. L. Chuang, K. B. Whaley, Decoherence-free subspaces for quantum computation, Physical Review Letters 81 (12) (1998) 2594.

[73] A. Blais, R.-S. Huang, A. Wallraff, S. Girvin, R. J. Schoelkopf, Cavity quantum electrodynamics for superconducting electrical circuits: An architecture for quantum computation, Physical Review A 69 (6) (2004) 062320.

[74] A. Baust, E. Hoffmann, M. Haeberlein, M. Schwarz, P. Eder, J. Goetz, F. Wulschner, E. Xie, L. Zhong, F. Quijandria, et al., Ultrastrong coupling in two-resonator circuit qed, arXiv preprint arXiv:1412.7372.

[75] A. Blais, J. Gambetta, A. Wallraff, D. Schuster, S. Girvin, M. Devoret, R. Schoelkopf, Quantum-information processing with circuit quantum electrodynamics, Physical Review A 75 (3) (2007) 032329.

[76] J. Bylander, S. Gustavsson, F. Yan, F. Yoshihara, K. Harrabi, G. Fitch, D. G. Cory, Y. Nakamura, J.-S. Tsai, W. D. Oliver, Noise spectroscopy through dynamical decoupling with a superconducting flux qubit, Nature Physics 7 (7) (2011) 565–570.

[77] P. De Groot, J. Lisenfeld, R. Schouten, S. Ashhab, A. Lupaşcu, C. Harmans, J. Mooij, Selective darkening of degenerate transitions demonstrated with two superconducting quantum bits, Nature Physics 6 (10) (2010) 763–766.

[78] F. Deppe, M. Mariantoni, E. Menzel, A. Marx, S. Saito, K. Kakuyanagi, H. Tanaka, T. Meno, K. Semba, H. Takayanagi, et al., Two-photon probe of the jaynes–cummings model and controlled symmetry breaking in circuit qed, Nature Physics 4 (9) (2008) 686–691.

[79] M. Mariantoni, H. Wang, T. Yamamoto, M. Neeley, R. C. Bialczak, Y. Chen, M. Lenander, E. Lucero, A. Oconnell, D. Sank, et al., Implementing the quantum von neumann architecture with superconducting circuits, Science 334 (6052) (2011) 61–65.

[80] O. Astafiev, A. M. Zagoskin, A. Abdumalikov, Y. A. Pashkin, T. Yamamoto, K. Inomata, Y. Nakamura, J. Tsai, Resonance fluorescence of a single artificial atom, Science 327 (5967) (2010) 840–843.

[81] L. S. Bishop, J. Chow, J. Koch, A. Houck, M. Devoret, E. Thuneberg, S. Girvin, R. Schoelkopf, Nonlinear response of the vacuum rabi resonance, Nature Physics 5 (2) (2009) 105–109.

[82] L. DiCarlo, M. Reed, L. Sun, B. Johnson, J. Chow, J. Gambetta, L. Frunzio, S. Girvin, M. Devoret, R. Schoelkopf, Preparation and measurement of three-qubit entanglement in a superconducting circuit, Nature 467 (7315) (2010) 574–578.

[83] D. Bozyigit, C. Lang, L. Steffen, J. Fink, C. Eichler, M. Baur, R. Bianchetti, P. Leek, S. Filipp, M. Da Silva, et al., Antibunching of microwave-frequency photons observed in correlation measurements using linear detectors, Nature Physics 7 (2) (2011) 154–158.

[84] B. Johnson, M. Reed, A. Houck, D. Schuster, L. S. Bishop, E. Ginossar, J. Gambetta, L. DiCarlo, L. Frunzio, S. Girvin, et al., Quantum non-demolition detection of single microwave photons in a circuit, Nature Physics 6 (9) (2010) 663–667.

[85] N. Bergeal, R. Vijay, V. Manucharyan, I. Siddiqi, R. Schoelkopf, S. Girvin, M. Devoret, Analog information processing at the quantum limit with a josephson ring modulator, Nature Physics 6 (4) (2010) 296–302.

[86] F. Mallet, F. R. Ong, A. Palacios-Laloy, F. Nguyen, P. Bertet, D. Vion, D. Esteve, Single-shot qubit readout in circuit quantum electrodynamics, Nature Physics 5 (11) (2009) 791–795.

[87] R. Schoelkopf, S. Girvin, Wiring up quantum systems, Nature 451 (7179) (2008) 664–669.

[88] J. You, F. Nori, Atomic physics and quantum optics using superconducting circuits, Nature 474 (7353) (2011) 589–597.

[89] M. Hofheinz, H. Wang, M. Ansmann, R. C. Bialczak, E. Lucero, M. Neeley, A. O'Connell, D. Sank, J. Wenner, J. M. Martinis, et al., Synthesizing arbitrary quantum states in a superconducting resonator, Nature 459 (7246) (2009) 546–549.

[90] M. Mariantoni, H. Wang, R. C. Bialczak, M. Lenander, E. Lucero, M. Neeley, A. OConnell, D. Sank, M. Weides, J. Wenner, et al., Photon shell game in three-resonator circuit quantum electrodynamics, Nature Physics 7 (4) (2011) 287–293.

[91] E. Zakka-Bajjani, F. Nguyen, M. Lee, L. R. Vale, R. W. Simmonds, J. Aumentado, Quantum superposition of a single microwave photon in two different/'colour/'states, Nature Physics 7 (8) (2011) 599–603.

[92] S. T. Merkel, F. K. Wilhelm, Generation and detection of noon states in superconducting circuits, New Journal of Physics 12 (9) (2010) 093036.

[93] H. Wang, M. Mariantoni, R. C. Bialczak, M. Lenander, E. Lucero, M. Neeley, A. OConnell, D. Sank, M. Weides, J. Wenner, et al., Deterministic entanglement of photons in two superconducting microwave resonators, Physical review letters 106 (6) (2011) 060401.

[94] S. Aldana, Y.-D. Wang, C. Bruder, Greenberger-horne-zeilinger generation protocol for n superconducting transmon qubits capacitively coupled to a quantum bus, Physical Review B 84 (13) (2011) 134519.

[95] M.-Y. Chen, M. W. Tu, W.-M. Zhang, Entangling two superconducting l c coherent modes via a superconducting flux qubit, Physical Review B 80 (21) (2009) 214538.

[96] Y. Hu, L. Tian, Deterministic generation of entangled photons in superconducting resonator arrays, Physical review letters 106 (25) (2011) 257002.

[97] P.-B. Li, F.-L. Li, Engineering squeezed states of microwave radiation with circuit quantum electrodynamics, Physical Review A 83 (3) (2011) 035807.

[98] M. Mariantoni, F. Deppe, A. Marx, R. Gross, F. K. Wilhelm, E. Solano, Two-resonator circuit quantum electrodynamics: A superconducting quantum switch, Physical Review B 78 (10) (2008) 104508.

[99] G. M. Reuther, D. Zueco, F. Deppe, E. Hoffmann, E. P. Menzel, T. Weißl, M. Mariantoni, S. Kohler, A. Marx, E. Solano, et al., Two-resonator circuit quantum electrodynamics: Dissipative theory, Physical Review B 81 (14) (2010) 144510.

[100] J.-Q. Liao, J.-F. Huang, Y.-x. Liu, L.-M. Kuang, C. Sun, Quantum switch for single-photon transport in a coupled superconducting transmission-line-resonator array, Physical Review A 80 (1) (2009) 014301.

[101] F. W. Strauch, K. Jacobs, R. W. Simmonds, Arbitrary control of entanglement between two superconducting resonators, Physical review letters 105 (5) (2010) 050501.

[102] A. Zagoskin, E. Ilichev, M. McCutcheon, J. F. Young, F. Nori, Controlled generation of squeezed states of microwave radiation in a superconducting resonant circuit, Physical review letters 101 (25) (2008) 253602.

[103] L. Chirolli, G. Burkard, S. Kumar, D. P. DiVincenzo, Superconducting resonators as beam splitters for linear-optics quantum computation, Physical review letters 104 (23) (2010) 230502.

[104] S. Kumar, D. P. DiVincenzo, Exploiting kerr cross nonlinearity in circuit quantum electrodynamics for nondemolition measurements, Physical Review B 82 (1) (2010) 014512.

[105] S. Rebić, J. Twamley, G. J. Milburn, Giant kerr nonlinearities in circuit quantum electrodynamics, Physical review letters 103 (15) (2009) 150503.

[106] C. Deng, J. Gambetta, A. Lupaşcu, Quantum nondemolition measurement of microwave photons using engineered quadratic interactions, Physical Review B 82 (22) (2010) 220505.

[107] P. Kok, W. Munro, K. Nemoto, T. Ralph, J. P. Dowling, G. Milburn, Publisher's note: Linear optical quantum computing with photonic qubits (rev. mod. phys. 79, 135 (2007)), Reviews of Modern Physics 79 (2) (2007) 797.

[108] S. Lloyd, S. L. Braunstein, Quantum computation over continuous variables, Physical Review Letters 82 (8) (1999) 1784.

[109] R. A. Pinto, A. N. Korotkov, M. R. Geller, V. S. Shumeiko, J. M. Martinis, Analysis of a tunable coupler for superconducting phase qubits, Phys. Rev. B 82 (2010) 104522. doi:10.1103/PhysRevB.82.104522.
URL http://link.aps.org/doi/10.1103/PhysRevB.82.104522

[110] Y.-x. Liu, L. Wei, J. Tsai, F. Nori, Controllable coupling between flux qubits, Physical review letters 96 (6) (2006) 067003.

[111] R. Harris, A. Berkley, M. Johnson, P. Bunyk, S. Govorkov, M. Thom, S. Uchaikin, A. Wilson, J. Chung, E. Holtham, et al., Sign-and magnitude-tunable coupler for superconducting flux qubits, Physical review letters 98 (17) (2007) 177001.

[112] E. Ilichev, S. Shevchenko, S. van der Ploeg, M. Grajcar, E. Temchenko, A. Omelyanchouk, H.-G. Meyer, Multiphoton excitations and inverse population in a system of two flux qubits, Physical Review B 81 (1) (2010) 012506.

[113] S. Srinivasan, A. Hoffman, J. Gambetta, A. Houck, Tunable coupling in circuit quantum electrodynamics using a superconducting charge qubit with a v-shaped energy level diagram, Physical review letters 106 (8) (2011) 083601.

[114] H. Paik, D. Schuster, L. S. Bishop, G. Kirchmair, G. Catelani, A. Sears, B. Johnson, M. Reagor, L. Frunzio, L. Glazman, et al., Observation of high coherence in josephson junction qubits measured in a three-dimensional circuit qed architecture, Physical Review Letters 107 (24) (2011) 240501.

[115] Z. Kim, B. Suri, V. Zaretskey, S. Novikov, K. Osborn, A. Mizel, F. Wellstood, B. Palmer, Decoupling a cooper-pair box to enhance the lifetime to 0.2 ms, Physical review letters 106 (12) (2011) 120501.

[116] C. Rigetti, J. M. Gambetta, S. Poletto, B. Plourde, J. M. Chow, A. Córcoles, J. A. Smolin, S. T. Merkel, J. Rozen, G. A. Keefe, et al., Superconducting qubit in a waveguide cavity with a coherence time approaching 0.1 ms, Physical Review B 86 (10) (2012) 100506.

[117] X. Deng, Y. Hu, L. Tian, Protecting superconducting qubits with a universal quantum degeneracy point, Superconductor Science and Technology 26 (11) (2013) 114002.

[118] R. W. Boyd, Nonlinear optics, Academic press, 2003.

[119] A. Sharypov, A. Wilson-Gordon, Narrowband-biphoton generation due to long-lived coherent population oscillations, Physical Review A 84 (3) (2011) 033845.

[120] H. Schmidt, A. Imamoglu, Giant kerr nonlinearities obtained by electromagnetically induced transparency, Optics letters 21 (23) (1996) 1936–1938.

[121] A. Imamolu, H. Schmidt, G. Woods, M. Deutsch, Strongly interacting photons in a nonlinear cavity, Physical Review Letters 79 (8) (1997) 1467.

[122] F. G. Brandao, M. J. Hartmann, M. B. Plenio, Light-shift-induced photonic nonlinearities, New Journal of Physics 10 (4) (2008) 043010.

[123] M. J. Hartmann, M. B. Plenio, Strong photon nonlinearities and photonic mott insulators, Physical review letters 99 (10) (2007) 103601.

[124] Y. Shih, An introduction to quantum optics, CRC press, 2011.

[125] J. Drummond, The anharmonic oscillator: perturbation series for cubic and quartic energy distortion, Journal of Physics A: Mathematical and General 14 (7) (1981) 1651.

[126] F. W. Strauch, Theory of superconducting phase qubits.

[127] R. Barends, L. Lamata, J. Kelly, L. García-Álvarez, A. Fowler, A. Megrant, E. Jeffrey, T. White, D. Sank, J. Mutus, et al., Digital quantum simulation of fermionic models with a superconducting circuit, arXiv preprint arXiv:1501.07703.

[128] I. Bloch, J. Dalibard, S. Nascimbène, Quantum simulations with ultracold quantum gases, Nature Physics 8 (4) (2012) 267–276.

[129] R. Blatt, C. Roos, Quantum simulations with trapped ions, Nature Physics 8 (4) (2012) 277–284.

[130] P. Schindler, M. Müller, D. Nigg, J. T. Barreiro, E. A. Martinez, M. Hennrich, T. Monz, S. Diehl, P. Zoller, R. Blatt, Quantum simulation of dynamical maps with trapped ions, Nature Physics 9 (6) (2013) 361–367.

[131] J. Cai, A. Retzker, F. Jelezko, M. B. Plenio, A large-scale quantum simulator on a diamond surface at room temperature, Nature Physics 9 (3) (2013) 168–173.

[132] A. Aspuru-Guzik, P. Walther, Photonic quantum simulators, Nature Physics 8 (4) (2012) 285–291.

[133] M. Devoret, R. Schoelkopf, Superconducting circuits for quantum information: an outlook, Science 339 (6124) (2013) 1169–1174.

[134] A. A. Houck, H. E. Türeci, J. Koch, On-chip quantum simulation with superconducting circuits, Nature Physics 8 (4) (2012) 292–299.

[135] J. Mooij, Coherence in superconducting networks, Physica B: condensed matter 152 (1/2).

[136] R. Fazio, H. Van Der Zant, Quantum phase transitions and vortex dynamics in superconducting networks, Physics Reports 355 (4) (2001) 235–334.

[137] C. Bruder, R. Fazio, G. Schön, The bose-hubbard model: from josephson junction arrays to optical lattices, Annalen der Physik 14 (9-10) (2005) 566–577.

[138] M. Reagor, H. Paik, G. Catelani, L. Sun, C. Axline, E. Holland, I. M. Pop, N. A. Masluk, T. Brecht, L. Frunzio, et al., Reaching 10 ms single photon lifetimes for superconducting aluminum cavities, Applied Physics Letters 102 (19) (2013) 192604.

[139] R. Barends, J. Kelly, A. Megrant, A. Veitia, D. Sank, E. Jeffrey, T. White, J. Mutus, A. Fowler, B. Campbell, et al., Superconducting quantum circuits at the surface code threshold for fault tolerance, Nature 508 (7497) (2014) 500–503.

[140] J. M. Chow, J. M. Gambetta, E. Magesan, D. W. Abraham, A. W. Cross, B. Johnson, N. A. Masluk, C. A. Ryan, J. A. Smolin, S. J. Srinivasan, et al., Implementing a strand of a scalable fault-tolerant quantum computing fabric, Nature communications 5.

[141] A. Baust, E. Hoffmann, M. Haeberlein, M. J. Schwarz, P. Eder, J. Goetz, F. Wulschner, E. Xie, L. Zhong, F. Quijandría, B. Peropadre, D. Zueco, J.-J. García Ripoll, E. Solano, K. Fedorov, E. P. Menzel, F. Deppe, A. Marx, R. Gross, Tunable and switchable coupling between two superconducting resonators, Phys. Rev. B 91 (2015) 014515. doi:10.1103/PhysRevB.91.014515.
URL http://link.aps.org/doi/10.1103/PhysRevB.91.014515

[142] R. Bialczak, M. Ansmann, M. Hofheinz, M. Lenander, E. Lucero, M. Neeley, A. OConnell, D. Sank, H. Wang, M. Weides, et al., Fast tunable coupler for superconducting qubits, Physical review letters 106 (6) (2011) 060501.

[143] Y. Chen, C. Neill, P. Roushan, N. Leung, M. Fang, R. Barends, J. Kelly, B. Campbell, Z. Chen, B. Chiaro, et al., Qubit architecture with high coherence and fast tunable coupling, Physical review letters 113 (22) (2014) 220502.

[144] S. Schmidt, J. Koch, Circuit qed lattices: towards quantum simulation with superconducting circuits, Annalen der Physik 525 (6) (2013) 395–412.

[145] M. Leib, M. J. Hartmann, Bose–hubbard dynamics of polaritons in a chain of circuit quantum electrodynamics cavities, New Journal of Physics 12 (9) (2010) 093031.

[146] A. van Oudenaarden, J. Mooij, One-dimensional mott insulator formed by quantum vortices in josephson junction arrays, Physical review letters 76 (26) (1996) 4947.

[147] O. Viehmann, J. von Delft, F. Marquardt, Observing the nonequilibrium dynamics of the quantum transverse-field ising chain in circuit qed, Physical review letters 110 (3) (2013) 030601.

[148] J. You, Z. Wang, W. Zhang, F. Nori, Encoding a qubit with majorana modes in superconducting circuits, Scientific reports 4.

[149] M. P. Fisher, P. B. Weichman, G. Grinstein, D. S. Fisher, Boson localization and the superfluid-insulator transition, Physical Review B 40 (1) (1989) 546.

[150] W. S. Bakr, J. I. Gillen, A. Peng, S. Fölling, M. Greiner, A quantum gas microscope for detecting single atoms in a hubbard-regime optical lattice, Nature 462 (7269) (2009) 74–77.

[151] W. S. Bakr, A. Peng, M. E. Tai, R. Ma, J. Simon, J. I. Gillen, S. Foelling, L. Pollet, M. Greiner, Probing the superfluid–to–mott insulator transition at the single-atom level, Science 329 (5991) (2010) 547–550.

[152] M. J. Hartmann, F. G. Brandao, M. B. Plenio, Quantum many-body phenomena in coupled cavity arrays, Laser & Photonics Reviews 2 (6) (2008) 527–556.

[153] J. Koch, K. Le Hur, Superfluid–mott-insulator transition of light in the jaynes-cummings lattice, Physical Review A 80 (2) (2009) 023811.

[154] M. J. Hartmann, F. G. Brandao, M. B. Plenio, Strongly interacting polaritons in coupled arrays of cavities, Nature Physics 2 (12) (2006) 849–855.

[155] A. D. Greentree, C. Tahan, J. H. Cole, L. C. Hollenberg, Quantum phase transitions of light, Nature Physics 2 (12) (2006) 856–861.

[156] S.-L. Zhu, Z.-D. Wang, Y.-H. Chan, L.-M. Duan, Topological bose-mott insulators in a one-dimensional optical superlattice, Physical review letters 110 (7) (2013) 075303.

[157] F. Grusdt, M. Höning, M. Fleischhauer, Topological edge states in the one-dimensional superlattice bose-hubbard model, Physical review letters 110 (26) (2013) 260405.

[158] M. H. Devoret, J. M. Martinis, Implementing qubits with superconducting integrated circuits., Quantum Information Processing 3.

[159] J. Zhang, R. Dong, Exact diagonalization: the bose–hubbard model as an example, European Journal of Physics 31 (3) (2010) 591.

[160] E. T. Jaynes, F. W. Cummings, Comparison of quantum and semiclassical radiation theories with application to the beam maser, Proceedings of the IEEE 51 (1) (1963) 89–109.

[161] D. G. Angelakis, M. F. Santos, S. Bose, Photon-blockade-induced mott transitions and x y spin models in coupled cavity arrays, Physical Review A 76 (3) (2007) 031805.

[162] K. Seo, L. Tian, Quantum phase transition in a multi-connected superconducting jaynes-cummings lattice, arXiv preprint arXiv:1408.2304.

[163] A. Houck, D. Schuster, J. Gambetta, J. Schreier, B. Johnson, J. Chow, L. Frunzio, J. Majer, M. Devoret, S. Girvin, et al., Generating single microwave photons in a circuit, Nature 449 (7160) (2007) 328–331.

[164] A. Sharypov, X. Deng, L. Tian, Parametric four-wave mixing toolbox for superconducting resonators, Physical Review B 86 (1) (2012) 014516.

[165] B. Peropadre, D. Zueco, F. Wulschner, F. Deppe, A. Marx, R. Gross, J. J. García-Ripoll, Tunable coupling engineering between superconducting resonators: From sidebands to effective gauge fields, Physical Review B 87 (13) (2013) 134504.

[166] S. Sachdev, Quantum phase transitions, Wiley Online Library, 2007.

[167] L. C. Venuti, M. Cozzini, P. Buonsante, F. Massel, N. Bray-Ali, P. Zanardi, Fidelity approach to the hubbard model, Physical Review B 78 (11) (2008) 115410.

[168] C. Jia, B. Moritz, C.-C. Chen, B. S. Shastry, T. Devereaux, Fidelity study of the superconducting phase diagram in the two-dimensional single-band hubbard model, Physical Review B 84 (12) (2011) 125113.

[169] M. Rigol, B. Sriram Shastry, S. Haas, Effects of strong correlations and disorder in d-wave superconductors, Physical Review B: Condensed Matter and Materials Physics 79 (5) (2009) 052502_1–052502_4.

[170] L. C. Venuti, P. Zanardi, Quantum critical scaling of the geometric tensors, Physical review letters 99 (9) (2007) 095701.

[171] W.-L. You, Y.-W. Li, S.-J. Gu, Fidelity, dynamic structure factor, and susceptibility in critical phenomena, Physical Review E 76 (2) (2007) 022101.

[172] P. Zanardi, N. Paunković, Ground state overlap and quantum phase transitions, Physical Review E 74 (3) (2006) 031123.

[173] D. L. Underwood, W. E. Shanks, J. Koch, A. A. Houck, Low-disorder microwave cavity lattices for quantum simulation with photons, Physical Review A 86 (2) (2012) 023837.

[174] I. Danshita, A. Polkovnikov, Superfluid-to-mott-insulator transition in the one-dimensional bose-hubbard model for arbitrary integer filling factors, Physical Review A 84 (6) (2011) 063637.

[175] S. Ejima, H. Fehske, F. Gebhard, Dynamic properties of the one-dimensional bose-hubbard model, EPL (Europhysics Letters) 93 (3) (2011) 30002.

[176] A. Wallraff, D. I. Schuster, A. Blais, L. Frunzio, R.-S. Huang, J. Majer, S. Kumar, S. M. Girvin, R. J. Schoelkopf, Strong coupling of a single photon to a superconducting qubit using circuit quantum electrodynamics, Nature 431 (7005) (2004) 162–167.

[177] M. Grajcar, S. Van der Ploeg, A. Izmalkov, E. Ilichev, H.-G. Meyer, A. Fedorov, A. Shnirman, G. Schön, Sisyphus cooling and amplification by a superconducting qubit, Nature physics 4 (8) (2008) 612–616.

[178] S. O. Valenzuela, W. D. Oliver, D. M. Berns, K. K. Berggren, L. S. Levitov, T. P. Orlando, Microwave-induced cooling of a superconducting qubit, Science 314 (5805) (2006) 1589–1592.

[179] J. You, Y.-x. Liu, F. Nori, Simultaneous cooling of an artificial atom and its neighboring quantum system, Physical review letters 100 (4) (2008) 047001.

[180] Y. Chen, P. Roushan, D. Sank, C. Neill, E. Lucero, M. Mariantoni, R. Barends, B. Chiaro, J. Kelly, A. Megrant, et al., Emulating weak localization using a solid-state quantum circuit, Nature communications 5.

[181] C. Lang, C. Eichler, L. Steffen, J. Fink, M. Woolley, A. Blais, A. Wallraff, Correlations, indistinguishability and entanglement in hong-ou-mandel experiments at microwave frequencies, Nature Physics 9 (6) (2013) 345–348.

[182] D. Riste, M. Dukalski, C. Watson, G. de Lange, M. Tiggelman, Y. M. Blanter, K. Lehnert, R. Schouten, L. DiCarlo, Deterministic entanglement of superconducting qubits by parity measurement and feedback, Nature 502 (7471) (2013) 350–354.

[183] Y. Yin, Y. Chen, D. Sank, P. OMalley, T. White, R. Barends, J. Kelly, E. Lucero, M. Mariantoni, A. Megrant, et al., Catch and release of microwave photon states, Physical review letters 110 (10) (2013) 107001.

[184] A. Niskanen, K. Harrabi, F. Yoshihara, Y. Nakamura, S. Lloyd, J. Tsai, Quantum coherent tunable coupling of superconducting qubits, Science 316 (5825) (2007) 723–726.

[185] M. Mirrahimi, Z. Leghtas, V. V. Albert, S. Touzard, R. J. Schoelkopf, L. Jiang, M. H. Devoret, Dynamically protected cat-qubits: a new paradigm for universal quantum computation, New Journal of Physics 16 (4) (2014) 045014.

[186] A. Sarlette, J.-M. Raimond, M. Brune, P. Rouchon, Stabilization of nonclassical states of the radiation field in a cavity by reservoir engineering, Physical review letters 107 (1) (2011) 010402.

[187] A. Roy, Z. Leghtas, A. D. Stone, M. Devoret, M. Mirrahimi, Continuous generation and stabilization of mesoscopic field superposition states in a quantum circuit, Physical Review A 91 (1) (2015) 013810.

[188] Z. Leghtas, S. Touzard, I. M. Pop, A. Kou, B. Vlastakis, A. Petrenko, K. M. Sliwa, A. Narla, S. Shankar, M. J. Hatridge, et al., Confining the state of light to a quantum manifold by engineered two-photon loss, arXiv preprint arXiv:1412.4633.

[189] M. Atala, M. Aidelsburger, J. T. Barreiro, D. Abanin, T. Kitagawa, E. Demler, I. Bloch, Direct measurement of the zak phase in topological bloch bands, Nature Physics 9 (12) (2013) 795–800.

[190] A. Polkovnikov, K. Sengupta, A. Silva, M. Vengalattore, Colloquium: Nonequilibrium dynamics of closed interacting quantum systems, Reviews of Modern Physics 83 (3) (2011) 863.

[191] M. Cazalilla, R. Citro, T. Giamarchi, E. Orignac, M. Rigol, One dimensional bosons: From condensed matter systems to ultracold gases, Reviews of Modern Physics 83 (4) (2011) 1405.

[192] C.-C. Chien, M. Di Ventra, M. Zwolak, Landauer, kubo, and microcanonical approaches to quantum transport and noise: A comparison and implications for cold-atom dynamics, Physical Review A 90 (2) (2014) 023624.

[193] X. Deng, C. Jia, C.-C. Chien, Sitewise manipulations and mott insulator-superfluid transition of interacting photons using superconducting circuit simulators, Phys. Rev. B 91 (2015) 054515.

[194] P. Lähteenmäki, G. Paraoanu, J. Hassel, P. J. Hakonen, Dynamical casimir effect in a josephson metamaterial, Proceedings of the National Academy of Sciences 110 (11) (2013) 4234–4238.

[195] J. Teufel, T. Donner, D. Li, J. Harlow, M. Allman, K. Cicak, A. Sirois, J. D. Whittaker, K. Lehnert, R. W. Simmonds, Sideband cooling of micromechanical motion to the quantum ground state, Nature 475 (7356) (2011) 359–363.

[196] C. Wilson, G. Johansson, A. Pourkabirian, M. Simoen, J. Johansson, T. Duty, F. Nori, P. Delsing, Observation of the dynamical casimir effect in a superconducting circuit, Nature 479 (7373) (2011) 376–379.

[197] C. Kittel, P. McEuen, P. McEuen, Introduction to solid state physics, Vol. 8, Wiley New York, 1976.

[198] Y. B. Zel'Dovich, The quasienergy of a quantum-mechanical system subjected to a periodic action, Soviet Physics JETP 24 (5) (1967) 1006–1008.

[199] M. Silveri, J. Tuorila, M. Kemppainen, E. Thuneberg, Probe spectroscopy of quasienergy states, Physical Review B 87 (13) (2013) 134505.

[200] F. Wilczek, Quantum time crystals, Physical review letters 109 (16) (2012) 160401.

[201] M. Abramowitz, I. A. Stegun, et al., Handbook of mathematical functions, Vol. 1, Dover New York, 1972.